THE UNIVERSITY *of* EDINBURGH

Studies of the Higgs boson using the $H \to ZZ \to 4l$ decay channel with the ATLAS detector at the LHC

Francisca Garay Walls

Doctor of Philosophy
The University of Edinburgh
August 2016

Abstract

Following the announcement of the discovery of a new particle on the 4th of July 2012 at the ATLAS and CMS experiments at the LHC [1, 2], many efforts were needed for the understanding of its properties and to discern whether it is the Standard Model Higgs boson.

The research presented in this thesis is based on the $H \rightarrow ZZ^{(*)} \rightarrow 4l$ decay channel. Three main contributions are discussed: the Standard Model Higgs boson mass measurement, the search for a heavy Higgs boson, and lastly, the implementation of a kinematic likelihood fitter as a new approach to improve the invariant mass resolution of the final states.

The Standard Model Higgs boson mass measurement is presented. The measured mass is $124.51 \pm 0.52(\text{stat}) \pm 0.06(\text{syst})$ GeV [3] for the combined data taken during 2011 and 2012 (4.6 fb^{-1} at 7 TeV and 20.7 fb^{-1} at 8 TeV). Contributing to the mass measurement, a tool was developed to validate the model used by generating several pseudo datasets from Monte Carlo samples and fitting them with the profile likelihood. The results show that the model is correct and only small deviations are seen in the parameters of interest, m_H, and the signal strength, μ. Studies in the asymptotic limit show that these deviations are a symptom of low statistics in some of the final states.

The search for a heavy Higgs boson is presented as well. No significant excess of events over the Standard Model prediction is found. A simultaneous fit to the profile likelihood gives 95% confidence level upper limits on the production cross-section of a heavy Higgs times the branching ratio to Z boson pairs in the mass range from 140 GeV to 1 TeV. Contributing to this search, a pseudo dataset, called Asimov dataset, is created from the Monte Carlo samples to test the profile likelihood fits and validate the model used. The results show that fit the model is correct. In addition, the limits are also interpreted in the context of Type I and Type II Two Higgs Doublet Models (2HDM).

Finally, a Kinematic Likelihood Fitter (KLFitter) is studied and used to constrain

the Z boson mass as an alternative to the standard tool used for the 2011 and 2012 measurement. This affects the distribution of the invariant mass, m_{4l}, from which the Higgs boson mass is inferred. Small improvements are seen in the invariant mass resolution when higher hypothetical Higgs boson masses are considered.

Lay summary

The understanding of the complex structure of nature at the smallest scales has been pursued throughout history. The most accepted current theory that describes this is called the Standard Model. This theory predicts the existence of a neutral boson, called the Higgs boson, which is key to explaining how fundamental particles acquire mass. The search and discovery of this boson was an essential piece of this theory. The design of the Large Hadron Collider (LHC) and the ATLAS experiment at CERN were inspired by this and the discovery came true in 2012. It was first observed with a mass of around 125 GeV by the ATLAS and CMS experiments at the LHC. Since then, many efforts have been combined to determine the properties of this new particle and to discern if it is the Higgs boson predicted by the Standard Model theory or not.

The Higgs boson is studied by its decay products, which allow us to reconstruct the decay chain back to the Higgs boson itself, and therefore to calculate its properties like the mass. One of the decay channels is into a pair of Z bosons, which themselves can decay into leptons (only electrons or muons are considered). All the research presented on this thesis is based on this decay chain.

Three main contributions are discussed: The Standard Model Higgs boson mass measurement, the search of an additional and heavier Higgs boson (assuming that there is physics beyond the Standard Model) and finally, the implementation of a Kinematic Likelihood Fitter as a new approach to improve the precision of the Higgs boson mass measurement.

The Standard Model Higgs boson mass measurement is presented in detail. The measured mass is 124.53 GeV, with a statistical error of 0.5 GeV and a systematic error of 0.06 GeV for the combined data taken during 2011 and 2012. To infer the mass a model is constructed assuming that we know how the observed data are going to behave (using simulations), therefore an extensive validation of it is needed. Contributing to this, a tool was developed to perform several fits to the mass given artificial simulated

datasets where a hypothetical Higgs mass is known. The results validate the model is correct and only small deviations from the input mass are seen. As the probability of producing a Higgs boson is very low in this channel, low statistics are expected in the decay final states. Therefore, by creating high statistic artificial datasets, it is shown that these deviations are a symptom of too few events in some of the Higgs boson decay final states.

Besides the Standard Model, there are other theories that predict the existence of more than one Higgs boson. These are also addressed by the ATLAS experiment. A search looking for additional and heavier Higgs bosons was conducted and is presented in detail as well. There is no evidence of a heavier boson. From this, upper limits for the rate of the production of a heavier Higgs boson times the probability of it decaying into a pair of Z bosons are calculated. The search was performed in the mass range from 140 GeV to 1 TeV. The model used for this search had to be validated as well. For this a different approach from the mass measurement was taken. The model is fitted to only one artificial dataset, created from the simulated samples from where the model was constructed. The results validate the model. In addition, the calculated upper limits are interpreted in a beyond the Standard Model theory called the Two Higgs Doublet Model (2HDM).

Finally, a fitter that constructs a likelihood based on the kinematics of particle decays (Kinematic Likelihood Fitter or KLFitter) is studied and used to obtain a better calculation of the Z boson mass involved in the decay chain. This is explored as an alternative to the standard approach used for the data taken during 2011 and 2012. Having a better measurement of the Z boson mass gives a better calculation of the invariant mass from which the Higgs boson mass is extracted. Small improvements are seen in the Higgs boson mass precision as higher hypothetical Higgs boson masses are considered.

For Teo.

Declaration

This dissertation is the result of my own work, except where explicit reference is made to the work of others, and has not been submitted for another qualification to this or any other university.

(*Francisca Garay Walls, August 2016*)

Acknowledgements

First, I would like to thank my parents because without them I would not be where I am today. To my brother and sister for all their love and support. Especially, I would like to thank my husband, Juan Pablo, for always being there when I needed him and helping me to improve myself everyday and, also, to my son, Teo, who makes my days brighter and happier. I would like to also thanks my friends: Sebastián and Claudia for their support and friendship throughout these years.

Finally, I want to thank all the professors, post-docs and PhD students for all the support that they gave me over these 5 years, especially to Philip Clark, Robert Harrington and Nick Edwards, who gave me the opportunity to work with them and also for their unconditional support.

This work was funded by CONICYT via the "Capital Humano Avanzado" scholarship.

Contents

Abstract i

Lay summary iii

Declaration vii

Acknowledgements ix

1 Introduction 1

2 The Higgs boson: theoretical foundations 3

2.1 The Standard Model 3

2.1.1 Quantum electrodynamics 4

2.1.2 Quantum chromodynamics 5

2.1.3 Electroweak interactions 6

2.2 The Higgs-Brout-Englert mechanism 9

2.2.1 Gauge bosons 11

2.2.2 Fermions 11

2.2.3 The theoretical Higgs mass 12

2.3 Production mechanisms 14

2.4 Decay modes 16

2.5 The Standard Model Higgs boson today 19

2.6 Beyond the Standard Model: the Two Higgs Doublet Model 22

3 The Large Hadron Collider and the ATLAS detector 27

3.1 The Large Hadron Collider 27

3.2 The ATLAS experiment 30

3.2.1 Coordinate system 31

3.2.2 Magnet system 33

3.2.3 The inner detector 34

3.2.4 Calorimetry system 41

3.2.5 The muon spectrometer 45

3.2.6 Forward detectors 48

3.2.7 Trigger and data 48

4 Statistics for searches at the ATLAS detector 53

4.1 Formalism 53

4.2 Tests based on the profile likelihood ratio 55

4.3 Approximate pdf distribution for the test statistic t_μ 57

4.4 Distribution of q_0 and q_μ 59

4.5 The CL_s method 60

4.6 Treatment of nuisance parameters 61

5 The $H \to ZZ^{(*)} \to 4l$ channel 63

5.1 The features of the signal and the background 63

5.2 Event selection 67

5.2.1 Trigger 67

5.2.2 Electron reconstruction 69

5.2.3 Electron identification 70

5.2.4 Improvements in the electron energy calibration 72

5.2.5 Muon reconstruction and identification 74

5.2.6 Jet reconstruction and identification 76

5.2.7 Candidates 77

5.2.8 The ZZ discriminant 79
5.3 Mass resolution 81
5.3.1 Final state radiation recovery 83
5.3.2 Z mass constraint 84
5.4 The estimation of the reducible background 84
5.4.1 The $ll + \mu\mu$ background estimate 85
5.4.2 The $ll + ee$ background estimate 86
5.4.3 Reducible background in the range $110 < m_{4l} < 140$ GeV 87

6 The Standard Model Higgs boson mass measurement 89
6.1 Data samples 89
6.1.1 Collision data 89
6.1.2 Monte Carlo samples 90
6.2 Signal modelling 92
6.2.1 Signal probability distribution function from MC 92
6.2.2 Continuous parametrisation in m_H of signal shapes 93
6.3 Irreducible background modelling 96
6.4 Reducible background modelling 96
6.5 Systematic uncertainties 97
6.6 The model for the mass and signal strength measurements 99
6.7 Validation studies for the models 102
6.7.1 Pseudo-experiments for the Higgs boson mass measurement 102
6.8 Mass and signal strength measurement results 110
6.8.1 The systematic uncertainty 113

7 Search for an additional heavy Higgs boson in the $H \to ZZ^{(*)} \to 4l$ channel 115
7.1 Data samples 115
7.1.1 Monte Carlo samples 116

7.2 Event categorisation 120
7.3 Irreducible background modelling 121
7.4 Reducible background estimation and modelling 123
7.5 Signal modelling 123
7.6 Systematic uncertainties 126
7.7 Statistical interpretation of the model 129
7.7.1 MC statistical and systematic uncertainties 130
7.8 Validation studies for the model 131
7.8.1 Study of the effect of the inclusion of the 125 GeV Higgs boson in the background model 132
7.8.2 Validation by fitting to the MC Asimov data 133
7.9 Cross-section limits in the Narrow Width Approximation 135
7.10 Two Higgs Doublet Model interpretations 137
7.10.1 Overview of the combined search 138
7.10.2 Combined cross-section times branching ratio limits in the Narrow Width Approximation 139
7.10.3 2HDM interpretations 140

8 Kinematic Likelihood Fitter tool with the Z mass constraint 145

8.1 The Z mass constraint 145
8.2 The Kinematic Likelihood Fitter 148
8.3 Permutations and first results 149
8.4 Results using the KLFitter through pseudo-experiments 151
8.4.1 Results for $110 < m_{4l} < 140$ GeV 153
8.4.2 Results for $140 < m_{4l} < 500$ GeV 153
8.5 Possible improvements of the results 154

9 Conclusions 159

Bibliography 161

List of Figures 169

List of Tables 177

Chapter 1

Introduction

The Large Hadron Collider (LHC) together with its detectors at CERN was built to achieve a fuller understanding of nature and its interactions. One of the main purposes of the LHC is to probe the experimental consistency of the Standard Model (SM), where the understanding of the electroweak symmetry breaking mechanism (EWSB) is an essential aspect. The EWSB mechanism is used in the SM to give mass to the fundamental particles and introduces a new scalar boson, called the Higgs boson. The mass of this particle cannot be predicted by the theory, therefore its experimental discovery was of great importance. This was achieved by the ATLAS and CMS experiments on the 4th of July, 2012, when both claimed that a new particle was discovered with a mass of approximately 125 GeV [1, 2].

Among the possible decays of the Higgs boson, the one characterised by four leptons in its final state (electrons and muons) from the intermediate $ZZ^{(*)}$ state is extremely relevant despite its low branching ratio. This is due to its clean decay signature with energetic and isolated leptons that give a reduced background rate and an excellent mass resolution. In addition, all the decay products can be fully reconstructed. This thesis is based on studies of the Higgs boson in this decay chain: $H \to ZZ^{(*)} \to 4l$.

Chapter 2 introduces the Standard Model (SM) of particle physics. Beginning with the fundamentals of Quantum Field Theory it then explores the electroweak interactions showing that the Lagrangian only contains massless fields. Here, is where the Higgs-Brout-Englert mechanism takes its part and provides masses to the massless fields with a caveat: it predicts the existence of a new particle, the Higgs boson. The theoretical limits on the Higgs boson mass are described and an overview of its different production and decay modes is given. In addition, the current ATLAS results of the discovered

Higgs boson and the measurement of its properties are presented. Lastly, an extension of the SM Higgs sector is introduced with two Higgs doublets, called the Two Higgs Doublet Model (2HDM), and its theoretical foundations.

Chapter 3 is an overview of the Large Hadron Collider (LHC) and the ATLAS detector, discussing the design parameters and different ATLAS subdetectors with their role in particle identification and measurement.

In Chapter 4, an introduction is given to the statistical methods used to test the existence of a signal. This serves as an introduction to the fit employed in the Higgs boson mass measurement, and the upper limits in the search of an additional heavy Higgs boson, using the $H \to ZZ^{(*)} \to 4l$ decay channel.

Chapter 5 serves as an introduction to the $H \to ZZ^{(*)} \to 4l$ decay channel, describing the signal, its most important backgrounds and the invariant mass spectrum. The ATLAS object reconstruction and the event selection are explained. The full chapter is a common ground for the analysis in the two following chapters.

Chapters 6 and 7 describe two analysis in detail. The former reports the latest SM Higgs boson mass measurement in the ATLAS detector, starting with the description of how the model was built to finally showing the results. The work done by myself includes a validation of the models, through pseudo-experiments, used to infer the mass and the signal strength. The latter reports the latest result on the search for an additional heavy Higgs boson for the same four lepton final state. It starts with a description of the model and finishes by setting 95% CL upper limits on the cross-section times branching ratio. Also, the validation of the model used in this search, through a pseudo-dataset, called the Asimov dataset, is shown. Finally, interpretations in the context of the Type I and II models of the 2HDM are established. This last two parts were my contribution to the search.

Last, but not least, Chapter 8 shows a study using the Kinematic Likelihood Fitter with the Z mass constraint using the $H \to ZZ^{(*)} \to 4l$ decay channel, which was completely done by myself. It starts with a description of the Z mass constraint used in both analyses described in this thesis and an introduction to the Kinematic Likelihood Fitter. Results are presented through pseudo-experiments for two models, one representing the KLFitter results and the other the standard approach (the one used for the analysis previously discussed). Finally, improvements on these results are discussed proposing a new approach.

Chapter 2

The Higgs boson: theoretical foundations

2.1 The Standard Model

In nature there are four known forces: electromagnetic, weak, strong and gravitational. The first three are dominant at the elementary particle physics scale. The Standard Model (SM) describes the matter, at subatomic level, and its interactions, through the first three forces, by using Quantum field theory (QFT). The SM is the best description of the strong and electroweak interactions.

Particles in QFT are described by local fields $\psi(x)$ evaluated in space-time. The dynamics are illustrated using the Lagrangian density $\mathcal{L}(\psi, \partial_\mu \psi)$ and the classical Euler-Lagrange equations of motion are determined by requiring the action

$$S = \int d^4x \mathcal{L}(\psi, \partial_\mu \psi) \tag{2.1}$$

to be stationary ($\delta S = 0$). Every local continuous transformation of the fields $\psi(x)$, where δS remains unchanged, forms a continuous group of QFT called the gauge group. The gauge structure of the Lagrangian density of the SM is motivated by the observed symmetries in nature. Since, by Noether's theorem, each continuous symmetry of the Lagrangian density leads to a conserved current, observed symmetries are accounted for by symmetries of $\mathcal{L}$ under field transformation operator, U. For example, a conserved current is the electric charge, which is conserved always. This conservation law follows from, and it is represented by, the invariance of the Lagrangian density with respect to

the unitary gauge transformation: $\psi(x) \rightarrow U\psi(x)$.

The SM is a gauge theory with a Lagrangian density,

$$\mathcal{L}_{\mathrm{SM}} = \mathcal{L}_{\mathrm{QCD}} + \mathcal{L}_{\mathrm{EW}}, \tag{2.2}$$

where the first term is the Lagrangian density representing the strong interaction between quarks and gluons modelled by the theory of Quantum Chromodynamics (QCD). The second term represents the weak interaction described by the Electroweak (EW) theory. Equation (2.2) is locally invariant under gauge transformations that belong to the symmetry group

$$\mathrm{SU(3)_C} \otimes \mathrm{SU(2)_L} \otimes \mathrm{U(1)_Y}. \tag{2.3}$$

The $\mathrm{SU(3)_C}$ group refers to colour, which is the conserved charge in QCD. The $SU(2)_L \otimes U(1)_Y$ group refers to electroweak interactions, where $SU(2)_L$ refers to the weak isospin charge conservation, while $U(1)_Y$ to the hypercharge.

2.1.1 Quantum electrodynamics

Quantum electrodynamics (QED) is an Abelian gauge theory which describes light (photons) interacting with matter. The ingredients here are:

- An electrically charged particle with spin 1/2 and mass m represented by the field, ψ.
- An electromagnetic (EM) field for the photon represented by a massless vector boson field, A^μ.

The QED Lagrangian density is

$$\mathcal{L}_{QED} = -\frac{1}{4}F^{\mu\nu}F_{\mu\nu} + \bar{\psi}(i\gamma^\mu D_\mu - m)\psi, \tag{2.4}$$

where γ^μ are the Dirac matrices of dimension 4×4, $\bar{\psi} = \psi^\dagger\gamma^0$ is the adjoint spinor, $F^{\mu\nu} = \partial^\mu A^\nu - \partial^\nu A^\mu$ is the EM field tensor, $D_\mu = \partial_\mu - ieA_\mu$ is the covariant derivative and e is the coupling constant between the fermion and the photon which is the electric charge of the fermion field.

To see how the Lagrangian in Equation (2.4) represents light interacting with matter, the equation must be rewritten as

$$\mathcal{L}_{QED} = -\frac{1}{4}F^{\mu\nu}F_{\mu\nu} + \bar{\psi}(i\gamma^{\mu}\partial_{\mu} - m)\psi - e\bar{\psi}\gamma^{\mu}A_{\mu}\psi. \tag{2.5}$$

The first term in Equation (2.5) is the Lagrangian density for Maxwell's equations in the absence of any sources, the second term is the Dirac Lagrangian representing a free fermion and the third term is the interaction term.

The QED Lagrangian is invariant under local gauge transformations belonging to the U(1) group. They are represented by

$$\psi \rightarrow U(x)\psi(x) = e^{i\alpha(x)}\psi(x),$$

$$A_{\mu}(x) \rightarrow U(x)A_{\mu}(x) = A_{\mu} + \frac{1}{e}\partial_{\mu}\alpha(x).$$

A consequence of the invariance of Equation (2.4) with respect to U(1) transformations is the conservation of Noether's current $j^{\mu} = \bar{\psi}\gamma^{\mu}\psi$ and hence the conservation of the electric charge.

2.1.2 Quantum chromodynamics

Quantum chromodynamics is a non-Abelian gauge theory which describes strong interactions, i.e., gluons interacting with quarks. The ingredients here are:

- a spin 1/2 fermion represented by the quark field, q_f, of flavour f,
- a spin 1 boson represented by the vector gluon field G^a_{μ}.

In this theory, colour is the conserved charge of these interactions. Quarks and anti-quarks appear in six different colours (red, green, blue and the corresponding anti-colours) and in six different flavours. In addition, particles are not observed singularly due to colour confinement, i.e. only colour neutral states can be observed in nature.

The complete QCD Lagrangian density is

$$\mathcal{L}_{QCD} = -\frac{1}{4}F^{a}_{\mu\nu}F^{a,\mu\nu} + \bar{q}_f(i\gamma^{\mu}D_{\mu} - m_f)q_f, \tag{2.6}$$

where $F^a_{\mu\nu} = \partial_\mu G^a_\nu - \partial_\nu G^a_\mu + g_s f^{abc} G^b_\mu G^c_\nu$ is the gluon field strength tensor with the f^{abc} the SU(3) structure constants, and with $g_s = 4\pi\alpha_S$ the strength of the interaction. Also, $D_\mu = \partial_\mu + i g_s \frac{\lambda^a}{2} G^a_\mu$ is the covariant derivative with λ^a the eight generators of SU(3). In Equation (2.6), summation is implied in two ways: repeated latin indices are to be summed (they will be maintained as superscript) and repeated greek indices (one as subscript, one as superscript) are to be summed as well. Here, $a = 1, ..., 8$ is the index for the number of gluons, and $q_f = (q_r, q_b, q_g)_f$ is the quark triplet whose indices refer to the colour charge and $f = 1, ..., 6$ is the quark flavour index.

The Lagrangian density in Equation (2.6) is invariant under local SU(3) transformations as

$$q(x) \to U(x)q(x) = e^{-ig\alpha^a(x)\frac{\lambda^a}{2}} q(x),$$
$$G^a_\mu \to G^a_\mu - \frac{1}{g}\partial_\mu \alpha^a - f^{abc}\alpha^b G^c_\mu,$$

where $\alpha^a(x)$ are arbitrary functions.

Lets decompose the Lagrangian in Equation (2.6) into its different parts:

$$\begin{aligned}\mathcal{L}_{QCD} = &-\frac{1}{4}(\partial_\mu G^a_\nu - \partial_\nu G^a_\mu)(\partial^\mu G^{a,\nu} - \partial^\nu G^{a,\mu}) + \bar{q}_f(i\gamma^\mu\partial_\mu - m_f)q_f \\ &- g_s \bar{q}_f \gamma^\mu \left(\frac{\lambda^a}{2}\right) G^a_\mu q_f \\ &- \frac{g_s}{2} f^{abc}(\partial_\mu G^a_\nu - \partial_\nu G^a_\mu) G^{b,\mu} G^{c,\nu} - \frac{g_s^2}{4} f^{abc} f^{ade} G^b_\mu G^c_\nu G^{d,\mu} G^{e,\nu}.\end{aligned} \tag{2.7}$$

The first line in Equation (2.7) contains the kinetic terms for the different fields. The interaction between quarks and gluons is given by the second line. Finally, due to the non-Abelian character of SU(3), the $F^a_{\mu\nu}F^{a,\mu\nu}$ term, of Equation (2.6), generates the cubic and quartic gluon self-interaction in the last line. This is a very important difference with respect to QED where these kinds of self-interaction do not exist for the photon. Another fundamental feature of QCD is *asymptotic freedom*: quarks interact relatively weakly at high energies, hence allowing for perturbative calculations, but strongly at low energies, preventing the unbinding of baryons and mesons.

2.1.3 Electroweak interactions

Weak interactions are caused by the emission or absorption of W or Z bosons and it is called weak because its strength, over a given distance, is several orders of magnitude smaller than the strong or electromagnetic force. There are two types of interactions:

charged-current interactions, mediated by $W^{\pm}$ bosons, and neutral-current interactions, mediated by the Z boson. At tree level, the first type of interaction is capable of changing flavour but the second one does not.

The electroweak theory is the unified description of the weak and electromagnetic interactions. The unification is accomplished under transformations of the gauge symmetry group:

$$\mathrm{SU(2)_L} \otimes \mathrm{U(1)_Y}. \tag{2.8}$$

The first ingredients of this theory are four massless gauge fields: a triplet of vector bosons W_i^{μ} (i=1,2,3) for $\mathrm{SU(2)_L}$ and a singlet B^{μ} for $\mathrm{U(1)_Y}$. The physical fields, corresponding to the four observed bosons (the photon, the Z and the $W^{\pm}$ bosons), can be obtained by the linear combinations:

$$\begin{aligned} A^{\mu} &= \sin\theta_W W_3^{\mu} + \cos\theta_W B^{\mu}, \\ Z^{\mu} &= \cos\theta_W W_3^{\mu} - \sin\theta_W B^{\mu}, \\ W_{\pm}^{\mu} &= \frac{W_1^{\mu} \mp i W_2^{\mu}}{\sqrt{2}}, \end{aligned} \tag{2.9}$$

where θ_W is the weak mixing angle.

The next ingredients are fermions which are grouped, according to their chirality, by left-handed or right-handed fields as

$$\begin{aligned} \psi_L &= P_L\psi = \frac{1}{2}(1-\gamma_5)\psi, \\ \psi_R &= P_R\psi = \frac{1}{2}(1+\gamma_5)\psi, \end{aligned}$$

where $P_{L,R}$ is the left(right)-handed projection operator and $\gamma^5 = i\gamma^0\gamma^1\gamma^2\gamma^3$.

Left handed fermions are paired in doublets with weak isospin $I = 1/2$, while right-handed fermions are grouped in singlets with $I = 0$. There are three families of quarks:

$$\begin{pmatrix} u \\ d \end{pmatrix}_L, \begin{pmatrix} c \\ s \end{pmatrix}_L, \begin{pmatrix} t \\ b \end{pmatrix}_L, \qquad \Big(u\Big)_R, \Big(d\Big)_R, \Big(c\Big)_R, \Big(s\Big)_R, \Big(t\Big)_R, \Big(b\Big)_R,$$

and similarly, three families of leptons:

$$\begin{pmatrix} \nu_e \\ e \end{pmatrix}_L, \begin{pmatrix} \nu_\mu \\ \mu \end{pmatrix}_L, \begin{pmatrix} \nu_\tau \\ \tau \end{pmatrix}_L, \qquad \Big(e\Big)_R, \Big(\mu\Big)_R, \Big(\tau\Big)_R.$$

In this theory, weak hypercharge plays the same role as the electric charge in QED or colour in QCD. Therefore, in any weak interaction, weak isospin is conserved. Another property of the electroweak theory is the relation between weak isospin Y and the electric charge Q as:

$$Q = I_3 + \frac{Y}{2},$$

where I_3 is the third component of the weak isospin.

Assuming a single fermion field, ψ, the electroweak Lagrangian density is given by

$$\mathcal{L}_{EW} = -\frac{1}{4}W^a_{\mu\nu}W^{a,\mu\nu} - \frac{1}{4}B_{\mu\nu}B^{\mu\nu} + i\bar{\psi}\gamma^\mu D_\mu\psi, \tag{2.10}$$

where $W^a_{\mu\nu} = \partial_\mu W^a_\nu - \partial_\nu W^a_\mu - g\varepsilon^{abc}W^b_\mu W^c_\nu$ and $B^{\mu\nu} = \partial_\nu B_\mu - \partial_\mu B_\nu$ are the field strength tensors and, $D_\mu = \partial_\mu + igW^a_\mu I^a + i\frac{g'}{2}B_\mu Y$ is the covariant derivative. Here g and g′ are the SU(2) and U(1) coupling constants, respectively. They relate to the weak mixing angle θ_W as:

$$\begin{aligned}\sin\theta_W &= \frac{g'}{\sqrt{g^2+g'^2}},\\ \cos\theta_W &= \frac{g}{\sqrt{g^2+g'^2}}.\end{aligned} \tag{2.11}$$

The generalisation of the electroweak Lagrangian density for all fermion fields, f, can be expressed as,

$$\mathcal{L}_{EW} = -\frac{1}{4}W^a_{\mu\nu}W^{a,\mu\nu} - \frac{1}{4}B_{\mu\nu}B^{\mu\nu} + i\sum_f \bar{f}\gamma^\mu D_\mu f \tag{2.12}$$

where $D_\mu = \partial_\mu - ig_V(\lambda^a V^a)_\mu$. Here g_V is a generic coupling constant of the fermion to gauge boson fields V, λ^a are the generators of the corresponding symmetry group and V_a is the field vector.

The Lagrangian density is invariant under local transformations of the $\mathrm{U(1)_Y}$ group as,

$$\psi_{L,R} \to e^{i\alpha(x)\frac{Y}{2}}\psi_{L,R},$$

which involves both chiralities, while the invariance under the $\mathrm{SU(2)_L}$

$$\psi_L \to e^{i\beta^a(x)\frac{\tau^a}{2}}\psi_L$$

only involves left-handed doublets. Here, τ^a $(a = 1, 2, 3)$ are the Pauli matrices.

The gauge symmetry forbids writing a mass term for the gauge bosons. Fermionic masses are also not possible, because they would communicate the left-handed and right-handed fields, which have different transformation properties, and therefore would produce an explicit breaking of the gauge symmetry. Thus, the $\mathrm{SU(2)_L} \otimes \mathrm{U(1)_Y}$ Lagrangian in Equation (2.12) only contains massless fields. This theoretical description does not fit the experimental observation and calls for a technique that preserves gauge invariance and, at the same time, allows non-zero fermion and vector boson masses.

2.2 The Higgs-Brout-Englert mechanism

As it was mentioned before, the $\mathrm{SU(2)} \times \mathrm{U(1)}$ gauge invariance of the electroweak theory requires that the masses of the gauge bosons are zero since the presence of a mass term violates gauge invariance. One way to modify the electroweak Lagrangian density to obtain masses for fermions and vector bosons is the Higgs-Brout-Englert mechanism [4, 5].

The mechanism begins with a gauge invariant theory having massless gauge bosons and ends with a spectrum with massive gauge bosons, after algebraic transformations on the Lagrangian. For this, a $SU(2)_L$ doublet, is introduced,

$$\Phi(x) = \begin{pmatrix} \phi^+(x) \\ \phi^0(x) \end{pmatrix} = \begin{pmatrix} \phi_1(x) + i\phi_2(x) \\ \phi_3(x) + i\phi_4(x) \end{pmatrix},$$

where ϕ^+ and ϕ^0 are complex scalar fields. The corresponding Lagrangian density, imposing $\mathrm{SU(2)} \times \mathrm{U(1)}$ gauge invariance, for this field is

$$\mathcal{L}_H = (D_\mu \Phi)^\dagger (D^\mu \Phi) - V(\Phi), \tag{2.13}$$

where the potential term has the form

$$V(\Phi) = \mu^2 \Phi^\dagger \Phi + \lambda (\Phi^\dagger \Phi)^2. \tag{2.14}$$

Vacuum stability demands λ to be greater than zero, i.e, the potential is bounded from below. Depending on the value of μ^2 the potential in Equation (2.14) will acquire a unique or degenerate minimum values. As shown in Figure (2.1), when $\mu^2 > 0$ the potential has a global minimum at $\Phi = 0$. If $\mu^2 < 0$, the potential has a local minimum

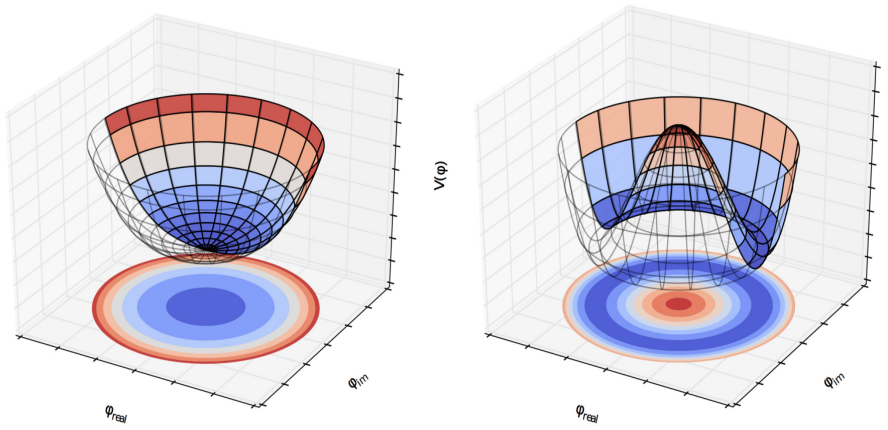

Figure 2.1 Illustration of the Higgs potential $V(\Phi)$ for $\lambda > 0$ with $\mu^2 > 0$ (left) and $\mu^2 < 0$ (right).

at $\Phi = 0$, but the true minimum is at the circumference $\Phi^\dagger\Phi = -\mu^2/2\lambda$. By choosing a particular minima, one spontaneously breaks the symmetry in the ground state. The following choice is made for the vacuum expectation value (VEV):

$$\langle 0|\Phi|0\rangle = \begin{pmatrix} 0 \\ v/\sqrt{2} \end{pmatrix} \qquad \text{with} \quad v = \left(-\frac{\mu^2}{\lambda}\right)^{1/2}. \tag{2.15}$$

Due to conservation of electric charge only a neutral field can acquire a VEV. Therefore, with the choice above, ϕ^0 is interpreted as the neutral field, and thus the vacuum carries no electric charge, i.e, $Q\langle\Phi\rangle_0 = 0$. That is, electromagnetism remains unbroken.

Choosing a perturbation of the field around the minimum of Equation (2.15) and replacing it in Equation (2.13) we end up with two particles associated to the complex field Φ: a massless field known as the Goldstone boson and a massive field with mass of $\sqrt{2\lambda}v$. However, we do not observe scalar massless bosons.

The workaround is to choose the unitary gauge, possible because $\mathcal{L}_{SM}$ is invariant under local gauge transformations. This leads to the following expression for the Higgs doublet,

$$\Phi \to e^{-\phi_a(x)\tau^a(x)}\Phi(x) = e^{-\phi_a(x)\tau^a(x)}\frac{1}{\sqrt{2}}\begin{pmatrix} 0 \\ v + H(x) \end{pmatrix}, \tag{2.16}$$

where the unphysical ϕ fields (Goldstone bosons) disappear. With this, the Lagrangian is reinterpreted as a theory with a real scalar boson, the Higgs boson represented by the field, $H(x)$, and massive gauge bosons.

2.2.1 Gauge bosons

We can expand $\mathcal{L}_H$ in the unitary gauge, using Equation (2.13), as

$$\begin{aligned}\mathcal{L}_H =&\frac{1}{2}\partial_\mu H\partial^\mu H + \frac{1}{8}(v+H)^2\left[g^2|W_\mu^1 + iW_\mu^2|^2 + |gW_\mu^3 - g'B_\mu|^2\right]\\ &- \frac{\mu^2}{2}(v+H)^2 - \frac{\lambda}{4}(v+H)^4\\ =&\frac{1}{2}\partial_\mu H\partial^\mu H + \frac{1}{4}(v+H)^2\left[g^2W_\mu^+W^{-\mu} + \frac{g^2+g'^2}{2}Z_\mu^0 Z^{0\mu}\right]\\ &- \lambda v^2H^2 - \lambda vH^3 - \frac{\lambda}{4}H^4. \end{aligned} \tag{2.17}$$

Where we used the relation $(g\cos\theta_W + g'\sin\theta_W)^2 = g^2 + g'^2$ taken from Equation (2.11) and Equations (2.26). Now, the previously massless $W^\pm$ and Z^0 boson fields have acquired mass, while the photon field remains massless:

$$\begin{aligned} m_W &= \frac{1}{2}gv,\\ m_Z &= \frac{1}{2}(g^2+g'^2)^{1/2}v = \frac{m_W}{\cos\theta_W},\\ m_\gamma &= 0. \end{aligned} \tag{2.18}$$

From the Fermi constant, the value of the Higgs field VEV can be obtained as,

$$G_F = \frac{\sqrt{2}g^2}{8m_W^2} = \frac{1}{\sqrt{2}v^2} \Rightarrow v = 246\,\text{GeV}. \tag{2.19}$$

In addition, from Equation (2.17), in the last line we can see the Higgs boson mass term, the Higgs triple and quartic self-coupling interaction terms, respectively.

2.2.2 Fermions

As it was mentioned in Section (2.1.3), mass terms for fermions are not possible because they do not preserve the $\mathrm{SU(2)_L} \otimes \mathrm{U(1)_Y}$ symmetry. To fix this, Yukawa terms are introduced in the SM Lagrangian density. For example, in the case of electrons the terms are:

$$\mathcal{L}_{e\Phi} = -y_e(\bar{l}_L\Phi e_R + \bar{e}_R\Phi^\dagger l_L), \tag{2.20}$$

where $l_L = (\nu_e\, e)_L^T$, is the left-handed doublet of fermion fields, e_R is the right-handed singlet, and y_e is the electron Yukawa coupling.

Using the definition of the Higgs field, Φ, in the unitary gauge from Equation (2.16), the Lagrangian density takes the form

$$\mathcal{L}_{e\Phi} = -\frac{y_e v}{\sqrt{2}}(\bar{e}_L e_R + \bar{e}_R e_L) - \frac{y_e h}{\sqrt{2}}(\bar{e}_L e_R + \bar{e}_R e_L) \tag{2.21}$$

where the electron mass can be extracted:

$$m_e = \frac{y_e v}{\sqrt{2}}. \tag{2.22}$$

The expression for the rest of the fermions is analogous. Therefore, in general, the coupling of the Higgs boson to fermions is:

$$y_f = \sqrt{2}\frac{m_f}{v},$$

and it is proportional to their mass.

2.2.3 The theoretical Higgs mass

From Equation (2.17), the mass of the Higgs boson can be extracted from the mass term in the Lagrangian:

$$m_H = \sqrt{2\lambda}v = \sqrt{-2\mu^2}. \tag{2.23}$$

The Higgs-Brout-Englert mechanism in the SM Lagrangian does not give a precise value for the mass of the scalar boson, since is a free parameter in the theory. However, some constraints can be made from the theory [6].

Unitarity

Interactions of the longitudinal components of the massive gauge bosons grow with their momenta. Thus, the calculation of the scattering cross-section for longitudinal polarised W and Z bosons, for example $W_L^+W_L^- \to W_L^+W_L^-$, would violate unitarity, since it increases with the energy of the process. This problem is solved by adding two new diagrams, which take into account the interaction between the weak vector boson and the Higgs boson [7]. Calculating the amplitude of the scattering of W bosons involving the Higgs boson it follows that:

$$M_H^2 \leq \frac{2\pi\sqrt{2}}{G_F} \approx (870 \text{ GeV})^2$$

Vacuum stability and triviality

The coupling constants depend on the energy scale, Q^2, of the process. Therefore, the self-interaction coupling of the Higgs, λ, is dependent (running) on the energy scale of the process: $\lambda = \lambda(Q^2)$. Consider the one-loop radiative corrections to the Higgs boson quartic coupling, λ, in a SM theory with no fermions or gauge bosons, then we have:

$$\lambda(Q) = \frac{\lambda(v)}{1 - \frac{3\lambda(v)}{4\pi^2}\ln(Q^2/v^2)} \tag{2.24}$$

We can distinguish two different behaviours of the coupling constant according to Q^2:

- If $Q^2 << v^2$ the system cannot reach the energy needed for the symmetry breaking. Thus, the coupling constant λ in the Higgs potential, see Equation (2.14), is very small making the quartic coupling term disappear. Therefore, the theory becomes trivial.

- As the value of Q^2 of the process increases, the energy of the system reaches the scale of the electroweak symmetry breaking. The coupling constant gets larger and larger until it diverges (Landau pole) and the theory is no longer perturbative.

Therefore, the definition of a cut-off scale, Λ_c, is needed below which the theory is valid.

Assuming that λ is small and if we include all the virtual contributions to the coupling constant (at one-loop), we obtain:

$$\lambda(Q^2) = \lambda(v^2) + \frac{1}{16}\left[-12\frac{m_t^4}{v^4} + ...\right]\log\frac{Q^2}{v^2}. \tag{2.25}$$

From here one can see that if $\lambda(v^2)$ is small then $\lambda(Q^2) < 0$ and the stability of the vacuum state is lost. Therefore, given the dependence of the Higgs mass on the coupling constant, λ, Equation (2.25) implies a lower limit on m_H. The stability conditions together with the triviality conditions gives an upper and a lower limit on the Higgs mass that gives an allowed range in the $\Lambda - m_H$ phase-space as it is shown in Figure (2.2). As the cut-off scale Λ increases, the limits on the allowed Higgs masses gets tighter, favouring a low mass Higgs boson scenario.

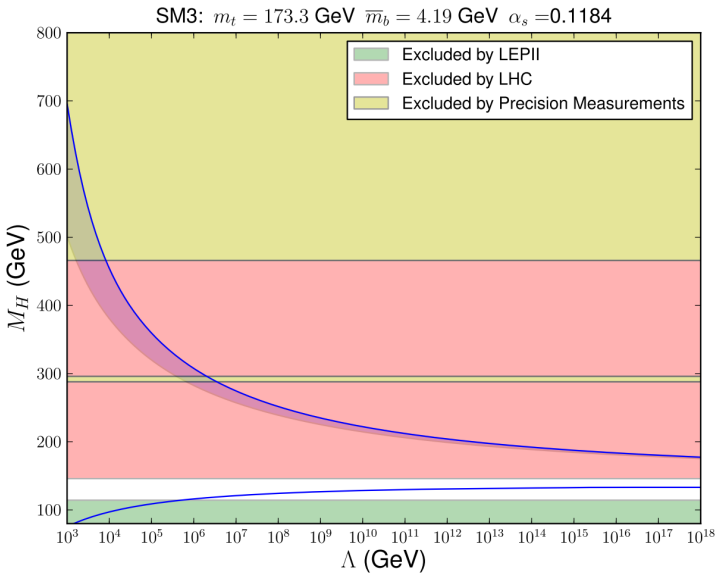

Figure 2.2 Illustration of the stability lower bound and the triviality upper bound on the Higgs mass (blue lines), from [8]. The horizontal lines indicate exclusions from LEP and LHC before the July 2012 observation[1, 2], and electroweak precision measurements of the other parameters of the SM theory.

2.3 Production mechanisms

There are four major processes in which the SM Higgs boson is produced at the LHC. They are shown in Figure (2.3) and their production rates are shown in Figure (2.4a) for $\sqrt{s} = 8$ TeV , which is taken from the latest calculations by the LHC Higgs Physics working group [9]. The production mechanisms are:

The **gluon-gluon fusion (ggF)** mechanism is given by,

$$pp \rightarrow gg \rightarrow H.$$

It is the dominant production mode at the LHC. Its cross-section is known at next-to-next-to leading order (NNLO) with a ∼10% uncertainty, where at a Higgs mass of $m_H = 125$ GeV, the predicted cross-section is ∼19 pb. Gluons do not couple directly to the Higgs boson, but both interact strongly with top quarks, so ggF production is mediated via a heavy-quark loop. Since the Yukawa coupling is proportional to the fermion mass, the greatest contribution comes from the top quark.

The **vector boson fusion (VBF)** mechanism is given by:

$$pp \rightarrow qq \rightarrow qqV^*V^* \rightarrow qqH,$$

where V = W or Z. It is the sub-leading production mode at the LHC. Its cross-section is known at next-to leading order (NLO) with a ∼10% uncertainty, where at a Higgs mass of $m_H = 125$ GeV, the predicted cross-section is ∼1.6 pb (∼8.2% of ggF). This process leaves a well defined signature in the ATLAS detector with highly energetic jets in the very forward regions and nearly collinear to the proton beams.

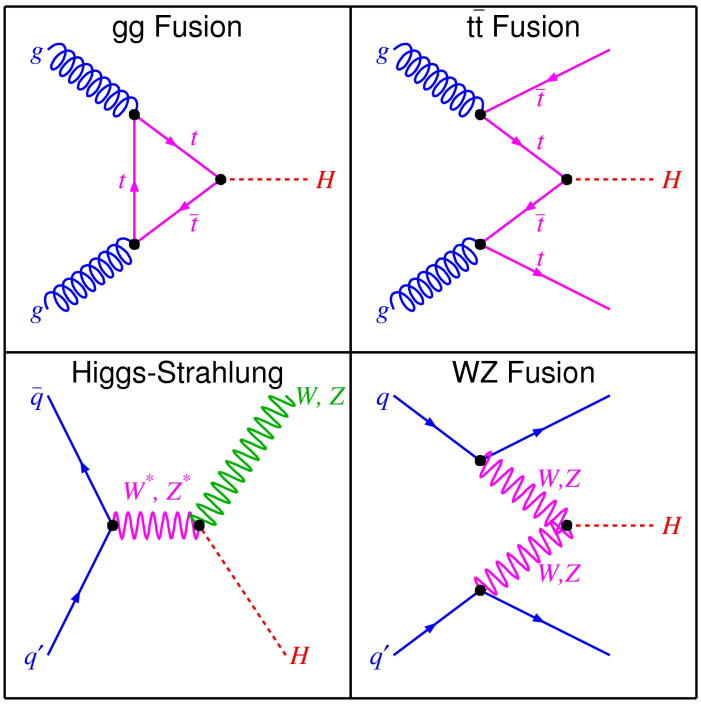

Figure 2.3 Lowest order feynman diagrams of the main production modes of the Higgs boson at the LHC.

The **Higgs-strahlung (VH)** mechanism is the associated production of a Higgs boson with a Z or a W boson. It is given by,

$$pp \to q\bar{q} \to V \to VH,$$

where V = W or Z. Its cross-section is known at NNLO with a ∼5% uncertainty where, at a Higgs mass of $m_H = 125$ GeV, the predicted cross-sections are ∼0.7 pb and ∼0.4 pb (∼3.7% and ∼2.2% of ggF), respectively. It also has a clean signature with two massive particles that can be identified through their decay products. Their production rates become very small for $m_H > 300$ GeV, however they are still important for a 125 GeV Higgs.

The **associated production with a top quark pair (ttH)** mechanism is given by,

$$pp \to gg \to t\bar{t}t\bar{t} \to t\bar{t}H.$$

Its cross-section is much lower than the previous ones, where at a Higgs mass of $m_H = 125$ GeV, the predicted cross-section is ∼0.1 pb (∼0.7% of ggF). This process can probe the direct coupling of the Higgs boson to fermions. However, besides the fact that its cross-section is very small, it has an experimentally challenging final state that involves W bosons, b quarks and the Higgs itself.

The total SM cross-sections for $\sqrt{s} = 7, 8$ and 14 TeV are shown in Figure (2.4b). The plots were based on perturbative QCD calculations [9–11] and the uncertainties on the cross-sections arise mainly due to the QCD scale, parton distribution functions and α_s [10].

Unfortunately it is not straightforward to measure all these five processes. We measure the Higgs boson only after it decays, so what we actually measure is the rate for a particular production process multiplied by the probability that the Higgs decays in a particular way. Therefore, we need to study the SM Higgs boson decay modes as well.

2.4 Decay modes

Depending on the value of the Higgs boson mass, there are different decay channels, and thus different possible cross-section times branching ratio values, which set the relative magnitude between the different total processes. Figure (2.5) shows the SM Higgs boson decay branching ratio and the production cross-section times branching ratio for $\sqrt{s} = 8$ TeV for $m_H < 200$ GeV and Figure (2.6) has the same plots but for $m_H < 1$ TeV. The rates are determined by the couplings, which are proportional to the fermion mass, or to the square of the W or Z boson mass, as long as the interaction is direct. Hence, decays to heavy particles are more likely than those to lightweight particles. The main decay probabilities of a 125 GeV Higgs boson are shown in Table (2.1) in order of importance, where the decay into $b\bar{b}$ decay occurs more often and the $Z\gamma$ decay is least probable. There are other decays less probable, but not worth mentioning.

Three different mass regions can be identified where the sensitivity of the various channels is different.

In the low mass region ($m_H < 130$ GeV), the dominant branching ratio is $H \to b\bar{b}$ (60% at $m_H = 125$ GeV). This channel is very challenging at hadron colliders, where a signal of ∼10 pb has to be distinguished from the QCD multi-jet production with a cross-section of ∼100 μb. For the $H \to \gamma\gamma$ channel the situation is better with a

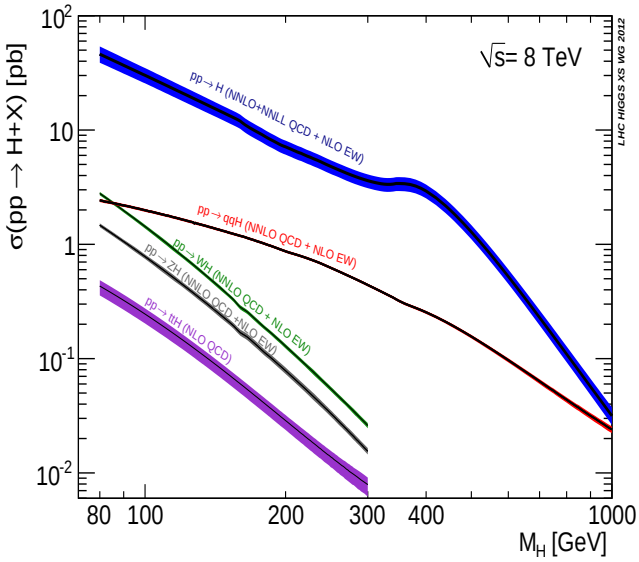

(a)

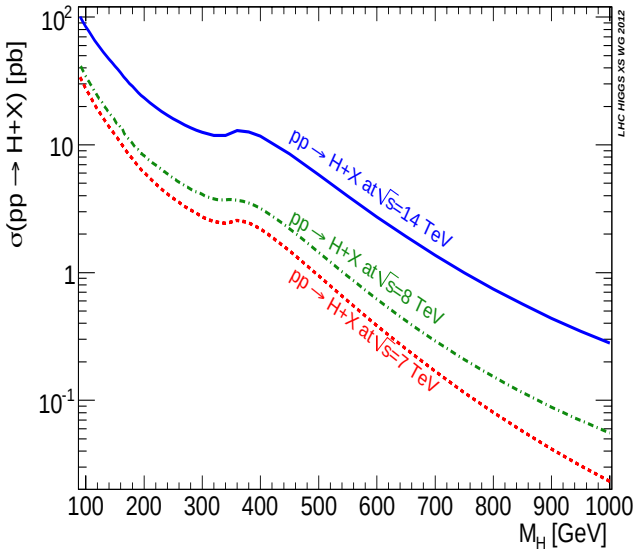

(b)

Figure 2.4 (a) Standard Model Higgs boson production cross-sections at $\sqrt{s} = 8$ TeV and (b) the total cross-sections for $\sqrt{s} = 7, 8$ and 14 TeV.

signal to background ratio (S/B) of $\sim 10^{-2}$ with a branching ratio of about 0.23%. It has a distinctive signature with two isolated and energetic photons, identifiable against a smooth background of di-photon production. For the $H \to ZZ^* \to 4l$ channel the S/B is even better, $\sim$1, when considering Z boson decays to charged leptons (electrons and muons), due to the presence of four leptons at the final state, and the $H \to ZZ^*$ branching ratio of 2.5%. It provides a clean experimental environment with an excellent mass resolution.

In an intermediate mass region (130 GeV $< m_H <$180 GeV), the two dominant channels

Decay process	Probability
$b\bar{b}$	60%
WW	21%
gg	9%
$\tau\bar{\tau}$	5%
$c\bar{c}$	2.5%
ZZ	2.5%
$\gamma\gamma$	0.2%
$Z\gamma$	0.15%

Table 2.1 The branching ratios of the decay modes of the Standard Model Higgs boson at $m_H = 125$ GeV.

are $H \to ZZ^*$ and $H \to W^+W^-$. The cross-section of $pp \to H \to WW$ is higher with respect to $H \to ZZ$ due to the stronger coupling of the Higgs field to heavier particles. The most promising final state of this channel is with the leptonic decays of the W bosons ($W \to l\bar{\nu}$), where its experimental signature consists of a high energy charged lepton and high missing transverse momentum. However, it is not possible to reconstruct the final state completely due to the presence of neutrinos in its final state. The Higgs boson is identified through the transverse mass distribution of the $l\bar{\nu}$ system and the resolution of the Higgs boson mass is very poor.

In the high mass region (180 GeV $< m_H <$ 1 TeV), the most promising channel for the identification of the Higgs boson is the $H \to ZZ$, with the subsequent decays to $llqq$, $ll\nu\nu$ and $llll$. In this region both Z bosons are on-shell which allows the further reduction of background by applying a more stringent kinematic selection on the leptons of the decay.

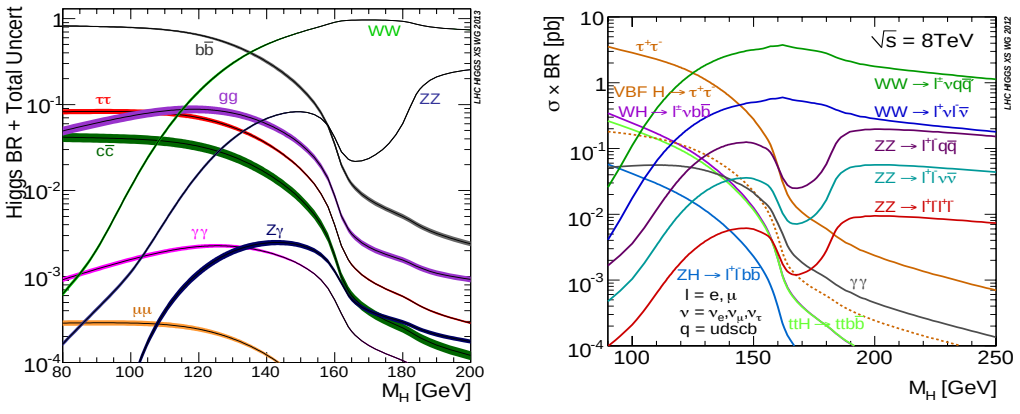

(a) **(b)**

Figure 2.5 (a) Standard Model Higgs boson decay branching ratios and (b) production cross-section times branching ratio at $\sqrt{s} = 8$ TeV for $m_H < 200$ GeV [9–11].

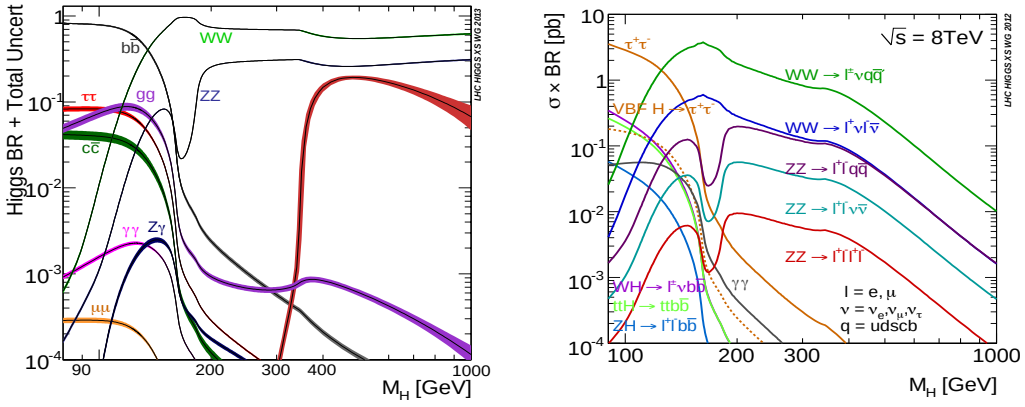

(a) **(b)**

Figure 2.6 (a) Standard Model Higgs boson decay branching ratios and (b) production cross-section times branching ratio at $\sqrt{s} = 8$ TeV for $m_H < 1$ TeV [9–11].

2.5 The Standard Model Higgs boson today

The ATLAS and CMS experiments at the LHC announced on the 4th of July of 2012 the discovery of a new boson with a mass of about $m_H = 125$ GeV and with properties consistent with what is expected from the Standard Model Higgs boson [1, 2].

The data used in the ATLAS detector correspond to integrated luminosities of $4.6 - 4.8$ fb^{-1} collected at $\sqrt{s} = 7$ TeV in 2011 and $5.8 - 5.9$ fb^{-1} at $\sqrt{s} = 8$ TeV in 2012. The results are due to individual searches in the channels $H \to \gamma\gamma$, $H \to ZZ^{(*)} \to 4l$ and $H \to WW^* \to l\nu l\nu$ for the 8 TeV data, plus the combination with previous results of searches in the $H \to ZZ^*$, WW^*, $b\bar{b}$ and $\tau^+\tau^-$. In addition, the analyses of the $H \to ZZ^{(*)} \to 4l$ and $H \to \gamma\gamma$ in the 7 TeV data were improved with respect to previous results. The invariant mass distributions for $H \to ZZ^{(*)} \to 4l$ and $H \to \gamma\gamma$ channels are shown in Figure (2.7) for 7 and 8 TeV data.

An excess of events over the background yield was observed with a local significance of 5.9 σ, corresponding to a probability of 1.7×10^{-9} that the background could produce such fluctuation. The ratio of the measured signal yield to the SM expectation was found to be $\mu = 1.4 \pm 0.3$, at a Higgs boson mass of about 125 GeV, compatible with the SM expectation. The local significance as a function of the Higgs boson mass is shown in Figure (2.8).

Given the discovery of the new boson, its properties has been investigated more precisely including its mass, couplings, spin and width to strengthen the hypothesis that this new particle is in fact a SM Higgs boson. Any deviations from the SM expectation

would mean a sign of new physics.

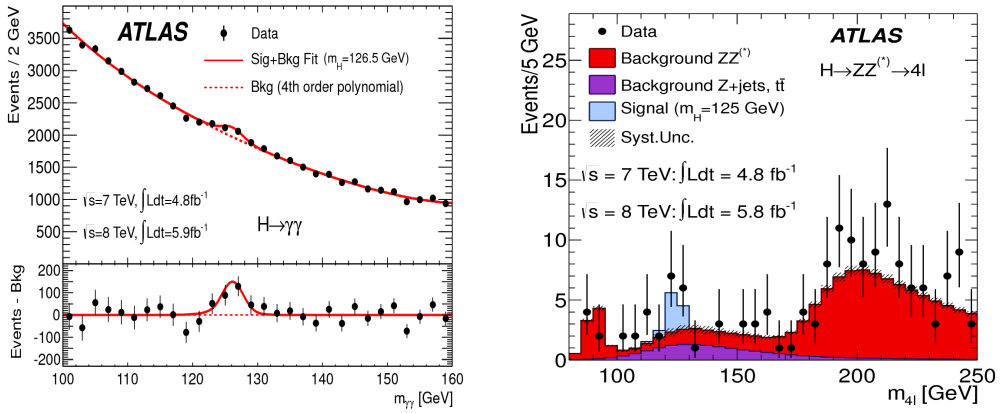

(a) (b)

Figure 2.7 Invariant mass distributions of (a) the di-photon system in the $H \to \gamma\gamma$ search and (b) of the four-lepton system in the $H \to ZZ^*$ search. Both taken from [1].

A combined mass measurement using the decays channels $H \to \gamma\gamma$ and $H \to ZZ^{(*)} \to 4l$ was performed using the pp collison data sample recorded by the ATLAS experiment at the centre of mass energies of 7 and 8 TeV [3]. The details of the Higgs boson mass measurement from the $H \to ZZ^{(*)} \to 4l$ decay channel is explained in detail in Chapter 6. To combine both analyses, a profile likelihood ratio defined as a function of the Higgs mass m_H was used, analogous to the model described in Chapter 4. The measured value of the SM Higgs boson mass is $m_H = 125.36 \pm 0.37(stat) \pm 0.18(syst)$ GeV. Figure (2.9), shows the $-2\ln\Lambda$, see Equation 4.6, value as a function of m_H for the individual $H \to \gamma\gamma$ and $H \to ZZ^{(*)} \to 4l$ channels and their combination. In addition, separate upper limits on the total width of the Higgs boson are derived from fits to the mass spectrum of these channels assuming that there is no interference with the background processes. In $H \to \gamma\gamma$, a 95% CL limit of 5.0(6.2) GeV is observed(expected). In the $H \to ZZ^{(*)} \to 4l$ channel, a 95% CL limit of 2.6(6.2) GeV is observed(expected). A detailed description of the updated SM Higgs boson mass measurement in the $H \to ZZ^{(*)} \to 4l$ channel will be described in Chapter 6.

The measurement of the discovered Higgs boson production and decay rates and coupling strengths are presented in [12], for the 2011 and 2012 data taking. The analyses combine specific analyses of the $H \to \gamma\gamma$, ZZ^*, WW^*, $Z\gamma$, $b\bar{b}$, $\tau\tau$ and $\mu\mu$ decay channels. These analyses use the pp collision data collected by the ATLAS experiment corresponding to integrated luminosities of up to 4.7 fb^{-1} at 7 TeV and 20.3 fb^{-1} at 8 TeV. In addition, the measured Higgs boson signal yields are compared to the SM expectations (using the signal strength, μ) at the measured Higgs boson mass of $m_H = 125.36$ GeV. The measured value is $\mu = 1.18 \pm 0.10(stat)^{+0.08}_{-0.07}(stat)$

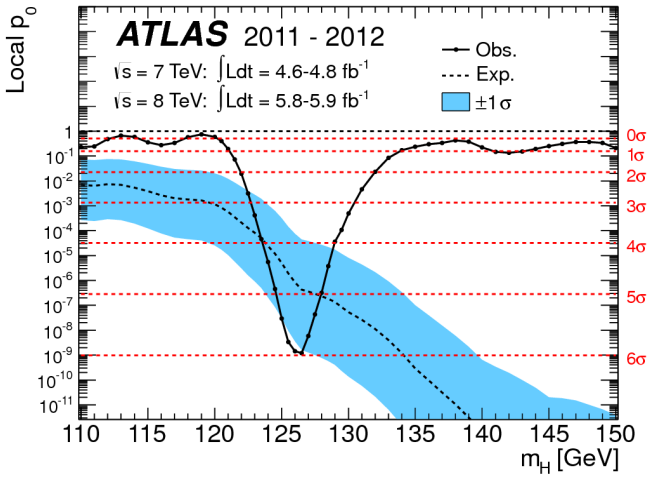

(a)

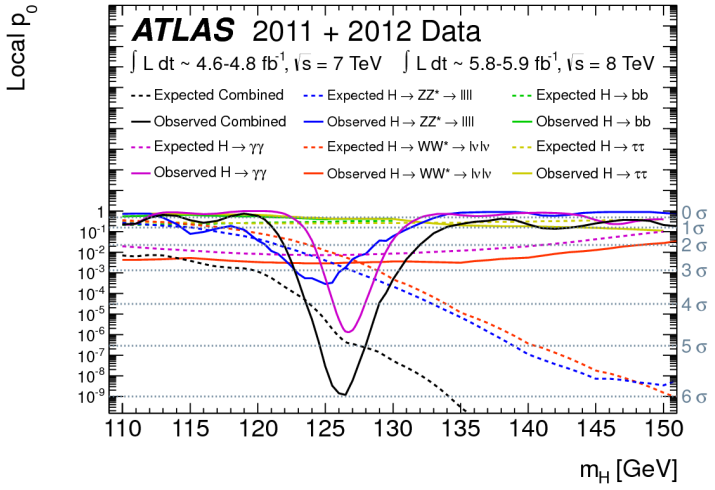

(b)

Figure 2.8 (a) The total and (b) individual observed local significance p_0 as a function of the Higgs boson mass. The dashed curved indicates the expectation values for the SM Higgs boson signal hypothesis ($\mu = 1$) at the given mass and the horizontal lines show the corresponding significances in σ levels [1].

compatible with the SM expectation.

The analysis provides confirmation of the ggF production mechanism with a significance exceeding 5σ and strong evidence of the VBF production mechanism with a significance of 4.3σ. Moreover, it supports the SM predictions of the VH and ttH production mechanisms. The Higgs boson couplings to up-type fermions and vectors bosons are found both with significances above 5σ and to down-type fermions with a significance of 4.3σ. Higgs boson couplings to leptons are found with a significance of 4.4σ. The coupling strengths to fermions and bosons are measured at the level of 16% and 7% respectively and are observed to be compatible with the SM prediction. Coupling

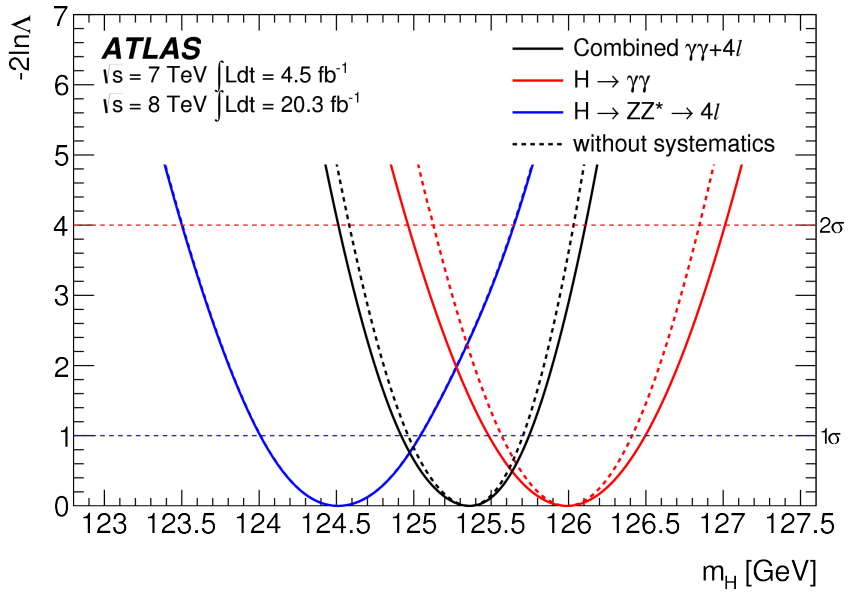

Figure 2.9 Value of $-2\ln\Lambda$ for the mass fit as a function of m_H for the individual $H \to \gamma\gamma$ and $H \to ZZ^{(*)} \to 4l$ channels and their combination. The dashed lines show the results without systematic uncertainties. For the $H \to ZZ^{(*)} \to 4l$ channel this is indstinguishable from the solid line which includes the systematic uncertainties [3].

strengths in loop precesses are measured at the 12% level. No significant deviation from the SM expectation are observed.

Updated studies of the spin and parity of the observed Higgs boson can be found in [13]. The SM Higgs boson hypothesis ($J^P = 0^+$) is tested against several alternative spin and parity models. The models considered include non-SM spin-0 and spin-2 models. The analysis combines $H \to \gamma\gamma$, $H \to ZZ^{(*)} \to 4l$ and $H \to WW^* \to e\nu\mu\nu$ decays processes resulting in the exclusion of all considered non-SM spin hypothesis at more than 99% CL in favour of the SM spin-0 hypothesis.

2.6 Beyond the Standard Model: the Two Higgs Doublet Model

There are many motivations for Two Higgs Doublet models (2HDMs). The best known motivation is supersymmetry [14] where more than a single Higgs doublet is needed to give mass to all the particle content.

The minimal extension of the Higgs sector is the Standard Model with two Higgs doublets [15]. Two complex $SU(2)_L$ doublet scalar fields Φ_1 and Φ_2 with hypercharge $Y = 1$ are introduced. The Higgs potential, which spontaneously breaks

$SU(2)_L \times U(1)_Y$ down to $U(1)_{EM}$, is given by:

$$\begin{aligned} V(\Phi_1, \Phi_2) =& m_{11}^2 \Phi_1^\dagger \Phi_1 + m_{22}^2 \Phi_2^\dagger \Phi_2 - m_{12}^2 (\Phi_1^\dagger \Phi_2 + \Phi_2^\dagger \Phi_1) + \frac{\lambda_1}{2} (\Phi_1^\dagger \Phi_1)^2 + \frac{\lambda_2}{2} (\Phi_2^\dagger \Phi_2)^2 \\ &+ \lambda_3 \Phi_1^\dagger \Phi_1 \Phi_2^\dagger \Phi_2 + \lambda_4 \Phi_1^\dagger \Phi_2 \Phi_2^\dagger \Phi_1 + \frac{\lambda_5}{2} \left[(\Phi_1^\dagger \Phi_2)^2 + (\Phi_2^\dagger \Phi_1)^2 \right], \end{aligned} \tag{2.26}$$

where m_{11}, m_{12} and m_{22} are mass parameters, and λ_n (n=1,...,5) are the interaction parameters, which are all real. This potential is subject to gauge invariance and discrete symmetries. The latter is to ensure that there is no flavour changing neutral currents (FCNC) which are not seen in nature. The minimisation of the potential gives

$$\langle 0|\Phi_1|0\rangle = \begin{pmatrix} 0 \\ v_1/\sqrt{2} \end{pmatrix}, \qquad \langle 0|\Phi_2|0\rangle = \begin{pmatrix} 0 \\ v_2/\sqrt{2} \end{pmatrix}, \tag{2.27}$$

where v_1 and v_2 are the vacuum expectation values (VEVs) of Φ_1 and Φ_2, respectively.

As we have two complex $SU(2)$ doublets, there are 8 corresponding fields:

$$\Phi_a = \begin{pmatrix} \phi_a^+ \\ (v_a + \rho_a + i\eta_a)/\sqrt{2} \end{pmatrix}, \qquad a = 1, 2. \tag{2.28}$$

where ρ_a and η_a are real scalar fields. Three of the fields in Equation (2.28) get eaten to give mass to the $W^\pm$ and Z^0 gauge bosons. The remaining five fields are physical scalar Higgs fields: two charged scalars, two neutral scalars and one pseudoscalar.

The gauge bosons are generated in the same way as in the SM, obtaining

$$m_W^2 = \frac{1}{4} g^2 (v_1^2 + v_2^2) \quad \text{and} \quad m_Z^2 = \frac{1}{4} (g^2 + g'^2)(v_1^2 + v_2^2). \tag{2.29}$$

These masses come from the Higgs kinetic terms, and there is a contribution from both Higgs fields. Thus, electroweak measurements imply $v^2 = v_1^2 + v_2^2 = 246$ GeV. The relative size of the two VEVs is undetermined, and it is defined,

$$\tan\beta = \frac{v_2}{v_1}, \tag{2.30}$$

where β is the angle that diagonalises the mass-squared matrices of the charged scalars and of the pseudoscalars.

With the chosen minima of Equation (2.27), the mass terms for the neutral scalars are

given by

$$\mathcal{L}_{\rho}^{mass} = -\left(\rho_1, \rho_2\right) \begin{pmatrix} m_{12}^2(v_2/v_1) + \lambda_1 v_1^2 & -m_{12}^2 + \lambda_{345} v_1 v_2 \\ -m_{12}^2 + \lambda_{345} v_1 v_2 & m_{12}^2(v_1/v_2) + \lambda_2 v_2^2 \end{pmatrix} \begin{pmatrix} \rho_1 \\ \rho_2 \end{pmatrix}, \tag{2.31}$$

with $\lambda_{345} = \lambda_3 + \lambda_4 + \lambda_5$. The mass-squared expression is much more complicated than for the charged scalars and the pseudoscalar, but it can be obtained by diagonalising the mass matrix by the angle α which is defined to be the rotation angle that performs that diagonalisation. The mass-squared term is:

$$m_{h,H}^2 = \lambda_1 v_1^2 + \lambda_2 v_2^2 \pm \sqrt{(\lambda_1 v_1^2 - \lambda_2 v_2^2)^2 + 4 v_1^2 v_2^2 \frac{1}{4}(\lambda_3 + \lambda_5)^2} \tag{2.32}$$

The two parameters α and β determine the interactions of the various Higgs fields with the vector bosons and (given the fermion masses) with fermions.

As it was mentioned before, the 2HDMs face a potential problem by having tree level Higgs-mediated FCNCs. In the SM, diagonalising the mass matrix automatically diagonalises the Yukawa interactions, therefore there are no tree-level FCNC. However, in the 2HDMs in general the mass matrix and the Yukawa interactions will not be simultaneously diagonalisable, and thus the Yukawa couplings will not be flavour diagonal. In the context of Chapter 7, only two types of the 2HDMs (they do not have FCNCs) will be discussed in this section and only the neutral scalars and their couplings to vector bosons will be mentioned. For any further details see [15].

In the Type I 2HDM all quarks couple to just one of the Higgs doublets, Φ_2, and the model is enforced by the discrete symmetry $\Phi_1 \to -\Phi_1$. In the Type II 2HDM the $Q = 2/3$ right-handed quarks couple to one of the Higgs doublets, Φ_2, and the $Q = -1/3$ right-handed quarks couple to the other, Φ_1. The Type II model is enforced with the discrete symmetry $\Phi_1 \to \Phi_1$, $d_R^i \to -d_R^i$. In these models, it is also assumed that there is no CP violation in the VEVs of the scalar doublets $\Phi_{1,2}$, i.e, $v_{1,2}$ will be assumed to be positive and real with $v_1 = v \sin\beta$ and $v_2 = v \cos\beta$. Therefore, the physical neutral scalars are a lighter h and a heavier H, which are orthogonal combinations of ρ_1 and ρ_2. They are given by:

$$h = \rho_1 \sin\alpha - \rho_2 \cos\alpha \text{ and } H = -\rho_1 \cos\alpha + \rho_2 \sin\alpha.$$

In both models, the couplings of the neutral Higgs bosons to the W and Z bosons are the same: the coupling of the light Higgs, h, to either WW or ZZ is the same as the

SM coupling times $\sin(\beta - \alpha)$ and the coupling of the heavier Higgs, H, is the same as the SM coupling times $\cos(\alpha - \beta)$. Therefore, the branching ratios will not depend exclusively on the mass, as in the SM, but also on the parameters α and β. The Higgs production mechanisms are affected as well. The ggF production mechanism, if only top-quarks are considered, changes by a factor of $(\sin\alpha/\sin\beta)^2$ the SM cross-section for H production, in both 2HDMs. In the case of VBF and VH production mechanisms, the SM cross-section is changed by a factor of $\sin^2(\alpha - \beta)$ for H production, in both type of models as well.

The Type I and Type II 2HDMs are analysed in the search for an additional heavy Higgs boson, described in Chapter 7, where the free parameters $\cos(\beta - \alpha)$ and $\tan\beta$, given the upper limits on the $\sigma \times BR(H \to ZZ)$, are experimentally constrained.

Chapter 3

The Large Hadron Collider and the ATLAS detector

Exploiting the energy frontier is, by its nature, an unprecedented technical and experimental challenge. It requires an outstanding design, construction and operation of the accelerator complex, together with a deep understanding of each detector subsystem. In this chapter a description of the LHC and of the ATLAS experiment is provided.

3.1 The Large Hadron Collider

The Large Hadron Collider (LHC) is the highest energy and largest particle accelerator on Earth. It is located in Geneva, Switzerland and it is part of the Organisation Conseil Européenne pour la Recherche Nucléaire (CERN). It is in a 27 km circumference tunnel buried deep underground (between 45 m and 170 m). It is designed to collide opposite particle beams of protons at a centre-of-mass energy up to $\sqrt{s} = 14$ TeV and at an instantaneous luminosity up to $\mathcal{L} = 10^{34}\text{cm}^{-2}\text{s}^{-1}$.

To achieve such high collision energies, the LHC depends on an acceleration chain before the beam reaches the actual LHC beam pipe, see schematic Figure (3.1). Hydrogen atoms are fed into a source chamber of the linear accelerator (LINAC2) where electrons are stripped off to leave only the proton of the hydrogen nuclei. The protons are accelerated by an electric field which increases their energy up to 50 MeV. Then, the proton beam is injected into the Proton Synchroton Booster (PSB) reaching an energy

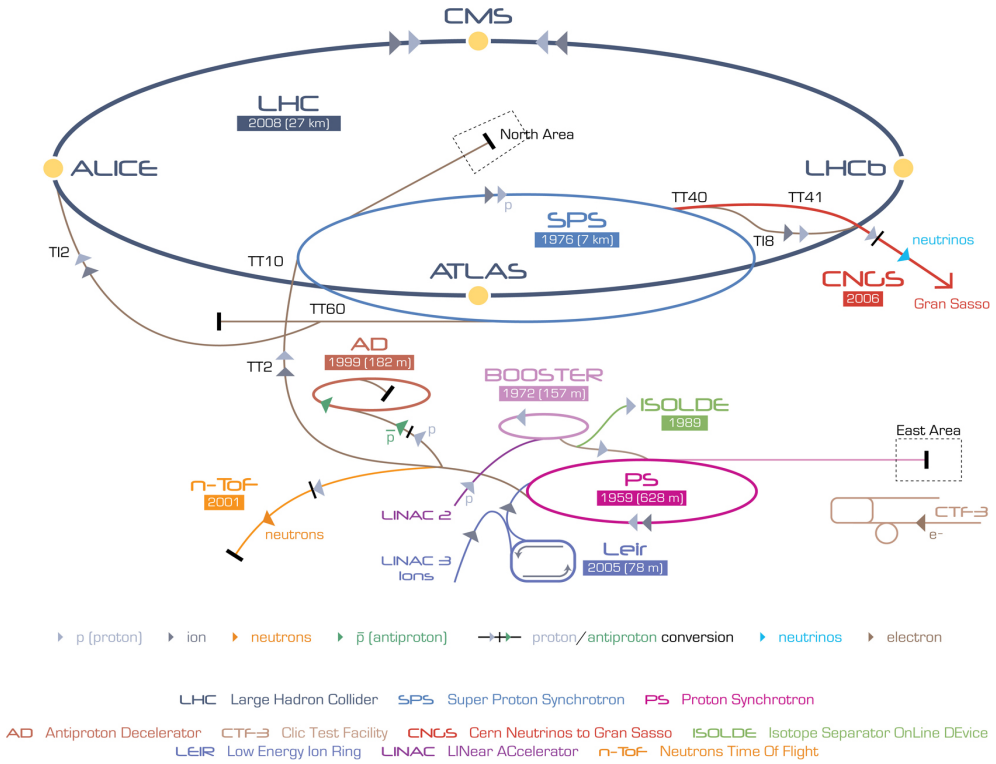

Figure 3.1 Schematic of the CERN accelerator complex. The LHC is represented in dark blue.

of 1.4 GeV. Next in the chain, the protons are injected in the Proton Synchroton (PS) to accelerate them to 25 GeV and then are passed to the Super Proton Synchroton (SPS) to finally inject the proton beams into the LHC with an energy of 450 GeV.

The LHC has two beam pipes where one is for the protons in a clockwise direction and the other one in a counterclockwise direction. The beams are accelerated by 485 keV in each turn through a superconducting Radio Frequency (RF) cavity system and are confined to the beam pipe by superconducting magnets with an 8.33 T field at temperatures below 1.9 K. This process is repeated until each of the proton beams reach the desired energy which was 3.5 TeV and 4 TeV for 2011 and 2012 respectively. The design energy is 7 TeV for each proton beam. These beams cross over at four different collision points in which there are different detectors: ALICE, designed to register data coming from heavy nuclei collisions, LHCb, designed for b-physics, and finally, CMS and ATLAS, multipurpose detectors. At design luminosity there are 2808 bunches per proton beam injected with a bunch spacing of 24.95 ns with each bunch containing $\approx 1.15 \times 10^{11}$ protons.

The produced number of events of a certain process is defined by

$$N_{\text{process}} = \sigma_{\text{process}} \times \int \mathcal{L} dt \tag{3.1}$$

where σ_{process} is the cross-section and $\mathcal{L}$ is the instantaneous luminosity. At the LHC, rare process cross-sections (Higgs boson or physics beyond the Standard Model) are usually many orders of magnitude smaller than the total LHC cross-section. Therefore, we need to maximise the integrated luminosity to obtain a statistically rich sample. Assuming round Gaussian beams, the integrated luminosity, $L = \int \mathcal{L} dt$, is defined by LHC characteristic parameters as:

$$\mathcal{L} = \frac{N_b^2 n_b f_{rev} \gamma_r}{4\pi \epsilon_n \beta^*} \times \frac{1}{\sqrt{1 + (\frac{\theta_c \sigma_z}{2\sigma^*})^2}} \tag{3.2}$$

where N_b is the number of protons in each bunch, n_b is the total number of circulating bunches in each proton beam, f_{rev} is the frequency of revolution in the ring, γ_r is the relativistic gamma factor for a given beam energy, ϵ_n the normalised transverse beam emittance and β^* the beta transverse function at the point of collision. The second term in Equation (3.2) is a geometric term which takes into account the luminosity reduction because of the beam crossing angle θ_c at the interaction point. Here, σ_z and σ^* are the RMS of the bunch length and beam width respectively. Therefore, the higher N_b and n_b, the smaller the emittance and the smaller the β^* function at the interaction point the greater the luminosity. A table of the LHC characteristic parameters is shown in Table (3.1).

LHC parameter	**2010**	**2011**	**2012**	**Nominal**
Beam energy [TeV]	3.5	3.5	4	7
Bunch spacing [ns]	150	75/50	50	25
n_b	368	1380	1380	2808
N_b	1.2×10^{11}	1.45×10^{11}	1.7×10^{11}	1.15×10^{11}
β^* [m]	2.0	1.5	0.6	0.55
ϵ_n [μm]	~ 2.0	~ 2.4	~ 2.5	3.75
Peak luminosity [$\text{cm}^{-2}\text{s}^{-1}$]	2.1×10^{32}	3.7×10^{33}	7.7×10^{33}	1×10^{34}

Table 3.1 LHC beam parameters and performance overview for 2010, 2011 and 2012 data taking in comparison with design values [16].

The LHC delivered to ATLAS a total integrated luminosity of 5.46 fb^{-1} and 22.8 fb^{-1} at $\sqrt{s} = 7$ TeV in 2011 and $\sqrt{s} = 8$ TeV in 2012, respectively. See Figure (3.2).

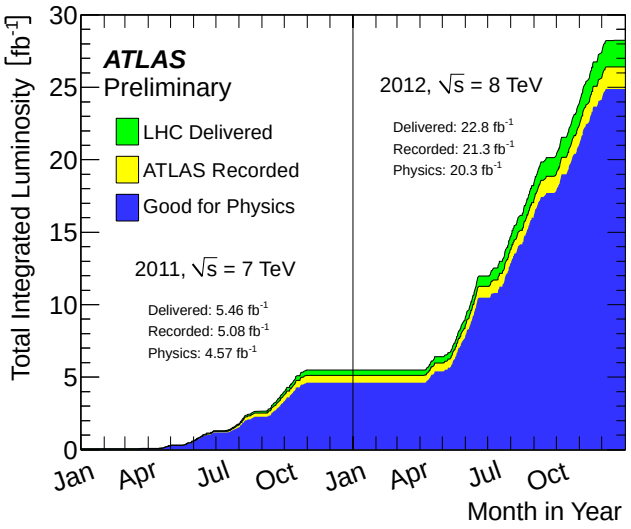

Figure 3.2 Total integrated luminosity delivered by the LHC and the data recorded by ATLAS in 2011 and 2012 [17].

3.2 The ATLAS experiment

ATLAS, A Toroidal LHC Aparatus, is the largest of the four detectors at the LHC and it has been designed for the high luminosity LHC environment. The experiment is lead by 3000 physicists from 38 different countries to reveal nature's properties at the high energy frontier. It is approximately 44 m long, has a diameter of 25 m and it is located approximately 92 m below the ground at the LHC Point 1.

The detector has a cylindrical shape with the interaction point at its centre, obeys a forward-backward symmetry and it has almost a complete coverage around the interaction point. It can be divided, in radial order, by subdetectors as: *Inner Detector, Electromagnetic Calorimeter, Hadronic Calorimeter, and Muon Spectrometer.*

Every subdetector was built with state of the art technologies, high granularity and radiation tolerance to perform high precision measurements which combined allow the reconstruction of particles. Each of them is specialised in a particular type of particle or property, as shown in Figure (3.3):

Electrons leave a track in the inner detector to be finally absorbed in the electromagnetic part of the calorimeter.

Photons which, if they do not convert into electrons during their path, are invisible to the inner detector (it identifies only charged particles). Their energy is absorbed in the electromagnetic calorimeter.

Hadrons are particles formed by quarks and gluons. If they are charged, they are tracked in the inner detector. All of them lose part of their energy in the electromagnetic calorimeter and most of their energy is absorbed in the hadronic calorimeter.

Muons are charged, so they leave tracks in the inner detector and in the muon system. They also deposit small amounts of energy in the calorimeters. As they are heavy they can pass through all the subdetectors.

Neutrinos are particles that escape undetected because they interact with matter through the weak force only and therefore give rise to missing energy.

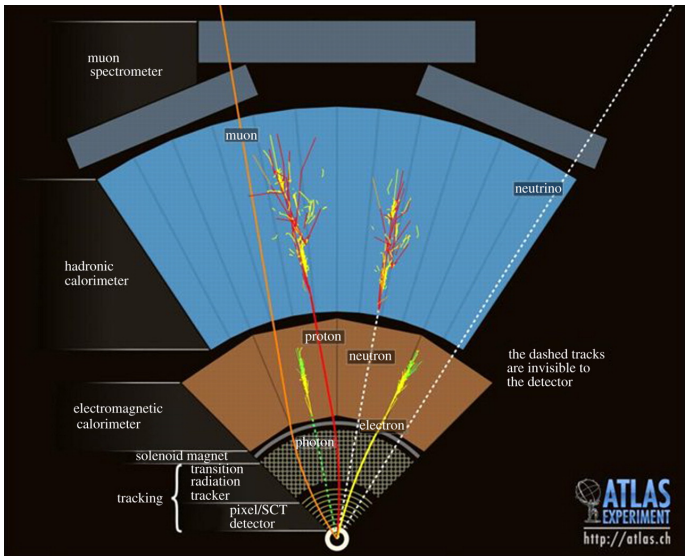

Figure 3.3 Schematic figure of the ATLAS detector at the LHC.

To achieve excellent particle identification, the ATLAS detector has to cope with challenging LHC conditions. It is required that the subdetectors have fast, radiation hard front-end electronics and sensors. They also need to have high granularity to handle high particle rates and overlapping interactions (pile-up). In addition, a highly efficient and fast trigger system to identify events of interest, and excellent particle reconstruction efficiencies, over a large acceptance range are necessary. The basic performance goals are summarised in Table (3.2).

More details of the detector components will be described in the following sections.

3.2.1 Coordinate system

The origin in the ATLAS coordinate system is the interaction point. The *z-axis* is defined as the beam axis with a right-handed orientation. The *x-axis* is perpendicular

Detector component	Resolution	Pseudorapidity coverage
Tracking	$\sigma_{p_T}/p_T = 0.05\% p_T \oplus 1\%$	± 2.5
EM calorimetry	$\sigma_E/E = 10\%\sqrt{E} \oplus 0.7\%$	± 3.2
Hadronic calorimetry		
$\hookrightarrow$ barrel and end-cap	$\sigma_E/E = 50\%\sqrt{E} \oplus 3\%$	± 3.2
$\hookrightarrow$ forward	$\sigma_E/E = 100\%\sqrt{E} \oplus 10\%$	$3.1 < \lvert\eta\rvert < 4.9$
Muon spectrometer	$\sigma_{p_T}/p_T = 10\%$ at $p_T = 1$ TeV	± 2.7

Table 3.2 ATLAS performance requirements for each detector component [18], where E is the energy, p_{T} is the transverse momentum, σ_E is the energy resolution, $\sigma_{p_{\mathrm{T}}}$ is the transverse momentum resolution and η the pseudorapidity.

to the beam and it is oriented to the centre of the LHC ring. The *y-axis* is perpendicular to the other two axes and it points upward. See Figure (3.4).

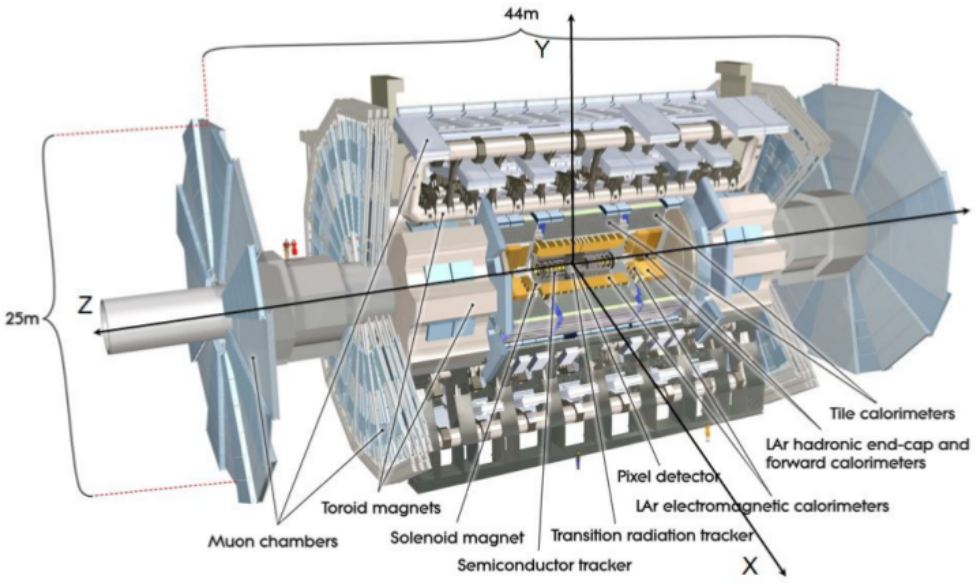

Figure 3.4 View of the ATLAS detector with its coordinate system.

As the ATLAS detector has a cylindrical geometry it is also useful to define ϕ and η coordinates, where ϕ is the azimutal angle that sweeps the plane perpendicular to the *z-axis* where it takes the values $-\pi < \phi < \pi$. The η coordinate is called the *pseudorapidity* which is the spatial coordinate describing the angle of a particle relative to the beam axis. See Figure (3.5).

The *pseudorapidity* is defined by:

$$\eta = -\ln\left[\tan\left(\frac{\theta}{2}\right)\right] \tag{3.3}$$

where θ is the angle between the particle momentum $\vec{p}$ and the positive direction of the beam axis. The η variable takes values of $-\infty < \eta < \infty$ as it is shown in Figure (3.5). Also, we can define *pseudorapidity* in terms of the particle momentum as:

$$\eta = \frac{1}{2} \ln \left[\frac{|\vec{p}| + p_L}{|\vec{p}| - p_L} \right] \tag{3.4}$$

where p_L is the component of the particle momentum along the beam axis. It is interesting to mention that in the limit where the particle is travelling close to the speed of light, or in the approximation that the mass of the particle is nearly zero, pseudorapidity is numerically close to the *rapidity*, defined by,

$$y = \frac{1}{2} \ln \left[\frac{E + p_L}{E - p_L} \right]. \tag{3.5}$$

The use of this variable is important because the difference of rapidity of two particles is invariant under Lorentz boosts along the beam axis.

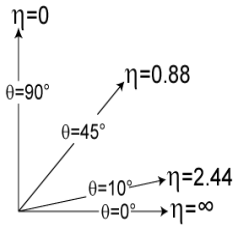

Figure 3.5 Pseudorapidity values for different θ.

3.2.2 Magnet system

The magnet system is divided into two parts [19], a central solenoid providing a 2 T axial magnetic field along the beam axis for the inner tracking detector and the external toroids providing a 0.5 T and 1 T toroidal magnetic field for the muon chambers in the barrel and end-cap regions, respectively. See Figure (3.6). The total magnetic field has a volume of 12,000 m^3.

The central solenoid is designed to minimise the amount of material in front of the calorimeter, achieving $\sim 0.66 X_0$ for incident particles. For this reason, it was installed in the same vacuum vessel as the LAr calorimeter. The solenoid is 5.8 m long with a 2.46 m inner diameter.

The toroidal magnet system is composed of 8 coils assembled radially with an eight fold symmetry. In the barrel region, each coil is 25 m long and 4.5 m tall and are cooled down to 4.5 K using individual cryostats. Coils in the end-cap are shorter (5 m) than in the central region and use a common cryostat. To optimise the bending power in

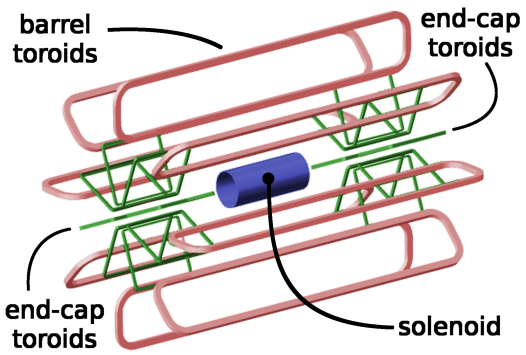

Figure 3.6 Geometry of the ATLAS magnet system.

the interaction regions, the end-cap coils are rotated 22.5^o with respect to the barrel ones.

3.2.3 The inner detector

The ATLAS Inner Detector (ID) is a tracking system designed to reconstruct the trajectories of charged particles, measure their momenta and the reconstruction of the primary and secondary vertices.

It consists of three types of subdetectors [20, 21], see Figure (3.7): Pixel Detector, Semi Conductor Tracker (SCT) and Transition Radiation Tracker (TRT). All of them are surrounded by the solenoid, see Section (3.2.2), that generates a uniform magnetic field of 2 T in the beam direction. The inner detector cavity has a diameter of 115 cm and its length is 7 m. It is divided in three parts: the barrel region and two end-caps on each side, as shown in Figures (3.12) and (3.13). The layout of the inner detector provides a full tracking coverage of $|\eta| < 2.5$. For details in the dimensions and the layout of the inner detector see Table (3.3).

As the ID is immersed in a uniform magnetic field, charged particles are subjected to the Lorentz force

$$\vec{F} = \frac{q}{m}\vec{p} \times \vec{B}, \tag{3.6}$$

which describes the force applied to a particle with charge q, mass m and momentum $\vec{p}$ due to the magnetic field $\vec{B}$. As the magnetic field is longitudinal, the trajectories are bent in the transverse plane xy (see Figure (3.9a)) and follow a helical path.

There are five parameters to be measured in the ID, such as:

$\mathbf{p_T}$ is the transverse momentum of the particle. It relates with the momentum as

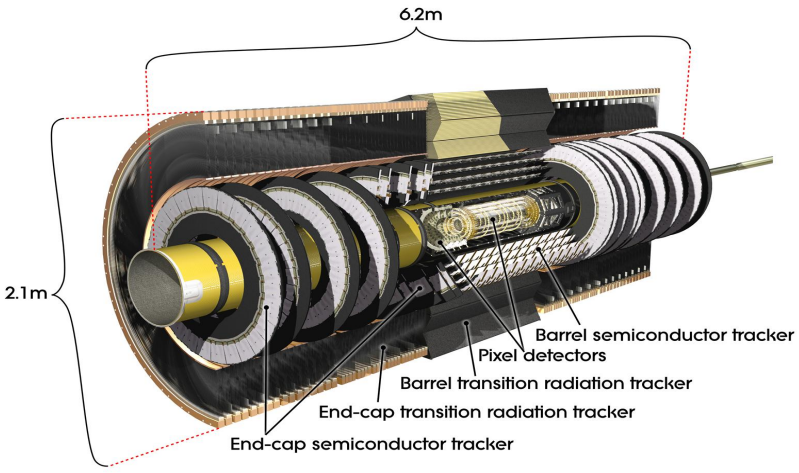

Figure 3.7 Sensors and structural elements of the inner detector (in radial order): Beam Pipe, Pixel Detectors, Semi Conductor Tracker (SCT) and the Transition Radiation Tracker (TRT).

$p_{\mathrm{T}} = p \sin\theta$.

$\boldsymbol{\phi}$ is the azimuthal angle of the track. It can be defined in terms of the momentum components as $\tan\phi = p_y/p_x$.

$\boldsymbol{\theta}$ is the polar angle θ, which in terms of the momentum components is defined by $\cot\theta = p_z/p_{\mathrm{T}}$.

$\mathbf{d}_0$ is the transverse impact parameter defined as the distance of closest approach to the beam line. Its sign is given by the angular momentum of the track with respect to the z axis. See Figure (3.8).

$\mathbf{z}_0$ is the longitudinal impact parameter defined as the value in the z axis of the point on the track that defines d_0. See Figure (3.8).

All these parameters describe the momentum of the particle as

$$\vec{p} = (d_0, z_0, \phi, \cot\theta, q/p_{\mathrm{T}}\,). \tag{3.7}$$

The charge q is determined by the direction of the track curvature as shown in Figure (3.9a).

Another important quantity to be calculated is the momentum resolution. As a simplified illustration in Figure (3.9b), the radius of the particle's track can be

Item	Radial Extension (mm)	Length (mm)
Pixel	$45.5 < R < 242$	$0 < \|z\| < 3092$
3 cylindrical layers	$50.5 < R < 122.5$	$0 < \|z\| < 400.5$
2×3 disks	$88.8 < R < 149.6$	$495 < \|z\| < 650$
SCT	$255 < R < 549$ (barrel)	$0 < \|z\| < 805$
	$251 < R < 610$ (end-cap)	$810 < \|z\| < 2797$
4 cylindrical layers	$299 < R < 514$	$0 < \|z\| < 749$
2×9 disks	$275 < R < 560$	$839 < \|z\| < 2735$
TRT	$554 < R < 1082$ (barrel)	$0 < \|z\| < 780$
	$617 < R < 1106$ (end-cap)	$827 < \|z\| < 2744$
73 straw planes	$563 < R < 1066$	$0 < \|z\| < 712$
160 straw planes	$644 < R < 1004$	$848 < \|z\| < 2710$

Table 3.3 Detailed dimension and layout of the ID.

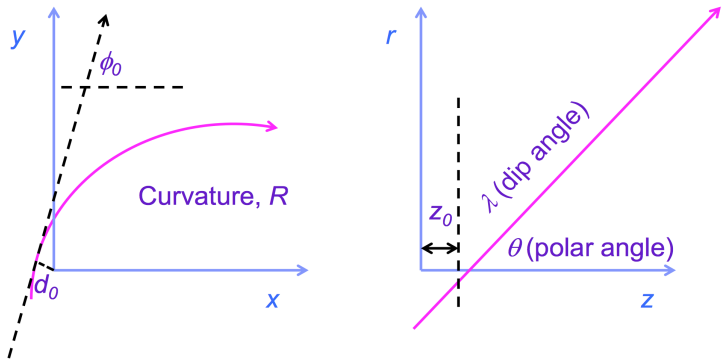

Figure 3.8 Ilustration of the parameters measured in the ID.

determined as a function of the sagitta s, as

$$R = \frac{s}{1-\cos(\alpha)} = \frac{s^2 + (L/2)^2}{2s} \approx \frac{L^2}{8s} \quad \text{for} \quad R >> L, \tag{3.8}$$

where 2α is defined as the arc's angle and L is the length of the detector region in the xy plane. The circular motion transverse to the uniform B field is given by

$$p_{\mathrm{T}}\,[\ \mathrm{GeV/c}] = q[\mathrm{e}]R[\mathrm{m}]B[\mathrm{T}] = \frac{0.3BL^2}{8s}. \tag{3.9}$$

The transverse momentum resolution, applying error propagation, is defined by

$$\frac{\sigma_{p_{\mathrm{T}}}}{p_{\mathrm{T}}} \approx \frac{\sigma_s}{s} = p_{\mathrm{T}}\,\frac{\sigma_s}{0.3BL^2}, \tag{3.10}$$

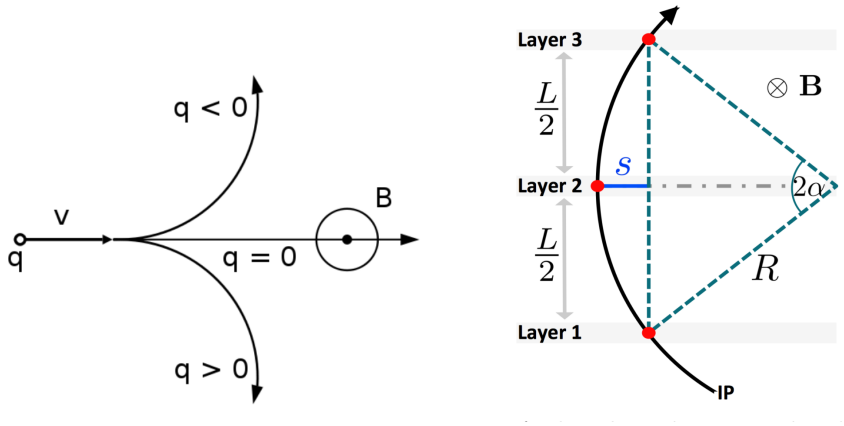

(a) (b)

Figure 3.9 Ilustration of (a) a charged particle's path through a magnetic field and (b) a charged particle traversing detector layers (red dots) perpendicular to a uniform B field, where R is the radius of the curvature, s the sagitta of the arc with angle ϕ and L/2 the separation of the detector layers.

where the sagitta uncertainty σ_s depends on the number of N layers and the spacing of track point measurements. At the limit $N \to \infty$ and assuming uniform spacing [22, 23], σ_s is

$$\sigma_s = \frac{\sigma_{\rho\phi}}{8}\sqrt{\frac{720}{N+5}}, \tag{3.11}$$

with $\sigma_{\rho\phi}$ the resolution of measuring a track point in the ρ-ϕ plane. There is also a term on the momentum resolution which considers multiple scattering. Therefore, the overall momentum resolution of the inner detector, as shown in Table (3.2), is

$$\frac{\sigma_{p_T}}{p_T} = 0.05\% p_T \oplus 1\%, \tag{3.12}$$

where $\oplus$ denotes the addition in quadrature.

From Equation (3.10), a good momentum resolution requires a strong magnetic field B, a large path length, L, and a very precise measurement of s. These requirements were a challenge to the design of the ID. Subject to the momentum of the particle, the ID needs the layers to be closer together (in the case of low momentum) or, for the layers to be well separated (in the case of high momentum).

The total material of the ID, together with the mechanical support structures, readout electronics and cooling system, is measured in radiation and interaction lengths, see

Figure (3.10). We want as little material as possible so the particles can reach the calorimeters. This mainly affects the efficiency of reconstructing low momentum tracks.

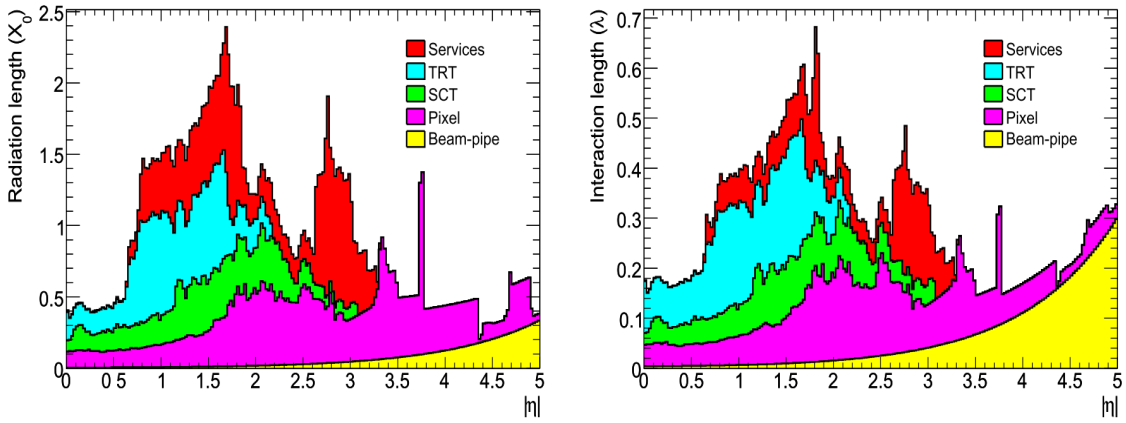

Figure 3.10 The ID material distribution in terms of radiation length X_0 (left) and interaction length λ (right) as a function of $|\eta|$ and averaged over ϕ [24].

When the tracks of charged particles have been reconstructed, they are extrapolated back inside the beam pipe to associate them with a pp collision, a common primary vertex. An important quantity to classify tracks is the impact parameter d_0. Good tracks of stable particles are expected to have small impact parameter compared to the impact parameter of long lived unstable particles such as b hadrons, which decay in a displaced secondary vertex.

More details of the ID subdetectors will be discussed in the following sections.

Pixel Detector

It is the most inner part of the detector, see Figure (3.11). Due to its closeness to the collision point, it is crucial for the reconstruction of the primary vertex and of secondary vertices from b-hadrons. The pixel detector consists of three concentric cylindrical silicon layers in the barrel region surrounding the bean pipe and three discs in each end-cap perpendicular to the beam pipe [25], see Figure (3.12) and (3.13).

The silicon layers and the discs are composed of pixel modules (1456 barrel modules and 288 disk modules), which help us to achieve a good granularity in the vertex region. A pixel module is a rectangular active device of approximately 6×2 cm^2 with 46080 pixels of 50×400 μm^2 of area, obtaining a high granularity. When a particle goes through one of these pixels, which is a reverse bias diode [25], electron hole pairs are produced in the silicon and if the resulting pulse exceeds a signal to noise threshold a hit is registered giving us information about the particle position and an estimate of

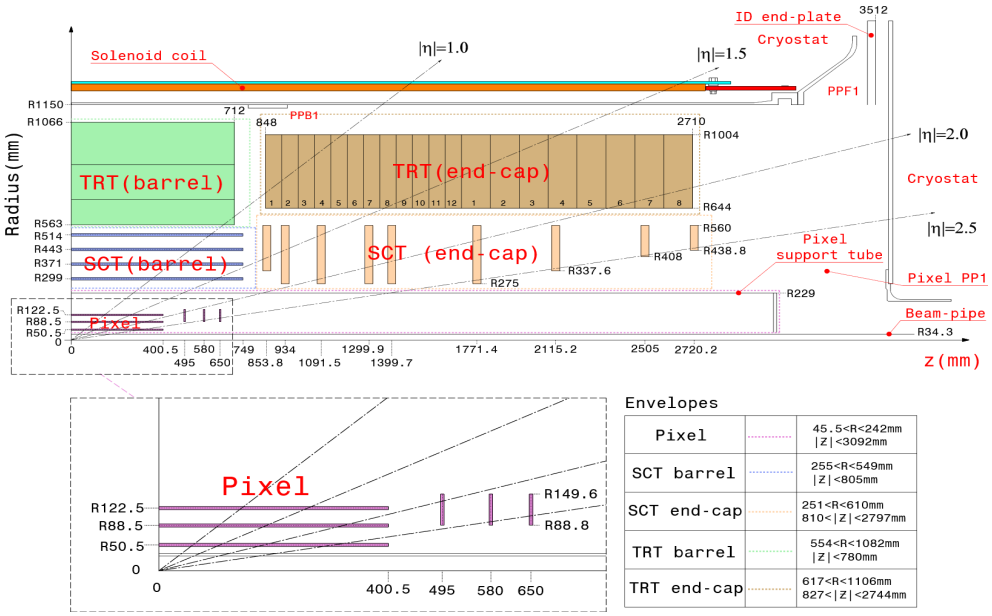

Figure 3.11 Detailed scheme of the Inner Detector, with a zoom on the pixel layers [18].

the amount of charge produced, and therefore, can be used for the reconstruction of the track (tracking). The detector provides on average three tracking points per charged track within $|\eta| < 2.5$, obtaining a position resolution of 10 μm in the ρ-ϕ plane and 115 μm along the z direction or ρ direction in the barrel or end-cap region respectively. The pixel detector has approximately 80.4 M readout channels.

During the recent LHC shutdown, an additional pixel layer closer to the interaction point was installed. It is called Insertable B-layer (IBL) [26], and it was designed to help the pixel detector layers to improve vertex resolution and achieve better identification of b-hadrons.

SemiConductor Tracker

This detector region gives us additional measurements of the position of the particle. It is built in four concentric layers in the barrel region with axially arranged strips along the beam line, see Figure (3.12). The end-cap region has nine discs per end-cap with SCT modules mounted in concentric circles [18], see Figure (3.13). Using similar technology as in the pixel detector, SCT micro-strip sensors [25] are rotated with respect to each other at a stereo angle of 40 mrad to measure space points in both ρ - ϕ and ρ or z plane, depending whether is placed in the end-cap or in the barrel region. The SCT measures on average four points on a charged track within $|\eta| < 2.5$ and with a mean strip pitch of 80 μm achieving an intrinsic position resolution of 17 μm in the ρ - ϕ plane and 580 μm along the z axis or ρ for the barrel or end-cap regions

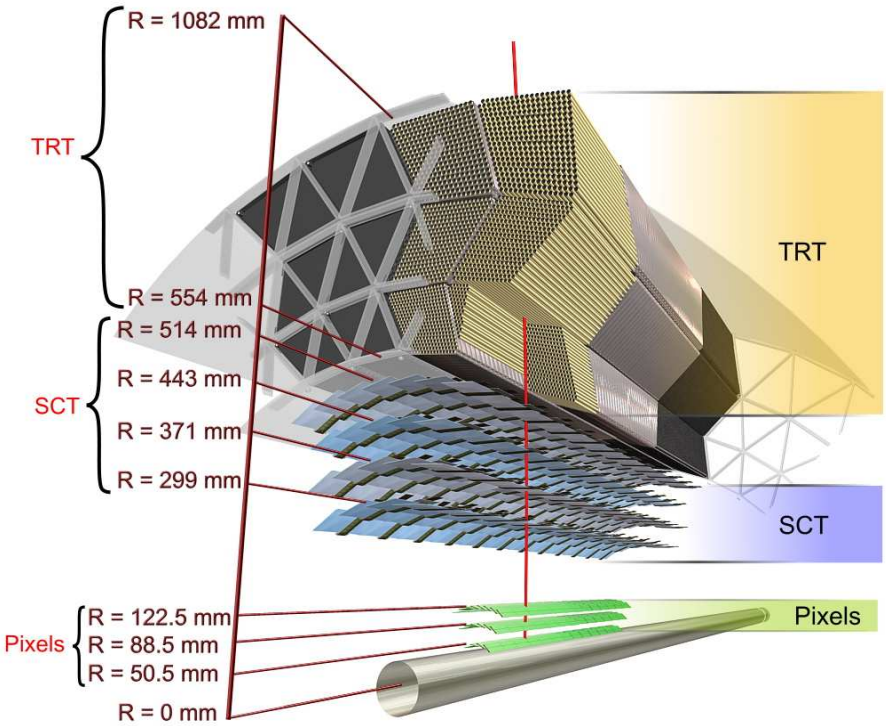

Figure 3.12 Ilustration of a charged track through the different barrel layers of the ATLAS inner detector from the interaction point [18].

respectively. The total number of readout channels is approximately 6.3 M.

Transition Radiation Tracker

The Transition Radiation Tracker consists of 4 mm straw tubes each containing a 31 μm gold-plated tungsten wire along their centre. The straws are filled with a gas mixture of 70% Xe, 27% CO_2 and 3% O_2. The barrel structure consists of 144 cm long straws parallel to the beam axis, see Figure (3.12). In the end cap, the 37 cm long tubes are arranged radially in wheels, see Figure (3.13).

When a charged particle passes through the straw the gas inside is ionised. The resulting free electrons drift towards the wire, because of the potential difference between the walls of the straw and the wire. This allows us to identify the excited straw, and therefore, the position of the particle and the distance of the particle to the straw. It provides an average of 36 hits per track.

The tubes are interleaved with polypropylene fibres in the barrel and foil fibres in the end-cap to produce transition radiation photons (emitted by relativistic charged particles passing through different dielectric constant media and depending on the Lorentz factor $\gamma = E/mc^2$). This makes the TRT specialised in detecting electrons

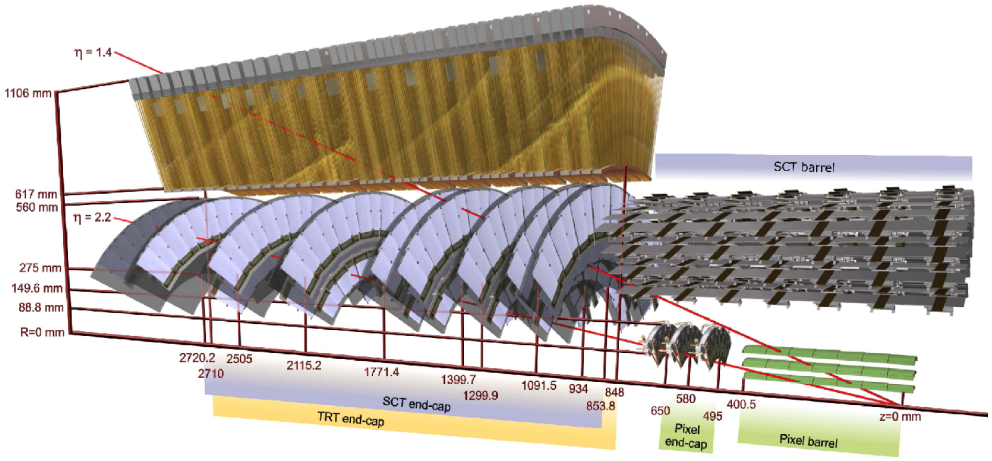

Figure 3.13 Ilustration of a charged track through the different end-cap layers of the ATLAS inner detector from the interaction point [18].

because they make more transition radiation photons than other heavier particles [18]. The track is followed until $|\eta| < 2.0$ and only information from the ρ - ϕ plane is provided, see Figure (3.11). The TRT has 351,000 readout channels. Each signal hit can be measured with an intrinsic resolution of 130 μm in the ρ - ϕ plane.

3.2.4 Calorimetry system

The ATLAS calorimetry system, see Figure (3.14), can be divided into the electromagnetic calorimeter for the identification of electromagnetic showers induced by electrons and photons, and of a hadronic calorimeter for the reconstruction of hadronic jets. It consist of sampling calorimeters which use alternating layers of active and absorber medium for the energy measurement [27].

The electromagnetic (EM) calorimeter is the innermost calorimeter and it uses liquid argon (LAr) as an active material and lead as an absorber. The hadronic calorimeter also uses LAr and copper as absorber in the forward region (HEC) and it uses active scintillating tiles with absorbing iron in the barrel region (TileCal). The TileCal is a cylinder divided into three sections: central barrel and two identical extended barrels. See Figure (3.14). The forward calorimeter (FCal) uses LAr and copper in the EM part and tungsten in the hadronic part. All together they provide a wide coverage of $|\eta| < 4.9$, see Table 3.4.

The energy measurement with the calorimeter is based on the fact that the energy released in the detector material, mainly through ionisation in ATLAS, by charged particles in the shower is proportional to the energy of the incident particle. The

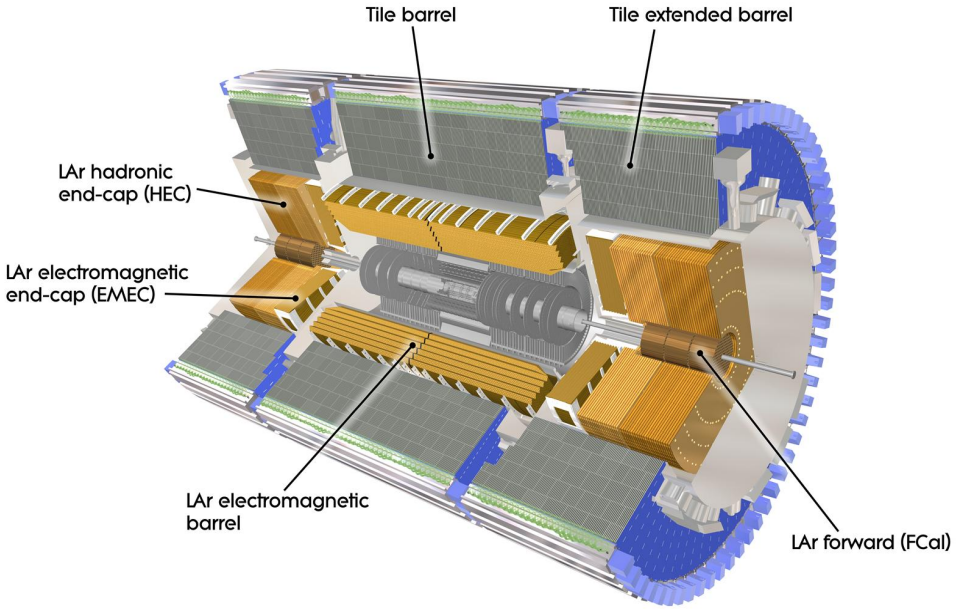

Figure 3.14 Ilustration of the ATLAS calorimeter system.

energies of electrons, photons and hadrons are all measured in the calorimeters. Muons leave small energy depositions as well. Also, the energy of particles that pass through the detector undetected, like neutrinos, can be inferred by the calorimeters. This energy is called *Missing Transverse Energy* ($E_{\mathrm{T}}^{\mathrm{miss}}$).

Calorimeter component	η
Electromagnetic Barrel (EMB)	$0 < \|\eta\| < 1.5$
Electromagnetic End-cap Calorimeter (EMEC)	$1.4 < \|\eta\| < 2.5$
Long Barrel TileCal	$0 < \|\eta\| < 1$
Extended Barrel TileCal	$0.8 < \|\eta\| < 1.7$
Hadronic End-cap Calorimeter (HEC)	$1.5 < \|\eta\| < 3.2$
Forward Calorimeter (FCal)	$3.1 < \|\eta\| < 4.9$

Table 3.4 ATLAS calorimeter range of pseudorapidity.

The resolution of the energy measurement can be generally approximated by,

$$\frac{\sigma_E}{E} = \frac{a}{\sqrt{E}} \oplus \frac{b}{E} \oplus c \tag{3.13}$$

where the first term is called the *stochastic term* which is due to sampling fluctuations related to the physical shower development. They originate from variations of the number of produced charged particles crossing the active layers and the energy loss in the interspaced absorbing layers. In general, the resolution of the energy improves with

the energy of the incident particle as $1/\sqrt{E}$. The second term is the *noise term* which comes from the electronic noise of the readout chain. The third term is the *constant term* which is independent from the particle's energy and comes from instrumental effects.

Electromagnetic calorimeter

The electromagnetic calorimeter is made principally of interspaced layers of lead and liquid argon in an accordion geometry, see Figure (3.15). When electrons or photons pass through the lead an *electromagnetic shower* is produced. This phenomena occurs because when a passing electron is deflected by a lead atom, photons are produced, this is called *Bremsstrahlung*. When the photons generated from the passing electron interact with a lead nuclei, they can be transformed into electron-positron pairs. If such pairs have enough energy to produce more photons, the photons will be transformed again into other electron-positron pairs and so forth producing the shower. The number of pairs produced is proportional to the initial energy. When the electromagnetic shower reaches the liquid argon, it ionises the material as it pass through. An electric field is applied to the material which produces a current with the free electrons in an external circuit connected to the calorimeter. Liquid argon is employed because the mean free path of the ionised electrons is adequate to register the generated current before the electrons are recaptured. Also, liquid argon has a high resistance to high voltage and it has insulating properties [18]. In order to fully absorb electromagnetic showers with incident particle energies < 5 TeV before reaching the hadronic calorimeter, the total thickness of the EM calorimeter is chosen to be $> 22X_0$ in the barrel and $> 24X_0$ in the end-cap regions.

The system has a barrel region covering $|\eta| < 1.475$ and two end-cap wheels on each side covering $|\eta| < 2.5$. A calorimeter module is shown in Figure (3.15). It consist of four layers defined according to the following characteristics from inner to outer radii:

Pre sampler is a single thin layer only of argon (active material) in front. The purpose is to correct for the energy loss in the ID, solenoid and cryostat wall.

Sampling 1 has a thickness of approximately $4.3X_0$ and it is composed of η strips of dimensions $\Delta\eta \times \Delta\phi = 0.0031 \times 0.098$. This provides an excellent resolution in the η coordinate for photon and π^0 separation.

Sampling 2 is composed of square towers of $\Delta\eta \times \Delta\phi = 0.025 \times 0.025$ at $|\eta| < 2.5$ with a thickness of approximately $16X_0$. It absorbs the main part of the EM shower.

Sampling 3 is composed of towers of $\Delta\eta \times \Delta\phi = 0.050 \times 0.025$ with thickness of approximately $2X_0$ used for the absorption of larger showers in η with $E_T > 50$ GeV.

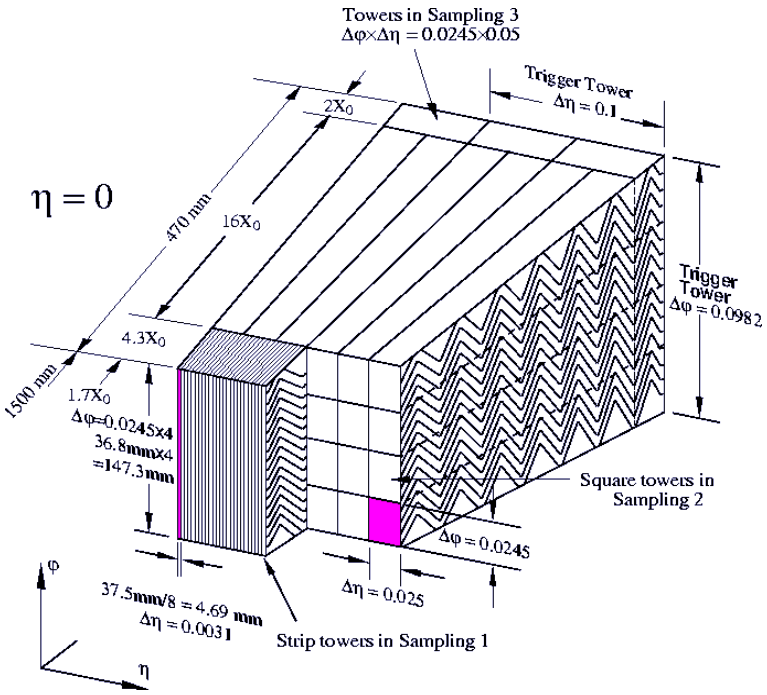

Figure 3.15 An ilustration of the different layers of a barrel module of the ATLAS electromagnetic calorimeter.

The overall energy resolution, see Table (3.2), is

$$\frac{\sigma_E}{E} = \frac{10\%}{\sqrt{E}} \oplus 0.7\%. \tag{3.14}$$

Hadronic calorimeter

It measures the hadrons energy, position and arrival time through *hadronic showers*. Hadrons interact with matter through the strong force. Hadronic showers are the consequence of the cascade production of other hadrons, nuclear deexcitation, and decays of pions. Their longitudinal development is characterised by the interaction length λ, which sets the geometrical size scale of the hadronic calorimeters. Shower shapes can also be studied to obtain information of the particle that originated it, for example, gluons produce a wider shower than quarks due to larger colour charge.

As mentioned before, the system is composed of the Tile Calorimeter (TileCal), the Hadronic End-cap Calorimeter (HEC) and the hadronic part of the Forward Calorimeter (FCAL).

The **TileCal** uses alternating layers of absorbing iron and fluorescent scintillator material that produces a rapid light pulse when the particle passes through. Special optical fibres collect this light and feed it into readout boxes where photodetectors amplify the signal. When the amount of light in a given region is summed up over many layers of tiles in depth, called a tower, it gives a measure of the energy of the particle [18]. It is divided into a central barrel covering $|\eta| < 1$ and extended barrels covering $0.8 < |\eta| < 1.7$. The iron plates are 14 mm thick and the scintillating tiles are 3mm thick. There are three layers with a segmentation of $\Delta\eta \times \Delta\phi = 0.1 \times 0.1$ in the first two layers and 0.2×0.1 in the last layer.

The **HEC** consist of two wheels in each end-cap covering a range of $1.5 < |\eta| < 3.2$ and uses a 25-50 mm copper plates as absorbers interspaced with 8.5 mm liquid argon (LAr) as active medium. The ionization charge from shower particles in the LAr is collected via an applied high voltage between electrodes, producing a pulse of current for readout. There are four layers with segmentation of $\Delta\eta \times \Delta\phi = 0.1 \times 2\pi/64$ at $|\eta| < 2.5$ and $0.2 \times 2\pi/32$ at larger $|\eta|$.

Finally, the **FCal** consists of three cylindrical modules in each end-cap covering the region of $3.1 < |\eta| < 4.9$. It is made of thin gap LAr of 2 mm, centred in tubes parallel to the z axis, with copper in the innermost layer (EM part) and tungsten (for the hadronic part) for the absorber.

The overall energy resolution, see Table (3.2), is

$$\frac{\sigma_E}{E} = \frac{50\%}{\sqrt{E}} \oplus 3\% \quad \text{and} \quad \frac{\sigma_E}{E} = \frac{100\%}{\sqrt{E}} \oplus 10\% \tag{3.15}$$

for the TileCal/HEC and FCal respectively.

3.2.5 The muon spectrometer

The aim of the muon spectrometer is to provide a precision measurement of the momentum of those particles which manage to survive after passing through the calorimeter system. Muons lose approximately 1 MeV per millimetre in materials like steel or copper, so we need 5 meters of material to absorb the energy of a 5 GeV muon. On the contrary, hadrons of any energy are completely absorbed in approximately 1.5 meters of steel. This is why any particle that passes through the calorimeters is most likely a muon.

The muon spectrometer measures the deflection of muon tracks in the ρ - z plane with the superconducting toroidal magnets, see Figure (3.16). These magnets produce a magnetic field whose field lines are concentric circles in the beam pipe and are orthogonal to the magnetic field produced in the ID.

The muon spectrometer is composed of two types of subdetectors:

Type I are high precision tracking chambers to reconstruct the momentum. This type of chambers are Monitored Drift Tubes (MDTs) and Cathode Strip Chambers (CSCs).

Type II are fast response chambers for online triggering on muons. This type of chambers are Resistive Plate Chambers (RPCs) and Thin Gap Chambers (TGCs).

All of them are gaseous detectors collecting the charge deposited through ionisation of the gas from passing muons.

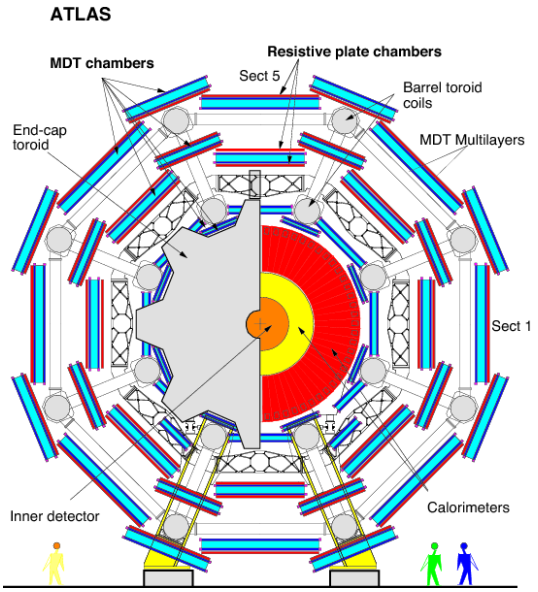

(a) Muon spectrometer in the xy plane.

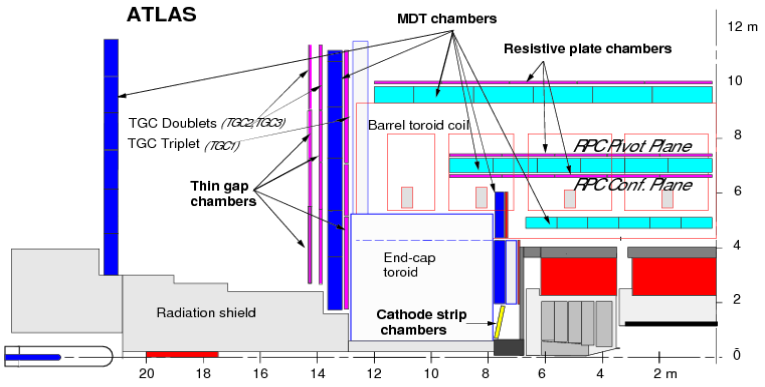

(b) Muon spectrometer in the $\rho\phi$ plane.

Figure 3.16 ATLAS Muon Spectrometer.

The **MDTs** are composed of several layers of drift tubes (three to eight) and contain a gas mixture of 93% Ar and 7% CO_2 at a pressure of 3 bar. The tubes are arranged along ϕ combined in layers and grouped into chambers, see Figure (3.16). They cover a range of $|\eta| < 2.7$, except the innermost end-cap layer reaching up to $|\eta| < 2.0$ where they are complemented by CSC chambers in this region.

The **CSCs** are composed of two disks, containing eight chambers each covering the region of $2.0 < |\eta| < 2.7$. They are multi-wire proportional chambers containing cathode planes segmented in strips along the orthogonal direction, allowing for measurements both in the bending and transverse planes. They use a gas mixture of 80% Ar and 20% CO_2.

The **RPCs** are composed of three concentric cylindrical trigger stations (for online event selection) attached to the MDT chambers in the barrel region with a coverage of $|\eta| < 1.05$. This system does not use wires, but uses two parallel resistive plates with a 2 mm spacing in each station with a gas mixture of 94.7% $C_2H_2F_4$, 5% Iso-C_4H_{10} and 0.3% SF_6. Metallic strips are connected to the plates to read out the signal.

The **TGCs** are composed of multi-wire proportional chambers. They are arranged in concentric wheels covering a range of $1.05 < |\eta| < 2.4$ and complement the MDTs with a measurement of the ϕ coordinate. They are similar to the CSC except that their wire strip spacing is smaller allowing faster charge collection which allows them to be used for the trigger. The gas mixture in the wire is of 55% CO_2 and 45% n-C_5H_{12}.

The main parameters of the muon spectrometer subdetectors are summarised in Table (3.5). In general, the precision of the momentum measurement for a high-pT muon track depends mainly on the resolution of the determination of the sagitta, s, which was discussed in Section (3.2.3). For high momentum muon tracks ($p_T \sim 1$ TeV) the precision is about 10%, while for low momentum tracks ($p_T \sim 3$ GeV) the measurement is complemented with the tracking information from the ID achieving a resolution of $2 - 3\%$.

Detector	**Chamber resolution**			**Measurements/track**		**Number of**	
	z/R	ϕ	time	barrel	end-cap	chambers	channels
MDT	35 μm (z)	-	-	20	20	1088	339k
CSC	40 μm (ρ)	5 mm	7 ns	-	4	32	30.7k
RPC	10 μm (z)	10 mm	1.5 ns	6	-	544	359k
TGC	2-6 μm (ρ)	3-7 mm	4 ns	-	9	3588	318k

Table 3.5 Summary of the main parameters of the different ATLAS muon spectrometer subdetectors [18].

3.2.6 Forward detectors

The ATLAS detector is extended on each side to the very forward region by: the LUminosity measurement using Čerenkov Integrating Detector (LUCID), the Zero-Degree Calorimeter (ZDC) and the Absolute Luminosity For Atlas (ALFA). See Figure (3.17).

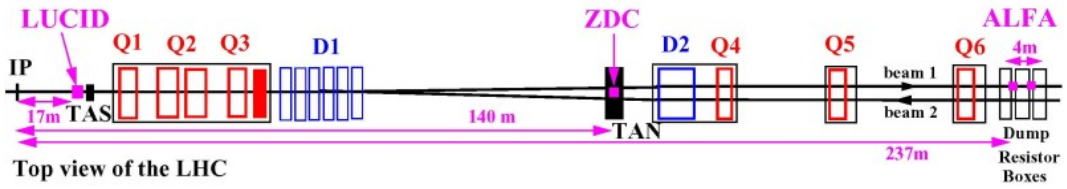

Figure 3.17 Placement of the forward detectors along the beam line with respect to the ATLAS interaction point (IP) [18].

LUCID is composed of Čerenkov counters placed at $z = \pm 17$ m and 10 cm from the beam pipe at $|\eta| \approx 5.8$. They are designed to detect inelastic p-p scattering for instantaneous/integrated luminosity measurements and for online monitoring of the beam conditions.

ZDC is composed of EM and hadronic calorimeter modules placed between the two beam pipes at $z = \pm 140$ m and at $|\eta| > 8.3$ to detect neutrons of heavy-ion collisions. Its main purpose is to determine the centrality of these collisions and it can also reduce beam-gas/halo background via a tight coincidence requirement between the ZDC arms located symmetrically on each side of the interaction point. In addition, the interaction point in ATLAS can be located independently with a 3 cm z coordinate resolution.

ALFA is the furthest detector from the interaction point. It is composed of scintillating-fibre trackers inside Roman-pot detectors at $z = \pm 240$ m, which can move as close as at 1 mm to the beam pipe to detect elastic scattering at small angles, where the amplitude is directly connected to the total cross-section via the optical theorem.

3.2.7 Trigger and data

One could wonder: how can ATLAS store the huge amount of information from all the collisions? At the design value of the LHC instantaneous luminosity ($\mathcal{L} = 10^{34}\text{cm}^{-2}\text{s}^{-1}$) the pp cross-section, with an interaction rate is of about 10^9 evt/s, is many orders of magnitude higher than the cross-section of interesting events, like Higgs boson events. ATLAS stores event data using millions of readout channels, but there are technological

constraints that limit the amount of data that can be recorded for offline physics analyses. Thus a strict online selection of interesting events must be employed and real time (online) hardware and software systems (trigger systems) are necessary to reduce the output event rate by a factor 10^6, while maintaining a high efficiency for interesting events.

The ATLAS Trigger and the Data Acquisition system (TDAQ) is in charge of this challenging task with the aim of reducing the final data storage rate from the incoming bunch crossing rate of 40 MHz (20 MHz at 8 TeV with a 50 ns bunch spacing) to 200 Hz (600 Hz in 2012). In simpler words, with an event size of 1.5 MB (1.6 MB in 2012), the TDAQ system must reduce the storage rate from 60 TB/s (32 TB/s in 2012) to 300 MB/s (960 MB/s in 2012).

The ATLAS Trigger system is divided in three levels as: Level 1 (L1), Level 2 (L2) and Event Filter (EF). Level 1 is hardware-based and, Level 2 and Event Filter are based on software algorithms which analyse the data on large computing farms, see Figure (3.18). This last two combined are called the High Level Trigger (HLT)[18].

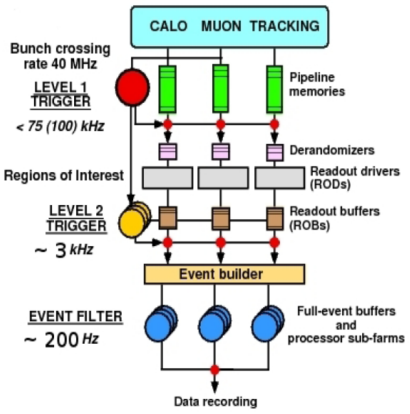

Figure 3.18 Schematic overview of the ATLAS Trigger and Data Acquisition system with design configuration [18]. The 2012 (Run-1) configurations are 20 MHz, 70 kHz, 6.5 kHz and 600 Hz [28–30].

The **L1** trigger system receives data at a bunch crossing rate of 40 MHz and must make its decision within 2.5 μs to reduce the output rate to 75 kHz. Therefore, it needs only fast detectors systems: calorimeters for electrons, jets, τ leptons and missing transverse energy, muon trigger chambers for muons. For the calorimeters [31], signals which cover $\Delta\eta \times \Delta\phi = 0.1 \times 0.1$ (trigger towers) in the region $\mid \eta \mid < 2.5$ are used to build clusters and compute their transverse energy E_{T}, summing up signals from EM and hadronic calorimeter cells, with a precision of about 1 GeV. For muons [32], the RPC and TGC

detectors are used from the muon system. Muon p_{T} thresholds are applied looking for hits within defined *coincidence windows* around the extrapolation to the interaction point of the first hit, see Figure (3.19).

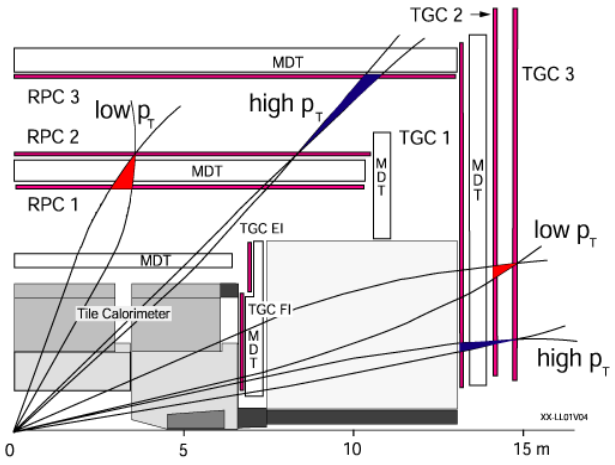

Figure 3.19 Quarter section of the muon system in the rz plane: coincidence windows (red and blue) are shown for low and high p_{T} muons.

The **L2** trigger system uses information from the HAD and EM calorimeters and, in addition, tracking information from the inner detector to refine the L1 selection [18]. All the information used is restricted to the *Region of Interest* (RoI) identified in L1, see Figure (3.20). The available processing time is about 10 ms and allows the first reconstruction of physics objects using various detector systems and optimised software algorithms. An event can be either selected to be moved to the Event Filter system, or discarded and removed from the data flow chain. The output event rate of L2 is about 1 kHz.

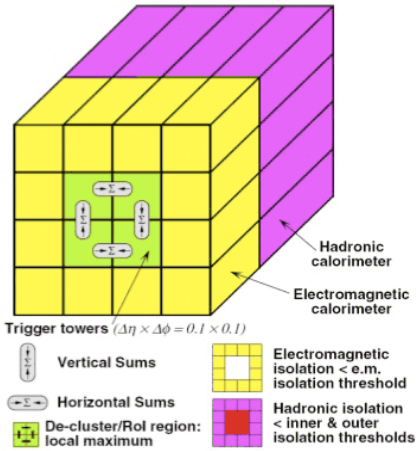

Figure 3.20 Structure of calorimeter towers. In yellow it is shown the EM calorimeter tower, in purple the HAD calorimeter towers, and in green is shown the region of interest (ROI).

The **EF** trigger system is the last step of the chain. The L2 accepted events are completely reconstructed using the full event information and are analysed to make a final decision whether the event is of interest to any offline physics analysis. The processing time is around 1 s and the final output is 100 Hz.

The EF data is transferred to the CERN computing facility (Tier-0), see Figure (3.21), which is the first step of the ATLAS offline analysis system. The full reconstruction is applied to the raw data to create the Event Summary Data (ESD) and the Analysis Object Data (AOD). The ESD contain the reconstructed quantities measured in the detector, together with the reconstructed physics objects and its size is around 500 kbytes. The AOD only has physics objects and its size is smaller, about 100 kbytes per event. There also exists a reduced format which is called D3PD. This is the data format generally used for the final physics analyses (there is a new data format that is being used for Run II which is called xAOD).

The data (AOD, ESD and D3PD), from the Tier-0 centre, are copied to the Tier-1 centres. These centres are located in different countries. They are required to reprocess raw data to obtain smaller sized and updated versions of the data formats. The physics analyses are mainly performed at Tier-2 and -3 centres. Every Tier-2 centres have access to Tier-1 centres. Monte Carlo simulated data are produced and stored in the Tier-1 and Tier-2 sites. All this data streaming relies on the presence of a cloud infrastructure called the LHC Computing Grid [33].

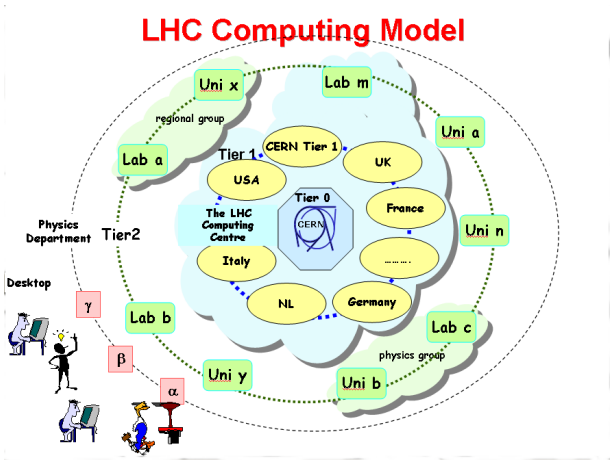

Figure 3.21 Ilustration of the LHC Tier structure. At the centre it is shown the Tier-0, located at CERN, surrounded by the Tier-1 structure (yellow ovals) and the Tier-2 structure (green rectangles).

Chapter 4

Statistics for searches at the ATLAS detector

For any analysis performed at the LHC, statistical methods are required for the interpretation of the results. In particle physics experiments, searches for new phenomena that have not yet been observed are often carried out. Therefore, it is of great importance to quantify the level of agreement between the data and a hypothesis, allowing to infer if the new phenomena is there or not.

This chapter will outline the general statistical procedure used for search and discovery at the ATLAS detector in the context of a frequentist statistical test [34].

4.1 Formalism

One must define the hypothesis to be tested. In general, the null hypothesis, H_0, is defined to be tested against an alternative hypothesis, H_1. Depending on what will be tested, the definitions of the hypothesis can vary. The null hypothesis is defined as the background only hypothesis, which in the case of SM Higgs searches, is translated as the SM without the Higgs boson. The alternative hypothesis is the one that contains signal plus background events, which can be translated as containing the SM Higgs boson in the case of its search.

The level of agreement between the observed data with a given hypothesis, H, must be calculated. This is done by computing a p-value which is the probability, under H, of finding data of equal or greater incompatibility with the predictions of H. The measure

of incompatibility can be based on a *profile likelihood ratio* for signal and background. One rejects the hypothesis if its p-value is below a certain threshold α. The p-value can be reinterpreted into an equivalent significance, defined as:

$$Z = \Phi^{-1}(1 - p), \tag{4.1}$$

where Φ^{-1} is the inverse of the cumulative distribution of the standard Gaussian. The relation between the significance Z and the p-value is illustrated in Figure (4.1).

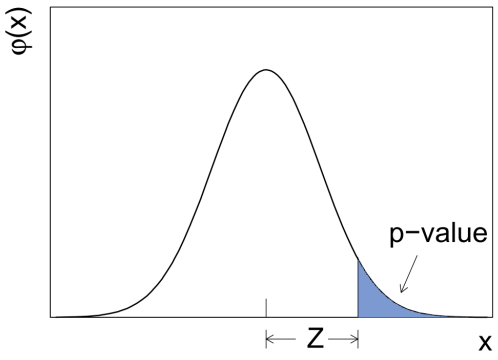

Figure 4.1 The standard Gaussian distribution showing the relation between the significance Z and the p-value, where the p-value is the blue area under the curve [34].

In particle physics a test of a p-value of size α for all possible values of the parameters is done. All of those values that are not rejected constitute what is called a confidence region for the parameters with a confidence level of CL $= 1 - \alpha$. Therefore, the true value of the parameters are contained in the confidence region with a probability of $1-\alpha$. For the standard choice, the background only hypothesis is rejected for discovery with a p-value of size 2.87×10^{-7} (99.99% CL) which corresponds to a significance of $Z = 5$. This means that the probability of the observed data behaving as if it only contains background is very low. For the purpose of exclusion limits on a parameter, the threshold α is typically of 0.05 (95% CL) which corresponds to a significance of $Z = 1.64$.

Consider an experiment where the signal process is not known to exist and the goal of the analysis is to search for it. For each selected event we measure a quantity, x. In the case of the $H \to ZZ^{(*)} \to 4l$ channel, this quantity could be the invariant mass of the final state denoted as m_{4l}. Let us assume that the expected number of background events is b and the expected number of signal events is s. The actual number of events, n, that could be found can be modelled as a Poisson distributed quantity whose mean can be written as $\mu s + b$, where μ is the parameter that specifies the strength of the

signal process. Therefore, the probability to find n events is

$$P(n|\mu) = \frac{(\mu s + b)^n}{n!} e^{-(\mu s+b)}. \tag{4.2}$$

The values of the observed variable follow a probability distribution function (pdf) which considers that two types of events can occur (signal or background),

$$f(x|\mu) = \frac{\mu s}{\mu s + b} f(x|s) + \frac{b}{\mu s + b} f(x|b), \tag{4.3}$$

where the coefficients of each component give the fraction of events of each type. Thus, the complete measurement consists of selecting n events and for each measuring the quantity, x. The complete likelihood function, from which the profile likelihood ratio is based, is given by

$$L(\mu, \boldsymbol{\theta}) = P(n|\mu) \prod_{i=1}^{n} f(x_i|\mu) = \frac{(\mu s + b)^n}{n!} e^{-(\mu s+b)} \prod_{i=1}^{n} \left[\frac{\mu s f(x_i|s) + b f(x_i|b)}{\mu s + b} \right], \tag{4.4}$$

where $\boldsymbol{\theta} = (\boldsymbol{\theta}_s, \boldsymbol{\theta}_b)$ contains the nuisance parameters (parameters which are not of immediate interest but which must be accounted for in the analysis because they affect the parameters of interest), where their dependence is hidden in the background and signal pdfs as: $f(x|s) = f_s(x; \boldsymbol{\theta}_s)$ and $f(x|b) = f_s(x; \boldsymbol{\theta}_b)$. In addition, the dependence of the nuisance parameters can be also hidden in $s = s(\theta)$ and $b = b(\theta)$, depending if they are treated as independent parameters or not. With Equation (4.4), one can estimate the values of the parameters by maximising the function as,

$$\frac{\partial L}{\partial \theta_i} = 0, \qquad \text{i=1, ..., m.} \tag{4.5}$$

This is called the Maximum Likelihood (ML) method and θ_i are the ML estimators.

With all of the above, we can define the *profile likelihood ratio* to test different hypothesised values of μ and infer if the signal search for is there or not.

4.2 Tests based on the profile likelihood ratio

To test a hypothesised value of μ, the profile likelihood ratio is defined as

$$\lambda(\mu) = \frac{L(\mu, \hat{\hat{\boldsymbol{\theta}}}(\mu))}{L(\hat{\mu}, \hat{\boldsymbol{\theta}})} \tag{4.6}$$

where $\hat{\hat{\boldsymbol{\theta}}}$, called the profile values of the nuisance parameters, are the values that maximise the likelihood for a specific μ. In the denominator, $\hat{\mu}$ and $\hat{\boldsymbol{\theta}}$ are the values of the parameters that maximise the likelihood.

The profile likelihood ratio $\lambda(\mu)$ can take values from 0 to 1. Values of $\lambda(\mu)$ closer to one means that the data is in good agreement with the hypothesised value of μ.

From Equation (4.6), it is convenient to define the statistic

$$t_\mu = -2 \ln \lambda(\mu) \tag{4.7}$$

as the basis for the statistical test. The values that t_μ can take go from 0 to ∞, meaning that higher values imply greater incompatibility between the data and the tested μ.

Usually the signal process is such that only positive values of μ are taken into account. So, we would choose the critical region of the null hypothesis test to correspond to data outcomes with $\hat{\mu} > 0$ even though it could happen that $\hat{\mu} < 0$ (observed number of events can fluctuate below what is expected from background only). Negative values of $\hat{\mu}$ also indicate an incompatibility with the null hypothesis, however we do not want to exploit this if discovery of a positive signal wants to be declared, as in the case of SM Higgs boson searches. Assuming that we want to test the background only hypothesis and discovery wants to be claimed for a positive signal process, a new definition of Equation (4.7) can be written:

$$q_0 = \begin{cases} -2 \ln \lambda(0) & \hat{\mu} \geq 0 \\ 0 & \hat{\mu} < 0 \end{cases} \tag{4.8}$$

where $\lambda(0)$ is the profile likelihood ratio defined in Equation (4.6) evaluated at $\mu = 0$.

If we were interested in an upper limit for the parameter μ, we can define a new function as well:

$$q_\mu = \begin{cases} -2 \ln \lambda(\mu) & \hat{\mu} \leq \mu, \\ 0 & \hat{\mu} > \mu, \end{cases} \tag{4.9}$$

where $\lambda(\mu)$ is the profile likelihood ratio defined in Equation (4.6). When setting an upper limit, one would not take into account data with $\hat{\mu} > \mu$ as representing less compatibility with μ than the data obtained, and therefore $q_\mu = 0$.

One has to acknowledge that the definition of these tests only gives a hint of the disagreement between the data and a hypothesis. To quantify this, a p-value must be

computed by

$$p_\mu = \int_{t_{\mu,obs}}^{\infty} f(t_\mu|\mu,\theta)dt_\mu, \tag{4.10}$$

where $t_{\mu,obs}$ is the value of t_μ observed from data and $f(t_\mu|\mu,\theta)$ is the pdf of t_μ under the assumption of μ. This relation is illustrated in Figure (4.2). To obtain the upper limit, several μ values will be tested. The highest value of μ which is not rejected will be the upper limit.

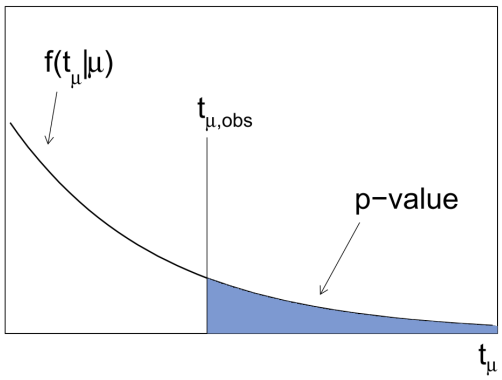

(a)

Figure 4.2 Illustration of the relation between the p-value obtained from an observed value of the test statistic t_μ, where $f(t_\mu|\mu,\theta)$ is the probability distribution function (pdf) of t_μ under the assumption of μ [34].

4.3 Approximate pdf distribution for the test statistic t_μ

To calculate the p-value from Equation (4.10) the pdf function of the test statistic is needed. For discovery, we are testing the background only hypothesis and thus we need $f(q_0|0)$. When setting upper limits, the value of μ for which $\alpha = 0.05$ is found using the $f(q_\mu|0)$ distribution. The notation used here is that the subscript of q refers to the hypothesis being tested and the second argument in $f(q_\mu|\mu)$ gives the value of μ assumed in the distribution of the data. There are various ways of obtaining these distributions, for example by means of Monte Carlo calculations which can be computationally expensive. Instead, assuming sufficiently large data samples, one can show that the distribution approaches an asymptotic form related to a chi-square distribution [34] where the number of degrees of freedom is equal to the number of parameters of interest, in our case only one, μ. The approximate method is based on theorems due to Wilks [35] and Wald [36].

Assuming that the conditions for the asymptotic approximations hold, the Wald

approximation [36] for a single parameter of interest (POI) is:

$$-2\ln\lambda(\mu) = \frac{(\mu-\hat{\mu})^2}{\sigma^2} + \mathcal{O}(1/\sqrt{N}), \tag{4.11}$$

where $\hat{\mu}$ is distributed as a Gaussian with mean μ', and N is the size of the data sample. Neglecting the $\mathcal{O}(1/\sqrt{N})$ term, the test statistic t_μ follows a non-central χ^2 distribution:

$$\mathrm{f(t_\mu|\mu')} = \frac{1}{2\sqrt{t_\mu}}\frac{1}{\sqrt{2\pi}}\left[\exp\left(-\frac{1}{2}\left(\sqrt{t_\mu}+\frac{\mu-\mu'}{\sigma}\right)^2\right)+\exp\left(-\frac{1}{2}\left(\sqrt{t_\mu}-\frac{\mu-\mu'}{\sigma}\right)^2\right)\right]. \tag{4.12}$$

In general, the standard deviation, σ, depends on the hypothesised value of μ, thus the upper limit is found numerically as the value of μ for which $p_\mu = \alpha$. However, there are two ways of estimating σ and we will explain the one used for the search described in Chapter 7, for more details see [34]. The standard deviation, σ, is estimated by using an artificial dataset called the *Asimov dataset*. The Asimov dataset is defined as the dataset such that when one uses it to evaluate the estimators for the parameters one obtains the true parameter values. From Equation (4.5), one can obtain the ML estimators of the parameters by:

$$\frac{\partial \ln L}{\partial\theta_j} = -\frac{\partial(\mu' s+b)}{\partial\theta_j} + \sum_{i=1}^{n}\frac{1}{\mu' s f(x_i|s)+b f(x_i|b)}\frac{\partial(\mu' s f(x_i|s)+b f(x_i|b))}{\partial\theta_j} = 0 \tag{4.13}$$

The equation above is only valid if the Asimov data, n_A, is equal to their expectation values: $n_A = E[n] = \mu' s(\theta) + b(\theta)$. Here the parameter values represent those implied by the assumed distribution of the data and they are usually estimated from MC using a very large data sample. Using the above result, the profile likelihood can be rewritten as an Asimov likelihood:

$$\lambda_A(\mu) = \frac{L_A(\mu,\hat{\hat{\theta}})}{L_A(\hat{\mu},\hat{\theta})} = \frac{L_A(\mu,\hat{\hat{\theta}})}{L_A(\mu',\theta)} \tag{4.14}$$

where $\hat{\mu} = \mu'$ for the Asimov dataset. Therefore, from Equation (4.11), we have

$$-2\ln\lambda_A(\mu) \approx \frac{(\mu-\mu')^2}{\sigma^2}. \tag{4.15}$$

Given that $q_{\mu,A} = -2\ln\lambda_A(\mu)$, we can find an expression for the standard deviation, σ:

$$\sigma_A = \frac{(\mu-\mu')^2}{q_{\mu,A}}. \tag{4.16}$$

4.4 Distribution of q_0 and q_μ

In the terms of the Asimov dataset, limit setting and discovery can be reevaluated. The special case of discovery is:

$$q_0 = \begin{cases} \hat{\mu}^2/\sigma^2 & \hat{\mu} \geq 0, \\ 0 & \hat{\mu} < 0, \end{cases} \tag{4.17}$$

for Equation (4.8).

From this it can be shown that for the special case of $\mu' = 0$ the pdf is

$$f(q_0|0) = \frac{1}{2}\delta(q_0) + \frac{1}{2}\frac{1}{\sqrt{2\pi}}\frac{1}{q_0}e^{-q_0/2} \tag{4.18}$$

which corresponds to a half chi-square distribution. Therefore, the p-value and its corresponding significance are:

$$p_0 = 1 - \Phi(\sqrt{q_0}) \text{ and } Z_0 = \sqrt{q_0}. \tag{4.19}$$

For setting upper limits, Equation (4.9) can be written as

$$q_\mu = \begin{cases} \frac{(\mu-\hat{\mu})^2}{\sigma^2} & \hat{\mu} \leq \mu, \\ 0 & \hat{\mu} > \mu, \end{cases} \tag{4.20}$$

where for the special case $\mu = \mu'$ one can find

$$f(q_\mu|\mu) = \frac{1}{2}\delta(q_\mu) + \frac{1}{2}\frac{1}{\sqrt{2\pi}}\frac{1}{q_\mu}e^{-q_\mu/2}. \tag{4.21}$$

Therefore, the p-value and its corresponding significance are:

$$p_\mu = 1 - \Phi(\sqrt{q_\mu}) \text{ and } Z_\mu = \sqrt{q_\mu}. \tag{4.22}$$

As mentioned before, the upper limit on μ is the largest μ with $p_\mu \leq \alpha$. Therefore, solving the Equation $p_\mu = \alpha$ for μ using Equations (4.20) and (4.22) one obtains

$$\mu_{up} = \hat{\mu} + \sigma\Phi^{-1}(1-\alpha). \tag{4.23}$$

4.5 The CL_s method

An important issue arises when setting limits from an experiment. For example, it can happen that every hypothesised value of μ is rejected in a test of size α. This can occur if the number of observed events, n, fluctuates below the expected number of background events, b. Therefore, is not possible to obtain useful upper limits. By construction at 95% CL, this can happen with a probability of α (5% of the time). The same problem arises when testing a hypothesis in which the experiment has low sensitivity (the distribution of whatever statistic we are using is almost the same under any assumption of μ). If we have no sensitivity to a model we do not want to reject it, since the measurement cannot produce any evidence to justify the rejection.

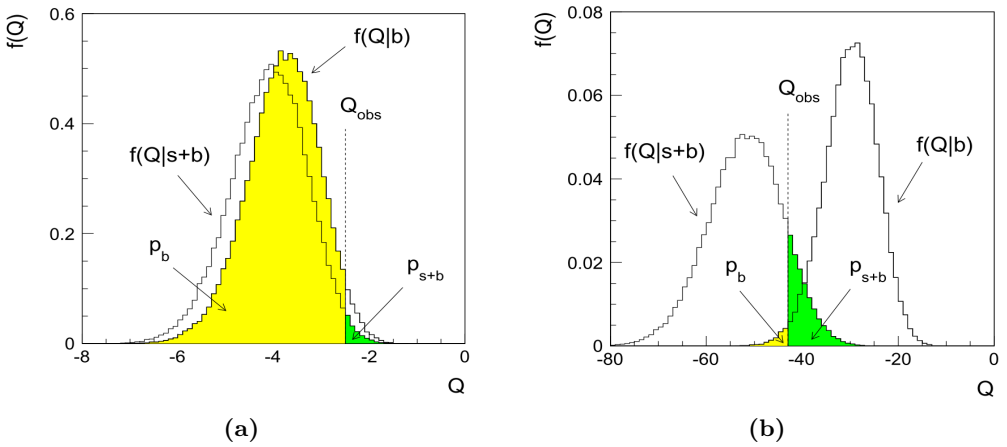

Figure 4.3 Distributions of the probability distribution function, $f(Q)$, of the statistic Q under the assumption of s+b ($\mu = 1$) and background only hypothesis ($\mu = 0$) for the (a) low sensitivity case [37] and (b) high sensitivity case.

This problem can be solved by the CL_s procedure [38], where the threshold α is redefined in a way that prevents one from rejecting a model when having low sensitivity but it reverts to the usual frequentist procedure when the sensitivity is high. This is achieved by:

$$\mathrm{CL_s} = \frac{p_{s+b}}{1 - p_b}, \tag{4.24}$$

where

$$p_{s+b} = \int_{t_{\mu,obs}}^{\infty} f(t_\mu|s+b)dt_\mu,$$
$$p_b = \int_{-\infty}^{t_{\mu,obs}} f(t_\mu|b)dt_\mu.$$

This quantity is then used instead of the p-value, p_{s+b}. Then, the s+b model is rejected

if one finds $\mathrm{CL_s} \leq \alpha$. The ingredients are illustrated in Figure (4.3b).

Lets consider the case illustrated in Figure (4.3a) where the distributions of Q under two different hypothesis are close together. Assuming that the Q_{obs} is such that the p-value $p_{s+b} < \alpha$ so we would reject s+b, the quantity $1-p_b$ will be small and Equation (4.24) will be greater than p_{s+b}. Then the model s+b will not be rejected. On the other hand, when the distributions of Q, assuming different hypothesis, are not close together the value of p_b is small so $1 - p_b$ will be close to unity making Equation (4.24) behave like p_{s+b} recovering the previous frequentist approach.

The largest value of μ not rejected by the $\mathrm{CL_s}$ criterion gives the corresponding $\mathrm{CL_s}$ upper limit. To follow the traditional notation in terms of the signal strength parameter of μ, Equation (4.24) is equivalent to $\mathrm{CL}_1 = p_1/1 - p_0$.

4.6 Treatment of nuisance parameters

The observed data to be analysed is subject to multiple uncertainties that are managed by introducing the nuisance parameters θ. With this, the signal and background models become functions of the nuisance parameters ($s(\theta)$ and $b(\theta)$) [39].

The systematic uncertainties are defined by the pdfs $\rho(\theta|\tilde{\theta})$, where $\tilde{\theta}$ is the best estimate of the nuisance parameter θ with a width of σ. The uncertainties are taken to be uncorrelated, so they can be factorised in the likelihood. The choices for these pdfs can be many. Among the most common ones, used in an ATLAS Higgs analysis, are:

- The Gaussian pdf:

$$\rho(\theta) = \frac{1}{\sqrt{2\pi}\sigma} \exp\left(-\frac{(\theta-\tilde{\theta})^2}{2\sigma^2}\right), \tag{4.25}$$

  is the standard choice in case of shape systematics and it is well suited for describing uncertainties on parameters that can have positive or negative values.

- The log-normal distribution:

$$\rho(\theta) = \frac{1}{\sqrt{2\pi} ln(\kappa)} \exp\left(\frac{(\ln(\theta/\tilde{\theta}))^2}{2(\ln(\kappa))^2}\right) \frac{1}{\theta}, \tag{4.26}$$

  describes the cases of parameters bounded to positive values. The parameter κ characterises the width of the log-normal distribution. When κ tends to be

small, the log-normal distribution is asymptotically a Gaussian distribution, see illustration of the log-normal distribution in Figure (4.4). This type of pdf is the standard choice for the normalisation systematics.

- The Γ distribution:

$$\rho(n) = \frac{1}{\alpha}\frac{(n/\alpha)^n}{N!}\exp\left(-\frac{n}{\alpha}\right) \tag{4.27}$$

is the choice of statistical uncertainties coming from the number of selected Monte Carlo (MC) events. The event rate of the data in the interesting region, n, is proportional to the number of MC events N as, $n = \alpha N$. Therefore, the Γ distribution describes the uncertainty on the rate n associated with the observation of N events.

- A flat pdf is used when no constraint or measurement exists on a particular nuisance parameter.

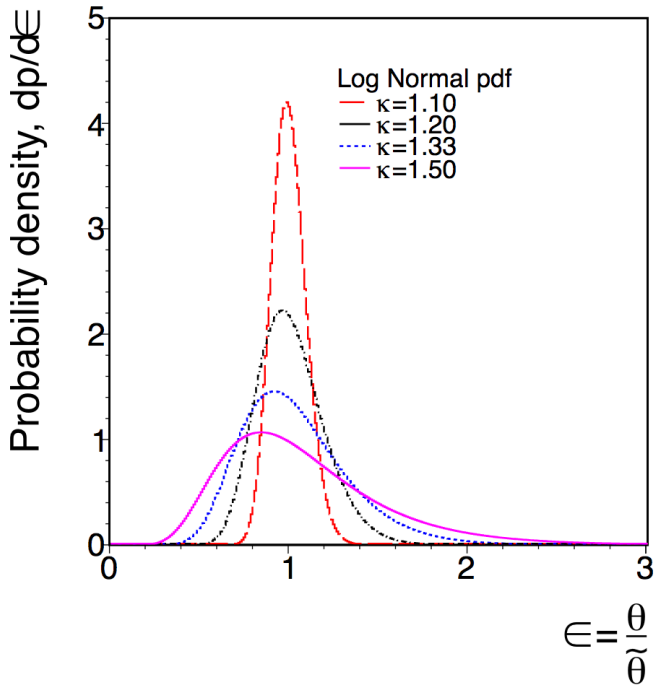

Figure 4.4 Log-normal distributions with $\kappa = 1.10$, 1.20, 1.33 and 1.50 [39].

Chapter 5

The $H \rightarrow ZZ^{(*)} \rightarrow 4l$ channel

In this chapter, the main characteristics of the $H \rightarrow ZZ^{(*)} \rightarrow 4l$ channel are summarised in the context of the Higgs boson mass measurement [40] and the search for additional Higgs bosons performed at the ATLAS detector [41]. This includes the description of the signal and background in this channel, the object reconstruction and identification in the ATLAS experiment, the Higgs candidates selection, the corrections applied to the invariant mass of the final states and, finally, the estimation of the reducible background.

5.1 The features of the signal and the background

The lowest order Feynman diagram for the $H \rightarrow ZZ^{(*)} \rightarrow 4l$ decay is in Figure (5.1). What favours the $H \rightarrow ZZ^{(*)} \rightarrow 4l$ decay channel is that the signal is extremely clean because the leptons and antileptons can be measured precisely at the ATLAS detector. Specifically, the leptons in question are electron and muons, not taus or neutrinos, which are far more difficult to handle. The signature of $H \rightarrow ZZ^{(*)} \rightarrow 4l$ decay is the presence of four isolated final state charged leptons (two pairs of opposite sign leptons), which come from the decay of two intermediate Z bosons which can be off-shell. Selection criteria are based on requirements on the kinematic variables (momentum, invariant mass of the dilepton pairs, lepton isolation, lepton impact parameter), aiming to select a pure signal sample therefore reducing the contribution from backgrounds. Also, the fact that the final state contains four charged leptons allows a complete reconstruction of the decay chain giving excellent measurement of the properties of the Higgs boson.

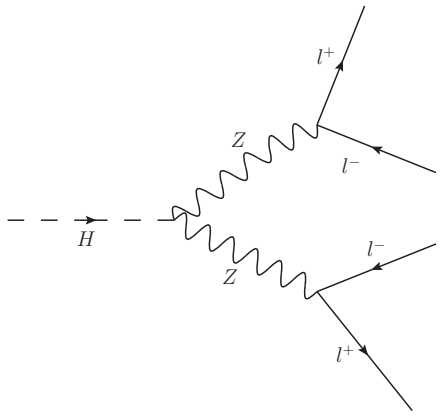

Figure 5.1 Lowest order Feynman diagram for the decay process $H \to ZZ^{(*)} \to 4l$.

What disfavours this decay channel is that for smaller Higgs masses the branching ratio of a Higgs decaying into a pair of Z bosons becomes small, see Figures (2.5) and (2.6), making it harder to study. For example, for a 125 GeV Higgs boson only about 1 in 9,000 Higgs particles decay this way. In addition, the probability of having four leptons in the final state is not very high. Only 3.3% of the time the Z boson decays into a electron/positron or muon/antimuon pair. Nevertheless, the background for this process is very small, so even with a few events this will be noteworthy. Let us not forget that this was one of the Higgs boson discovery channels in 2012 at the ATLAS detector.

The main background over the full mass range is $pp \to ZZ^{(*)} \to 4l$, which is called the irreducible background since it has the same final state as the signal. It is composed of three different backgrounds, depending upon where the Z bosons are coming from: $q\bar{q} \to ZZ^{(*)}$, $gg \to ZZ^{(*)}$ or from the single resonant production of a Z boson. The lowest order Feynman diagrams for these background processes are shown in Figures (5.2) and (5.3). The background contributions to the $H \to ZZ^{(*)} \to 4l$ channel are shown in Figure (5.4) for the $2e2\mu$ final state. For $m_H > 2m_Z$, where both Z bosons are on-shell and therefore the leptons have high p_{T}, the main contribution comes from $q\bar{q} \to ZZ^{(*)}$ because the $gg \to ZZ^{(*)}$ cross-section is less than 10% of the $q\bar{q} \to ZZ^{(*)}$cross-section. The effect of the inclusion of the single resonant contribution is relevant for $m_{4l} < 100$ GeV as shown in Figure (5.4b). Therefore, the m_{4l} mass spectrum of the irreducible background can be divided into three regions: the single-resonant region (below 100 GeV) where the peak at $m_{4l} \approx m_Z$ from the single resonant production is present, the low Higgs mass region (below $2m_Z$) which shows a rising shoulder (at ≈ 120 GeV) and the high Higgs mass region (above $2m_Z$) where the spectrum shows the fall of a second shoulder due to both Z bosons being real.

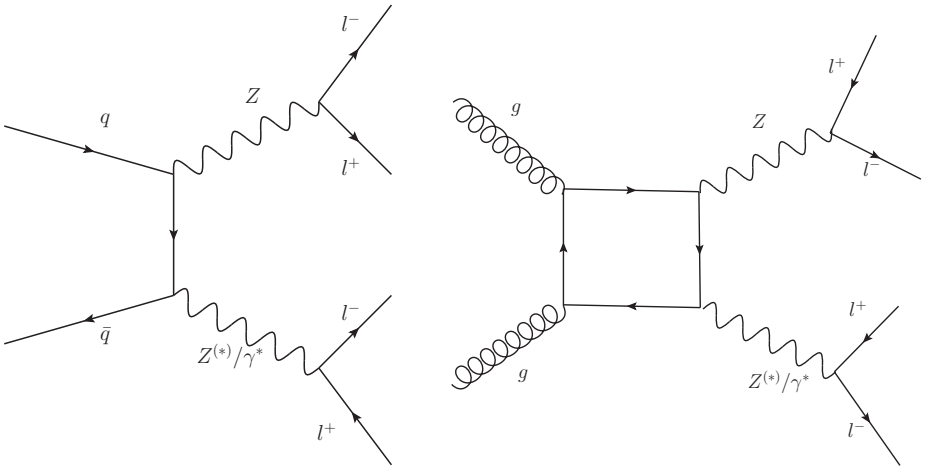

(a) $qq \to ZZ$ **(b)** $gg \to ZZ$

Figure 5.2 Lowest order Feynman diagrams for $q\bar{q} \to ZZ^{(*)}$and $gg \to ZZ^{(*)}$production.

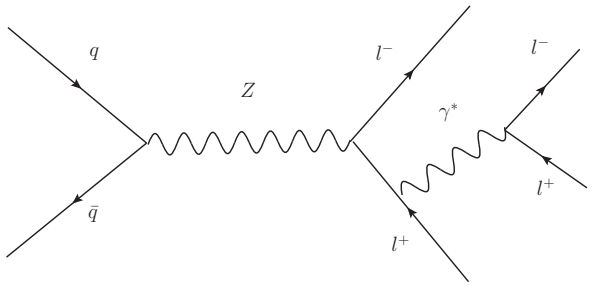

Figure 5.3 Lowest order Feynman diagram for the single resonant production mechanism.

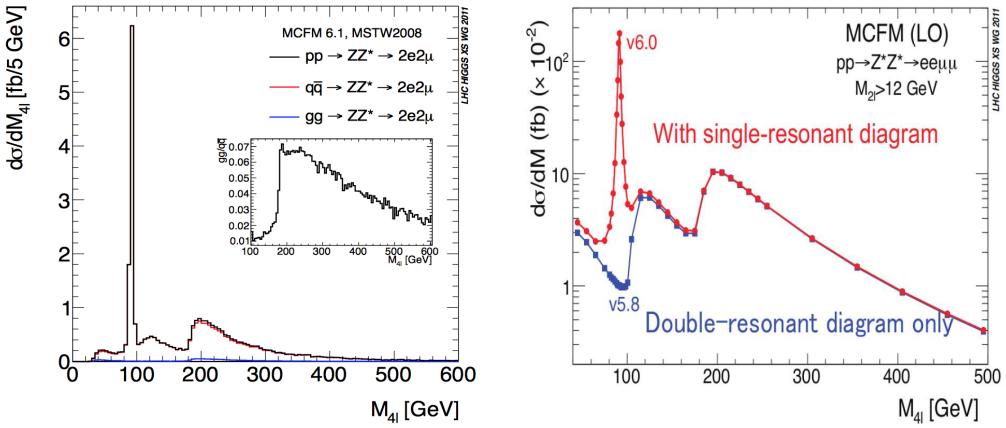

(a) **(b)**

Figure 5.4 (a) Next to leading order (NLO) $pp \to ZZ \to 2e2\mu$ cross-section as a function of m_{4l}. The plot inside shows the ratio between $gg \to ZZ^{(*)}$ and $q\bar{q} \to ZZ^{(*)}$ cross-section as a function of m_{4l}. (b) Effect of the inclusion of the single resonant diagram at leading order (LO) $qq \to ZZ \to 2e2\mu$ (double resonant) cross-section as a function of m_{4l}, where a cut on the dilepton mass $m_{2l} > 12$ GeV was applied. Both plots were taken from Ref. [11].

The other backgrounds that affect this channel are the ones that come from:

- The production of Z bosons in association with jets ($Z+jets$). It can be separated into two categories:
  - The production of Z bosons in association with light-flavour jets ($Z + jj$). The Z boson decays leptonically while two jets of the final state are mistakenly reconstructed as leptons, usually as fake electrons. See Figure (5.5a).
  - The production of Z bosons in association with heavy flavours ($Z + bb$). A real lepton coming from the decay of heavy flavours can be reconstructed. This lepton will not be isolated since it is produced in the vicinity of a jet. See Figure (5.5b).
- The production of $t\bar{t}$ pairs: top quarks decay to Wb and a four lepton signature is obtained when the two W bosons decay to $l\nu$ and another lepton is produced in the decay of hadrons produced by the hadronization of each of the two b quarks. See Figure (5.6).

These backgrounds are referred to as the reducible background and they are characterised by the presence of a lepton pair which has a softer p_{T} spectrum than leptons that would come from on-shell Z bosons, hence the reducible background is more relevant in the low m_H region where there is an off-shell Z boson. These leptons, contrary to signal leptons which are produced isolated, are usually surrounded by other particles, which results in an energy or momentum deposit that is wider in the detector. Selection

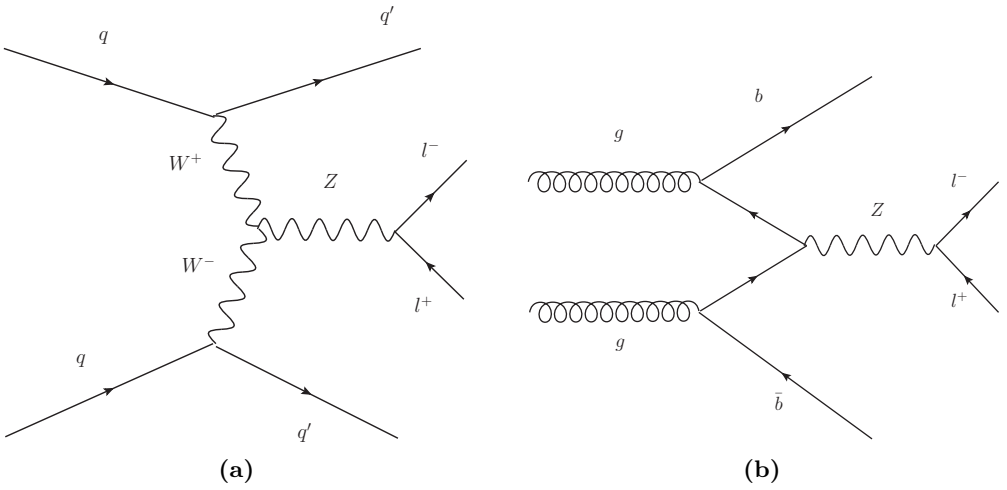

Figure 5.5 Example of one of the lowest order feynman diagrams for the (a) $Z + jj$ and (b) $Z + bb$ irreducible backgrounds.

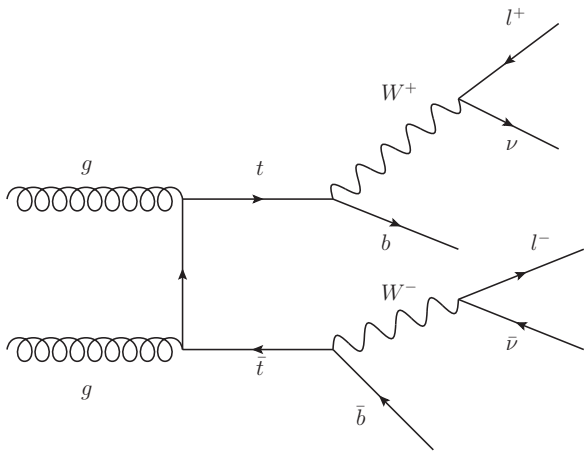

Figure 5.6 Example of one of the lowest order feynman diagram for the $t\bar{t}$ background.

criteria are based on the sum of the transverse energy deposits, E_{T}, in a cone of size $\Delta R = \sqrt{\Delta\eta^2 + \Delta\phi^2}$ around the reconstructed lepton, i.e. $\sum_{\Delta R_i < \Delta R} E_{\mathrm{T}}^i / E_{\mathrm{T}}$, or the sum of the transverse momenta, p_{T} , of the charged particles in a cone of size $\Delta R'$, i.e. $\sum_{\Delta R_i < \Delta R'} {p_{\mathrm{T}}}^i / p_{\mathrm{T}}$, are applied to reject non-isolated leptons. Further rejection can be done for leptons coming from heavy flavours (from displaced vertices) based on the significance of their impact parameter d_0/σ_{d_0}, where σ_{d_0} is the uncertainty on the d_0 measurement.

Discrimination between signal and background is done mainly through the m_{4l} distribution, since the signature of a Higgs boson is a narrow peak in the four lepton invariant mass distribution while the background is locally flat (except for the regions where $m_{4l} \approx m_Z, 2m_Z$). Further discrimination can be done over the invariant masses of the lepton pairs in the final state or the introduction of multivariate discriminants.

5.2 Event selection

The following sections will describe the event selection starting from a brief summary of the trigger used, followed by the object reconstruction and identification procedure. Finally, the selection of the final Higgs boson candidates will be explained.

5.2.1 Trigger

Events are accepted for analysis if they pass the online selection criteria, in our case, with four leptons in the final state. Single and dilepton triggers are used (an event must

pass either a single lepton or a dilepton trigger). The set of selection requirements are shown in Tables (5.1) and (5.2) for the 2011 and 2012 data taking.

Isolation requirements were applied at Event Filter level (only for 2012 for the single lepton trigger). They require that the scalar sum of the p_{T} (with $p_{\mathrm{T}} > 1$ GeV) of the inner detector tracks within a cone of $\Delta R < 0.2$ has to be less than 10% of the lepton p_{T}. Trigger p_{T} /E_{T} thresholds and the inclusion or exclusion of the isolation requirements have been chosen in order to keep the trigger output rate within the maximum design rate during data taking.

Channel	Single lepton	Dilepton
4μ	$p_{\mathrm{T}} > 18GeV$	$(p_{\mathrm{T}}{}^{(1)}, p_{\mathrm{T}}{}^{(2)}) > (10, 10)$ GeV
		$(p_{\mathrm{T}}{}^{(1)}, p_{\mathrm{T}}{}^{(2)}) > (13, 13)$ GeV
$4e$	$E_{\mathrm{T}} > 20 - 22$ GeV	$(E_{\mathrm{T}}^{(1)}, E_{\mathrm{T}}^{(2)}) > (12, 12)$ GeV
$2e2\mu$	$4\mu \vee 4e$	$4\mu \vee 4e$

Table 5.1 Summary of the triggers used during the 2011 data taking. The E_{T} threshold of the single electron trigger varied during the data taking, corresponding to different detector conditions (increasing interaction rate). When multiple triggers are indicated (rows), the logic OR ($\vee$) among them is requested. The index on the lepton p_{T} and E_{T} is to enumerate each lepton.

Channel	Single lepton	Dilepton
4μ	isolated, $p_{\mathrm{T}} > 24$ GeV	$(p_{\mathrm{T}}{}^{(1)}, p_{\mathrm{T}}{}^{(2)}) > (18, 8)$ GeV
		$(p_{\mathrm{T}}{}^{(1)}, p_{\mathrm{T}}{}^{(2)}) > (13, 13)$ GeV
$4e$	isolated, $E_{\mathrm{T}} > 24$ GeV	$(E_{\mathrm{T}}^{(1)}, E_{\mathrm{T}}^{(2)}) > (12, 12)$ GeV
$2e2\mu$	$4\mu \vee 4e$	$4\mu \vee 4e$
		$(E_{\mathrm{T}}^{(e)}, p_{\mathrm{T}}{}^{(\mu)}) > (12, 10)$ GeV
		$(E_{\mathrm{T}}^{(e)}, p_{\mathrm{T}}{}^{(\mu)}) > (24, 8)$ GeV

Table 5.2 Summary of the triggers used during the 2012 data taking. When multiple triggers are indicated (rows), the logic OR ($\vee$) among them is requested. The index on the lepton p_{T} and E_{T} is to enumerate each lepton.

The trigger efficiency for a ggF sample at a Higgs boson mass of $m_H = 130$ GeV is 97.6% for the 4μ channel, 97.3% for the $2e2\mu$ and 99.7% for the $4e$ channel. Trigger efficiency is measured in data and MC using events from $Z \to ee$ and $Z \to \mu\mu$.

5.2.2 Electron reconstruction

There are three electron reconstruction strategies followed in ATLAS:

1. The standard reconstruction is seeded from the isolated EM clusters searching for compatible ID tracks.

2. For $|\eta| > 2.5$, where the ID information is not available, the reconstruction relies only on the EM information.

3. There is also, an optimised reconstruction for low-p_{T} non-isolated electrons. It starts from an ID track and looks for a match with a relatively isolated energy deposit in the calorimeter.

The relevant algorithm for electron reconstruction used in the $H \to ZZ^{(*)} \to 4l$ channel is the first one, in the central region $|\eta| < 2.47$ with $E_{\mathrm{T}} > 7$ GeV. The reconstruction is achieved along the following three points: electron seed-cluster reconstruction and cluster building, electron track-candidate reconstruction and the Gaussian Sum Filter (GSF) refitting, and electron candidate reconstruction. These points will be summarised in the following paragraphs.

The standard electron reconstruction is seeded from an EM cluster. Candidates must satisfy a set of identification criteria that require the longitudinal and transverse shower profiles to be consistent with those expected for electromagnetic showers. Clusters are reconstructed using a *sliding window algorithm* [42] by scanning EM calorimeter cells with a window of size 3×5 towers in units of $\Delta\eta \times \Delta\phi = 0.025 \times 0.025$ and identifying energy deposits with a total $E_{\mathrm{T}} > 2.5$ GeV as a seed cluster. The cluster building efficiency is, measured using electrons from $Z \to ee$ decays, $\approx 100\%$.

Electrons are then reconstructed by matching the EM cluster to a track selected by the GSF algorithm [43], which allows for bremsstrahlung energy losses to be taken into account. If more that one match is possible, the track with hits in the silicon detectors and with lower distance in ΔR with respect to the cluster is preferred.

The electron momentum is then obtained using:

- The inner detector information for the measurement of d_0, z_0, η, ϕ and charge determination.

- The cluster information for the determination of the electron energy E, which

is calibrated considering different sources of energy loss (material in front of the calorimeter, dead material inside de calorimeter and energy leakage).

5.2.3 Electron identification

The objective of the electron identification is to provide a set of selection requirements which allow the discrimination of true isolated electrons from background, namely hadronic jets faking electrons, photon conversions and heavy flavour decays. We will describe in the following sections the set of requirements optimised for the $H \rightarrow ZZ^{(*)} \rightarrow 4l$ analysis which can be divided into cut-based and likelihood-based identification criteria.

Cut-based identification

The cut-based identification criteria are based on:

- The track quality requirements: number of hits in the B-layer, total number of hits in the pixel detector, the SCT and the TRT detectors to discriminate against photon conversions, and requirements over d_0 and its significance to also discriminate against photon conversions and, in addition, against heavy-flavour decays.
- The η and ϕ matching between the EM cluster and the ID track. It is expected to be poor for jets faking electrons.
- The ratio between the electron energy measured in the cluster and the track momentum from the ID. It is expected to be small for jets faking electrons.
- The hadronic leakage R_{had}: the ratio between the transverse energy deposit in the ECAL and HCAL. Electrons are expected to release most of their energy in the EM calorimeter.
- The ratio of the energy in the third layer to the total energy of the ECAL. It is expected that electron leave most of their energy in the first layer of the EM calorimeter.
- The cluster isolation R_η in η: defined in terms of the ratio of energy deposited in a window of 3×7 cells in units of $\Delta\eta \times \Delta\phi$ divided by the energy deposit in a window of 7×7 cells centred at the electron cluster position.

- The cluster isolation R_ϕ in ϕ: defined in terms of the ratio of the energy deposited in a window of 3×3 cells in units of $\Delta\eta \times \Delta\phi$ over the energy deposit in a window of 3×7 cells centred at the electron cluster position.

- The geometrical structure of the lateral shower created by the electron. Isolated electrons have narrower clusters than hadrons.

- Ratio of the difference in energy between the largest and the second largest energy deposit in the cluster over the sum of both energy deposits, E_{ratio}. This is to reject jets with one or more neutral particles (like π^0) which can cause a significant second energy maximum in the layers of the ECAL.

The $H \rightarrow ZZ^{(*)} \rightarrow 4l$ analysis uses this cut-based identification criteria, also called *MultiLepton menu*, for the first part of the 2012 data taking at $\sqrt{s} = 8$ TeV . For the $\sqrt{s} = 7$ TeV dataset, the electron identification is still cut-based, called *loose++ menu*, yet with a smaller set of variables, i.e., hadronic leakage, cluster isolation R_η, shower widths, E_{ratio}, the number of pixel and silicon hits and on the $\Delta\eta$ match between the inner detector track and the electromagnetic cluster.

Likelihood-based identification

For the remaining $\sqrt{s} = 8$ TeV dataset, a multivariate analysis (MVA) technique was used to define the electron identification. The MVA chosen was the maximum Likelihood (LH) approach because of its simple construction. The electron LH uses signal and background pdfs of the discriminating variables to calculate an overall probability for the object to be signal or background. The signal and background pdfs are combined into a discriminant upon which a cut is applied:

$$d_{\mathcal{L}} = \frac{\mathcal{L}_s}{\mathcal{L}_s + \mathcal{L}_b}, \text{ with } \mathcal{L}_{s(b)}(\vec{x}) = \prod_{i=1}^{n} P_{s(b),i}(x_i), \tag{5.1}$$

where $\vec{x}$ is the vector of the variable values and $P_{s(b)}(x_i)$ is the value of the signal (background) probability distribution function (pdf) of the i^{th} variable evaluated at x_i. The signal and background pdfs used were obtained from data. Each cut on the likelihood discriminant is made with a different set of variables entering into the parametrisation of the signal and background pdfs depending on the type of likelihood menu. For instance, the loose likelihood selection is characterised by a set of variables that is essentially in common with the cut-based menu. The chosen cut value on the

discriminant determines the signal efficiency and background rejection of the likelihood.

The loose likelihood identification menu was chosen for electrons in this analysis (LH LOOSE). The likelihood-based approach replaced the cut-based identification [44], in which both have the same particle identification efficiency, but the former improves the light-flavour jet rejection by a factor of 2.

5.2.4 Improvements in the electron energy calibration

A precise calibration of the energy measurement of electrons is a fundamental need of many physics measurements in ATLAS particularly for the measurement of the Higgs boson mass discussed in Chapter 6.

The objective of the calibration is to estimate the true energy of the particle from the quantities measured by the calorimeter. The energy of an electron candidate is built from the cell responses in the electromagnetic calorimeter as summarised in Section (5.2.2). Several effects distort this calculation (energy lost by the candidate electron in the matter in front of the calorimeter, energy leakage behind the calorimeter and the energy outside the defined cluster of the calorimeter cells), therefore, a calibration is applied to produce corrections to the electron energy.

The full calibration procedure for the electrons and photons in the ATLAS experiment was revisited [45] exploiting the potential of multivariate techniques to improve the calibration with respect to the previous calculations [24]. In addition, other studies were made: an intercalibration of the longitudinal layers of the calorimeter was performed from data, a measurement of the detector material achieving an improved simulation, a simulation-based calibration and a measurement of the energy scale from Z boson decays. The calorimeter response was found to be stable with respect to time and pile-up to 0.05%. The uncertainty on the intercalibration of the calorimeter layers varies from 1% to 2% and the relative calibration of the presampler gave an uncertainty of better than 5%. The uncertainty on the material in front of the EM calorimeter was found to be between 0.03 to 0.05 radiation lengths and the material is well described by simulation.

Once the corrected energy of the electron candidate is returned by the calibration, a likelihood-based combination of the electron energy and track momentum is performed, called the E-p combination. The objective of this combination is to improve the electron energy resolution, particularly for low E_{T} electrons and of electrons in problematic regions of the electromagnetic calorimeter, which tends to be very poor.

The final uncertainty on the electron energy scale depending on E_{T}. It varies from 0.03% (for $|\eta| < 1.37$) to 0.2% (for $1.37 < |\eta| < 1.82$) for a $E_{\mathrm{T}} = 40$ GeV electron, giving a 6% to 15% improvement with respect to previous results [24]. To fully validate the procedure of the energy scale extraction, an independent check is performed using sample of $J/\Psi \to e^+e^-$ decays. The results are in very good agreement with the values determined from the $Z \to e^+e^-$ sample. Figure 5.7 summarises the verification of the electron energy scale from $Z \to e^+e^-$ and $J/\Psi \to e^+e^-$ samples in bins of the pseudorapidity, η, where the band represents the calibration systematic uncertainty. This combination was studied in the $H \to ZZ^{(*)} \to 4l$ channel where the largest improvement was seen in the 4e and the $2\mu 2e$ final states. The approximate reduction on the width of the m_{4l} distribution is of around 4% and 3.5% respectively. In addition, the combination produces a reduction of the tails of the m_{4l} distribution, with the largest effect being on the $4e$ final state.

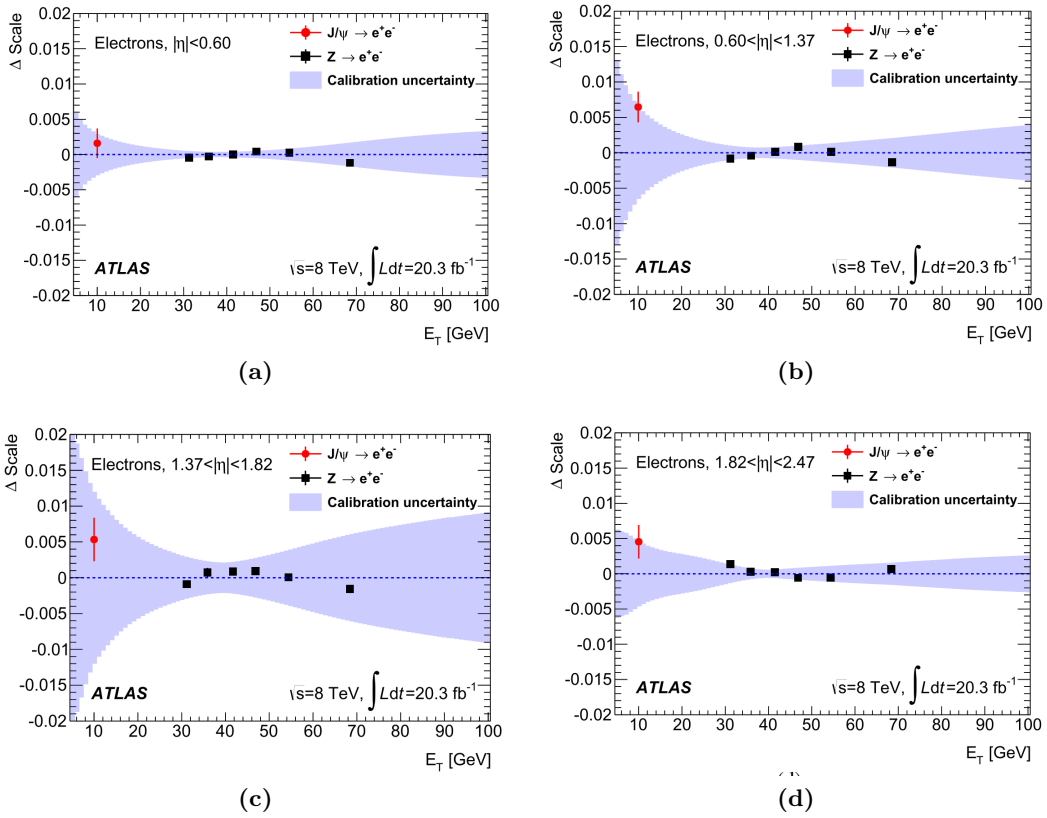

Figure 5.7 Relative scale difference, ΔScale, between the measured electron energy scale and the nominal energy scale, as a function of E_{T} using $J/\Psi \to e^+e^-$ and $Z \to e^+e^-$ events (points with error bars), for four different η regions: (a) $|\eta| < 0.6$, (b) $0.6 < |\eta| < 1.37$, (c) $1.37 < |\eta| < 1.82$ and (d) $1.82 < |\eta| < 2.37$. The uncertainty on nominal energy scale for electrons is shown as the shaded area. The error bars include the systematic uncertainties specific to the $J/\Psi \to e^+e^-$ measurement [45].

5.2.5 Muon reconstruction and identification

Muons are charged, minimum ionising and penetrating particles that leave an Inner Detector (ID) track that can be associated with low calorimetric deposits and a track in the muon spectrometer (MS). Muon reconstruction strategies [46] exploit the fact that they leave a signal in all detector systems.

ATLAS muon reconstruction and identification techniques take into account the different acceptance of the subdetector systems in terms of geometrical coverage (η, ϕ) and transverse momentum as follows:

- The acceptance in the ID is $|\eta| < 2.5$. Therefore, inner tracker information is not available in the forward region of the detector.
- The acceptance in the MS is $|\eta| < 2.7$. There is no information available further in η.
- The overall quantity of material of the ID, ECAL and HCAL systems is expected to reduce the muon momenta by 3 GeV before they reach the muon spectrometer.
- In the muon spectrometer there are uninstrumented regions for $|\eta| < 0.1$ and for $1.1 < \eta < 1.3$ due to the presence of detector services.

Given the different acceptance of the subdetector systems, four types of muons can be reconstructed:

- *Standalone muons* (SA): are based entirely on the reconstructed tracks in the MS. The track parameters are obtained from the MS and are extrapolated to the interaction point, taking into account the effect from multiple scattering and energy loss in the transverse material. These muons are used in the $|\eta| > 2.5$ region, where the ID has no coverage, to increase the overall analysis acceptance.
- *Combined muons* (CB): to improve the momentum resolution, the tracks reconstructed in the MS are combined with the tracks reconstructed in the ID. The tracks in the ID also contain information about the impact parameter of the muon with respect to the primary vertex.
- *Segment-tagged muons* (ST): when there is no accurate track on the MS, the association of an ID track to a track segment in the muon system is done. The ST muons adopt the measured parameters of the associated ID track.

- *Calorimeter-tagged muons* (CT): as mentioned before, if there is no accurate track measurement in the MS, the association of an ID track to a calorimeter deposit consistent with a minimum ionising particle is done. These muons help cover the region of $|\eta| < 0.1$.

Figure (5.8) shows the muon reconstruction efficiency for a sample of muons of $p_{\mathrm{T}} > 20$ GeV coming from Z decays as a function of η. The reconstruction efficiency is approximately uniform in the whole pseudorapidity range with approximately 98% of efficiency. The efficiency recovery due to calo-tagged muons is shown for $|\eta| < 0.1$ where the efficiency improvement with respect to CB+ST muons ($\approx 65\%$) can be seen. Figure (5.9) also shows the muon reconstruction efficiency but as a function of p_{T}. As it can be seen, the reconstruction efficiencies are almost independent of the muon transverse momentum.

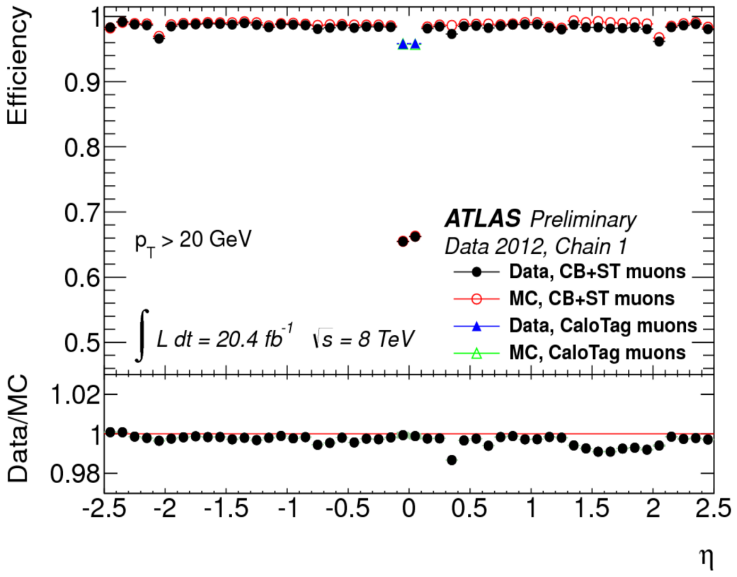

Figure 5.8 Muon reconstruction efficiency as a function of η for muons with $p_{\mathrm{T}} > 20$ GeV, for different muon reconstruction types. Calo-tagged muons are used only in the region $|\eta| < 0.1$. Ratio between data and MC efficiencies is also shown. The deviation from 1 at $1.5 < \eta < 2.2$ is due to mismodelling of pixel subdetectors in the MC simulation [46].

In the $H \to ZZ^{(*)} \to 4l$ channel analysis, CB muons are used for the pseudorapidity region of $|\eta| < 2.5$, while SA muons are used for $2.5 < |\eta| < 2.7$. In both cases, a p_{T} cut at 6 GeV is applied. As was mentioned before, acceptance is recovered in the central region of the detector by using CT muons for $|\eta| < 0.1$ if they have $p_{\mathrm{T}} > 15$ GeV and if they do not share the same ID track of any reconstructed electron.

The same selection cut as for electrons is used, $|z_0| < 10$ mm, to reject muons displaced

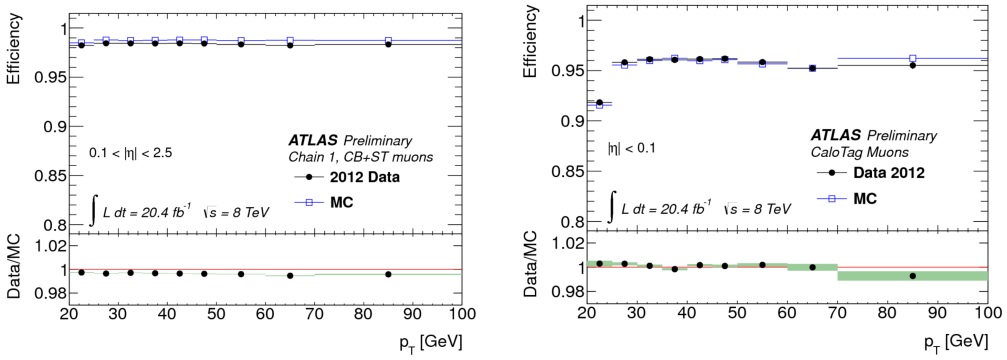

(a) **(b)**

Figure 5.9 Muon reconstruction efficiency as a function of muon p_{T} for (a) Combined and segment-tagged muons ($0.1 < |\eta| < 2.5$) and (b) Calo-tagged muons ($|\eta| < 0.1$). Ratio between data and MC efficiencies as also shown [46].

from the primary vertex. Muons coming from cosmic rays are rejected by a requirement on their transverse impact parameter, $d_0 < 1$ mm.

5.2.6 Jet reconstruction and identification

In the detector, jets are characterised as collimated bunches of hadrons that arise from gluons and quarks after fragmentation and hadronisation. In the analysis described in Chapter 7, jets are selected for the classification of events by production mechanisms.

For the reconstruction of jets [47], topological clusters [48] (topoclusters), formed by jet deposits, are extracted in the hadronic calorimeter using neighbouring cells with significant energy deposit over the noise. All topoclusters found in a given event are input objects to the jet finding algorithm. The algorithm used is the anti-k_t algorithm [49] with a radius parameter $R = 0.4$, which models the size of the jet. Intuitively, the anti-k_t algorithm is based on a sequential recombination of nearby particles with respect to a certain distance R. Once the algorithm is completed, the jet energy and four-momenta is computed by the sum of all the energy and four-momenta of the topocluster.

For effects on energy from pile-up, a correction was also performed: for jets with $p_{\mathrm{T}} > 50$ GeV within the acceptance of the ID ($|\eta| < 2.4$), the fraction of the summed scalar p_{T} of the tracks associated with the jet (within a ΔR= 0.4 cone around the jet axis) contributed by those tracks originating from the primary vertex must be at least 50%, i.e., $|JVF| > 0.5$. This ratio is called the jet vertex fraction (JVF), and this requirement reduces the number of jet candidates originating from pile-up vertices

[50, 51].

The energy obtained from the topoclusters needs to be properly calibrated to account for: inactive regions of the detector where the energy deposits are not properly recorded, electromagnetic leakage and calorimeter non-compensation (the energy response for hadrons is lower that for electrons). For the 7 and 8 TeV analysis, a calibration approach, called jet energy scale (JES), had been carried out and applied to the simulation. Therefore, the jet energies and directions are calibrated using energy and η dependent correction factors derived using MC simulations, with an additional calibration applied to data samples derived from in situ measurements [52].

5.2.7 Candidates

Higgs candidates are formed using two lepton pairs (dileptons) in which the leptons have opposite charge and same flavour, forming a quadruplet, in an event. Muons are required to have $p_{\mathrm{T}} > 6$ GeV and $|\eta| < 2.7$ and electrons are required to have $E_{\mathrm{T}} > 7$ GeV and $|\eta| > 2.47$. In addition, the p_{T} thresholds for the three leading leptons are required to be > 20, > 15 and > 10 GeV.

Within each quadruplet, the dileptons are organised according to the distances between their invariant masses and the nominal Z boson mass. The dilepton with the invariant mass closest to the Z boson mass is labelled as Z_1 and it has a mass called m_{12}. The next closest dilepton pair (possibly off-shell) is labelled as Z_2 and it has a mass called m_{34}. If there is more than one selected quadruplet in the event, the one with lower $\delta_Z = |m_{12} - m_Z|$ is selected. If two candidates share the same δ_Z, then the quadruplet with m_{34} closest to the Z mass is taken.

The following selection criteria is applied to each selected quadruplet:

- The four leptons have to be well separated with $\Delta R > 0.1$ for same flavour leptons and $\Delta R > 0.2$ for opposite flavour leptons (to reject photons coming from muon bremsstrahlung which are misidentified as electrons).

- The invariant mass of each possible dilepton within the quadruplet cannot have $m_{ll} < 5$ GeV, to remove contamination from J/ψ decays.

- The mass m_{12} must satisfy the relation $50 < m_{12} < 106$ GeV.

- The mass m_{34} must satisfy the relation $m_{\mathrm{threshold}} < m_{34} < 115$ GeV, where

$m_{\text{threshold}}$ depends on m_{4l} as

$$m_{\text{threshold}} = \begin{cases} 12 \text{ GeV} & \text{if } m_{4l} < 140 \text{ GeV}, \\ 12 \text{ GeV} + \left(\dfrac{m_{4l} - 140 \text{ GeV}}{190 \text{ GeV} - 140 \text{ GeV}} \right) \cdot 38 \text{ GeV} & \text{if } 140 < m_{4l} < 190 \text{ GeV}, \\ 50 \text{ GeV} & \text{if } m_{4l} > 190 \text{ GeV}. \end{cases}$$

- Track isolation criteria applied on each lepton of the quadruplet:

$$\sum_{\Delta R<0.2} {p_{\text{T}}}^{(i)}/E_{\text{T}} < 0.15 \text{ for electrons},$$
$$\sum_{\Delta R<0.2} {p_{\text{T}}}^{(i)}/p_{\text{T}} < 0.15 \text{ for CB, ST and CT muons},$$

  where the sum runs over all the tracks reconstructed in the inner detector within $\Delta R < 0.2$, without taking into account the tracks of the quadruplet.

- Calorimetric isolation criteria is applied:

$$\sum_{\Delta R<0.2} E_{\text{T}}^{(i)}/E_{\text{T}} < 0.2(0.3) \text{ for electrons},$$
$$\sum_{\Delta R<0.2} E_{\text{T}}^{(i)}/p_{\text{T}} < 0.3 \text{ for CB, ST and CT muons},$$
$$\sum_{\Delta R<0.2} E_{\text{T}}^{(i)}/p_{\text{T}} < 0.15 \text{ for SA muons},$$

  where the two values indicated for electrons correspond to the 8(7) TeV analyses. The contribution from leptons within the quadruplet, within a cone of $\Delta R < 0.2$ around the considered lepton, is removed.

- There is an impact parameter significance cut for all leptons of the quadruplet:

$$d_0/\sigma_{d_0} < 6.5 \text{ for electrons}, \tag{5.2}$$
$$d_0/\sigma_{d_0} < 3.5 \text{ for muons}. \tag{5.3}$$

Figure (5.10) shows the behaviour of the invariant masses of the two Z bosons for a MC sample generated at $m_H = 125$ GeV and $m_H = 300$ GeV with the Higgs boson produced by the ggF mechanism for the 4μ final state using POWHEG+PYTHIA as generators. One can see that, for $m_H < 2m_Z$, the distribution of the mass of Z_1 does not follow a BreitWigner distribution. This effect is reduced at $m_H > 2m_Z$. The distribution of Z_2 at low m_H is shown in Figure (5.10b) which clearly shows that Z_2 is off-shell. On the contrary, it is also shown the distribution for a high m_H sample

(300 GeV) where the distribution has the same behaviour as Z_1 because Z_2 is also on-shell.

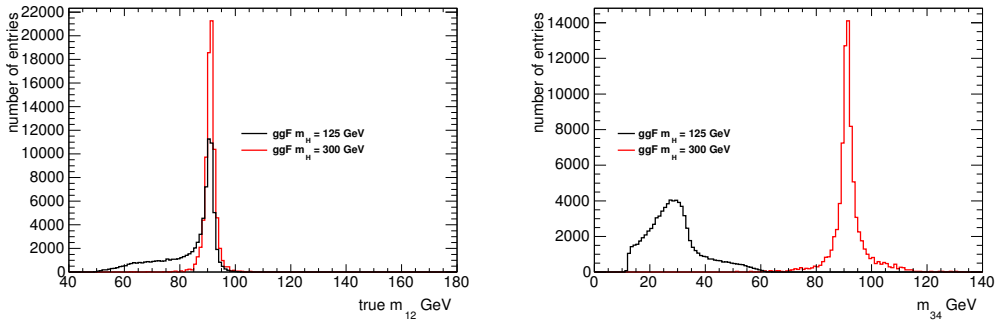

(a) **(b)**

Figure 5.10 Invariant mass distributions at generator level of (a) Z_1 at $m_H = 125$ GeV and (b) Z_2 at $m_H = 300$ GeV for gluon fusion production mechanism in the 4μ final state.

5.2.8 The ZZ discriminant

The new mass measurement approach, that will be described in Chapter 6, takes the analysis further by introducing additional variables to improve the discrimination between signal and the leading ZZ^* background. Studies have been made using a discriminant variable derived from a Matrix-Element-based Kinematic Discriminant incorporated into a Boosted Decision Tree (BDT) [53] with two additional variables: the p_T and η of the four-lepton system. The kinematics of the Higgs boson in a pp collision can be described by its transverse momentum p_T^H and by its pseudo-rapidity η^H. The decay into four leptons is described by a Matrix-Element-based Kinematic Discriminant, which is sensitive to the Spin and CP nature of the Higgs boson. These variables are used to built a BDT, which increases the discrimination power between signal and the ZZ^* background.

The BDT is trained using simulated signal events with $m_H = 125$ GeV and simulated ZZ^* background events, that pass the event selection in the mass window $115 < m_{4l} < 130$ GeV (contains over 95% of the signal events). The three variables, mentioned earlier, are used as an input for the training. The Matrix-Element based on a kinematic discriminant, called KD, is defined as:

$$KD_{ZZ^*} = \ln\left(\frac{|\mathcal{M}_{sig}|^2}{|\mathcal{M}_{ZZ^*}|^2}\right), \tag{5.4}$$

where $\mathcal{M}_{sig}$ and $\mathcal{M}_{ZZ^*}$ are the matrix elements for signal and the ZZ^* background, respectively. The equation above comprises the kinematical information of the signal

and the ZZ background where the required input variables are the angular distributions of the leptons as well as the masses of the reconstructed Z bosons, m_{12} and m_{34}. The matrix elements are computed using MadGraph [54] at LO by setting the process $pp \to H \to ZZ \to 4l$ for signal matrix elements (according to the SM hypothesis of a 0^+ scalar boson) and $pp \to ZZ^* \to 4l$ for the ZZ background. In addition, for the signal Matrix-Element computation, the Higgs boson mass, m_H, is set to be the reconstructed m_{4l} in an event-by-event basis. Figure (5.11) shows the p_T, η and KD distributions for the signal (blue) and the ZZ background (red) after the event selection in the mass range $115 < m_{4l} < 130$ GeV used for the training of the BDT. It is clear that each single variable does not have high signal-background separation power and it is impossible to apply a cut without losing a significant amount of the signal.

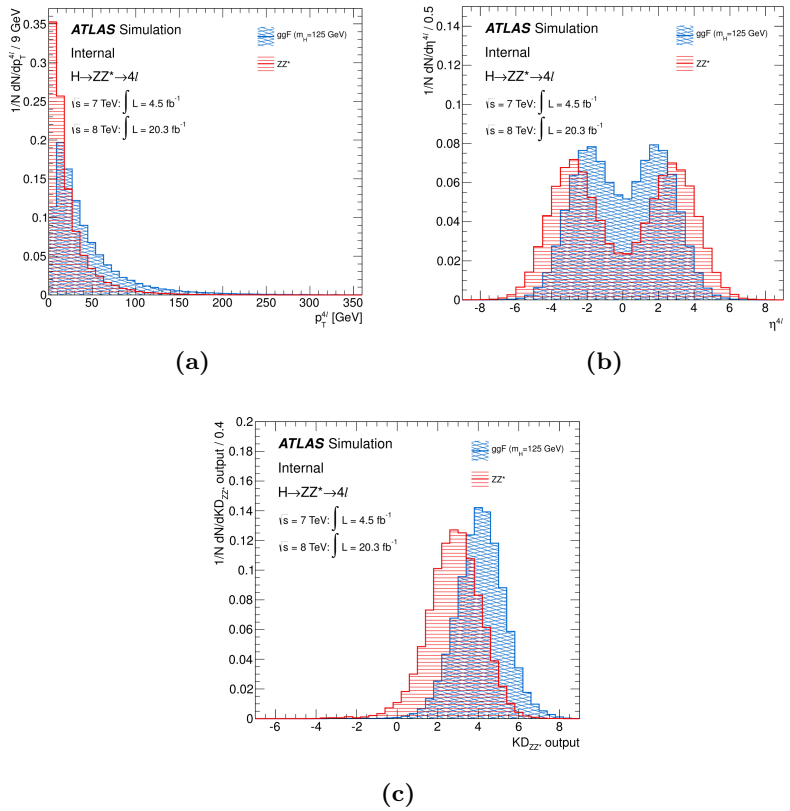

(a) **(b)**

(c)

Figure 5.11 (a) p_T, (b) η and (c) KD distributions for the signal (blue) and the ZZ background (red) after the event selection in the mass range $115 < m_{4l} < 130$ GeV used for the training of the BDT discriminant.

The BDT response or score is used as an observable to a 2D model, see Section (6.6), to better evaluate the Higgs boson mass. Figure (5.12a) shows the distribution of the BDT response that allows the signal-background separation, for signal (blue) and the ZZ^* background (red). In Figure (5.12b), the background rejection versus signal efficiency curves are shown when using the KD only as a discriminant (red) and when using the

BDT (black). Noticeably, adding the information of η and p_{T} of the four-lepton system the discrimination power is much higher. The training of the BDT was performed with MC samples because there is very good agreement between the MC and the data for the input variables used in the training. Figure (6.19c) shows the BDT_{ZZ^*} output final distribution for the combined 7 and 8 TeV data samples for the selected candidates in the mass range $110 < m_{4l} < 140$ GeV. Good agreement is seen between MC samples and data, showing that the BDT_{ZZ^*} output was correctly obtained.

Since the events used in this multivariate analysis are obtained using the selection criteria described in Section (5.2), most of the systematics uncertainties, such as lepton reconstruction and identification, electron energy scale uncertainty, muon momentum scale uncertainty, theoretical uncertainties, background normalisation, luminosity uncertainties, are exactly the same as those described in Section (6.5). In addition, shape systematics uncertainties, corresponding to the variation of the shape of the BDT discriminant due to systematic effects are also considered.

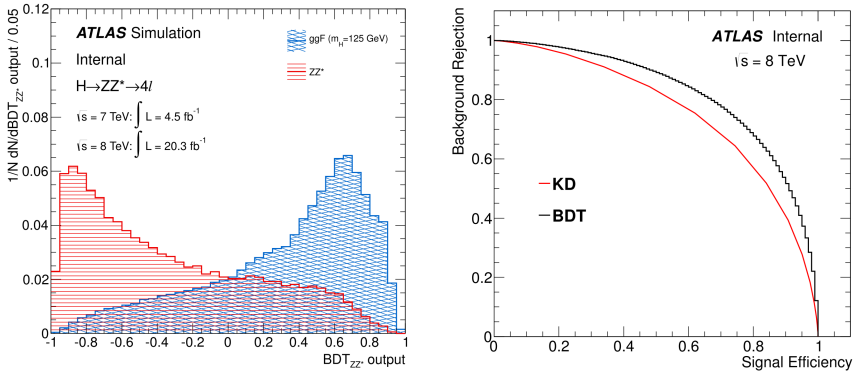

(a) **(b)**

Figure 5.12 (a) Distribution of the BDT response that allows the signal-background separation for the signal (blue) and the ZZ^* background (red) normalized to the same area. (b) Background rejection versus signal efficiency curves using only the KD discriminant (red) and the BDT (black).

5.3 Mass resolution

The invariant mass of the four lepton system, m_{4l}, is one of the most important discriminating variables between signal and background. The Higgs mass resolution depends on both energy and momentum uncertainties of the lepton measurements and the final state radiation. The true mass of the Higgs boson is fitted from the m_{4l} distribution. Therefore is of great importance to obtain a four lepton mass resolution as good as possible.

Figure (5.13a) shows the intrinsic width of the Higgs boson, Γ_H, and Figure (5.13b) shows the resolution of m_{4l} for each of the final states, as a function of m_H. Experimental resolution effects are dominant up to 350 GeV, hence improvements in the mass resolution yield significant improvements in the signal sensitivity in the low mass region.

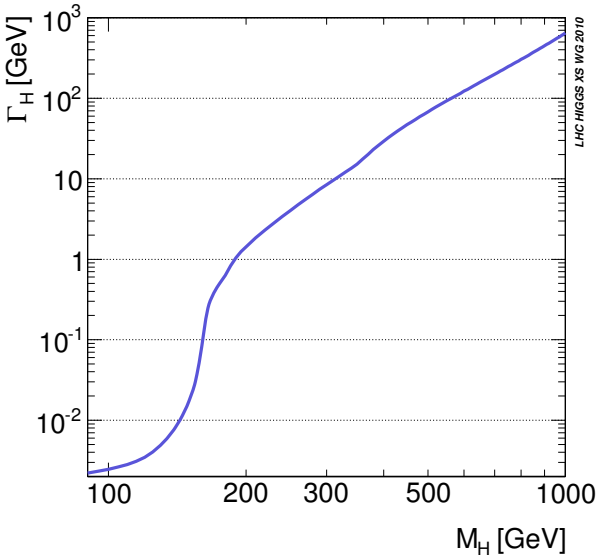

(a)

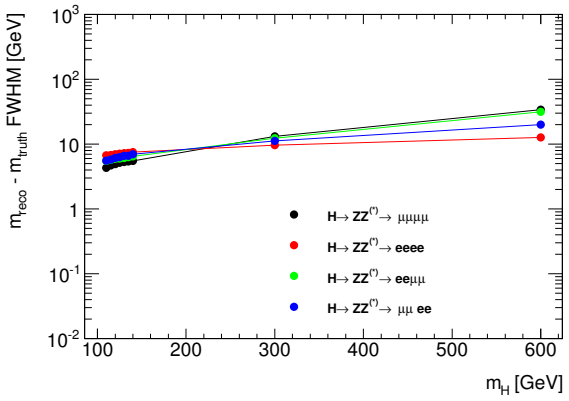

(b)

Figure 5.13 (a) Total decay width of the Standard Model Higgs boson Γ_H as a function of its mass [9–11] and (b) Mass resolution for the four lepton final states as a function of m_H. The mass resoultion is estimated from signal MC as the full width half maximum (FWHM) of the resolution $m_{4l} - \mathrm{m}_{4\mathrm{l}}^{\mathrm{true}}$, where $\mathrm{m}_{4\mathrm{l}}^{\mathrm{true}}$ is the true mass of the Higgs boson in the generated event.

In the $H \to ZZ^{(*)} \to 4l$ channel analysis, two corrections are applied to improve the m_{4l} mass resolution: recovery of photons from final state radiation and the Z mass constraint fit.

5.3.1 Final state radiation recovery

Final state radiation (FSR) of photons is taken into account in the reconstruction of Z bosons. This procedure enables the recovery of events having their reconstructed mass away from the signal region because of the energy depletion produced by the FSR photon. There are two types of FSR photons that are included in the analysis:

- **Collinear FSR photons** are emitted in a narrow cone around the final state muons or electrons in the Z decays. They are only included coming from muons in the final state. The photons must have an energy above 1 GeV and they must be within $\Delta R < 0.08$ to 0.15, with a threshold depending on the photon E_{T}. Photons between 1 GeV $< E_{\mathrm{T}} <$ 3.5 GeV are reconstructed using the topological algorithm [55], which builds clusters of variable size collecting cells around the seeding cell with an energy above a certain signal to noise threshold. Photons above 3.5 GeV are reconstructed using the same sliding window algorithm used for electrons, see Section (5.2.3). This collinear FSR photon is added in the final state if $66 < m_{12} < 89$ GeV and the new m_{12} invariant mass satisfies $m_{\mu\mu\gamma} < 100$ GeV. It affects $\approx 4\%$ of all selected signal events.

- **Non-collinear FSR photons** are emitted in a wider area around the final state leptons. They are included for both electrons and muons in the final state. The non-collinear photon candidate must be beyond a distance, $\Delta R > 0.15$, from the muon or electron, the transverse energy of its cluster must be $E_{\mathrm{T}} > 10$ GeV and it must be isolated with $E_{\mathrm{T}}^{\mathrm{cone40}} < 4$ GeV. This correction is applied if $m_{ll} < 81$ GeV and $m_{ll\gamma} < 100$ GeV for $m_{4l} < 190$ GeV. For $m_{4l} > 190$ GeV, if both Z satisfy $m_{ll} < 81$ GeV the FSR correction is applied to the pair with $m_{ll\gamma}$ closest to the pole Z boson mass and $m_{ll\gamma} < 100$ GeV. It affects $\approx 1\%$ of all selected events.

In this analysis the FSR photon addition is applied to the events that pass all the selections. FSR photons are searched for all lepton candidates of the final quadruplet but a maximum of one FSR photon candidate is included in the m_{4l} distribution and it is only applied to m_{12}. Priority is given to collinear photons associated to muons. If the collinear search fails then the non collinear FSR photon with the highest E_{T} is added. This recaptures events which have their reconstructed m_{4l} mass shifted out of the signal region. This avoids correcting for this loss statistically with the MC, particularly in the case of this analysis, where the statistics are limited. Figure (5.14), shows the effect of including FSR photons both on m_{12} and m_{4l} mass distributions for a simulated Higgs boson of 125 GeV.

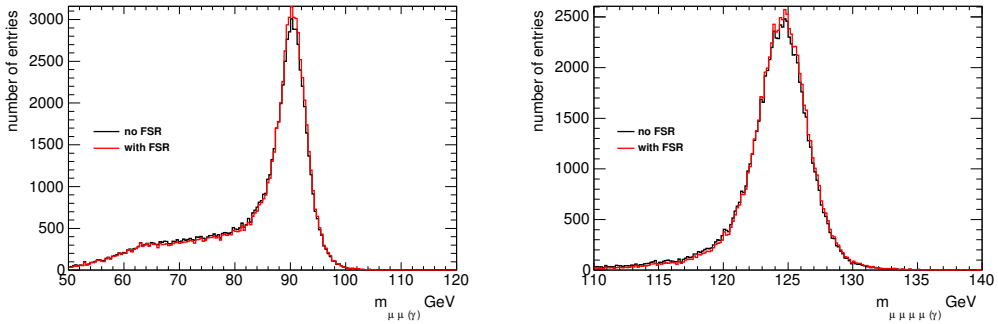

(a) (b)

Figure 5.14 Effect of the FSR recovery on (a) m_{12} and (b) m_{4l} mass distributions in the 4μ final state for a simulated Higgs boson of 125 GeV from ggF production.

5.3.2 Z mass constraint

After the FSR correction, the lepton four-momenta of the leading dilepton can be further improved by means of a Z mass constrained kinematic fit, see details in Chapter 8. The fit uses a Breit-Wigner Z line shape and a single Gaussian which describes the smearing of the reconstructed dilepton mass. If $m_{4l} > 190$ GeV, then the Z mass constraint is also applied to the subleading dilepton. The Z-mass constraint improves the m_{4l} resolution by about 15% [56].

5.4 The estimation of the reducible background

The rate and composition of the reducible Z+jets and $t\bar{t}$ backgrounds, described in Section (5.1), is estimated from data. The general procedure for estimating the reducible background is as follows:

- The background composition and shapes are studied in control regions (CR). The control regions are constructed by relaxing or inverting the selection and/or lepton identification requirements.
- An extrapolation is computed to estimate the expected background in the signal region (SR). This is done by using transfer factors. These factors are usually determined from the simulation of control regions or by the ratio of the expected yields between the signal and control regions.

As was mentioned in Section (5.1), the composition of the reducible backgrounds depends on the flavour of the subleading dilepton. Different approaches are used to

estimate the reducible backgrounds in the $ll + \mu\mu$ and the $ll + ee$ final states.

5.4.1 The $ll + \mu\mu$ background estimate

For the $ll+\mu\mu$ final state, the background consists mainly of $\mathrm{Z} + \mathrm{b\bar{b}}$ events, Z production accompanied by π/K in-flight decays from within light flavour jets ($\mathrm{Z} + \mathrm{jj}$) and a small contribution from the $t\bar{t}$ background.

The m_{12} distribution is key to be able to distinguish between Z+jets and $t\bar{t}$ events, where the former has a peak at the Z boson mass and the latter has a broader distribution. Four CRs were defined and fitted simultaneously to extract the different components of the reducible background. The fit is performed on the m_{12} distribution. The four control regions are selected such that there is no contamination from the Higgs signal, little contamination as possible from the WZ and the irreducible $ZZ^{(*)}$ backgrounds and that they are enriched in the specific reducible background components. They are defined as:

- **Inverted $\mathbf{d_0}$ CR**: the impact parameter significance selection is inverted and the isolation criteria is not applied for at least one lepton of the subleading dilepton. This region is enhanced in $Z + b\bar{b}$ and $t\bar{t}$ since leptons from b-quarks are characterised by a large d_0 significance.
- **Inverted isolation CR**: the isolation criteria is inverted for at least one lepton of the subleading dilepton and the standard impact parameter significance is applied to both leptons. This region is enhanced in the $Z + jj$ component.
- **Same sign CR**: neither the impact parameter significance, nor the isolation criteria are applied to the subleading dilepton. The leptons in the pair are required to have the same sign charge. Here all the backgrounds have a significant contribution.
- **$e\mu + \mu\mu$ CR**: the leading dilepton is required to have opposite-charge and different-flavour leptons and it must satisfy the standard four lepton selection criteria. Neither the impact parameter significance, nor the isolation criteria, are applied to the subleading dilepton while both opposite and same charge leptons are accepted. Z bosons decaying into pair of electrons or muons are vetoed. This region is enhanced by $t\bar{t}$ background.

A simultaneous unbinned maximum likelihood fit is performed on m_{12} for the four control regions describe above. The $t\bar{t}$ background component is modelled by a 2^{nd}

order Chebychev polynomial and the Z + jets ($Z + b\bar{b}$ plus $Z + jj$) is modelled by a convolution of a Crystal Ball with a Breit-Wigner. The estimated number of events derived from each CR is extrapolated to the signal region by calculating a selection efficiency obtained from simulation. It is defined as $\epsilon = \mathcal{N}_{\text{all}}/\mathcal{N}_{\text{relaxed}}$ where $\mathcal{N}_{\text{all}}$ is the number of muons that pass all the analysis criteria in a CR, see Section (5.2.7), and $\mathcal{N}_{\text{relaxed}}$ is the number of muons surviving the selection specific of that given CR. This term is calculated for each muon, then these efficiencies are combined for the subleading dilepton to obtain the total transfer factor of the event. This factor is then multiplied by the number of events in the CR to obtain the number of events in the signal region.

The final reducible background estimations from $ll + \mu\mu$ are shown in Table (5.3) for the 7 and 8 TeV data. The fit uncertainty is assigned as the statistical error and the transfer factor uncertainty as the systematic uncertainty of the method.

Reducible Background	4μ	$2e2\mu$
	7 TeV data	
Z+jets ($Z + b\bar{b} + Z + jj$)	$0.44 \pm 0.24(\text{stat}) \pm 0.08(\text{syst})$	$0.30 \pm 0.17(\text{stat}) \pm 0.05(\text{syst})$
$t\bar{t}$	$0.08 \pm 0.02(\text{stat}) \pm 0.02(\text{syst})$	$0.06 \pm 0.01(\text{stat}) \pm 0.02(\text{syst})$
	8 TeV data	
Z+jets ($Z + b\bar{b} + Z + jj$)	$3.11 \pm 0.46(\text{stat}) \pm 0.56(\text{syst})$	$2.58 \pm 0.39(\text{stat}) \pm 0.43(\text{syst})$
$t\bar{t}$	$0.51 \pm 0.03(\text{stat}) \pm 0.09(\text{syst})$	$0.49 \pm 0.03(\text{stat}) \pm 0.08(\text{syst})$

Table 5.3 Summary of the estimated yields of the $ll + \mu\mu$ reducible backgrounds for the 7 and 8 TeV data in the full m_{4l} range. The systematic uncertainties are estimated from the transfer factor error.

5.4.2 The $ll + ee$ background estimate

As it was mentioned in Section (5.1), the reducible background contributing to the ll+ee final states is mainly composed of jets misidentified as electrons, which occur in three ways: light-flavour hadrons misidentified as electrons, photon conversions reconstructed as electrons, and non-isolated electrons from heavy-flavour hadronic decays.

The ll+ee background is estimated using three data-driven methods where the selection is relaxed or inverted for one or two of the subleading electrons. Two of these methods were used as cross-checks while the baseline method, called 3l+X, was used for the final estimate of the background. For more details see [56].

For the 3l+X method, a control region is defined where it requires that the three highest p_{T} leptons (3l) satisfy the full selection, with the third lepton being an electron. In

addition, the remaining electron (X) has to have the electron identification fully relaxed except for the requirement on the number of hits in the silicon tracker (at least seven silicon hits with at least one in the pixel detector). Also, X is required to have the same charge as the other subleading electron to minimise the contribution from the ZZ^* background.

The background components in this control region are evaluated according to electrons not passing a cut from the reconstruction described in Section (5.2.2). For example, if an electron does not fulfil the B-layer requirement, to reduce the amount of photon conversion, then it is categorised as a fake electron and will contribute to the background component to form the distribution. The same is for the requirement on the number of hits in the TRT to suppress hadrons faking electrons. Then templates are created from these background components and the yields are extracted from the fit to the control region. The fitted yields in the CR are extrapolated to the SR using efficiencies, as in the muon case, but they are obtained from a large sample of Z bosons produced with a single additional electron candidate satisfying the relaxed selection.

The final reducible background estimations from $ll + ee$ are shown in Table (5.4) for the 7 and 8 TeV data.

Reducible Background	$4e$	$2\mu 2e$
$ll + ee$ (7 TeV)	$3.29 \pm 0.49(\text{stat}) \pm 0.48(\text{syst})$	$2.93 \pm 0.47(\text{stat}) \pm 0.45(\text{syst})$
$ll + ee$ (8 TeV)	$2.88 \pm 0.28(\text{stat}) \pm 0.54(\text{syst})$	$2.91 \pm 0.33(\text{stat}) \pm 0.60(\text{syst})$

Table 5.4 Summary of the estimated yields of the $ll + ee$ reducible backgrounds for the 7 and 8 TeV data in the full m_{4l} range.

5.4.3 Reducible background in the range $110 < m_{4l} < 140$ GeV

Finally, a summary of the estimated reducible backgrounds in the m_{4l} range between 110 and 140 GeV is presented in Table (5.5).

	4μ	$2e2\mu$	$4e$	$2\mu 2e$
Background estimate (7 TeV)	0.26 ± 0.11	0.24 ± 0.09	1.14 ± 0.24	1.02 ± 0.23
Background estimate (8 TeV)	1.78 ± 0.28	1.55 ± 0.26	1.00 ± 0.21	1.01 ± 0.24

Table 5.5 Summary of the estimated yields of the reducible backgrounds for the 7 and 8 TeV data in the m_{4l} range $110 < m_{4l} < 140$ GeV.

Chapter 6

The Standard Model Higgs boson mass measurement

The updated Standard Model Higgs boson mass measurement with the full 7 and 8 TeV datasets in the mass range $110 < m_{4l} < 140$ GeV will be described in this chapter [40]. It also focuses on the measurement of the signal strength, μ. A few improvements have been made from previous measurements [57] and will be described. The object reconstruction and identification, and event selection for this analysis are explained in Chapter 5.

6.1 Data samples

The data samples used for this analysis will be described in the following sections. First there is a description of the data taken by the ATLAS experiment followed by the description of the Monte Carlo samples used for signal and background.

6.1.1 Collision data

Proton-proton collision data from 2011 and 2012 ATLAS data taking are used. The events recorded during periods where the relevant detector components were not fully operating are rejected (data quality requirements). The resulting integrated luminosities are 4.6 fb^{-1} at $\sqrt{s} = 7$ TeV and 20.7 fb^{-1} at $\sqrt{s} = 8$ TeV .

6.1.2 Monte Carlo samples

The MC samples are generated with the same conditions as the collision data and are very important to derive calibrating scale factors to match with data, to estimate signal and background events and to compare the measured data with different theoretical models. Events for signal and background processes are generated using Monte Carlo simulators. Full simulation of each event is performed using the ATLAS detector simulation [58] within the GEANT4 framework [59]. Additional pp interactions in the same and in nearby bunch crossings (pile-up) are included in the simulation.

Signal

The $H \to ZZ^{(*)} \to 4l$ signal is modelled using the POWHEG event generator [60, 61], where the gluon fusion (ggF) and vector boson fusion (VBF) production mechanisms are calculated separately up to next to leading order (NLO). The Higgs transverse momentum is reweighted to follow the calculations of transverse momentum resumation at the LHC [62] to include corrections to leading order plus next-to-next leading order logarithm (NLO+NNLL). POWHEG is interfaced with PYTHIA [63] for showering and hadronization, which in turn is interfaced to PHOTOS [64] for QED radiative corrections in the final state. PYTHIA is also used to simulate the production of a Higgs boson in association with a W or Z boson as well as the associated production with a top quark pair.

Production cross-sections and decay branching ratios, as well as their uncertainties, are taken from the LHC Higgs cross-section working group [10, 11]. Cross-sections for the ggF process have been calculated at NLO [65–67] and next-to-next leading order (NNLO) [68–70] in QCD and NNLL QCD soft-gluon resumations [71]. NLO electroweak radiative corrections [72, 73] were applied as well. Cross-sections for the VBF process are calculated with full NLO QCD and EW corrections [74–76] and with approximate NNLO QCD corrections [77]. For the associated production of the Higgs boson with a W or Z boson, cross-sections are calculated at NLO [78] and NNLO [79] in QCD, and NLO electroweak radiative corrections [80] are applied. For this analysis, the small contribution from the associated production of the Higgs boson with a $t\bar{t}$ pair was also included. The cross-sections for this process were estimated at NLO QCD [81–85]. The branching ratios to the four lepton final state [86] are calculated by PROPHECY4F [87, 88], which includes: the NLO QCD and electroweak corrections, the interference between identical final state fermions, and the leading two-loop heavy

Higgs boson corrections to the four fermion decay width.

The two main sources of uncertainties affecting the cross section comes from the QCD radiation corrections (QCD scale uncertainties) and the Parton Distribution Function (PDF) choice $+\alpha_S$. For the QCD scale, the uncertainty is calculated by varying the renormalisation and factorisation scales around a central value chosen to be the hard scale of the process. These scales are changed by a factor two up and down from their nominal value. The choice of this nominal parameter is $\mu_0 = m_H$ or $\mu_0 = m_H/2$ according to two different calculations [89, 90] leading to very similar results. For the PDF choice, the MSTW2008 PDF set [91] provides 40 different grids that allow the evaluation of the experimental uncertainties. These grid variations are then compared to other PDF set variations, namely NNPDF [92] and CTEQ [93]. Another related source of theoretical uncertainties comes from the value of the QCD coupling constant α_S. This value is known up to the order of 3-4% in the Higgs mass range from 100 to 300 GeV and its uncertainty is usually incorporated into the PDF-related systematics. The QCD scale uncertainties on the cross-section at $m_H = 125$ GeV are: $^{+7}_{-8}$% for the ggF process, ± 1% for the VBF and VH productions, and $^{+4}_{-9}$% for the $t\bar{t}$ production mechanism. The uncertainty on the cross-section due to PDF and α_s are of the order of 8% for the gluon-initiated and 3% for the quark-based processes.

The signal MC samples are generated between 120 and 130 GeV. For the ggF and VBF production mechanisms for both the 7 and 8 TeV datasets, 11 MC samples were generated in 1 GeV mass increments. For the 8 TeV dataset, 3 additional samples were generated at mass points of 123.5, 124.5 and 125.5 GeV. For WH and ZH production mechanisms, samples between $123 < m_H < 127$ GeV were generated in 1 GeV mass increments and, in addition, samples at mass points of 120 and 130 GeV. All ggF and VBF production mechanism samples were simulated without τ leptons, and the WH and ZH samples were generated with τ leptons.

Irreducible background

The $ZZ^{(*)}$ background is modelled using POWHEG [94] for qq production and GG2ZZ [95] for gg production. PDF and α_s uncertainties are parametrised, depending on the mass, as recommended by the LHC Higgs cross-section working group [11]. For $m_H = 125$ GeV, the QCD scale uncertainty has an effect of ± 5% and the PDF+α_s uncertainties have an effect of ± 4%(± 8%) for qq(gg) processes on the expected $ZZ^{(*)}$ background cross-section.

Reducible background

The Z+jets background is simulated using ALPGEN [96] interfaced with PYTHIA for hadronisation and showering. It is divided into two sources: Z +jj (light jets), which includes $Z + c\bar{c}$ in the massless c-quark approximation and $Z + b\bar{b}$ from parton showers, and Z+$b\bar{b}$ taking into account the b-quark mass. The normalisation is taken from data control regions. For comparisons with simulation, QCD NNLO [97, 98] cross-section calculations are used.

The $t\bar{t}$ background is modelled using POWHEG [94] interfaced to PYTHIA [63], PHOTOS [64] and TAUOLA [99, 100] for parton shower hadronization, for QED radiative corrections and for the simulation of τ lepton decays. SHERPA [101] is used for the WZ production simulation.

6.2 Signal modelling

The procedure to obtain the signal models consists of two steps: create smoothed shapes from all MC samples available and then interpolate them to have a continuous pdf in the full hypothesised Higgs boson mass range. This section will describe these two steps. The 2D model, see more details in Section (6.6), uses two variables as observables: the invariant mass m_{4l} and the BDT discriminant. There is an approximation used for the signal pdfs that turns the 2D pdf into two 1D pdfs, more details will be explained in Section (6.6). Therefore, separate 1D signal pdfs are created for the m_{4l} and BDT distributions.

As it was mentioned in Section (6.1.2), the MC samples used for ggF and VBF production mechanisms are generated without Higgs decay to τ leptons. This does not affect the shape of the pdfs in the signal region since the reconstructed m_{4l} from τ leptons is typically below 120 GeV and contributes less than 0.4%.

6.2.1 Signal probability distribution function from MC

In order to remove the statistical fluctuations in the MC samples, the pdfs are obtained by smoothing the MC distribution using a *Kernel Estimating your Shape* (KEYS) Kernel Density Estimate [102].

The distribution is estimated as a sum of Gaussian kernels centred at each individual

data point, in our case, centred at each m_{4l} or BDT value. The width of the Gaussian kernels is estimated according to the shape of the distribution. Broader distributions will assign larger widths to the kernels. If the distribution is not normally distributed, as it is the general case, it is better to use a kernel width which varies dynamically. This is called the *adaptative kernel estimation*.

The adaptive kernel width is estimated using the local width of the input distribution and depends on a parameter which tunes the amount of smoothing applied to the distribution. This parameter has been tuned to remove the statistical fluctuations of the templates without biasing the distributions. The resulting shape is smoother than the input histogram and thus provides a better description for the signal model. Figure (6.1) shows the final shapes for the m_{4l} distribution in the four final states coming from the ggF production mechanism at $m_H = 125$ GeV. Note that the $2e2\mu$ final state distribution is narrower than the $2\mu 2e$ final state distribution because muons from the off-shell Z boson in the former have better resolution than the electrons from the off-shell Z boson in the latter. The same thing applies for 4μ and $4e$ final state distributions. A +2 GeV shift (dotted blue line) in m_H is shown to illustrate the possibility of providing a continuous parametrisation as a function of m_H and interpolate the signal shape for each hypothesised Higgs boson mass, more details will be explained in the following section.

6.2.2 Continuous parametrisation in $\mathbf{m_H}$ of signal shapes

Now that smoothed distributions were obtained from all MC samples, we can interpolate them to obtain the continuous pdf in the full mass range. The signal shapes between fully simulated mass points can be obtained by taking two shapes from the closest available mass points, shifting their m_{4l} distribution and vertically interpolating their shapes. This can be extended by using a piecewise function defined by polynomials, called B-Splines or a basis spline [103].

First, a control point is assigned to every point in m_H for which a MC sample is available, see Section (6.1.2). To obtain a new intermediate m_{4l} distribution, a weighted sum of the values from the m_{4l} distributions associated with control points found in the vicinity of m_H is performed. A cubic interpolation function is used to evaluate the weights from each control point, the highest weights are given to neighbouring control points, but points that are further away can also contribute. The basis functions for cubic interpolation are shown in Figure (6.2).

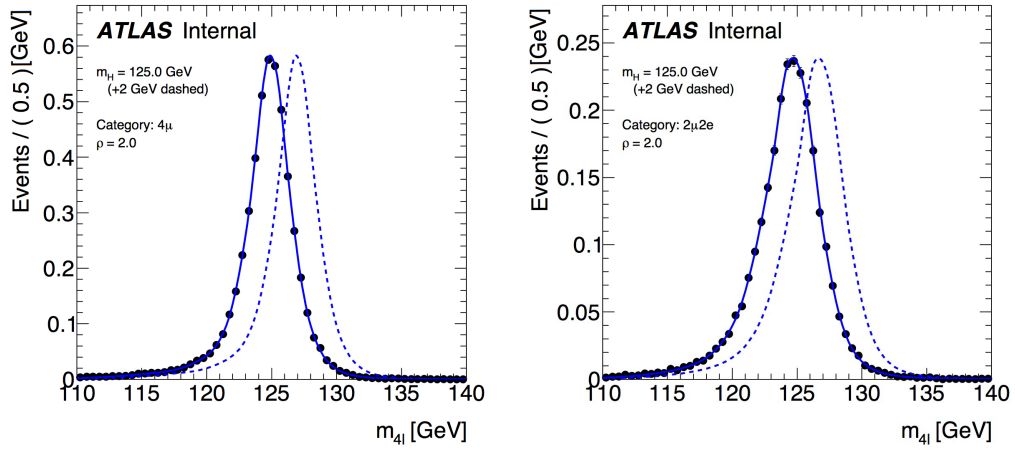

(a) $H \to ZZ^* \to 4\mu$

(b) $H \to ZZ^* \to 2\mu 2e$

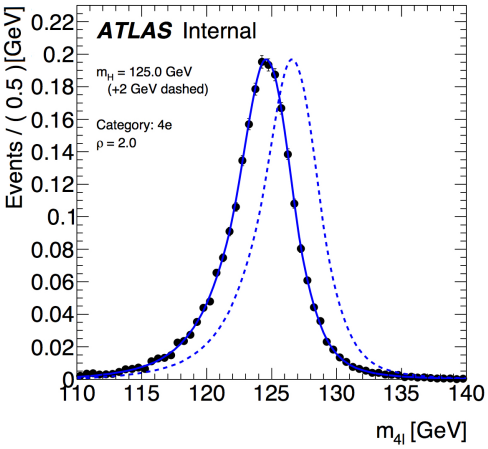

(c) $H \to ZZ^* \to 4e$

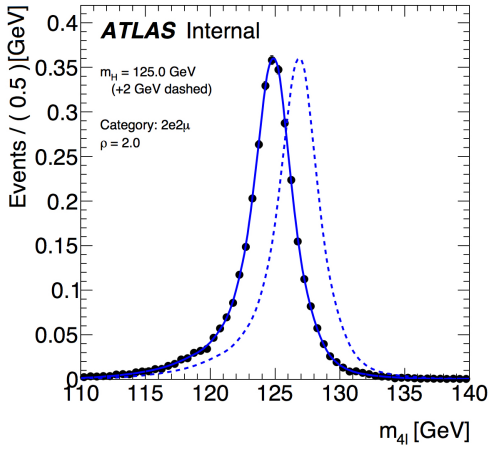

(d) $H \to ZZ^* \to 2e2\mu$

Figure 6.1 Invariant mass distribution for a simulated 8 TeV signal sample from the ggF production mechanism at $m_H = 125$ GeV. The comparison between the histogram (black dots) and the resulting smoothed distribution (blue line) is shown. A +2 GeV shift (dotted blue line) in m_H is shown for illustration.

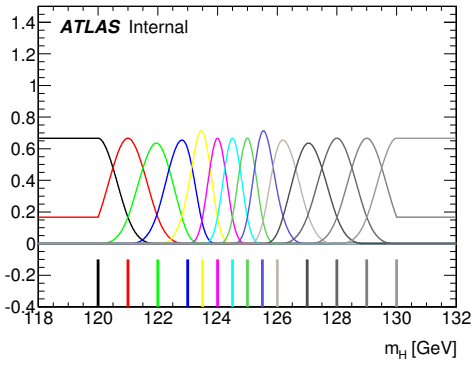

(a)

Figure 6.2 B-spline basis functions for each control point (cubic interpolation).

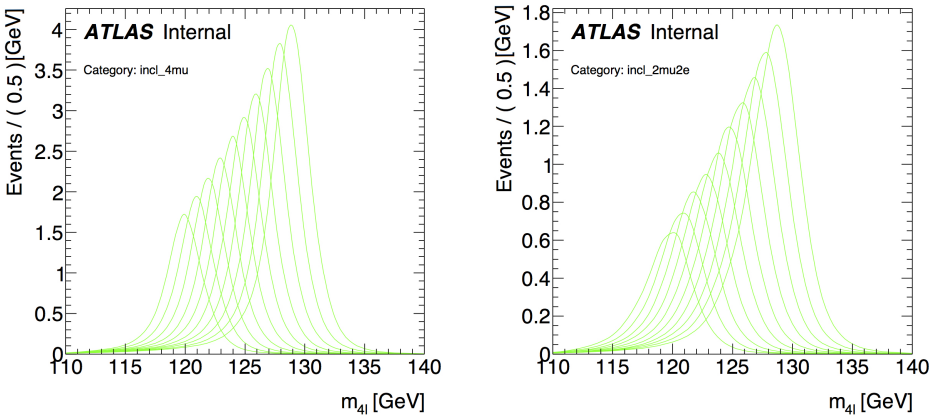

(a) $H \to ZZ^* \to 4\mu$

(b) $H \to ZZ^* \to 2\mu 2e$

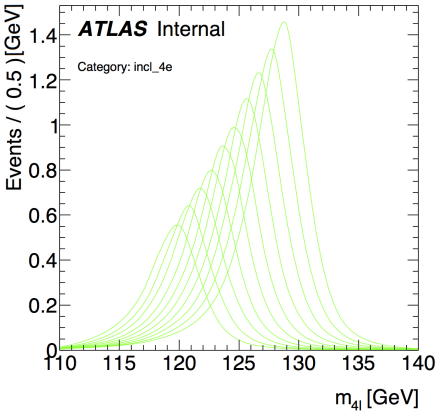

(c) $H \to ZZ^* \to 4e$

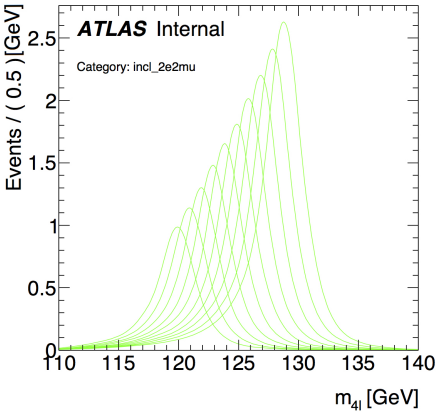

(d) $H \to ZZ^* \to 2e2\mu$

Figure 6.3 Continuous parametrisation in m_H for the four final states. The signal shapes shown are for the 8 TeV MC sampled in 1 GeV steps between 120 and 130 GeV and in steps of 0.5 GeV between 123 and 126 GeV.

The expected signal yields are obtained from MC samples for the same control points as the signal shapes. The yield at intermediate mass points is obtained using a second B-Spline on the same basis. Combining the signal shapes with the normalisations, results in the normalised signal shapes shown in figure (6.3). The shapes are continuously parametrised in m_H. The monotonically growth of the signal distributions is due to the rapid increase of the number of expected events in this mass range. This is a result of the $\sigma \times BR$ of the Higgs boson in this mass range which becomes larger for higher masses until it reaches the off/on-shell threshold of the subleading Z boson, see Figure (2.5). Another fact to consider is that the m_{4l} resolution increases in this range making the distributions wider. However, the m_{4l} resolution increases slightly as higher Higgs masses are considered here and the expected number of events increases much faster, therefore giving this behaviour on the signal distributions.

6.3 Irreducible background modelling

For the 2D model, the same approach as described in the previous section was used. The kernel estimation is done in two dimensions to obtain the smoothed shapes in m_{4l} and in BDT. Figures (6.4) and (6.5) shows the projections of the 2D shapes over the MC sample for 8 TeV for $q\bar{q} \to ZZ^{(*)}$.

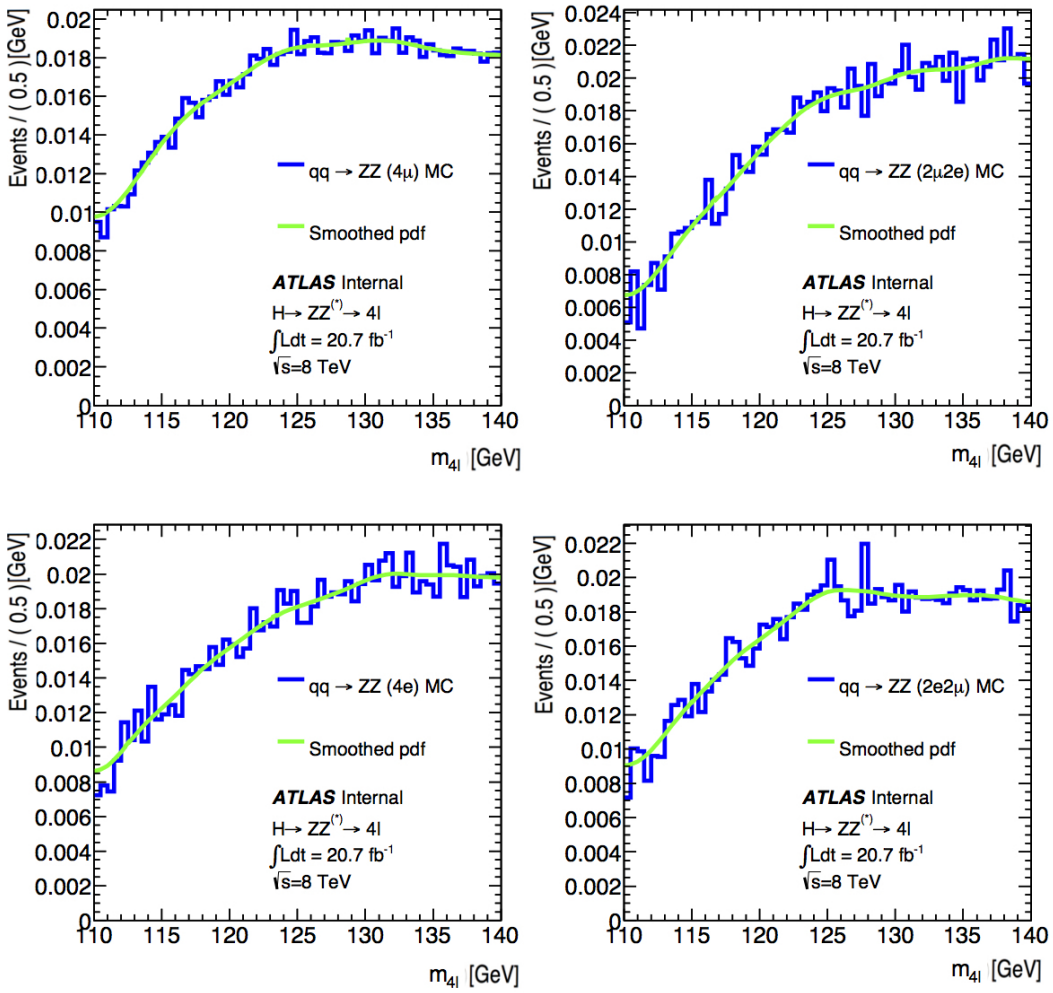

Figure 6.4 Projection of the 2D $q\bar{q} \to ZZ^{(*)}$ background in m_{4l} overlaid with the generated MC sample for 8 TeV.

6.4 Reducible background modelling

As described in Section (5.4), the shapes of the reducible background are obtained from Z+jets and $t\bar{t}$ MC in the muon subleading channels and from $3l+X$ data control region for the electron subleading channels. The reducible backgrounds are smoothed in the

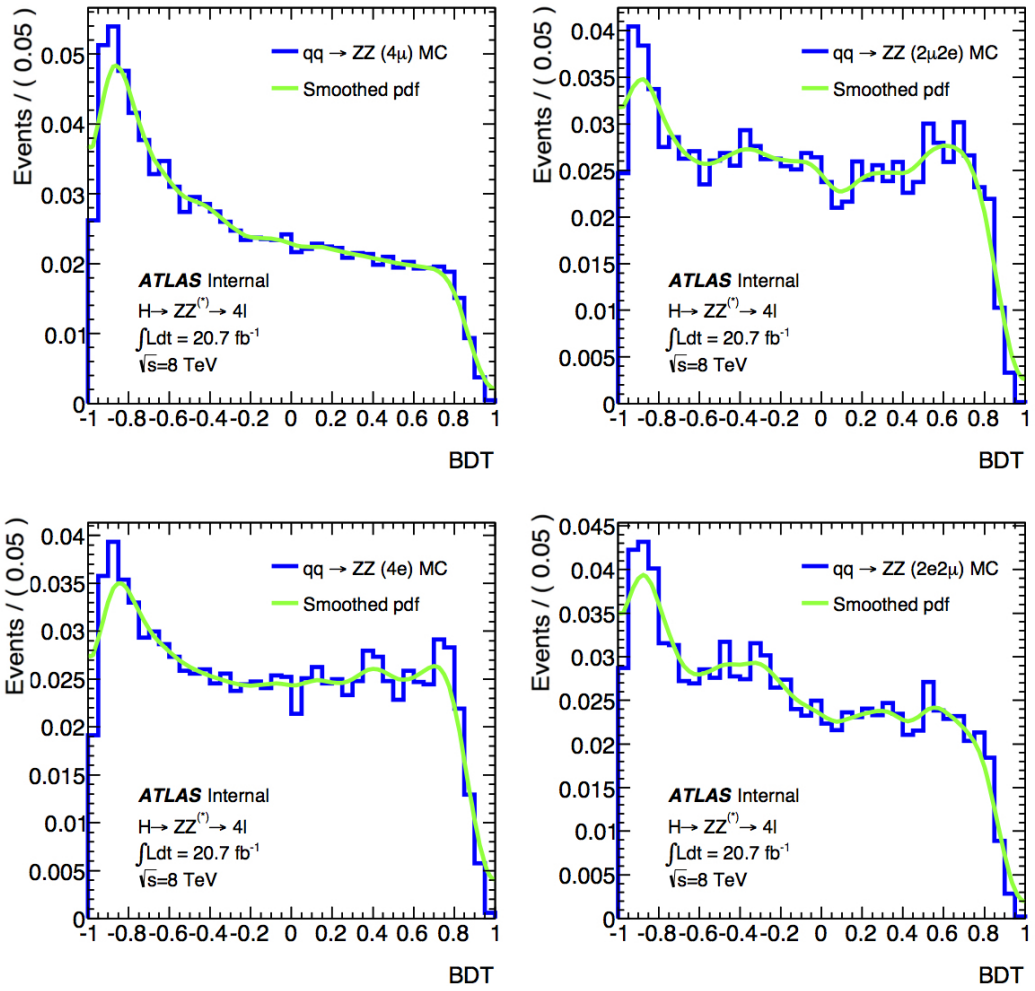

Figure 6.5 Projection of the 2D $q\bar{q} \to ZZ^{(*)}$ background in the BDT variable overlaid with the generated MC sample for 8 TeV.

same way explained in Section (6.2). Figure (6.6) shows the final reducible background distributions.

6.5 Systematic uncertainties

Several sources of systematic uncertainties on signal and background are considered. They were implemented in the signal and background models using nuisance parameters and evaluated using Monte Carlo studies to determine their impact on the final fit. They can be grouped as follows:

Lepton identification and reconstruction: uncertainty from the identification and reconstruction efficiencies of leptons (electrons and muons) affects the signal yield

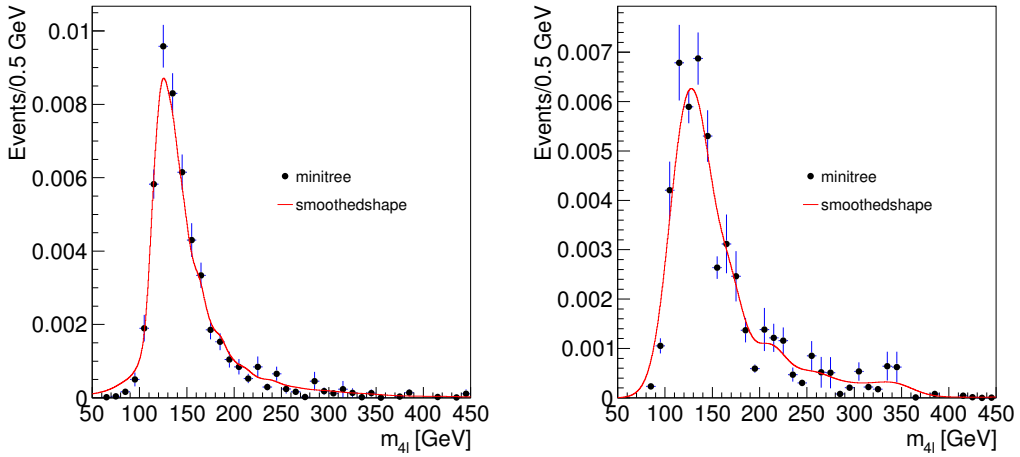

(a) $ll + \mu\mu$ **(b)** $ll + ee$

Figure 6.6 (a) $ll + \mu\mu$ and (b) $ll + ee$ reducible background distribution for the Z+jets and $t\bar{t}$ contribution to m_{4l} for the smoothed pdf templates (red) and the input histograms (black).

uncertainty. The effect from electron reconstruction and identification efficiencies gives a total uncertainty on the signal yields of $\pm 4.36\%$, $\pm 1.67\%$ and $\pm 3.29\%$ for $4e$, $2e2\mu$, and $2\mu 2e$, respectively at $m_{4l} = 125$ GeV. The effect from muons gives an uncertainty on the signal yield that is approximately uniform in m_{4l}. Its values are $\pm 1.86\%$, $\pm 0.77\%$ and $\pm 1.09\%$ for 4μ, $2\mu 2e$ and $2e2\mu$, respectively at $m_{4l} = 125$ GeV.

Luminosity: the overall uncertainty on the integrated luminosity is $\pm 1.8\%$ and $\pm 2.8\%$ for the 7 and 8 TeV datasets, respectively. It is assigned as a corresponding uncertainty for normalisations coming from MC.

Trigger: this uncertainty is calculated by checking the number of events that pass the event selection with or without the trigger requirement. It gives an uncertainty on the signal yields, coming from the electron and muon trigger efficiency uncertainty, of less than 0.7%.

Electron energy scale: it is determined from simulated $Z \to ee$ decays and verified using J/Ψ decays. The uncertainty on m_{4l} is 0.061%, 0.029% and 0.043% for $4e$, $2e2\mu$ and $2\mu 2e$, respectively, for $m_H = 125$ GeV.

Muon momentum scale: the uncertainties on the determination of the muon momentum scale are evaluated using simulated J/Ψ, Υ and Z decays. The total uncertainties, for $m_H = 125$ GeV, are 0.044%, 0.018% and 0.026% for 4μ, $2\mu 2e$ and $2e2\mu$ respectively.

Theory uncertainties: the theoretical systematic uncertainties affect the cross-section

of the signal and background. They are described in Section (6.1.2).

p_T and η related uncertainties: these two variables are used as input observables in the BDT training, hence it is essential to assess the theoretical uncertainties affecting them in order to estimate their impact on the BDT shape. The effect on the best m_H fit to Asimov data at $m_H = 125$ GeV is less than 0.01% while the impact on μ is approximately 0.1%. Due to the small impact of these systematics in the model, it was decided not to include them in the final nuisance parameter set.

Reducible background uncertainty: as the reducible backgrounds are estimated from data driven techniques, the uncertainties come from differences between the different estimation methods, from uncertainties in the transfer factors and from limited statistics in the control regions. The uncertainties on the yields are shown in Table (5.5).

The conditional 2D model from Section (6.6) is used to rank the systematic uncertainties by order of importance. Only those uncertainties which contribute more than 2% of the statistical uncertainty, 14 MeV for m_H and 0.006 for μ, are kept. Only 19 systematic uncertainties survived and are grouped by types in Tables (6.1) and (6.2).

Nuisance parameter	4μ		$2\mu 2e$		$4e$		$2e2\mu$		All final states	
Contribution to m_H [MeV]	Up	Down	Up	Down	Up	Down	Up	Down	Up	Down
Muon momentum scale	51	54	42	23	-	-	21	23	33	34
Muon ID and reconstruction efficiency	2	2	7	1	-	-	1	1	0	1
Electron energy scale	-	-	26	9	67	62	41	42	29	30
Electron ID and reconstruction efficiency	-	-	23	9	16	13	3	3	2	2
Theory	4	4	31	18	9	3	5	2	2	2
Luminosity	3	3	16	9	9	7	3	3	1	1
Reducible background	2	6	76	55	28	23	18	12	10	4
sum in quadrature	51	55	100	65	75	68	50	50	44	46

Table 6.1 Impact of the nuisance parameters on the m_H fit to data for individual final states and all final states combined for the 7 + 8 TeV data samples. All values are given in MeV.

6.6 The model for the mass and signal strength measurements

To improve the performance of the signal and background models for the Higgs mass and signal strength measurement, with respect to previous measurements [57], a BDT is used to increase the discrimination between signal and the irreducible ZZ^* background, see more details in Section (5.2.8). The $\mathrm{BDT_{ZZ^*}}$ output ($\mathrm{O_{BDT_{ZZ^*}}}$) is used as a second variable, along with m_{4l}, in the fit. Two other models are also used to measure the

Nuisance parameter	4μ		$2\mu 2e$		$4e$		$2e2\mu$		All final states	
Contribution to $\mu[\times 10^{-3}]$	Up	Down	Up	Down	Up	Down	Up	Down	Up	Down
Muon momentum scale	0.4	0.8	2.4	2.9	-	-	0.8	1.5	0.8	0.8
Muon ID and reconstruction efficiency	32.2	34.1	13.5	14.3	-	-	22.8	24.0	22.2	22.8
Electron energy scale	-	-	1.5	2.3	1.1	1.8	0.2	0.6	0.2	0.2
Electron ID and reconstruction efficiency	-	-	86	85	59	57	3	29	27	28
Theory	124	112	179	202	259	147	161	224	145	161
Luminosity	32	34	46	49	5	5	41	43	37	39
Reducible background	17	19	35	35	50	54	23	25	18	16
sum in quadrature	133	149	207	230	153	169	171	192	155	171

Table 6.2 Impact of the nuisance parameters on the μ fit to data for individual final states and all final states combined for the 7 + 8 TeV data samples. All values are given as per mille. The relative weights of 4μ, $2\mu 2e$, $4e$ and $2e2\mu$ are 0.36, 0.09, 0.18 and 0.37, respectively.

Higgs boson mass and signal strength. However, the 2D model is chosen as the baseline because it has the smallest expected uncertainty. It is reduced by 8% with respect to the 1D model (only m_{4l} as observable) used in the previous analysis[57].

The background model $\mathcal{P}_{bkg}(m_{4l}, O_{BDT_{ZZ^*}})$ is described by a 2D pdf that is derived as described in Sections (6.3) and (6.4).

The signal model is obtained as described in Section (6.2). The MC samples are normalised to the expected SM cross-section times branching ratio [9] to obtain the expected number of signal events after selection. The range of m_{4l} used for the fit is $110 < m_{4l} < 140$ GeV. The implementation of the full 2D model for the signal is technically challenging due to the dependence of the shape systematic uncertainties on m_{4l}, BDT and m_H. Therefore, to simplify the implementation, the pdf for the signal is modelled using a conditional pdf as:

$$\begin{aligned}\mathcal{P}_{sig}(m_{4l}, O_{BDT_{ZZ^*}}|m_H) &= \mathcal{P}(m_{4l}|O_{BDT_{ZZ^*}}, m_H)\mathcal{P}(O_{BDT_{ZZ^*}}|m_H) \\ &\simeq \left(\sum_{n=1}^{4} \mathcal{P}_n(m_{4l}|m_H)\theta_n(O_{BDT_{ZZ^*}})\right)\mathcal{P}(O_{BDT_{ZZ^*}}|m_H),\end{aligned} \tag{6.1}$$

where θ_n defines four equal sized bins for the value of the $\mathrm{BDT_{ZZ^*}}$ output and $\mathcal{P}_n$ represents the 1D signal pdf for m_{4l} in the corresponding $\mathrm{O_{BDT_{ZZ^*}}}$ bin. In this way, the signal pdf is basically a sum of four 1D distributions, one for each BDT bin, allowing to treat the shape systematics uncertainties as if it was a 1D model. The m_{4l} distribution in each $\mathrm{O_{BDT_{ZZ^*}}}$ bin is assumed to be the same. Studies indicate that this is correct and that also does not bias the mass measurement.

Figures (6.7a) and (6.8a) show the full m_{4l} and BDT pdfs at $m_H = 125$ GeV for the

4μ final state. Also, figures (6.7b) and (6.8b) show the signal ($gg \to H \to ZZ \to 4\mu$) and background ($q\bar{q} \to ZZ \to 4\mu$) component pdfs separately.

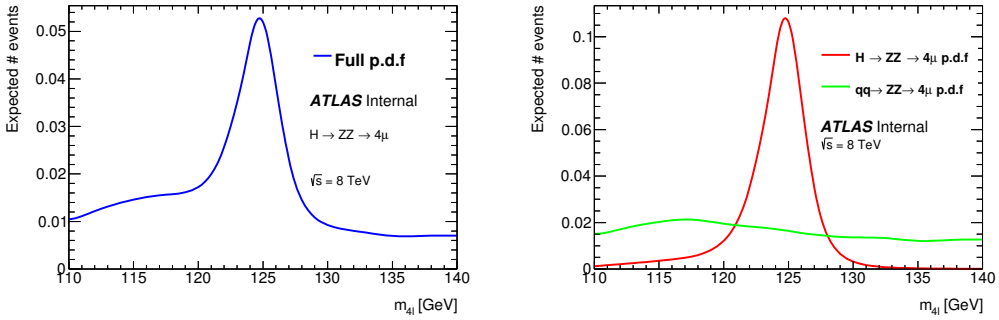

(a) **(b)**

Figure 6.7 (a) Full m_{4l} pdf for a signal at $m_H = 125$ GeV for the 4μ final state and (b) m_{4l} signal pdf for $gg \to H \to ZZ^* \to 4l$ at $m_H = 125$ GeV (red) and for background $q\bar{q} \to ZZ \to 4\mu$ pdf (green) using the 8 TeV MC dataset.

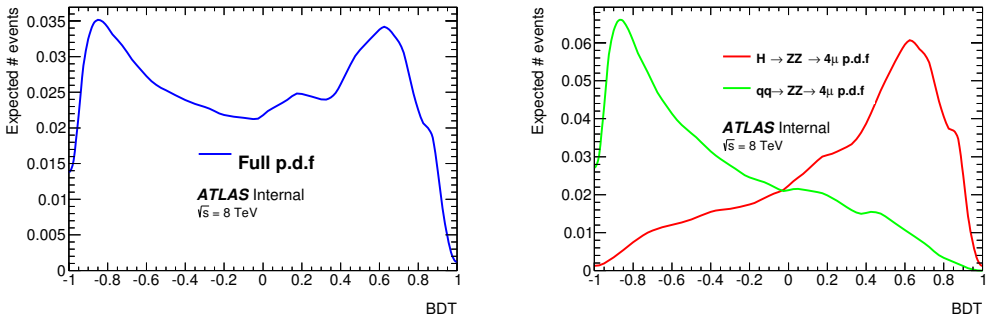

(a) **(b)**

Figure 6.8 (a) Full BDT pdf for a signal at $m_H = 125$ GeV for the 4μ final state and (b) BDT signal pdf for $gg \to H \to ZZ^* \to 4l$ at $m_H = 125$ GeV (red) and for background $q\bar{q} \to ZZ \to 4\mu$ pdf (green) using the 8 TeV MC dataset.

The m_{4l} and the $\mathrm{O}_{\mathrm{BDT}_{ZZ^*}}$ pdf distributions for eight sets of events (one for each final state for the 7 and 8 TeV datasets) are fitted simultaneously using an unbinned maximum likelihood. Following Equation (4.4), the full likelihood function is given by:

$$\mathcal{L}(m_H, \mu, \theta) = \prod_{i}^{\text{year}} \prod_{j}^{\text{final state}} \frac{(\mu S_{ij}(m_H, \boldsymbol{\theta}) + B_{ij}(\boldsymbol{\theta}))^{N_{ij}}}{N_{ij}!} e^{-(\mu S_{ij}(m_H, \boldsymbol{\theta}) + B_{ij}(\boldsymbol{\theta}))} \times \prod_{k=1}^{N_{ij}} \left[\frac{\mu S_{ij}(m_H, \boldsymbol{\theta}) f_s((m_{4l}, BDT)_k, m_H, \mu, \boldsymbol{\theta}) + B_{ij}(\boldsymbol{\theta}) f_b((m_{4l}, BDT)_k, \mu, \boldsymbol{\theta})}{\mu S_{ij}(m_H, \boldsymbol{\theta}) + B_{ij}(\boldsymbol{\theta})} \right], \tag{6.2}$$

where m_H and μ are the parameters of interest, $\boldsymbol{\theta}$ are the set of nuisance parameters

that model the systematic uncertainties from Section (6.5), S_{ij} and B_{ij} are the expected number of events for signal and background and f_s and f_b are the pdfs for signal and background described above.

6.7 Validation studies for the models

As it is clear from the previous sections, there is a strong effort to measure the SM Higgs boson mass as accurately as possible. To achieve this, the model to predict the parameters of interest, i.e. the likelihood, must be validated extensively. Pseudo-experiments were carried out to validate the conditional 1D and 2D likelihoods used to measure the SM Higgs boson mass.

6.7.1 Pseudo-experiments for the Higgs boson mass measurement

Pseudo-experiments were performed over the 1D and 2D likelihoods. The objective is to study if there are some significant deviations from the input values of the mass m_H and the signal strength μ used to create each experiment when fitting to the models. 2000 pseudo-datasets are generated for each of the 8 TeV 1D and 2D likelihoods, as well as for the combined (7 + 8 TeV) 1D and 2D likelihoods. Each pseudo-dataset contains signal and irreducible background events. They are obtained from the MC samples, with the number of events for each production mechanism and background determined using the expected numbers of events taking into account Poisson fluctuations, see figure (6.9). Finally, the reducible background events are also added to the pseudo-dataset, but are sampled directly from the model pdf due to low statistics from the MC samples. Events from the bbH production mechanism are obtained from the ggF MC sample, but scaled to the corresponding bbH rate.

A tool was developed to perform pseudo-experiments over different likelihoods, having in mind transparency and flexibility depending on what is required to be studied or compared among these models. The tool can handle any model including analytical models and also models with one or two observables. It can sample pseudo-datasets directly from the model pdfs or from MC simulation. In figures (6.10) and (6.11) a pseudo-dataset is shown with 10000 times the number of expected events generated from MC (blue) and from pdf (red) as a function of m_{4l} and the BDT observables. A very good agreement between the pdf and the MC pseudo-datasets is seen in both figures.

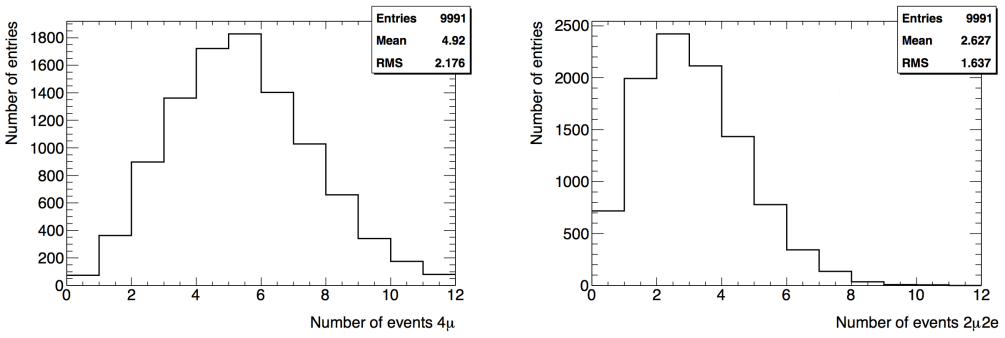

(a) $gg \to H \to ZZ^* \to 4\mu$ **(b)** $gg \to H \to ZZ^* \to 2\mu 2e$

(c) $gg \to H \to ZZ^* \to 4e$ **(d)** $gg \to H \to ZZ^* \to 2e2\mu$

Figure 6.9 Number of events generated for each pseudo-dataset for the ggF production mechanism for the four final states.

A Higgs boson mass of $m_H = 125$ GeV and a signal strength of $\mu = 1$ is assumed to generate all the pseudo-datasets. When taking into account the systematic uncertainties, they are treated as an external measurement that has to be performed again for each pseudo-experiment and hence they are randomly varied according to a normal distribution. The likelihood is fitted to each pseudo-dataset to obtain a distribution of the fitted m_H and μ values that allows the infer of their expected mean and error. The pull distributions are also analysed and constructed according to the asymmetric pull distribution definition in [104] taking into account asymmetric errors calculated by MINOS [105]. The systematic uncertainties are also fitted when including them in the study.

In the following sections results for the pseudo-experiments over the 1D and 2D models with and without systematic uncertainties are shown. In addition, a study at the measured Higgs mass and signal strength is also performed.

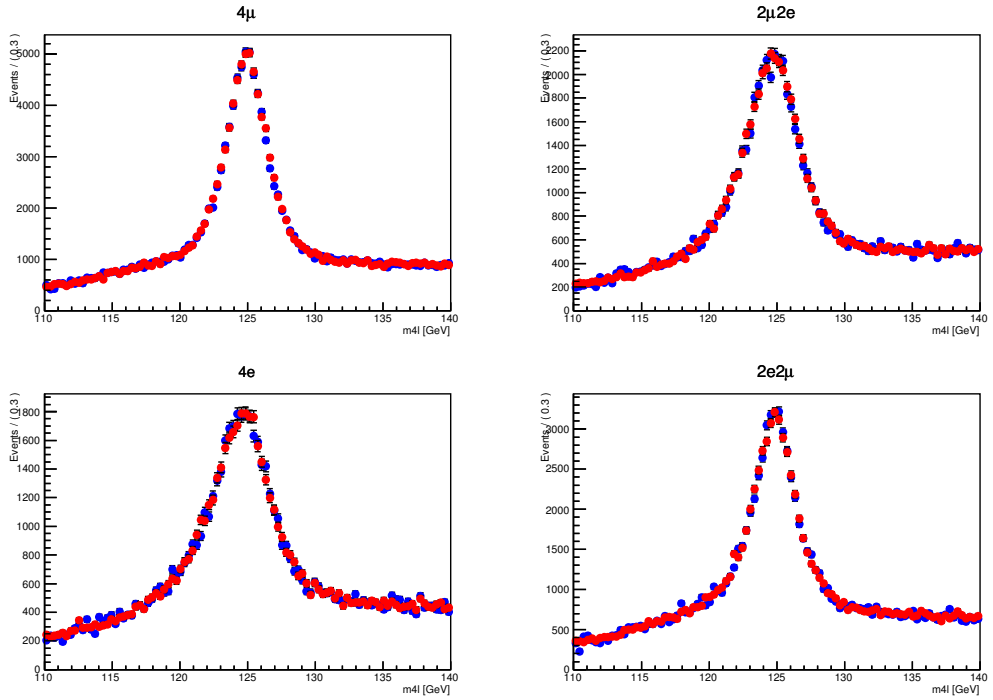

Figure 6.10 Example of a pseudo-dataset with 10000 times the number of expected events, from each pdf component, generated from the MC samples (blue) and from the pdfs (red) for the m_{4l} observable.

Validation of the models without systematic uncertainties

The 1D and 2D models provided do not include the nuisance parameter constraints. The results from the pseudo-experiments on the 8 TeV and 7 + 8 TeV 1D and 2D models, without taking into account the systematic uncertainties, are shown in Tables (6.3) and (6.4).

For both models, the distribution of the fitted m_H values from all the pseudo-experiments is fitted to a Gaussian distribution, see Figure (6.12), with mean values consistent with 125 GeV within fit uncertainties. The uncertainty is reduced, as expected, by 6% and 3% due to the combination of the 7 TeV and 8 TeV models for the 1D and 2D models, respectively. For the 8 TeV 1D and 2D models, the mean of the m_H pull and its width show small deviations from the mean of zero and a width of one. However, this behaviour is gone for the 7 + 8 TeV 1D and 2D models showing that is only a matter of low statistics in the pseudo-datasets.

As an approximation, the μ distributions are also fitted to Gaussian distributions, although the low statistics could indicate that the distribution is Poissonian, see Figure (6.13). For the 8 TeV 1D and 2D models, small biases are seen on the mean μ values and

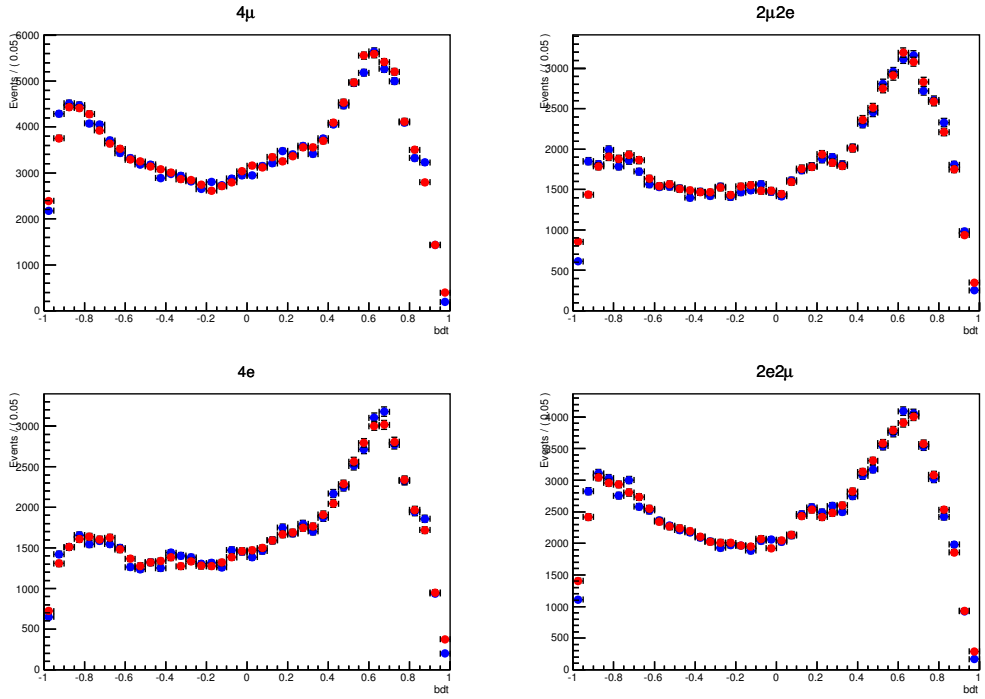

Figure 6.11 Example of a pseudo-dataset with 10000 times the number of expected events, from each pdf component, generated from the MC samples (blue) and from the pdfs (red) for the BDT observable.

	m_H	σ_{m_H}	Pull m_H	
			mean	width
8 TeV	124.98 ± 0.02	0.77 ± 0.02	0.04 ± 0.02	1.03 ± 0.02
7 + 8 TeV	125.00 ± 0.01	0.71 ± 0.01	0.00 ± 0.02	1.01 ± 0.02
	μ	σ_μ	Pull μ	
			mean	width
8 TeV	1.03 ± 0.01	0.31 ± 0.01	-0.08 ± 0.02	0.97 ± 0.02
7 + 8 TeV	1.01 ± 0.01	0.29 ± 0.01	-0.00 ± 0.02	0.99 ± 0.02

Table 6.3 Summary table of the results of a Gaussian fit on m_H and μ and their pull distribution. The fitted m_H and μ values comes from a conditional 1D likelihood fit using pseudo-datasets generated from MC at $m_H = 125$ GeV and $\mu = 1$.

over the pull distributions, indicating a possible overestimation of the error. However, as it was seen on the m_H results, these are all gone for the 7 + 8 TeV 1D and 2D models. Therefore, the model has no biases and behaves as expected.

The odd structures in Figures (6.12) and (6.13) is a binning effect. This was checked by decreasing the number of bins and running pseudo-experiments with high statistics. For both figures these effects went away.

	m_H	σ_{m_H}	Pull m_H	
			mean	width
8 TeV	124.95 ± 0.02	0.72 ± 0.01	0.07 ± 0.02	1.01 ± 0.02
7 + 8 TeV	125.00 ± 0.02	0.69 ± 0.01	0.01 ± 0.02	1.02 ± 0.02
	μ	σ_μ	Pull μ	
			mean	width
8 TeV	1.02 ± 0.01	0.29 ± 0.00	-0.02 ± 0.01	0.96 ± 0.02
7 + 8 TeV	1.01 ± 0.01	0.28 ± 0.00	0.01 ± 0.02	0.98 ± 0.02

Table 6.4 Summary table of the results of a Gaussian fit on m_H and μ and their pull distribution. The fitted m_H and μ values comes from a conditional 2D likelihood fit using pseudo-datasets generated from MC at $m_H = 125$ GeV and $\mu = 1$.

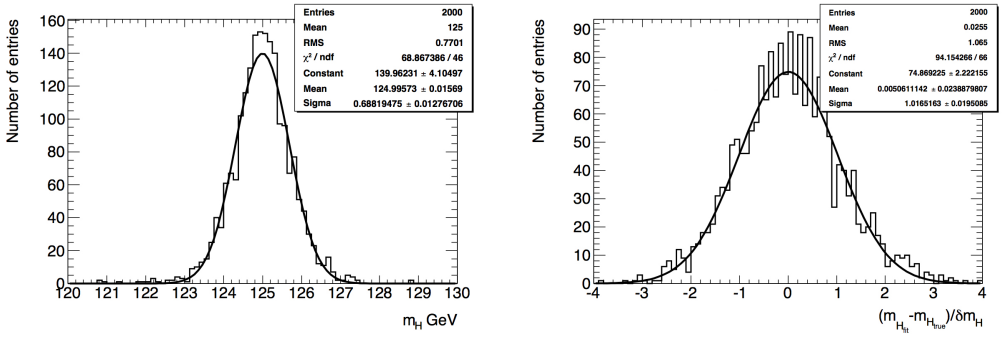

(a) **(b)**

Figure 6.12 (a) The m_H distribution and (b) the pull m_H distribution obtained from 2000 pseudo-experiments for the 7+ 8 TeV 2D model without systematic uncertainties.

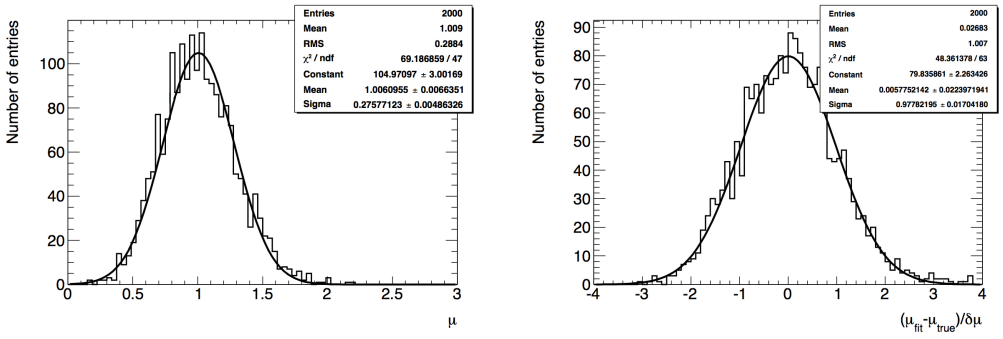

(a) **(b)**

Figure 6.13 (a) The μ distribution and (b) the pull μ distribution obtained from 2000 pseudo-experiments for the 7+ 8 TeV 2D model without systematic uncertainties.

Validation of the models with systematic uncertainties

The results from the pseudo-experiments over the 8 TeV and 7 + 8 TeV 1D and 2D models including the systematic uncertainties are shown in Tables (6.5) and (6.6).

For both the 1D and 2D models, when including the systematic uncertainties, biases appear in the m_H and μ pull distributions, see figures (6.14) and (6.15). The biggest ones appear in the 2D model: the m_H pull distribution has a 2% bias on its width and the μ pull distribution has a 1% bias on its mean value and the width of its pull distribution has a 3% deviation from one. The bias on the μ pull width may indicate an overestimation of the fitted uncertainties in μ of 3%, but also is consistent within 2σ. The deviations could also be due to the model not being correctly constructed or that there are some systematic uncertainties causing the biases.

	m_H	σ_{m_H}	Pull m_H	
			mean	width
8 TeV	124.96 ± 0.02	0.74 ± 0.02	0.02 ± 0.02	1.01 ± 0.02
7 + 8 TeV	124.97 ± 0.02	0.70 ± 0.01	0.04 ± 0.02	1.02 ± 0.02
	μ	σ_μ	Pull μ	
			mean	width
8 TeV	1.02 ± 0.01	0.34 ± 0.01	-0.04 ± 0.02	0.97 ± 0.02
7 + 8 TeV	1.02 ± 0.01	0.30 ± 0.01	0.00 ± 0.02	0.97 ± 0.02

Table 6.5 Summary table of the results of a Gaussian fit on m_H and μ and their pull distribution. The fitted m_H and μ values comes from a conditional 1D likelihood fit using toys generated from MC at $m_H = 125$ GeV and $\mu = 1$.

	m_H	σ_{m_H}	Pull m_H	
			mean	width
8 TeV	124.98 ± 0.02	0.72 ± 0.01	0.02 ± 0.02	1.02 ± 0.02
7 TeV + 8 TeV	125.01 ± 0.02	0.68 ± 0.01	-0.01 ± 0.02	1.02 ± 0.02
	μ	σ_μ	Pull μ	
			mean	width
8 TeV	1.02 ± 0.01	0.32 ± 0.01	0.00 ± 0.02	0.96 ± 0.02
7 TeV + 8 TeV	1.02 ± 0.01	0.30 ± 0.01	0.01 ± 0.02	0.97 ± 0.02

Table 6.6 Summary table of the results of a Gaussian fit on m_H and μ and their pull distribution. The fitted m_H and μ values comes from a conditional 2D likelihood fit using pseudo-datasets generated from MC at $m_H = 125$ GeV and $\mu = 1$.

Figure (6.16) shows the distribution of the fitted values for the two most important systematics for the parameters: the QCD scale uncertainty and the muon momentum scale uncertainty. The QCD scale uncertainty distribution has a mean of 0.00 ± 0.02 and a width of 0.96 ± 0.02 and the momentum scale uncertainty distribution has a mean of 0.00 ± 0.02 with a width of 1.01 ± 0.02. The latter distribution has an approximately Gaussian shape consistent with a mean of zero and a width of one as expected, however the former has a small deviation from the assumed width of one for the Gaussian shape.

To understand the biases, a study adding only one systematic to the 2D model was

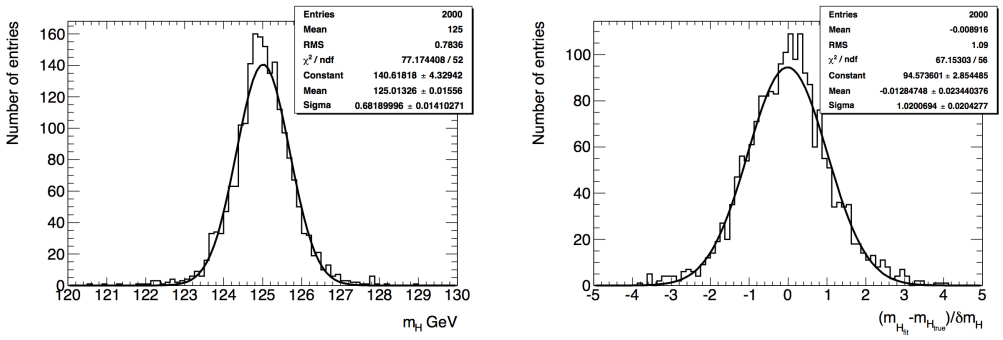

(a) **(b)**

Figure 6.14 (a) m_H distribution and (b) pull m_H distribution obtained from 2000 pseudo-experiments for the 7+8 TeV 2D model with systematic uncertainties.

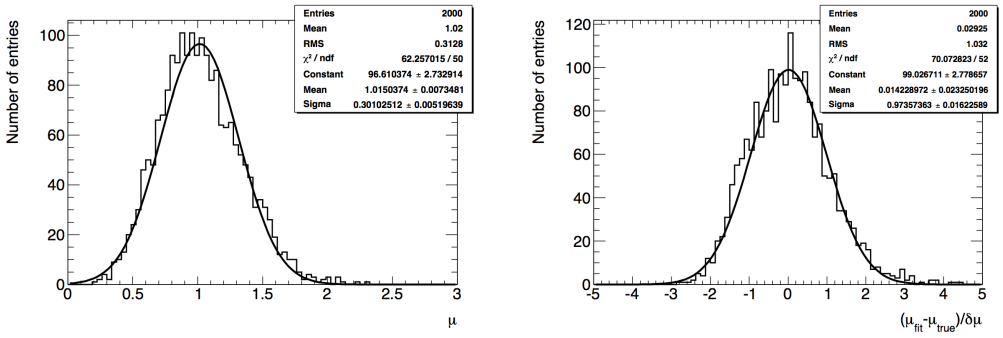

(a) **(b)**

Figure 6.15 (a) μ distribution and (b) pull μ distribution obtained from 2000 pseudo-experiments for the 7+8 TeV 2D model with systematic uncertainties.

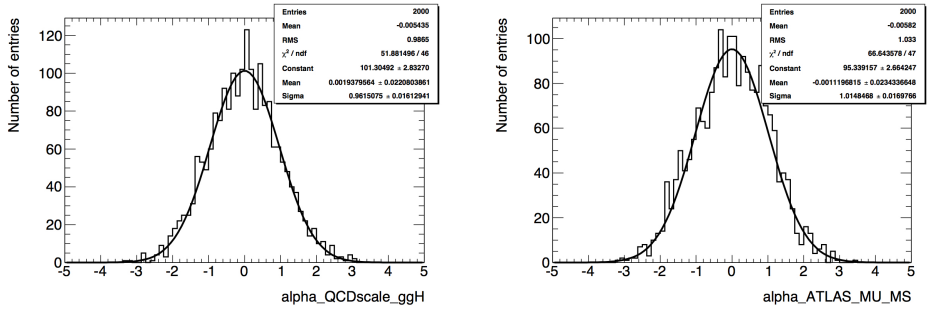

(a) **(b)**

Figure 6.16 Distribution of the fitted values of (a) QCD scale theory uncertainty and (b) muon momentum scale uncertainty obtained from 2000 pseudo-experiments for the 7+8 TeV 2D model including systematic uncertainties. This uncertainties are the ones that have the largest impact on μ and m_H.

performed to see how it affects m_H and μ, followed by repeating this for each systematic uncertainty. The results show that each systematic uncertainty produces more or less the same deviations on m_H and μ indicating that the biases are probably coming

from low statistics in the pseudo-datasets. The nuisance parameters are modelled as Gaussian distributions and this is only true in the asymptotic limit. Therefore, high statistics pseudo-datasets and models were created to study the behaviour of this biases including the systematic uncertainties. The number of events in the pseudo-dataset and the expected number of events from the model were amplified by 1000. The results are shown in Table (6.7), where it can be seen that clearly the biases are all gone in this regime. The fitted μ and its pull distributions is shown in figure (6.17), where the biases seen before are gone and both distributions behave like a Gaussian distribution. The small bias seen in the QCD scale uncertainty is gone and each of the systematic uncertainties distributions are more Gaussian-like than before. Therefore, the models still behave as expected. Since, the biases are all within 2σ of their true values, no corrections were applied.

	m_H	σ_{m_H}	Pull m_H	
			mean	width
7 + 8 TeV 1D model	125.00 ± 0.00	0.02 ± 0.00	0.01 ± 0.02	0.99 ± 0.02
7 + 8 TeV 2D model	125.00 ± 0.00	0.02 ± 0.00	0.01 ± 0.02	0.99 ± 0.02
	μ	σ_μ	Pull μ	
			mean	width
7 + 8 TeV 1D model	1.00 ± 0.00	0.01 ± 0.00	-0.02 ± 0.02	1.00 ± 0.02
7 + 8 TeV 2D model	1.00 ± 0.00	0.01 ± 0.00	0.02 ± 0.02	1.01 ± 0.02

Table 6.7 Summary table of the results of a Gaussian fit on m_H and μ and their pull distribution for pseudo-experiments in the asymptotic limit. The fitted m_H and μ values comes from a conditional 1D and 2D likelihood fits using pseudo-datasets generated from MC at $m_H = 125$ GeV and $\mu = 1$.

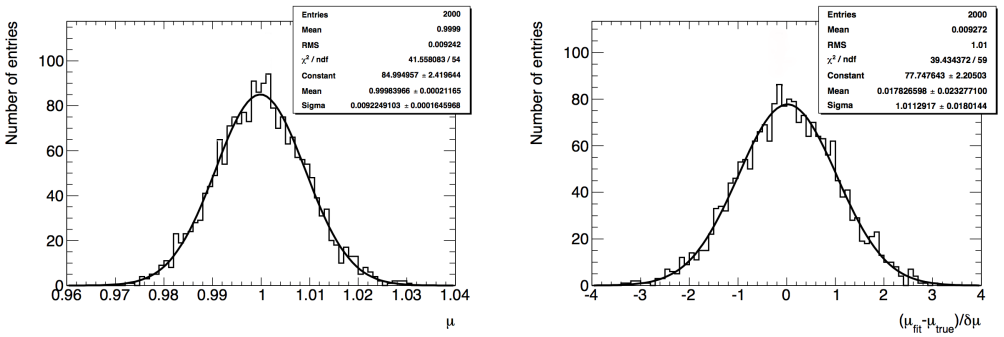

(a) **(b)**

Figure 6.17 (a) μ distribution and (b) pull μ distribution obtained from 2000 pseudo-experiments in the asymptotic limit for the 7 + 8 TeV 2D model including systematic uncertainties.

Pseudo-experiments are also done at the values observed in data with $m_H = 124.51$ GeV and $\mu = 1.64$. For this study, pseudo-datasets are generated directly from the pdfs, and not from MC due to missing the MC sample for this exact Higgs boson mass point. The results are shown in figure (6.18).

The fitted m_H value is 124.52 ± 0.01 GeV, consistent with the input m_H within the uncertainty. The width of the distribution is 0.50 ± 0.01 GeV consistent with the statistical error from Equation (6.3). The fitted μ value is 1.65 ± 0.01, consistent with the input value of μ. The uncertainty in μ is 0.37 ± 0.01 which is also consistent with the statistical uncertainty in Equation(6.4). The pull distributions for both have mean values consistent with zero and widths consistent with one.

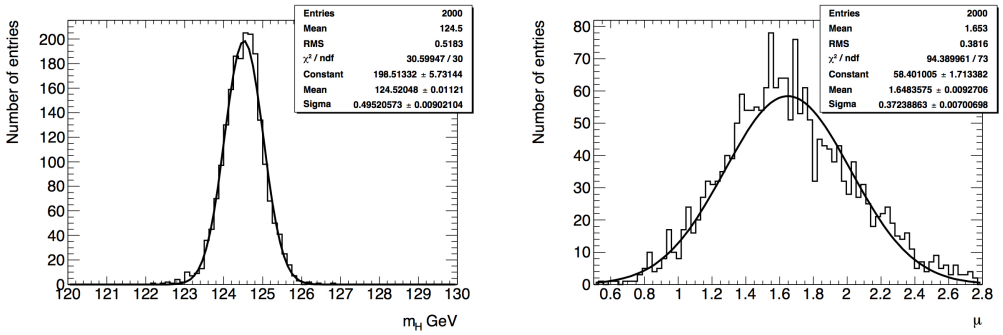

(a) **(b)**

Figure 6.18 (a) m_H and (b) μ distributions obtained from 2000 pseudo-experiments for the 7+8 TeV 2D model for the measured SM Higgs boson mass of 124.51 GeV and signal strength of 1.64.

6.8 Mass and signal strength measurement results

Figure (6.19a) shows the m_{4l} distribution of the selected candidates for the 7 and 8 TeV data samples. Also shown are the expected distributions for a $m_H = 124.5$ GeV signal and the ZZ* and reducible background components. The expected signal is normalised to the signal strength value shown below. Figures (6.19b) and (6.19c) show the BDT_{ZZ^*} output alone and versus m_{4l} for the selected candidates in the mass range $110 < m_{4l} < 140$ GeV.

Table (6.8) shows the expected and observed number of events for the 7 and 8 TeV data samples for the mass range $120 < m_{4l} < 130$ GeV. Total number of observed events is 37 and the expected number of events is of 26.5 ± 1.7.

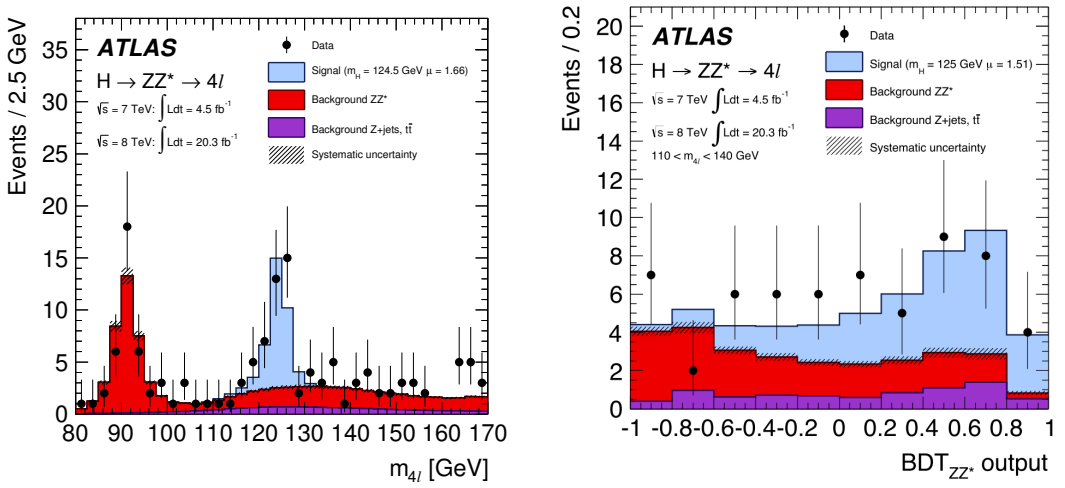

(a) (b)

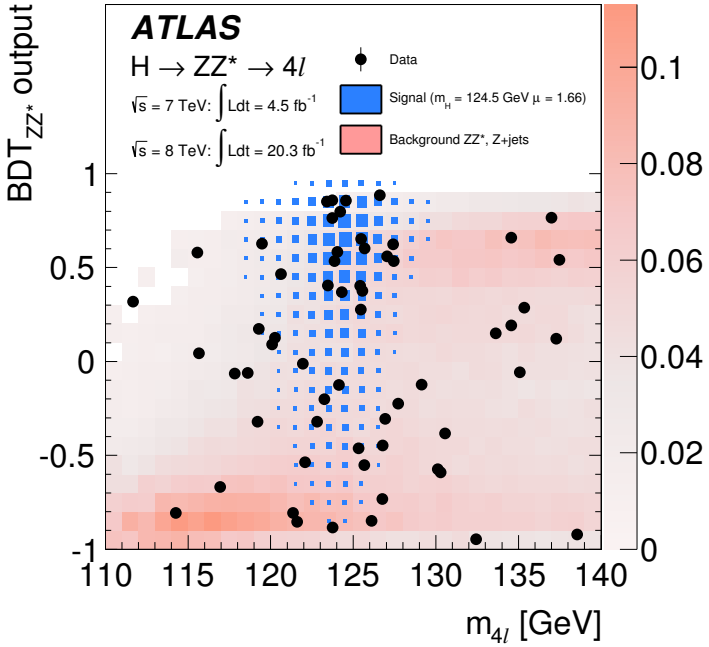

(c)

Figure 6.19 (a) Distribution of the four lepton invariant mass for the selected candidates for $80 < m_{4l} < 170$ GeV. Superimposed are the expected distributions of a SM Higgs boson signal for $m_H = 124.5$ GeV normalised to the measured signal strength, as well as the expected ZZ^* and reducible backgrounds. (b) Distribution of the BDT_{ZZ^*} output for the selected candidates for $110 < m_{4l} < 140$ GeV. The contribution of the reducible background is also separately displayed as well as the systematic uncertainties drawn as a hatched grey area. (c) Distribution of the BDT_{ZZ^*} output vs. m_{4l} for the selected candidates for $110 < m_{4l} < 140$ GeV. The expected distribution for a SM Higgs with $m_H = 124.5$ GeV is indicated by the size of the blue boxes, and the total background is indicated by the intensity of the red shading. All plot used the combined 7 and 8 TeV data samples.

Final state	Signal full mass range	Signal	ZZ^*	Z+jets,$t\bar{t}$	s/b	Expected	Observed
			7 TeV data				
4μ	1.00 ± 0.10	0.91 ± 0.09	0.46 ± 0.02	0.10 ± 0.04	1.7	1.47 ± 0.10	2
$2\mu 2e$	0.50 ± 0.05	0.44 ± 0.04	0.21 ± 0.01	0.36 ± 0.08	0.8	1.01 ± 0.09	1
$4e$	0.46 ± 0.05	0.39 ± 0.04	0.19 ± 0.01	0.40 ± 0.09	0.7	0.98 ± 0.10	1
$2e2\mu$	0.66 ± 0.06	0.58 ± 0.06	0.32 ± 0.02	0.09 ± 0.03	1.5	0.99 ± 0.07	2
Total	2.62 ± 0.26	2.32 ± 0.23	1.17 ± 0.06	0.96 ± 0.18	1.1	4.45 ± 0.30	6
			8TeV data				
4μ	5.80 ± 0.57	5.28 ± 0.52	2.36 ± 0.12	0.69 ± 0.13	1.7	8.33 ± 0.6	12
$2\mu 2e$	3.06 ± 0.31	2.71 ± 0.28	1.17 ± 0.07	0.36 ± 0.08	1.8	4.23 ± 0.30	5
$4e$	2.79 ± 0.29	2.38 ± 0.25	1.03 ± 0.07	0.35 ± 0.07	1.7	3.77 ± 0.27	7
$2e2\mu$	3.92 ± 0.39	3.45 ± 0.34	1.67 ± 0.08	0.60 ± 0.10	1.5	5.72 ± 0.37	7
Total	15.6 ± 1.6	13.8 ± 1.4	6.24 ± 0.34	2.00 ± 0.28	1.7	22.1 ± 1.5	31
			7 and 8 TeV data				
4μ	6.80 ± 0.67	6.20 ± 0.61	2.82 ± 0.14	0.79 ± 0.13	1.7	9.81 ± 0.64	14
$2\mu 2e$	3.56 ± 0.36	3.15 ± 0.32	1.38 ± 0.08	0.72 ± 0.12	1.5	5.24 ± 0.35	6
$4e$	3.25 ± 0.34	2.77 ± 0.29	1.2 ± 0.08	0.76 ± 0.11	1.4	4.75 ± 0.32	8
$2e2\mu$	4.58 ± 0.45	4.04 ± 0.40	1.99 ± 0.10	0.69 ± 0.11	1.5	6.72 ± 0.42	9
Total	18.2 ± 1.8	16.2 ± 1.6	7.41 ± 0.40	2.95 ± 0.33	1.6	26.5 ± 1.7	37

Table 6.8 The number of expected and observed events for a $m_H = 125$ GeV hypothesis for the four lepton final states. The second column shows the number of expected signal events for the full mass range. The other columns show the number of expected signal events, the number of ZZ^* and reducible background events, the signal to background ratio (s/b) and the number of observed events in the mass range of $120 < m_{4l} < 130$ GeV for the 7 and 8 TeV data as well as for the combined sample.

Using the conditional 2D model, described in Section (6.6), the final result of the fit to the 7 and 8 TeV data combined is:

$$m_H = 124.51 \pm 0.52(\text{stat}) \pm 0.06(\text{syst}) \text{ GeV}, \tag{6.3}$$

$$\mu = 1.64 \pm 0.38(\text{stat}) \pm 0.18(\text{syst}), \tag{6.4}$$

where μ is the signal strength parameter defined as the ratio of the measured Higgs boson production cross-section and the Higgs boson production cross-section predicted by the Standard Model for a Higgs boson mass m_H. The μ value is consistent with the SM expectation of one.

The Higgs boson masses obtained with the 2D model in the 4 different final states and after combination of the final states, with and without systematics, are summarised in Table (6.9).

Figure (6.20) shows the scan of the profile likelihood ($-2\ln\Lambda(m_H)$), where Λ is defined in Equation (4.6), for the 2D model as a function of the Higgs boson mass for the four

final states, as well as for all the final states combined. The signal strength and all the nuisance parameters are allowed to float to the values that maximise the likelihood in the scan. The compatibility among the mass measurements in the four individual final states was studied and it was found to be compatible to within about 20%.

	$\mathbf{m_H}$[GeV]		$\boldsymbol{\mu}$	
7 TeV	no syst.	with syst.	no syst.	with syst.
4μ	$124.98^{+1.90}_{-2.75}$	$125.00^{+1.88}_{-2.77}$	$1.56^{+2.75}_{-1.18}$	$1.55^{+2.77}_{-1.17}$
$2\mu 2e$	$125.01^{+2.93}_{-2.25}$	$125.01^{+2.90}_{-2.22}$	$1.52^{+2.85}_{-1.41}$	$1.53^{+2.88}_{-1.41}$
$4e$	$123.20^{+2.56}_{-2.86}$	$123.20^{+2.55}_{-2.85}$	$2.51^{+4.64}_{-2.17}$	$2.53^{+4.69}_{-2.19}$
$2e2\mu$	$126.35^{+2.12}_{-2.42}$	$126.35^{+2.12}_{-2.42}$	$2.23^{+2.35}_{-1.43}$	$2.23^{+2.39}_{-1.44}$
Combined	$124.85^{+1.24}_{-1.16}$	$124.84^{+1.24}_{-1.16}$	$1.77^{+1.18}_{-0.84}$	$1.77^{+1.21}_{-0.85}$
8 TeV				
4μ	$124.18^{+0.83}_{-0.92}$	$124.18^{+0.83}_{-0.93}$	$1.41^{+0.69}_{-0.54}$	$1.41^{+0.72}_{-0.55}$
$2\mu 2e$	$122.49^{+1.47}_{-1.89}$	$122.50^{+1.46}_{-0.91}$	$2.56^{+1.53}_{-1.14}$	$2.55^{+1.58}_{-1.15}$
$4e$	$126.31^{+1.20}_{-1.18}$	$126.32^{+1.20}_{-1.19}$	$1.73^{+1.00}_{-0.73}$	$1.73^{+1.04}_{-0.74}$
$2e2\mu$	$124.62^{+0.86}_{-0.77}$	$124.62^{+0.86}_{-0.77}$	$1.83^{+0.92}_{-0.72}$	$1.82^{+0.97}_{-0.73}$
Combined	$124.42^{+0.60}_{-0.54}$	$124.42^{+0.60}_{-0.54}$	$1.66^{+0.43}_{-0.38}$	$1.65^{+0.48}_{-0.40}$
7 TeV + 8 TeV				
4μ	$124.25^{+0.81}_{-0.84}$	$124.25^{+0.81}_{-0.84}$	$1.47^{+0.66}_{-0.52}$	$1.47^{+0.69}_{-0.53}$
$2\mu 2e$	$122.49^{+1.47}_{-1.89}$	$122.50^{+1.46}_{-1.91}$	$2.00^{+1.63}_{-0.91}$	$1.99^{+1.67}_{-0.92}$
$4e$	$124.18^{+0.83}_{-0.92}$	$124.18^{+0.83}_{-0.93}$	$1.72^{+0.95}_{-0.72}$	$1.72^{+0.99}_{-0.73}$
$2e2\mu$	$124.18^{+0.83}_{-0.92}$	$124.18^{+0.83}_{-0.93}$	$1.82^{+0.84}_{-0.66}$	$1.83^{+0.88}_{-0.67}$
Combined	$124.51^{+0.53}_{-0.51}$	$124.51^{+0.54}_{-0.51}$	$1.67^{+0.40}_{-0.35}$	$1.66^{+0.45}_{-0.38}$

Table 6.9 Measured Higgs boson masses and signal strengths in the different final states and after combination as obtained from the 2D conditional model using the 7 TeV and 8 TeV datasets.

6.8.1 The systematic uncertainty

The systematic uncertainty is calculated as:

$$\sigma^2_{syst} = \sigma^2_{tot} - \sigma^2_{stat}, \tag{6.5}$$

where σ_{tot} is the uncertainty obtained from fitting the data to the model including the systematic uncertainties and σ_{stat} is the uncertainty obtained from fitting the data to the model without the systematic uncertainties.

The SM Higgs boson mass in the $H \rightarrow ZZ^{(*)} \rightarrow 4l$ decay channel value has a predominantly statistical uncertainty with a nearly negligible contribution from the systematic uncertainties, reduced by a factor of approximately 8 with respect to

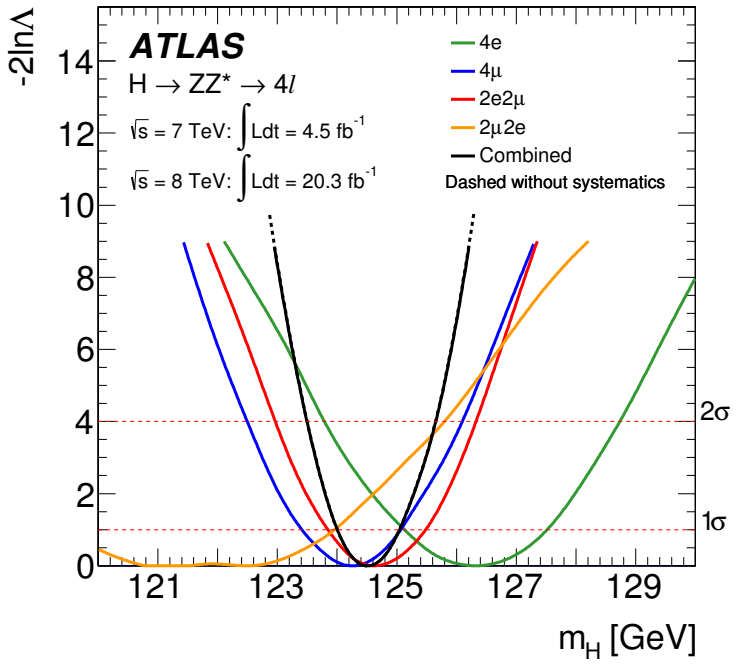

Figure 6.20 The profile likelihood as a function of m_H for the combination of all $H \to ZZ^* \to 4l$ final states and for the individual final states for the combined 7 and 8 TeV data samples. The combined result is shown both with and without systematics (solid and dashed line). The two are almost indistinguishable.

previous results, where the measured mass was $m_H = 124.3^{+0.6}_{-0.5}(\text{stat})^{+0.5}_{-0.3}$ [57]. This is due mainly to improvements on the uncertainties on the electron and muon energy scales [40]. A cross-check was done for the m_H systematic uncertainty, calculating the uncertainty by summing in quadrature all the individual contributions from each nuisance parameter, see Table (6.1). This gives a systematic uncertainty of 45 MeV which is consistent with the observed calculated uncertainty of 60 MeV.

The contributions of the nuisance parameters to m_H are given in Table (6.1) for the individual final states and combined for the 7 and 8 TeV dataset. For completeness, the contributions of the nuisance parameters to μ are given in Table (6.2) for the individual final states and combined for the 7 and 8 TeV dataset.

Chapter 7

Search for an additional heavy Higgs boson in the $H \to ZZ^{(*)} \to 4l$ channel

A search for a heavy Higgs boson is presented. The results of the search are interpreted in the scenario of a heavy Higgs boson with a width that is small compared with the experimental mass resolution. The Higgs boson mass range goes from 140 GeV to 1 TeV. No significant excess of events over the SM prediction is found. A simultaneous fit gives 95% confidence level upper limits on the production cross-section of the heavy Higgs times the branching ratio to Z boson pairs. The results are also interpreted in the context of the Type I and Type II 2HDMs.

The following sections will explain this analysis in detail. The interpretation of the results in the Type I and Type II 2HDM were done in a combined analysis, including in addition the $H \to ZZ \to l^+l^-\nu\bar{\nu}$, $H \to ZZ \to l^+l^-q\bar{q}$ and $H \to ZZ \to \nu\bar{\nu}q\bar{q}$ decay modes. An overview of this analysis will be given. For full details see [41].

7.1 Data samples

The collision data used in this search were collected by ATLAS at a centre-of-mass energy of $\sqrt{s} = 8$ TeV during 2012 and correspond to an integrated luminosity of 20.3 fb^{-1}. The following subsections will describe the MC signal and background samples used for this analysis.

7.1.1 Monte Carlo samples

Events for signal and background processes are generated using Monte Carlo simulators. Full simulation of each event is performed using the ATLAS detector simulation [58] within the GEANT4 framework [59]. Also, some samples, used a fast simulation based on a parameterisation of the performance of the ATLAS electromagnetic and hadronic calorimeters [106] and GEANT4 elsewhere. Additional pp interactions in the same and nearby bunch crossings (pile-up) are included in the simulation. Corrections are applied to the simulated samples to reproduce the observed data to account for differences of the lepton trigger and reconstruction efficiencies, and for the efficiency and misidentification rate of b-hadrons.

Interference effects

For a Higgs boson with a large width, the production cross-section as well as the kinematic variables are affected by the interference between the signal and non-resonant VV background production, where V stands for either a W or a Z boson. The impact of the interference increases with increasing Higgs width becoming not negligible for $\Gamma_H \geq 10$ GeV, which corresponds to a mass $m_H \geq 400$ GeV in the SM case [107, 108]. To avoid interference effects over the full mass range, the Narrow Width Approximation (NWA) [109, 110] is used for the signal samples, where the propagator becomes:

$$\frac{1}{(m_{4l}^2 - m_H^2)^2 + m_H^2\Gamma_H^2} \approx \frac{\pi}{m_H\Gamma_H}\delta(m_{4l}^2 - m_H^2). \tag{7.1}$$

The approximation in Equation (7.1) holds if the total width of the particle is much smaller than its mass ($\Gamma_H << m_H$), the daughter particles are much less massive than the parent and the scattering energy is much larger than the parent mass ($\sqrt{s} >> m_H$). Even though this approximation is not valid for lower Higgs masses, it is still a good one for higher Higgs masses where a heavier Higgs boson (not from the SM) could be expected. Therefore, to avoid interference effects with the non-resonant VV background the NWA approximation is still chosen for the whole mass range of this search.

Another source of interference in this search is the Higgs boson experimentally observed at $m_h = 125$ GeV. The main interference effect is between the ggF light Higgs production mechanism and the $gg \to ZZ^{(*)}$ continuum process and with a much smaller effect between the VBF light Higgs production and the $q\bar{q} \to ZZ^{(*)}$ process. Figure (7.1) shows the comparison of the m_{4l} spectrum for $2e2\mu$ events with and without

the contribution of the light Higgs. Both interference effects were included in these background MC samples, more details are in the following subsections.

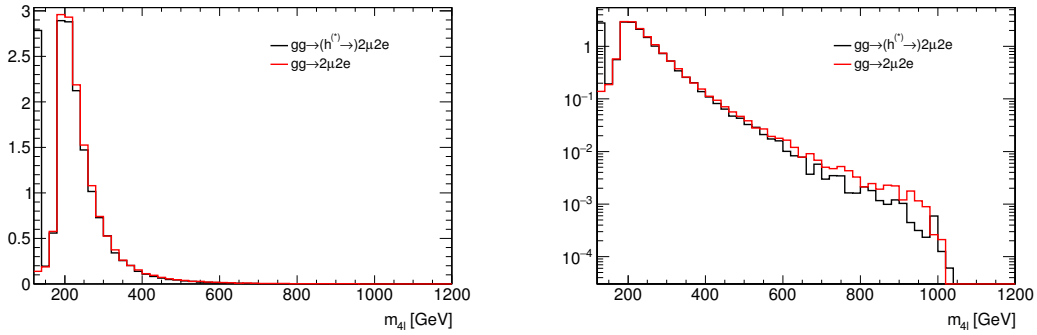

(a) **(b)**

Figure 7.1 The m_{4l} spectrum for the $gg \to ZZ$ process, comparing the expected spectrum with (black line) and without (red line) the light Higgs boson effect at $m_h = 125$ GeV, shown on (a) linear and (b) log scale.

Signal

The $H \to ZZ^{(*)} \to 4l$ signal is modelled using the POWHEG event generator [60, 61] which calculates separately the ggF and VBF production mechanisms up to NLO in α_s. The generated signal events are hadronized with PYTHIA 8.165 with NLO CT10 PDF set [63] using the AU2 set of tunable parameters for the underlying event. The associated production of Higgs bosons with a W or Z boson is significant for $m_H < 200$ GeV. It is therefore included as a signal process and simulated using PYTHIA 8 with the LO CTEQ6L1 PDF set [111] and the AU2 parameter set.

As mentioned in the previous Section, for $m_H > 300$ GeV, the Higgs lineshape is made from a Narrow Width Approximation (NWA). The Higgs is modelled with a Breit-Wigner distribution with a width of 4.07 MeV. For the VH samples, the SM width was assumed because is still very narrow.

The gluon-gluon fusion (ggF) samples:

- $140 < m_H \leq 200$ GeV generated in steps of 10 GeV.
- $200 < m_H \leq 300$ GeV generated in steps of 20 GeV.
- $300 < m_H \leq 600$ GeV generated in steps of 20 GeV.
- $600 < m_H \leq 1000$ GeV generated in steps of 50 GeV.

The vector boson fusion (VBF) samples:

- $140 < m_H \leq 200$ GeV generated in steps of 10 GeV.
- $200 < m_H \leq 300$ GeV generated in steps of 20 GeV.
- $300 < m_H \leq 600$ GeV generated in steps of 25 GeV.
- $600 < m_H \leq 1000$ GeV generated in steps of 50 GeV.

The associated production (ZH and WH) samples:

- $140 < m_H \leq 200$ GeV generated in steps of 5 GeV.
- $200 < m_H \leq 280$ GeV generated in steps of 20 GeV.

The uncertainty in the experimental acceptance for the Higgs boson signal models due to the modelling of Higgs boson production is estimated including QCD scale, PDF and ISR/FSR uncertainty effects, see details in Section (6.1.2). It is found to vary from 0.7% to 10% for the ggF production mode and from 0.5% to 5% for the VH production mechanism.

A search in the context of the Type I and Type II 2HDMs [15] is also presented. The production cross-sections for both ggF and VBF processes are calculated using SusHi 1.3.0 [112]. The branching ratios are calculated with 2HDMC 1.6.4 [113] and it was assumed that $m_A = m_H = m_{H^\pm}$, $m_h = 125$ GeV and $m_{12}^2 = m_A^2 \tan\beta/(1 + \tan\beta^2)$.

The width of the heavy Higgs boson varies over the 2HDM model parameter space and it may be significant compared to the experimental resolution. This analysis assumes a narrow width signal, therefore the 2HDM interpretations are limited to certain regions of the parameter space where the width is less that 0.5% of m_H. Another aspect to have in mind is the off-shell contribution from the light Higgs boson and its interference with the ZZ background. This contribution varies over the 2HDM model parameter space as well because the light Higgs boson couplings change from their SM values. Therefore, the interpretation is further limited to regions where the light Higgs couplings are changed by less than a factor of three from their SM values (in these regions the variation is found to have a negligible effect on the exclusion limits).

Background

The background processes that have four leptons in their final state are described in Section (5.1). There is an additional background contribution in this analysis coming from the Higgs boson experimentally observed at $m_h = 125$ GeV (light Higgs) through off-shell events and, as mentioned before, through its interference with the $q\bar{q} \to ZZ^{(*)}$ and $gg \to ZZ^{(*)}$ background processes.

The $\mathbf{q\bar{q} \to ZZ^{(*)}}$ **background** is modelled using POWHEG [94] which is NLO in α_S, using a renormalisation and factorisation scale of m_{ZZ} and the CT10 NLO PDF set. For hadronization and showering PYTHIA 8 [63] is used. A K-factor was applied to normalise to the NNLO calculation of [114]. The K-factor increases the cross-section in the high mass region by approximately 4% compared to the NLO calculation. The EW $q\bar{q} \to ZZ^{(*)} + 2j$ background down to $O(\alpha_W^6)$ plus the VBF light Higgs background and their interference is generated using MadGraph 5 plus Pythia 6 with PDF set CTEQ611 and scale set to m_W. The total number of expected background events of this process is 2.30 in the VBF category (events grouped by VBF production mechanism), 0.46 in the ggF 4μ, 0.28 in the ggF $4e$, 0.35 in the ggF $2e2\mu$, 0.30 in the ggF $2\mu 2e$ (events grouped by the ggF production mechanism with final states 4μ, $4e$, $2e2\mu$ and $2\mu 2e$) and 0.45 in the VH category (events grouped by the associated production of the Higgs boson with Z or W boson). In the fit this contribution is included in the total $q\bar{q} \to ZZ^{(*)}$background.

The PDF and α_s uncertainties on the $q\bar{q} \to ZZ^{(*)}$background are parametrised as a function of m_{4l} as recommended in [11]. They give an overall normalisation uncertainty of $\pm 3\%$. The QCD scale uncertainty gives an overall normalisation uncertainty of $\pm 4\%$. An additional uncertainty arises from the NLO EW corrections applied giving a normalisation uncertainty of 0.5% (2.6%, 1.9%) for ggF (VBF, VH) categories. The normalisation uncertainties on the acceptance of the different categories due to theoretical uncertainties are found to be 8% for the VBF category, 3% in the VH category and 4% in the ggF category.

The $\mathbf{gg \to ZZ^{(*)}}$ **background**, the ggF light Higgs background and their interference is generated to LO accuracy using MCFM [115] interfaced with PYTHIA 8 [63] for hadronisation and showering. The CT10 NNLO PDF set is used. The samples are corrected to NNLO as a function of m_{ZZ} [116] using the procedure as described in [117].

The PDF and α_s scale uncertainties on the $gg \to ZZ^{(*)}$background are parameterised

as a function of m_{4l} as well. They give an overall uncertainty of 8%. The QCD scale uncertainty gives an overall uncertainty of ±100%. The normalisation uncertainties in the acceptance are 92% for the VBF category, 91% for the VH category and 14% for the ggF category.

The Z+jets and the $t\bar{t}$ background MC samples are obtained as described in Section (6.1.2).

7.2 Event categorisation

Events passing the event selection described in Section (5.2) are organised according to their production mechanism as: ggF, VBF and VH categories. The selection is made in such a way that the events appear in one category only. This is shown in Figure (7.2), events are first tested for VBF properties, if the event passes it is assigned to the VBF category. If the event fails, then it is tested for the hadronic or leptonic VH criteria. If the event passes it is assigned to the VH category. Any remaining events are assigned to the ggF category.

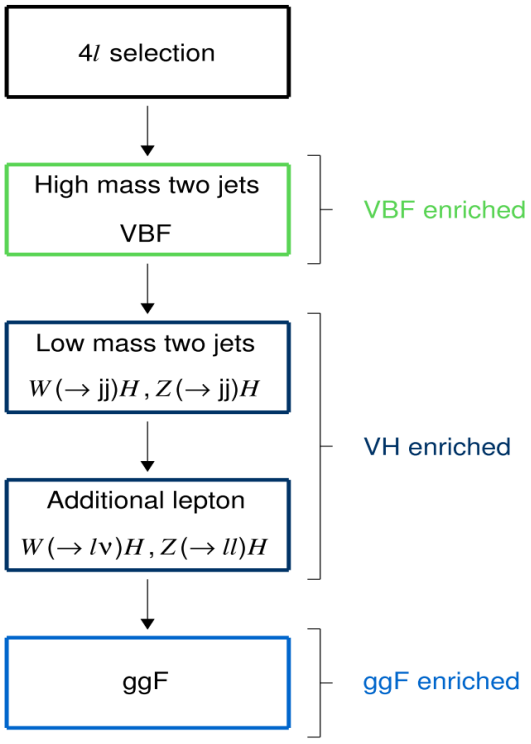

Figure 7.2 Schematic figure of the event categorisation.

The **VBF** selection criteria is:

1. Higgs candidates must be accompanied by two energetic jets with $p_{\mathrm{T}} > 25$ GeV and $|\eta| < 2.5$ or $p_{\mathrm{T}} > 30$ GeV and $2.5 < |\eta| < 4.5$. If more than two jets pass, the two highest p_{T} jets are tagged as VBF jets.
2. The invariant mass of the di-jet system has to be greater than 130 GeV.

The W or Z bosons associated with the Higgs candidates may decay into leptons or hadrons. Dedicated selections are employed for hadronic or leptonic decay, but both types of events are placed in the same VH category.

The **Hadronic VH** events are characterised by the vector boson invariant mass distribution peaking at $m_Z = 91.2$ GeV or $m_{W^{\pm}} = 80.4$ GeV. Therefore, the di-jet system in the event is required to have an invariant mass between $40 - 130$ GeV.

The **Leptonic VH** events are characterised by the presence of at least one extra lepton (electron or muon) in the event in addition to the four leptons used to reconstruct the Higgs candidate. For background rejection, this lepton is required to pass the standard identification criteria described in Sections (5.2.5) and (5.2.3), have a $p_{\mathrm{T}} > 8$ GeV and satisfy the same event selection criteria as for the leptons of the Higgs decay, see Section (5.2.7).

All remaining candidates that do not pass the criteria for VBF and VH categories are assigned to the ggF category. Due to differing background compositions and signal resolutions, events in the ggF category are further classified into subchannels according to their final state: $4e$, $2e2\mu$, 4μ and $2\mu2e$. The m_{4l} distributions for the three categories are shown in Figure (7.3).

7.3 Irreducible background modelling

In previous versions of this analysis, modelling the impact of limited MC statistics was deemed unnecessary, but this approach is no longer tenable, in particular for certain low statistics Higgs boson signal MC samples. In order to model the statistical uncertainties, an additional technique is introduced to reduce the number of bins in the input distribution (the MC statistical uncertainties require one nuisance parameter per bin which can be very large resulting in a fit with too many parameters). This technique is based on the adaptive kernel width function, see Section (6.2), to obtain a variable binning. The idea is that every m_{4l} event, which has more or less the same kernel width

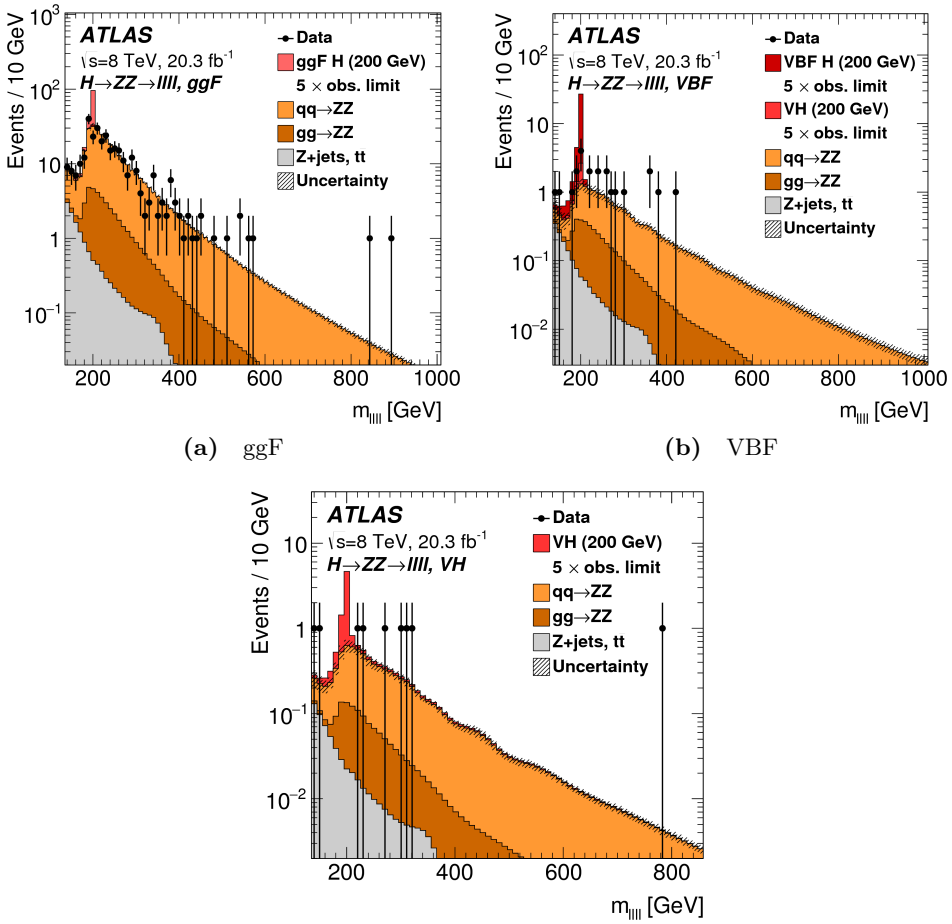

(a) ggF **(b)** VBF

(c) VH

Figure 7.3 The distributions used in the likelihood fit of the four-lepton invariant mass m_{4l} for the $H \to ZZ^{(*)} \to 4l$ search in the (a) ggF, (b) VBF and (c) VH categories. The Z+jets and $t\bar{t}$ entry includes all backgrounds other that ZZ, as measured from data. No events are observed beyond the upper limit of the plots. The simulated $m_H = 200$ GeV signal is normalized to a cross-section corresponding to five times the observed limit. Both the VBF and the VH signal modes are shown in (b) as there is a significant contamination of VH events in the VBF category [41].

values, will be grouped in the same bin. The adaptive binning gives smaller bins in areas where there are more events, which in general tend to be more important regions of the distribution. The assigned size of the bin is equal or smaller than the smallest adaptive width of the group. It is found that for the ZZ backgrounds the adaptive binning algorithm uses between 40 and 100 bins to model the m_{4l} distribution, which is much smaller than the 1000 bins that would have to be used without the adaptive binning assuming 1 GeV bins in the m_{4l} range.

The new MC samples are given to the KEYS algorithm to obtain the new smoothed distribution, see Section (6.2). The resulting distributions are shown in Figures (7.4) and (7.5) for the $q\bar{q} \to ZZ^{(*)}$ and the $gg \to ZZ^{(*)}$ backgrounds, respectively. The

bin boundaries used in the adaptive binning are indicated with red lines and the light blue band are the MC statistical uncertainties that are included in the final fit. The resulting pdfs are seen to be smooth and to describe the input MC well.

7.4 Reducible background estimation and modelling

To estimate the reducible background, the same approach as in Section (5.4) was used. The contribution of this background for $m_{4l} > 140$ GeV is found to be 4% of the total background.

The same sources of uncertainties as in the earlier mass measurement analysis are evaluated here. A summary of the reducible background estimates are shown in Table (7.1). For the $ll\mu\mu$ background, the uncertainty is 21% in the ggF channel, 100% in the VBF channel and 62% in the VH channel. For the $llee$ background, the uncertainty is 27% in the ggF channel, 117% in the VBF channel and 79% in the VH channel. The large uncertainties in the VBF channel are due to large statistical uncertainties on the fraction of Z+jets events falling in this channel. Uncertainties in the expected m_{4l} shape are estimated from differences in the shapes obtained using different methods for estimating the background. The same smoothing technique as described in the previous section is used for the reducible background and the distributions are the same as shown in Figure (6.6) from Chapter 6.

Channel	**ggF**	**VBF**	**VH**
$ll + \mu\mu$	4.60 ± 0.96	0.6 ± 0.6	0.15 ± 0.09
$ll + ee$	2.87 ± 0.79	0.36 ± 0.42	0.19 ± 0.15

Table 7.1 Summary of the reducible background estimates for $140 < m_{4l} < 1000$ GeV. The quoted uncertainties include the combined statistical and systematic components.

7.5 Signal modelling

The same smoothing technique as for the background is used. Figure (7.6) shows the smoothed m_{4l} pdfs obtained with the KEYS pdfs for the $m_H = 300$ GeV MC sample for the ggF production mechanism. The light blue band indicates the statistical uncertainty on the pdf.

As in the mass measurement analysis, only discrete values of m_H are available in the MC samples. A different method was used to obtain the distributions at m_H values

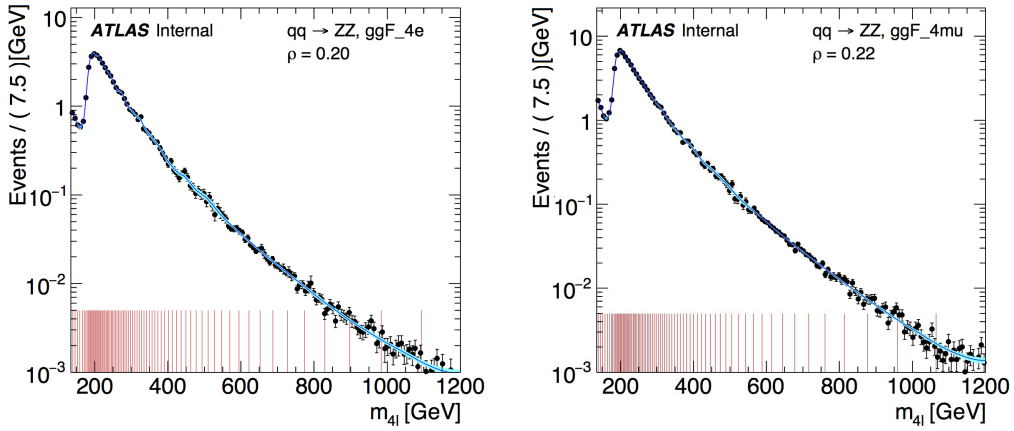

(a) ggF $4e$

(b) ggF 4μ

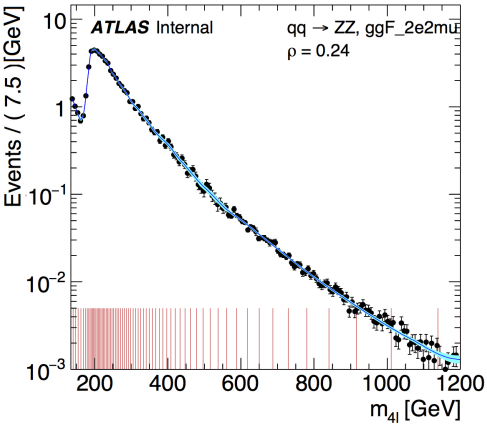

(c) ggF $2e2\mu$

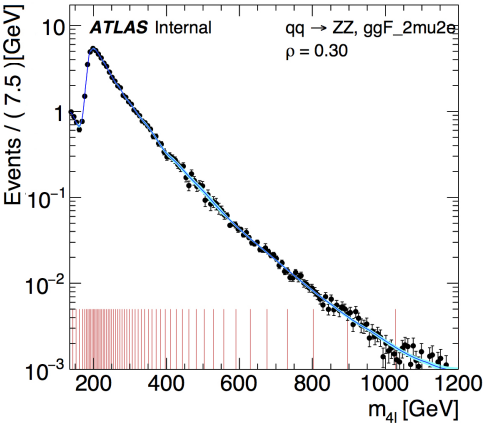

(d) ggF $2\mu2e$

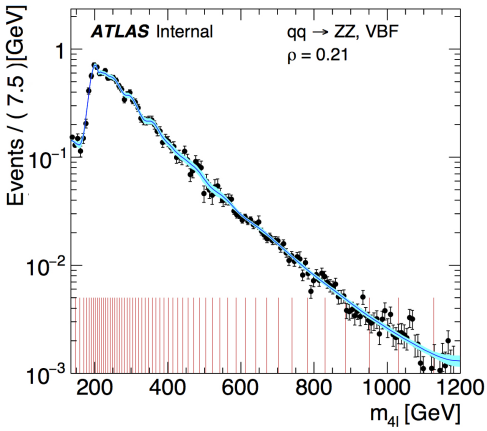

(e) VBF

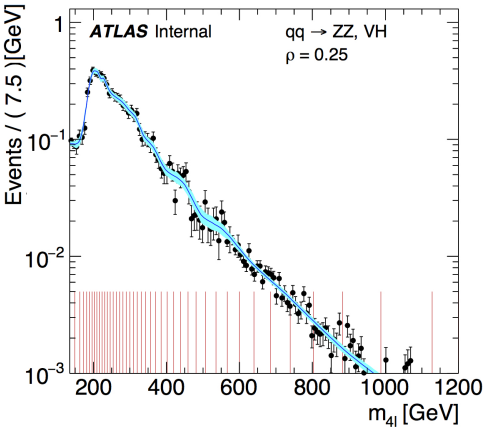

(f) VH

Figure 7.4 Smoothed KEYS pdf for the $q\bar{q} \to ZZ^{(*)}$ background compared with the generated MC events. The light blue band indicates the MC statistical uncertainty. The red lines show the boundaries of the bins used in the adaptive binning procedure.

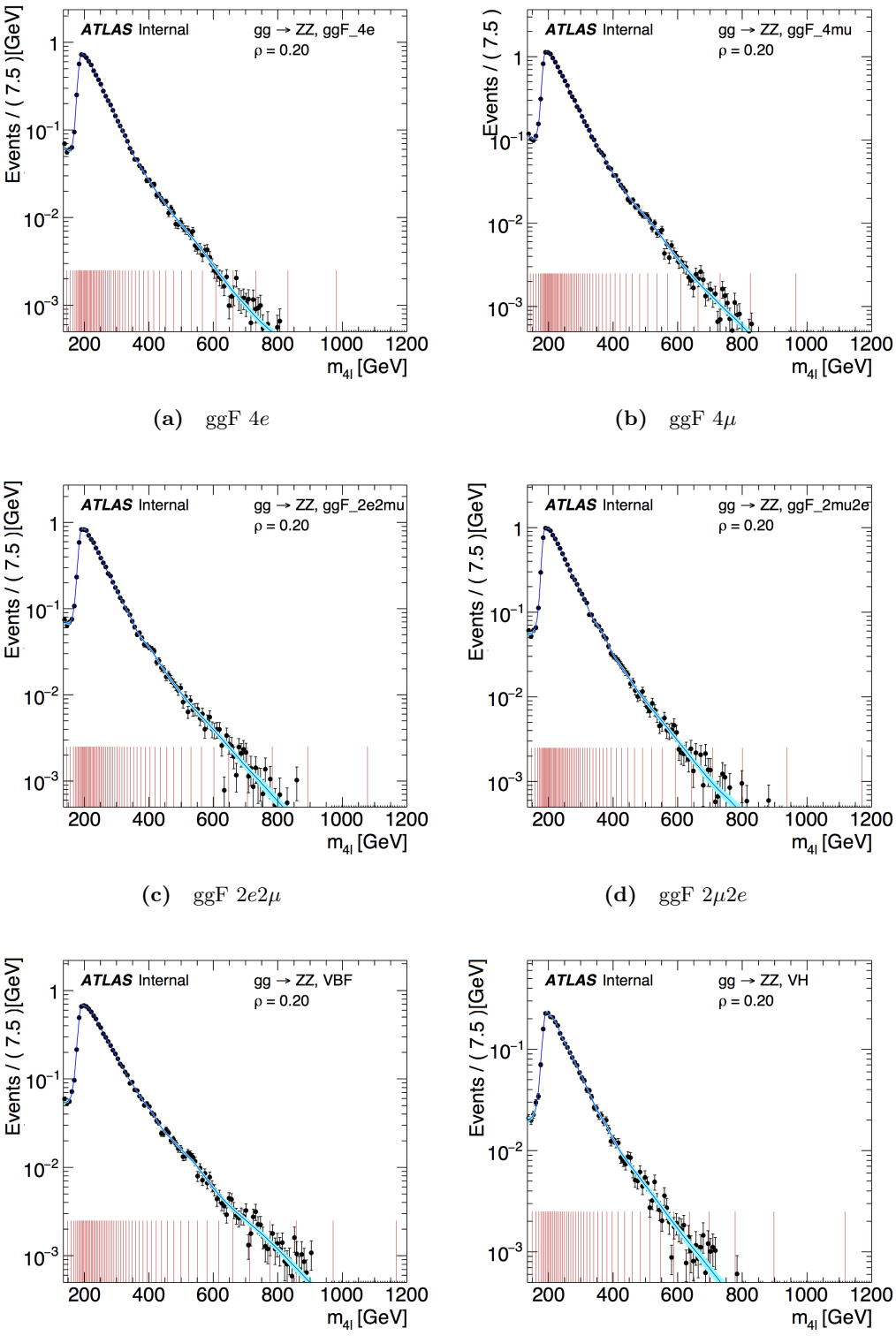

(a) ggF $4e$ **(b)** ggF 4μ

(c) ggF $2e2\mu$ **(d)** ggF $2\mu2e$

(e) VBF **(f)** VH

Figure 7.5 Smoothed KEYS pdf for the $gg \to ZZ^{(*)}$ background compared with the generated MC events. The light blue band indicates the MC statistical uncertainty. The red lines show the boundaries of the bins used in the adaptive binning procedure.

in between the available samples by using the moment-morphing method [118], where instead of using B-Spline functions for each m_H point a parametric approximation function for an arbitrary m_H is constructed. Figure (7.7) shows the resulting pdfs for the ggF production mechanism as a function of m_H in 50 GeV steps for $m_H > 300$ GeV, where the pdfs are normalised to 1. The decreasing behaviour of the peaks of the distributions is due to the same reason as explained in Section (6.2.2), however the $\sigma \times BR$ of the Higgs boson in this mass range decreases, see Figure (2.6). Therefore the number of expected events decreases at higher Higgs masses, this effect is also shown in Figure (7.8). There are distributions peaking a bit lower than the next one, for example in Figure (7.7a) at 250 GeV, this is a normalisation effect.

The number of expected events used is obtained by multiplying the acceptance by the SM Higgs cross-section and branching ratios calculated by the LHC Higgs Cross Section working group [9]. The acceptance is estimated using the same MC samples as the signal shapes and defined as the fraction of generated $H \to ZZ^{(*)} \to 4l$ events that pass the selection and categorisation criteria. The acceptance for intermediate m_H values is obtained using a B-Spline, see Section (6.2) to interpolate between the yields from neighbouring signal samples. The resulting expected signal yields are shown in Figure (7.8). The shaded bands indicate the MC statistical uncertainty.

7.6 Systematic uncertainties

The same sources of systematic uncertainties mentioned in Section (6.5) are considered for signal and background in this analysis. In addition, other systematic uncertainties were considered and they can be grouped as follows:

Jet energy scale: jets are used to categorise events in this analysis. The most relevant uncertainties are those associated with insitu calibration techniques, flavour composition, the difference in response between quark-initiated and gluon-initiated jets and those due to pile up. For a Higgs boson mass of $m_H = 400$ GeV the total uncertainty on m_{4l} is approximately 2.5% for the ggF category and 8%(7.6%) for the VBF(VH) category.

Theory uncertainties: for the irreducible ZZ background, PDF and QCD scale uncertainties give rise to uncertainties on the overall normalisation, the shape of m_{4l} distribution and the acceptance of the different categories. For signal, theoretical uncertainties on the acceptance of the event selection and the categorisation are taken into account. They are described in Sections (7.1.1) and (7.1.1).

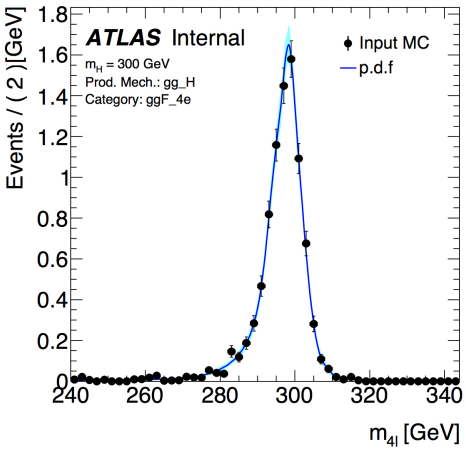

(a) ggF $4e$

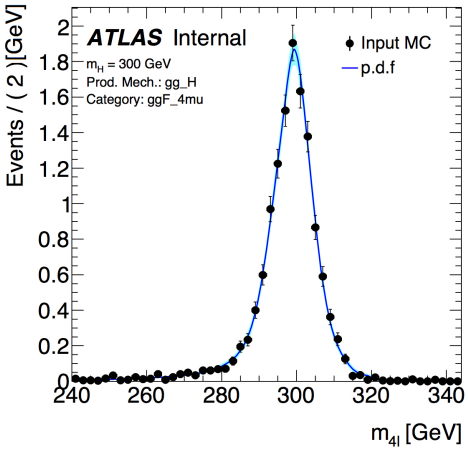

(b) ggF 4μ

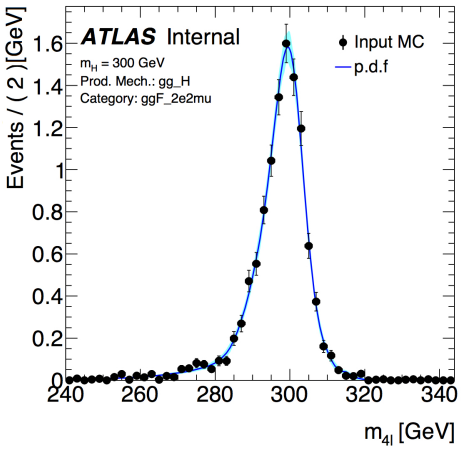

(c) ggF $2e2\mu$

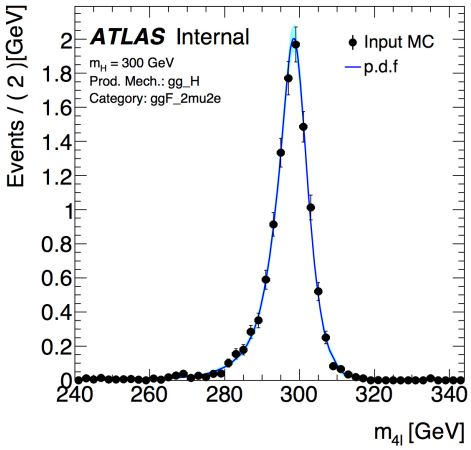

(d) ggF $2\mu2e$

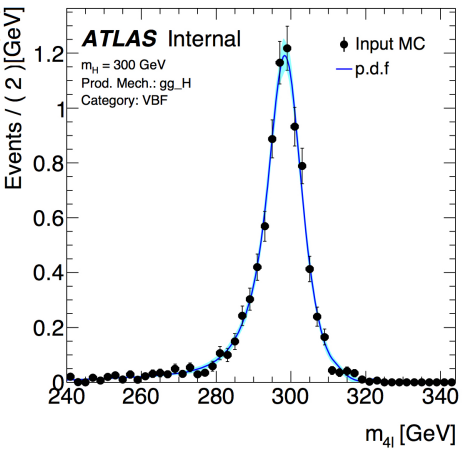

(e) VBF

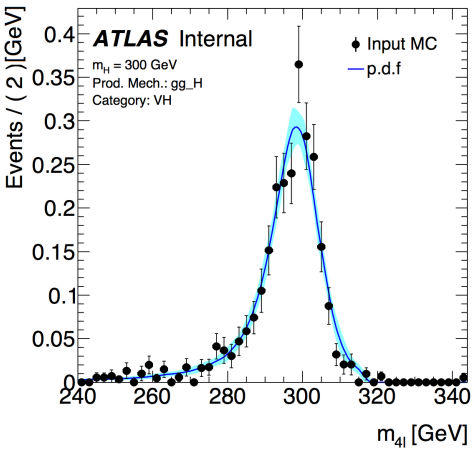

(f) VH

Figure 7.6 Smoothed KEYS pdfs for the ggF signal at $m_H = 300$ GeV (solid blue line) over the generated MC events (black dots). The light blue band indicates the MC statistical uncertainty.

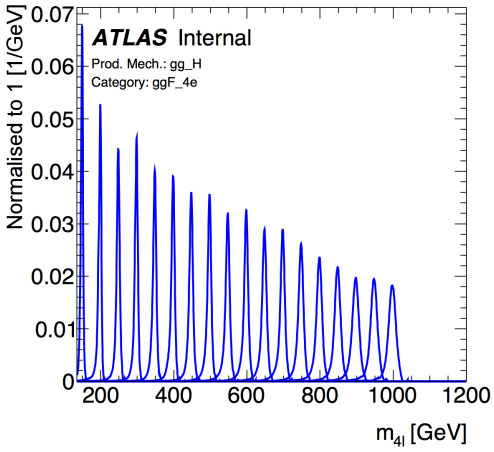

(a) ggF $4e$

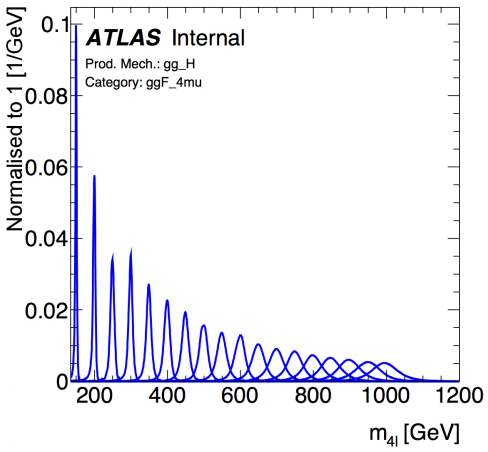

(b) ggF 4μ

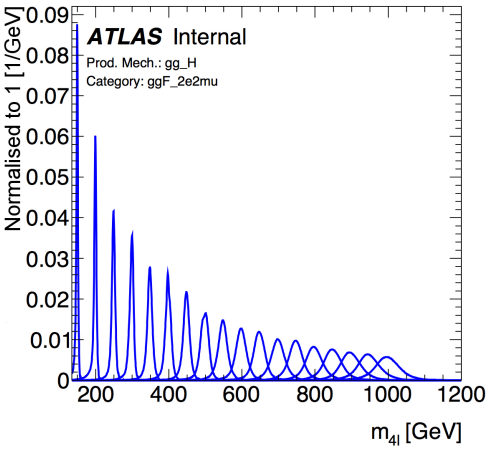

(c) ggF $2e2\mu$

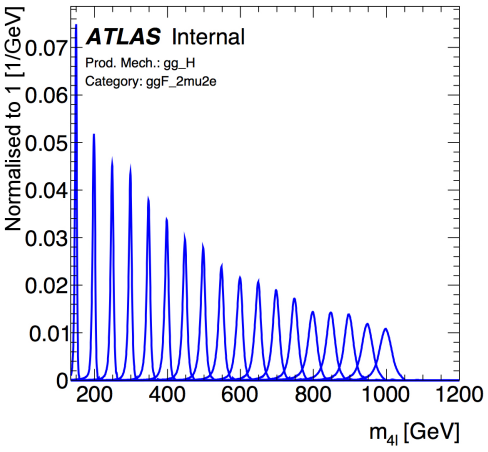

(d) ggF $2\mu2e$

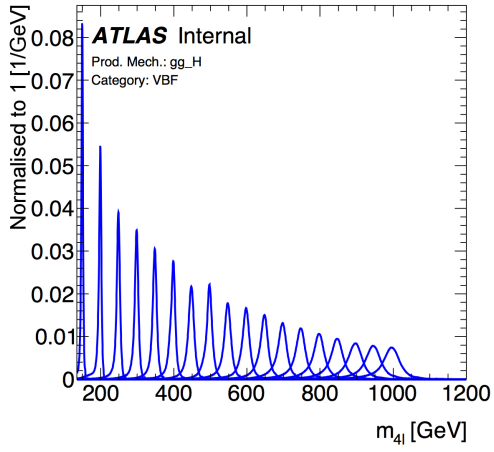

(e) VBF

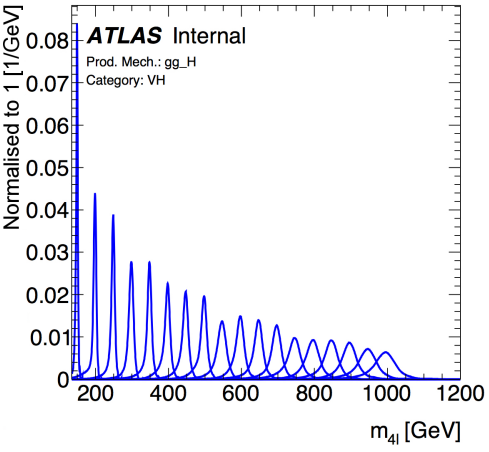

(f) VH

Figure 7.7 Signal shapes as a function of m_H for the ggF production mechanism for each of the categories. The pdf has unit normalisation.

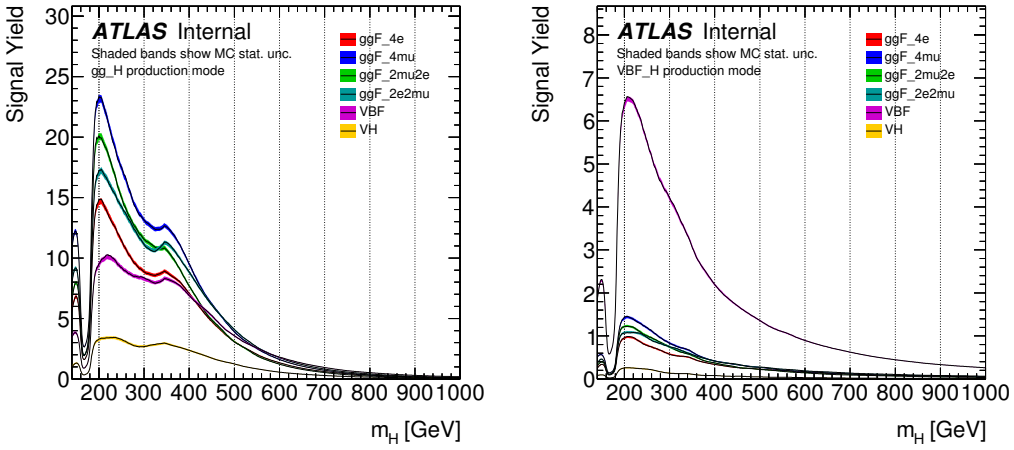

(a) ggF

(b) VBF

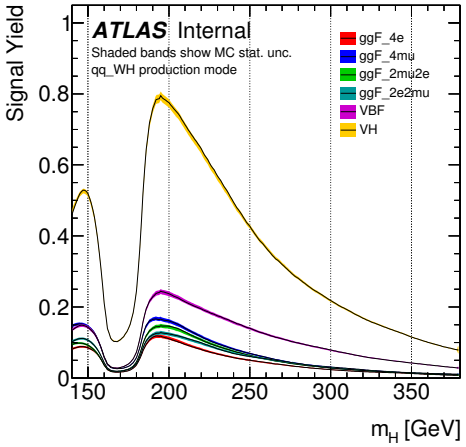

(c) WH

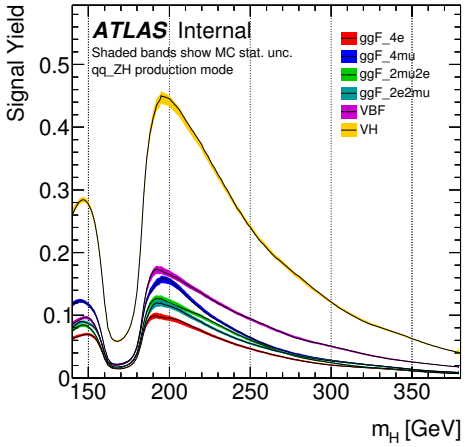

(d) ZH

Figure 7.8 Expected yields, assuming the SM cross-sections and branching ratios, for the different production mechanisms and categories. The shaded band indicates the MC statistical uncertainties on the yield.

7.7 Statistical interpretation of the model

Limits on an additional and heavier Higgs boson are obtained using unbinned profile likelihood fits. The likelihood function is a product of a Poisson term representing the probability of observing the observed number of events and a weighted sum of signal and background pdfs, see Equation (4.4). The signal strength μ is the parameter of interest in the fit and its defined as:

$$\mu = \frac{\sigma \times BR}{\sigma_{SM} \times BR_{SM}} \tag{7.2}$$

The cross-sections that can be used in the denominator can be of any choice. The SM cross-section and BR are used for convenience since they are cancelled to obtain the final limits. The observable used in the pdfs is the reconstructed invariant mass m_{4l} and the signal pdfs depend on m_H in the sense that we have a different signal pdf for a given m_H.

The dependence of the expected number of signal and background events and the shape of the pdfs, on the systematic uncertainties is described by a set of nuisance parameters θ_i described in Section (7.6). Gaussian constraints (for the systematic uncertainties) and Poisson constraints (for MC statistical uncertainties) are used to restrict the nuisance parameters to their nominal values within their estimated uncertainties. The constraints are implemented via penalty terms added to the likelihood which decrease the likelihood when any nuisance parameter is shifted from its nominal value. Therefore, the likelihood function depends on μ, m_H and θ_i.

The best fitted value for μ at a given m_H is obtained by setting the m_H parameter constant at the desired value and maximising the likelihood function with respect to μ and the nuisance parameters. To measure the compatibility of the data with the background only model ($\mu = 0$) the test statistic q_μ from Equation (4.8) is used. This test statistic is used with the CL_s method, see Section (4.5), to obtain the exclusion limits.

The signal and background shapes, and the expected yields described in Sections (7.3), (7.4) and (7.5), are used to create the final signal and background models. The events are categorised as VBF, VH, ggF 4μ, ggF $4e$, ggF $2\mu 2e$ and ggF $2e2\mu$. Separate signal and background models are used for each category and the 6 categories are fitted simultaneously.

For the model independent limits, the relative ratio of ggF and VBF production is not known, so limits are set separately on the signal strength for ggF and VBF+VH. When setting limits on the ggF signal strength (μ_{ggF}) the VBF+VH signal strength (μ_{VBF+VH}) is allowed to float freely in the fit and vice versa.

7.7.1 MC statistical and systematic uncertainties

As was mentioned in Section (7.3), uncertainties on both the overall normalisation and the shape of the pdfs arising from the limited MC statistics are included in the fit, for all signal and background models. To estimate the impact of including the MC statistical uncertainties, expected limits were set without including the systematic uncertainties

and varying the threshold for which MC statistical uncertainties to be included. It was found that the difference in the expected limits between including or not the MC statistical uncertainties was found to be less than 0.3% for the expected limits and 0.8% for the $+2\sigma$ expectation. Furthermore, it was found that neglecting the background MC statistical uncertainties gives a change of less that 0.1% in the expected limits therefore the background MC statistical uncertainties are omitted from the fit.

The 1D model was used to rank the systematic uncertainties by order of importance. Only those uncertainties which contribute more than 4% to the statistical uncertainty for either μ_{ggF} or μ_{VBF+VH} are included in the fit. Only 22 nuisance parameters survived the ranking and are included in the model: 7 from the jet energy scale uncertainties, 8 from the signal and background theory uncertainties, 3 from the reducible background modelling uncertainties, 2 from the lepton ID and reconstruction uncertainties, 1 from the underlying event uncertainty and the luminosity uncertainty.

7.8 Validation studies for the model

Validation studies were done for the heavy Higgs search model by fitting it to a pseudo-dataset, this dataset is called the *Asimov dataset*. This dataset is defined as the dataset that, when used to evaluate the estimators for all the parameters, gives as a result the true value of those parameters. The dataset can be generated from the MC samples described in Section (7.1.1) and from the signal and background pdfs, which we will refer to as the MC Asimov dataset and the pdf Asimov dataset, respectively. Figure (7.9) shows the signal plus background model assuming a heavy Higgs mass of $m_H = 600$ GeV for the full m_{4l} mass range for a signal strength of $\mu = 1$, equivalent to the SM expectation.

An Asimov validation tool, used in other analyses using the $H \to ZZ^{(*)} \to 4l$ channel, was updated for this search. The MC Asimov data is obtained by choosing m_{4l} events in between 140 GeV and 1 TeV applying appropriate weights to each event so that the normalisation of the distribution of the data is in agreement with the expected number of events. The MC Asimov data obtained for $m_H = 600$ GeV are also shown in Figure (7.9) as black dots. Good agreement is seen between the model and the dataset.

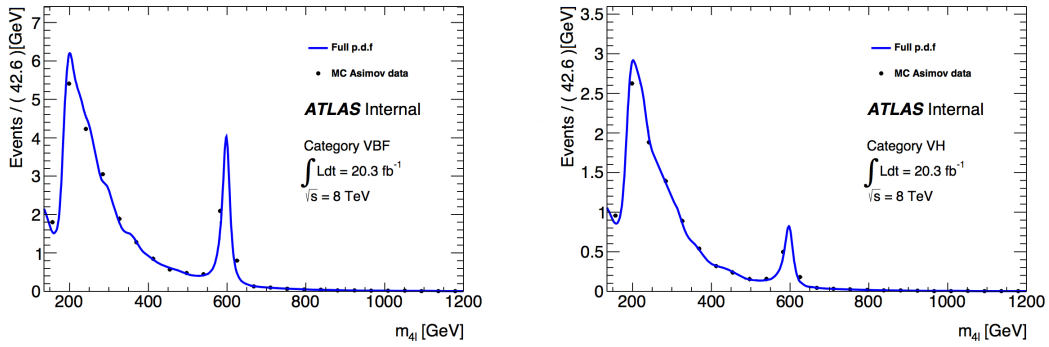

(a) VBF

(b) VH

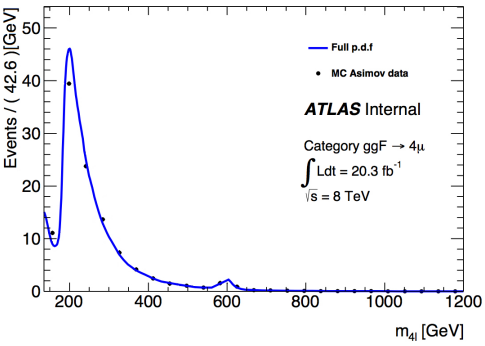

(c) ggF $\rightarrow$ H $\rightarrow 4\mu$

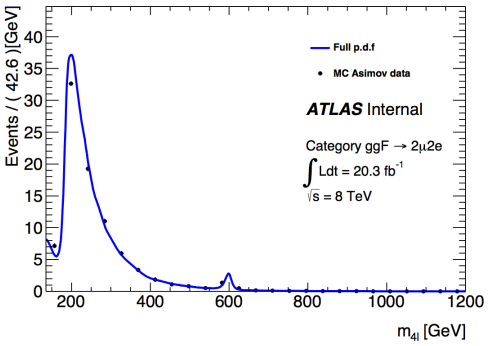

(d) ggF $\rightarrow$ H $\rightarrow 2\mu$2e

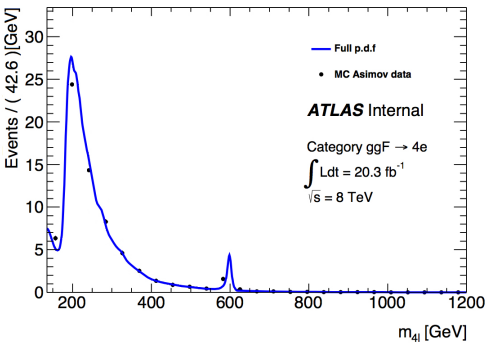

(e) ggF $\rightarrow$ H $\rightarrow$ 4e

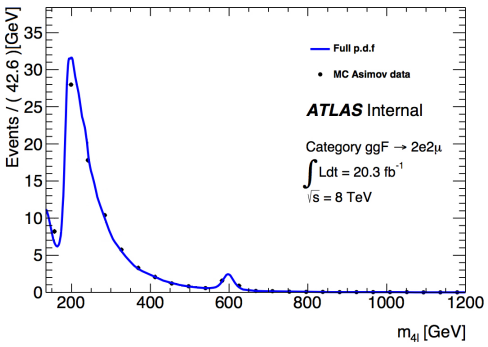

(f) ggF $\rightarrow$ H $\rightarrow$ 2e2μ

Figure 7.9 Signal plus background model (blue) assuming the SM Higgs cross-section with $\mu = 1$ and $m_H = 600$ GeV, showing the full m_{4l} range. The black points show the generated MC pseudo-dataset.

7.8.1 Study of the effect of the inclusion of the 125 GeV Higgs boson in the background model

A study on the inclusion the light Higgs boson as a background in the model was performed. The results are shown in Table (7.2). The expected values that are shown were obtained by fitting the model to a pdf Asimov dataset generated at $m_H = 140$, 300, 600 and 900 GeV and at $\mu = 1$, with and without the light Higgs included in

the background. The results are practically the same with and without the light Higgs contribution for $m_H = 300$ and 600 GeV. Small differences are seen for $m_H = 140$ and 900 GeV. In the case of $m_H = 140$ GeV the errors increase, which is expected because the contribution from the light Higgs increases the background in this region. While for the case of $m_H = 900$ GeV, the errors decrease slightly by 1% and 2% because the background decreases. For both effects, see Figure (7.1). In addition to this, the effect of the inclusion of the light Higgs on the limit calculation was studied. A 2% improvement on the limit was seen for $m_H > 500$ GeV. Therefore, the light Higgs contribution is included in the model and, also, in the Asimov data for future studies.

$\mu = 1$	Fit μ_{ggF} and error		Fit μ_{VBF+VH} and error	
	without h_{125}	with h_{125}	without h_{125}	with h_{125}
$m_H = 140$ GeV	$1.00^{+0.24}_{-0.22}$	$1.00^{+0.24}_{-0.23}$	$1.00^{+1.18}_{-0.83}$	$1.00^{+1.20}_{-0.84}$
$m_H = 300$ GeV	$1.00^{+0.20}_{-0.19}$	$1.00^{+0.20}_{-0.19}$	$1.00^{+0.91}_{-0.65}$	$1.01^{+0.91}_{-0.65}$
$m_H = 600$ GeV	$1.00^{+0.52}_{-0.46}$	$1.00^{+0.52}_{-0.46}$	$1.00^{+2.17}$	$1.01^{+2.16}$
$m_H = 900$ GeV	$1.00^{+1.92}$	$1.01^{+1.91}$	$1.00^{+3.63}$	$1.02^{+3.61}$

Table 7.2 Expected results from Asimov data generated from the pdfs for $m_H = 140, 300, 600$ and 900 GeV and $\mu = 1$, with and without light Higgs included in the background. No lower errors are assigned for some of the values because they escape the allowed range of the signal strength assuming that it has to be positive.

7.8.2 Validation by fitting to the MC Asimov data

The fit model used to extract the limits is validated by fitting the model to an Asimov dataset obtained from background MC events together with signal MC events at a hypothesised m_H value. Since these MC samples were used to produce the model, the fit should return the signal strength, μ, assumed when creating the Asimov dataset. When fitting for the ggF signal strength (μ_{ggF}), the VBF+VH signal strength is profiled and vice versa. One can also fit for the total signal strength, μ, where it is assumed that $\mu_{ggF} = \mu_{VBF+VH}$.

Figure (7.10) shows the negative logarithmic likelihood (NLL) as a function of μ, μ_{ggF} and μ_{VBF+VH} for $m_H = 600$ GeV and $\mu = 1$, where the minimum is the best fitted value. Here, the definition of NLL is $-\ln(\Lambda)$, where Λ is the profile likelihood ratio defined in Equation (4.6). The intersection of the black line perpendicular to the x axis with the red line represents the asymmetric errors. In the case of μ_{VBFVH} no lower error is found for the interval from 0 to 6.

Table (7.3) shows the results from fitting the model to a MC Asimov dataset, assuming $\mu = 1$ and for m_H values of 300, 600 and 900 GeV. The results are shown with and without systematic uncertainties in the fit. The effect of this is seen to be small compared to the statistical uncertainty. The best fitted values for the total μ and for μ_{ggF} are compatible with one.

A bias of up to 10% is seen in μ_{VBFVH}. Since the values for the total μ are generally correct, it is assumed that this bias in μ_{VBFVH} arises from the fact that the model has insufficient sensitivity to fully separate the two processes. If this were the case the bias would be expected to get smaller as μ increased. A study with $\mu = 10$ was performed to confirm this. The results are shown in Table (7.4). The biases seen for μ_{VBFVH} are reduced to 3.2%, 0.4% and 1.3% for $m_H = 300$, 600 and 900 GeV, respectively. These results demonstrate that the bias is an effect of having too few events at $\mu = 1$ to be able to distinguish ggF and VBF+VH production rather than a mismodelling of the signal or background.

$\mu = 1$	Fit μ and error		Fit μ_{ggF} and error		Fit μ_{VBF+VH} and error	
	no syst	with syst	no syst	with syst	no syst	with syst
$m_H = 300$ GeV	$1.00^{+0.16}_{-0.14}$	$1.00^{+0.17}_{-0.15}$	$0.99^{+0.23}_{-0.22}$	$0.99^{+0.26}_{-0.24}$	$1.06^{+1.19}_{-1.03}$	$1.08^{+1.36}$
$m_H = 600$ GeV	$1.00^{+0.40}_{-0.33}$	$1.00^{+0.40}_{-0.33}$	$0.99^{+0.64}_{-0.61}$	$0.99^{+0.65}_{-0.62}$	$1.08^{+3.20}$	$1.07^{+3.32}$
$m_H = 900$ GeV	$1.01^{+1.11}_{-0.68}$	$1.01^{+1.12}_{-0.68}$	$1.01^{+2.28}$	$1.00^{+2.27}$	$1.11^{+4.24}$	$1.10^{+4.26}$

Table 7.3 Expected results from pseudo-data generated from MC samples for $m_H = 300, 600$ and 900 GeV and $\mu = 1$, with and without systematic uncertainties. The "no syst" columns include the statistical MC uncertainties. No lower errors are assigned for some of the values because they escape the allowed range of the signal strength assuming that it has to be positive.

$\mu = 10$	Fit μ and error		Fit μ_{ggF} and error		Fit μ_{VBFVH} and error	
	no syst	with syst	no syst	with syst	no syst	with syst
$m_H = 300$ GeV	$10.00^{+0.42}_{-0.41}$	$10.00^{+0.64}_{-0.59}$	$9.94^{+0.53}_{-0.52}$	$9.94^{+0.84}_{-0.82}$	$10.32^{+2.37}_{-2.16}$	$10.31^{+2.56}_{-2.31}$
$m_H = 600$ GeV	$10.01^{+1.07}_{-1.00}$	$10.00^{+1.17}_{-1.11}$	$9.93^{+1.40}_{-1.35}$	$9.94^{+1.51}_{-1.48}$	$10.04^{+5.38}_{-4.33}$	$10.04^{+5.87}_{-4.76}$
$m_H = 900$ GeV	$10.00^{+2.73}_{-2.32}$	$10.00^{+2.86}_{-2.42}$	$9.88^{+4.83}_{-4.47}$	$9.89^{+4.94}_{-4.53}$	$10.13^{+8.46}_{-5.97}$	$10.13^{+8.65}_{-6.02}$

Table 7.4 Expected results from pseudo-data generated from MC for $m_H = 300, 600$ and 900 GeV and $\mu = 10$, with and without systematic uncertainties. The "no syst" columns include the statistical MC uncertainties.

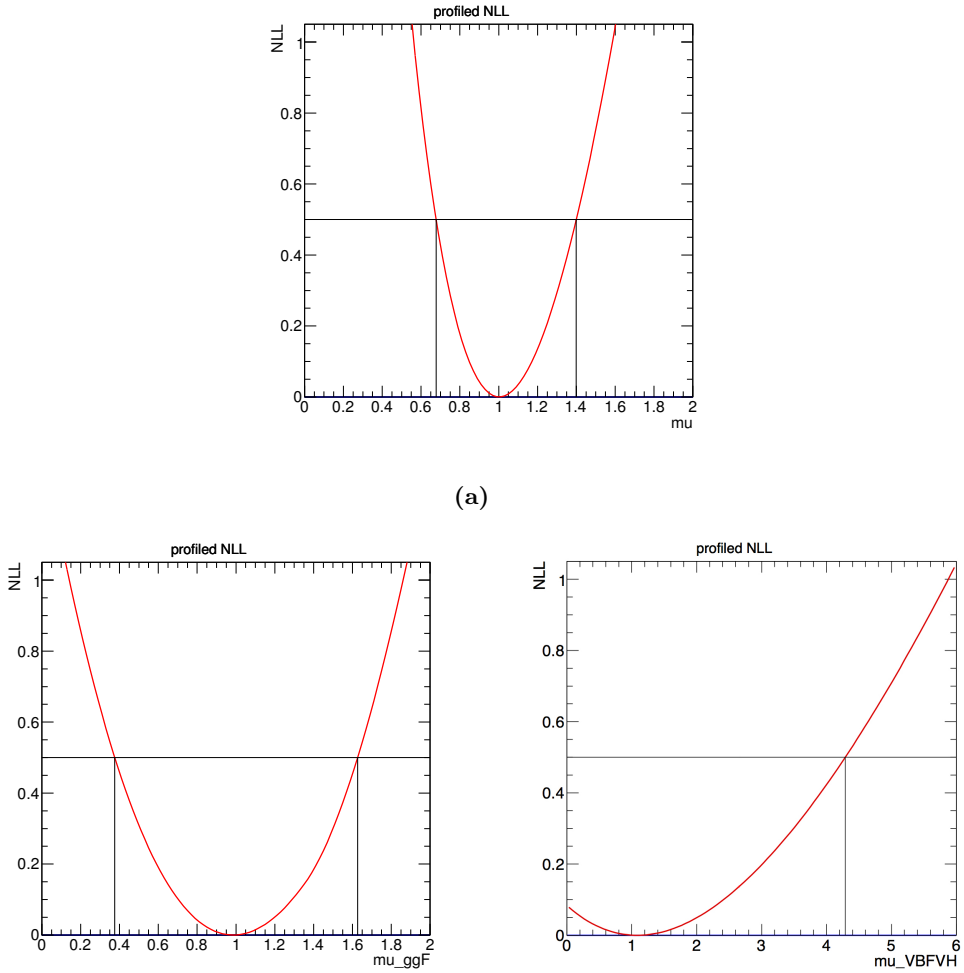

(a) **(b)** **(c)**

Figure 7.10 Negative logarithmic likelihood (NLL) function for (a) μ, (b) μ_{ggF} and (c) μ_{VBFVH} for $m_H = 600$ GeV and $\mu = 1$.

7.9 Cross-section limits in the Narrow Width Approximation

The number of selected events compared to the fitted background predictions in the ggF, VBF and VH channels are shown in Table (7.5). Also, the signal predictions are shown for $m_H = 400$ GeV and $m_H = 900$ GeV normalised to $\sigma \times BR = 1$ pb. The observed event rates are compatible with the MC prediction for the irreducible SM production of ZZ^* and the data driven estimates for minor background contributions due to Z+jets and the $t\bar{t}$ production. Upper limits on the cross-section times branching ratio in the NWA approximation are obtained as a function of m_H with the CL_s procedure in the asymptotic limit using the test statistic q_μ, see details in Chapter 4. Figure (7.11) shows the expected and observed 95% CL limits on $\sigma \times BR(H \to ZZ)$ for the ggF and

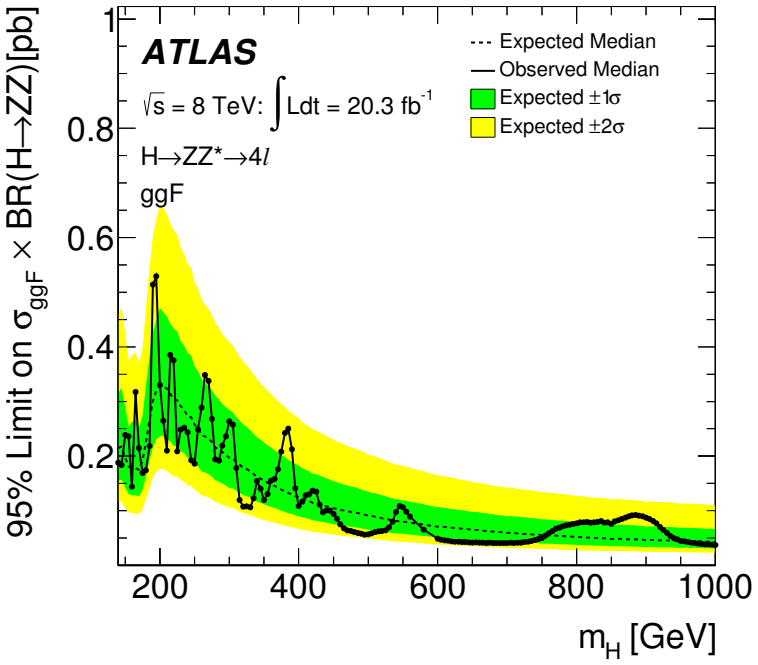

(a) ggF production mechanism

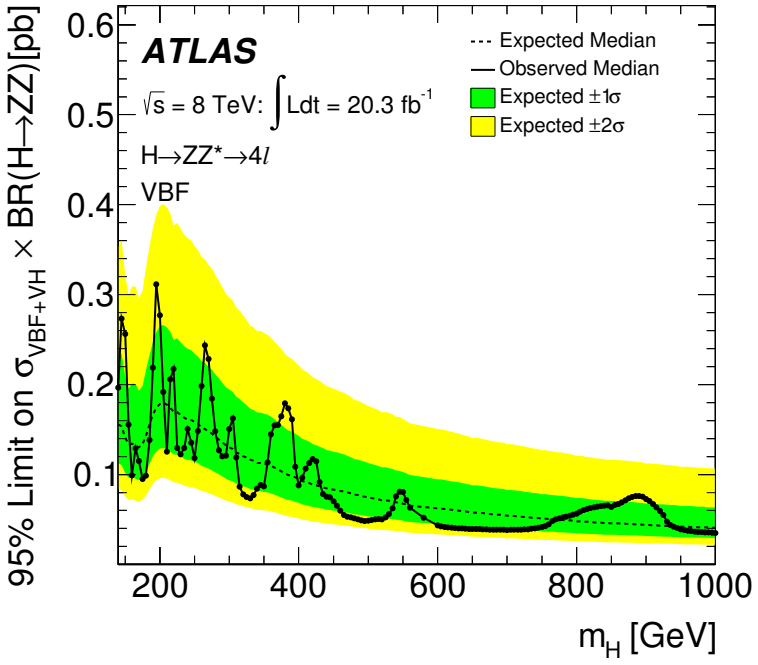

(b) VBF+VH production mechanism

Figure 7.11 Results for the heavy Higgs search in the NWA approximation in the $H \to ZZ^{(*)} \to 4l$ channel. The solid curve shows the observed 95 % CL limits on $\sigma \times BR(H \to ZZ)$. The dashed curve shows the expected limit and the coloured bands are the 1σ and 2σ ranges around the expected limit.

VBF+VH production mechanisms. When generating the null hypothesis pseudo-data for the expected limits, both μ_{ggF} and μ_{VBFVH} are set to zero and the remaining nuisance parameters are conditioned to data. For the null hypothesis pseudo-data for extracting the observed limits, the signal strength for the other signal (for example, VBF when setting limits on ggF) is conditioned to data along with the other nuisance parameters.

Component	Subchannel		
	ggF	VBF	VH
$q\bar{q} \to ZZ^*$	280 ± 20	15 ± 2	7 ± 1
$gg \to ZZ^*$	50 ± 20	5 ± 4	2 ± 1
Reducible (Z+jets , $t\bar{t}$)	12 ± 3	1 ± 1	0.5 ± 0.3
Total expected	340 ± 20	21 ± 4	9 ± 1
ggF ($m_H = 400$ GeV)	11 ± 1	2.3 ± 0.3	0.8 ± 0.1
VBF ($m_H = 400$ GeV)	6 ± 1	8 ± 1	0.31 ± 0.04
ggF ($m_H = 900$ GeV)	12 ± 1	5 ± 1	1.6 ± 0.2
VBF ($m_H = 900$ GeV)	8 ± 1	10 ± 1	0.32 ± 0.03
Observed	316	22	9

Table 7.5 Number of selected events compared to the fitted background predictions for the $H \to ZZ^{(*)} \to 4l$ search in the ggF, VBF and VH channels. Also, the signal predictions are shown for $m_H = 400$ GeV and $m_H = 900$ GeV normalised to $\sigma \times BR = 1$ pb.

In the ggF channel, for a heavy Higgs mass of $m_H = 200$ GeV ($m_H = 1$ TeV) a 95% CL limit on $\sigma_{ggF} \times BR(H \to ZZ)$ of 0.33(0.04) pb is set with an expected limit of 0.32(0.04) pb. The corresponding limit on $\sigma_{VBFVH} \times BR(H \to ZZ)$ for a heavy Higgs mass of $m_H = 200$ GeV($m_H = 1$ TeV) is 0.28 pb (0.04 pb) with an expected limit of 0.18(0.04) pb. The locations where the observed limits move into the 2σ band originates from local deviations of the input distributions from the observed data. For example, the excess occurring around 200 GeV and the deficit occurring around 300 GeV arise from observed data points that do not agree with the distribution, see Figure (7.3).

7.10 Two Higgs Doublet Model interpretations

As was mentioned at the beginning of the chapter, the interpretation of the limits in the 2HDM was done using a combined analysis, which besides the $H \to ZZ^{(*)} \to 4l$ channel, the $H \to ZZ \to l^+l^-\nu\bar{\nu}$, $H \to ZZ \to l^+l^-q\bar{q}$ and the $H \to ZZ \to \nu\bar{\nu}q\bar{q}$ channels are also included, where l stands for either an electron or a muon. For simplicity the

channels will be referred respectively as $llll$, $ll\nu\nu$, $llqq$ and $\nu\nu qq$.

Previous publications of the ATLAS collaboration [119–121] exclude a SM heavy Higgs boson with 95% CL in the ranges $182 < m_H < 233$ GeV, $256 < m_H < 265$ GeV and $268 < m_H < 415$ GeV by the $llll$ search; in the ranges $300 < m_H < 322$ GeV and $353 < m_H < 410$ GeV by the $llqq$ search; and in the range $319 < m_H < 558$ GeV by the $ll\nu\nu$ search. The improvements of this search with respect to the previous one include: using a larger dataset of 20.3 fb^{-1} of pp collision data at higher centre of mass ($\sqrt{s} = 8$ TeV), adding the $\nu\nu qq$ decay mode, further optimising the event selection and, lastly, by combining the results of all four searches.

The CMS collaboration has also published a search for a heavy Higgs boson in the $H \to ZZ$ decay channel. Here, the combined upper limit at 95% confidence level on the cross-section times the branching ratio excludes a Higgs boson with SM-like couplings and decays in the range $145 < mH < 1000$ GeV [122].

7.10.1 Overview of the combined search

The range of the Higgs boson mass used in this search goes from 140 GeV up to 1 TeV. The different channels used in this search contribute in different ways to the m_H range. For Higgs masses in the range $140 < m_H < 200$ GeV, the $llll$ decay mode is the only one considered due to its excellent mass resolution and signal to background ratio. It also includes signals coming from VH production as well as the ggF and VBF production modes. The $llqq$ and $ll\nu\nu$ searches, covering m_H ranges down to 200 GeV and 240 GeV respectively, consider the ggF and the VBF production modes only, because the VH production is only significant for Higgs boson masses below 200 GeV. The $\nu\nu qq$ search covers the m_H range down to 400 GeV and does not distinguish between ggF and VBF production. The $llqq$, $ll\nu\nu$ and the $\nu\nu qq$ decay modes dominate at higher masses, due to their higher branching ratios, and contribute to the overall sensitivity of the combined results. All searches are included up to 1 TeV.

As was mentioned in the previous sections, the ggF production mode in the $llll$ channel is further divided into four categories according to the lepton flavour in the final state. The $ll\nu\nu$ divides the ggF and VBF production modes into two according to the two lepton flavours. For the $llqq$ and $\nu\nu qq$ searches, the ggF production mode is divided into two, each based on events containing exactly two b-tagged jets (called tagged) and less than two b-tagged jets (untagged). In addition, the $llqq$ search includes another ggF category for Higgs boson masses above 700 GeV for boosted jets coming from the

Z boson decay which are reconstructed as a single jet.

The observable used in the likelihood fit depends on the search channel. The $llll$ and $llqq$ searches use the invariant mass of the four fermion system while the $ll\nu\nu$ and $\nu\nu qq$ use the transverse mass distribution. The distribution of these observables are combined in a simultaneous likelihood fit which estimates the rate of the heavy Higgs boson production and also the nuisance parameters corresponding to systematic uncertainties.

Figure (7.12) shows the distributions of the observables used in the likelihood fit for the $ll\nu\nu$, $llqq$ and $\nu\nu qq$ searches for the ggF production mechanism. Also shown are the various background components considered in each the different searches. For all plots the bottom pane shows the ratio of the observed data to the predicted background and the simulated signal is normalised to a cross-section corresponding to 5 times the observed limit. The distributions used in the $llll$ search were shown earlier in Figure (7.3).

The upper limits for the combined search were calculated for a narrow width new Higgs boson and interpretations in the Type I and Type II 2HDMs are discussed in the following section.

7.10.2 Combined cross-section times branching ratio limits in the Narrow Width Approximation

Figure (7.13) shows the limits on the cross-section times branching ratio from the combination of all the searches. The expected limits calculated from the $llll$, $ll\nu\nu$ and the combined $llqq + \nu\nu qq$ searches are also shown. At lower Higgs boson masses the $llll$ search has the best sensitivity while at high Higgs boson masses the sensitivity of the combined $llqq + \nu\nu qq$ search is the greatest followed by the $ll\nu\nu$ channel, due to their higher branching ratios, see Figure (2.5).

The observed 95% CL upper limits on the cross-section times branching ratio for a heavy Higgs boson production vary between 0.53 pb at $m_H = 195$ GeV and 0.008 pb at $m_H = 950$ GeV in the ggF channel and between 0.31 pb at $m_H = 195$ GeV and 0.009 pb at $m_H = 950$ GeV in the VBF channel. The expected 95% CL upper limits vary between 0.32 pb at $m_H = 195$ GeV and 0.013 pb at $m_H = 950$ GeV in the ggF channel and between 0.17 pb at $m_H = 195$ GeV and 0.012 pb at $m_H = 950$ GeV in the VBF channel. As it was mentioned before, the fluctuations of the observed values into the 2σ band originate from local deviations in the input distributions. Deficits at

higher mass are driven by fluctuations in the $llqq$ search, see Figure (7.12).

7.10.3 2HDM interpretations

Given the upper limits on the cross-section times branching ratio for a heavy Higgs boson, interpretations in the context of the Two Higgs Doublet Model (2HDM) are presented. For further details see Section (2.6). The upper limits are used to exclude regions of the free parameter space in the Type I and Type II 2HDM: $\tan\beta$ vs. $\cos(\beta-\alpha)$ and $\tan\beta$ vs. m_H, where α and β are defined as the rotation angles that perform that diagonalisation of the mass-squared matrix of the neutral and charged scalars, respectively.

Figure (7.14) shows the exclusion limits in the $\cos(\beta-\alpha)$ versus $\tan\beta$ plane for the Type I and Type II 2HDM models for a heavy Higgs boson with a mass of $m_H = 200$ GeV. The choice of the heavy Higgs mass is to maintain the validity of the assumption of a narrow width Higgs boson over most of the parameter space of the 2HDMs. When calculating the limits at a given choice of $\cos(\beta-\alpha)$ and $\tan\beta$, the relative rate of ggF and VBF production in the fit is set according to the prediction of the 2HDM for that parameter choice. Figure (7.15) shows the exclusion limits as a function of the heavy Higgs mass, m_H, and the parameter $\tan\beta$ for $\cos(\beta-\alpha) = -0.1$. The grey area masks regions where the width of the boson is greater than 0.5% of m_H. For the choice of $\cos(\beta-\alpha) = -0.1$ the light Higgs couplings are not altered from their SM values by more than a factor of two.

The results from both figures, (7.14) and (7.15), exclude areas where $\cos(\beta-\alpha) < 0$ and $1 < \tan\beta < 2$ for the Type I model, and areas with $0.5 < \tan\beta < 2$ for the Type II model. The white regions in the exclusion plots indicate regions of the parameter space not excluded by the present analysis. In these regions the cross-section predicted by the 2HDM is below the experimental sensitivity. Comparing with recent studies of indirect limits [123], the exclusion presented from this analysis is more precise. The ATLAS publications on this matter [119–121], previously mentioned, assume a SM prediction of the ggF and the VBF production mechanisms. Thus, they are not directly comparable with the results results shown here, which assume that the heavy Higgs boson has a narrow width, but also allow the ggF and the VBF production rates to vary independently. Finally, these results are not comparable with the CMS collaboration results [122] due to different assumptions in the analysis (e.g. SM-like Higgs couplings and interpretations in a different extension of the SM called the electroweak singlet).

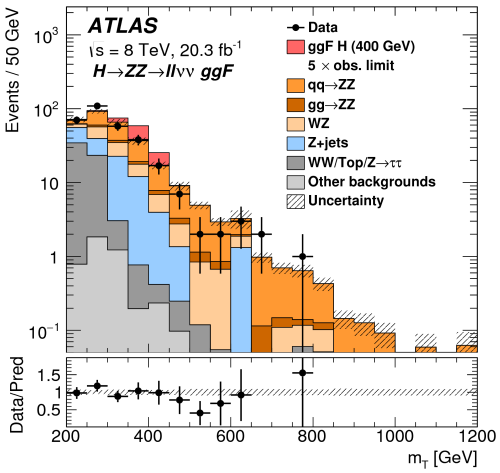

(a) $llνν$

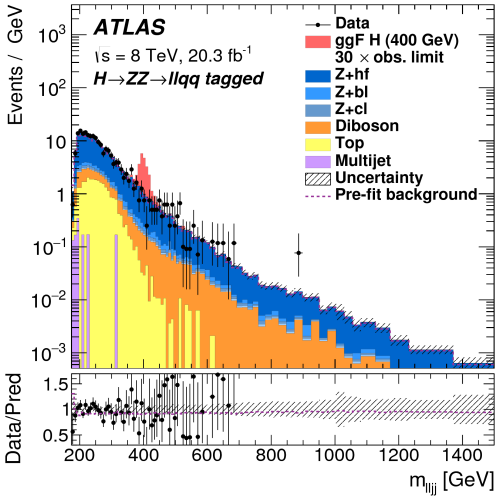

(b) $llqq$ tagged

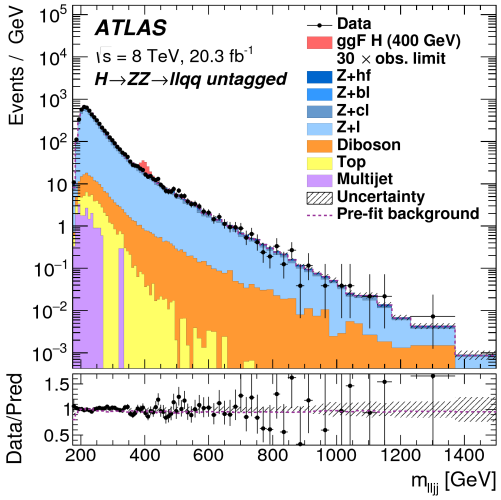

(c) $llqq$ untagged

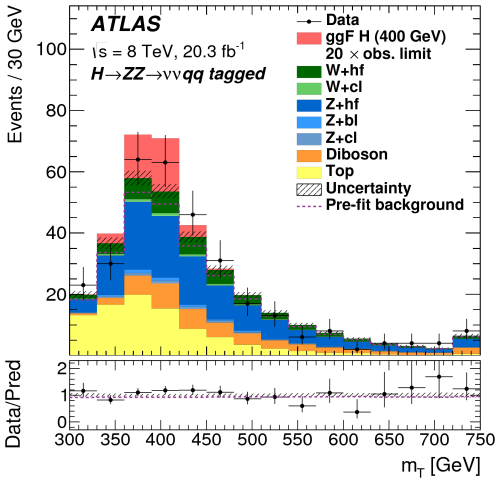

(d) $ννqq$ tagged

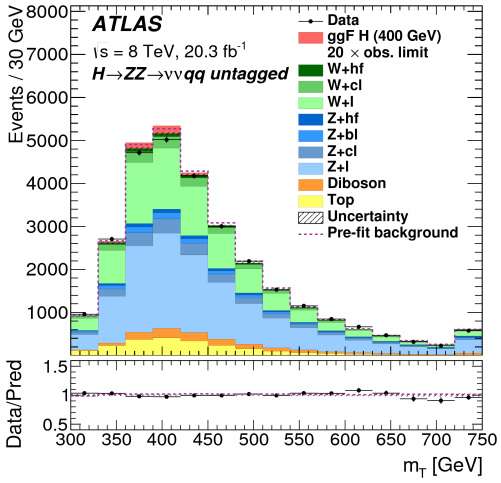

(e) $ννqq$ untagged

Figure 7.12 The distribution of (a) the transverse mass m_T^{ZZ} for the $llνν$ search from the ggF production mode, (b,c) the invariant mass of the dilepton+jet system m_{lljj} in the $llqq$ search for the tagged and untagged resolved ggF subchannels and (d,e) the distribution of the transverse mass m_T of the Z($νν$)Z(jj) system for the $ννqq$ search for the tagged and untagged subchannels of the ggF production mode at $m_H = 400$ GeV. For all plots the bottom pane shows the ratio of the observed data to the predicted background and the simulated signal is normalised to a cross-section corresponding to 5 times the observed limit [41].

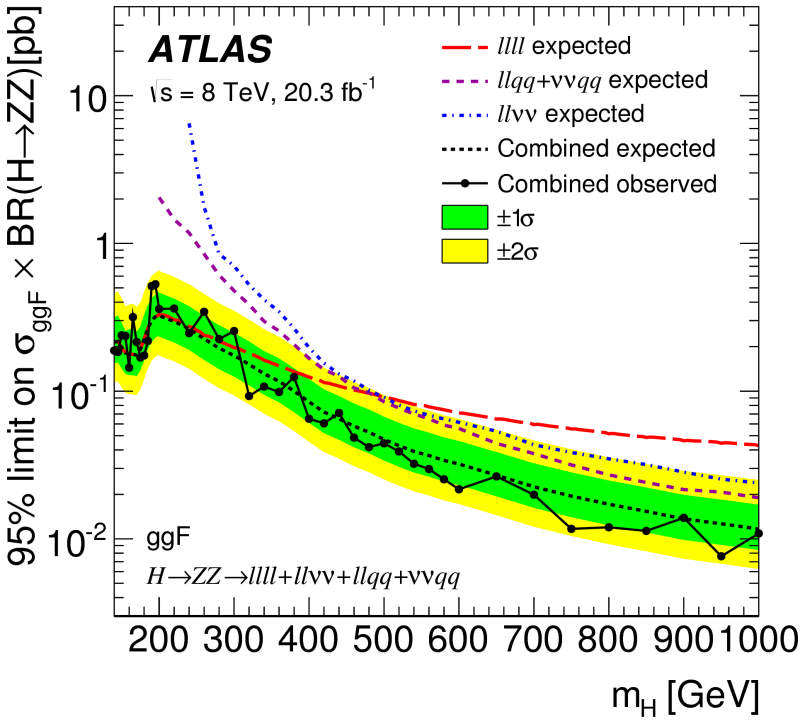

(a) ggF production mechanism

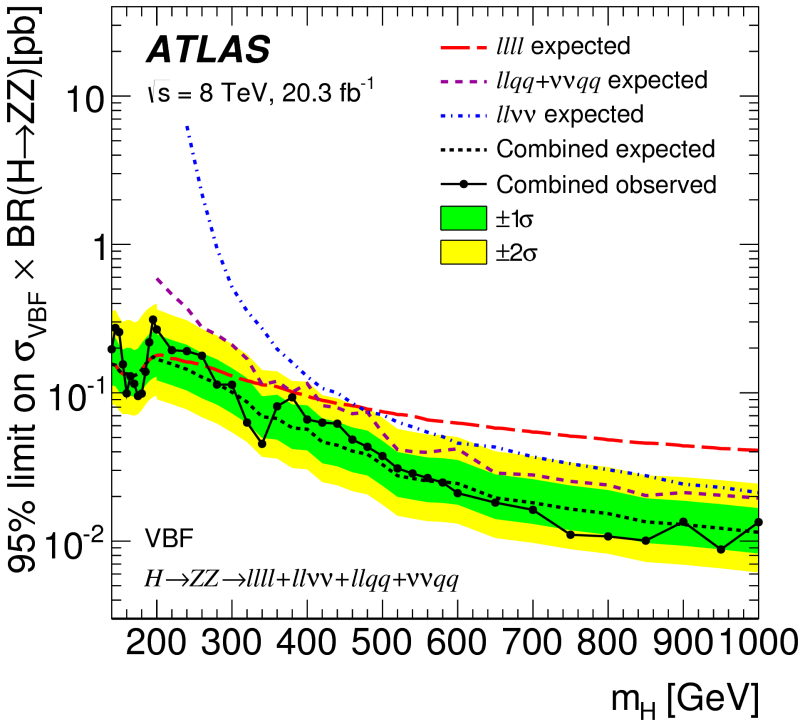

(b) VBF production mechanism

Figure 7.13 95% CL upper limits on $\sigma \times BR(H \to ZZ)$ as a function of m_H, resulting from the combination af all the searches in the (a) ggF and (b) VBF channels. The solid black line and points indicate the observed limit. The dashed black line indicate the expected limit and the bands the ± 1 and $\pm 2\sigma$ uncertainties on the expectation. The dashed coloured lines indicate the expected limits obtained from the individual searches. For the llqq and $\nu\nu$qq searches, only the combination of them is shown as they share control regions [41].

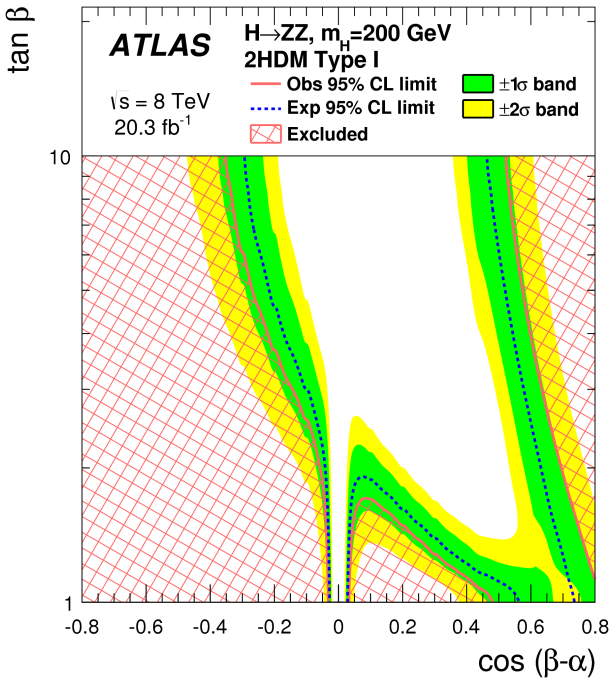

(a) Type I

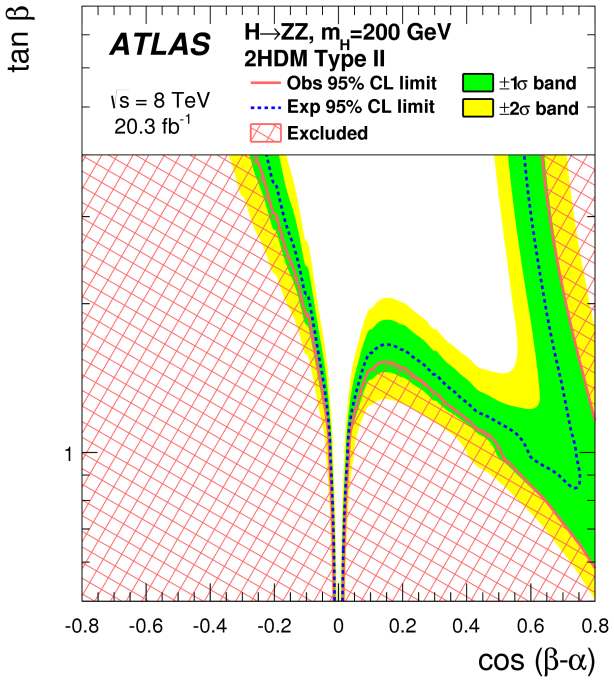

(b) Type II

Figure 7.14 95% CL exclusion contours in the 2HDM (a) Type I and (b) Type II models for $m_H = 200$ GeV, shown as a function of the parameters $\cos(\beta - \alpha)$ and $\tan\beta$. The red hatched area shows the observed exclusion coverage. The dashed blue line represents the expected exclusion contour and the coloured bands are ± 1 and $\pm 2\sigma$ uncertainties on the expectation value. The vertical axis range is set such that regions where the light Higgs couplings are enhanced by more than a factor of three from their SM values are avoided.

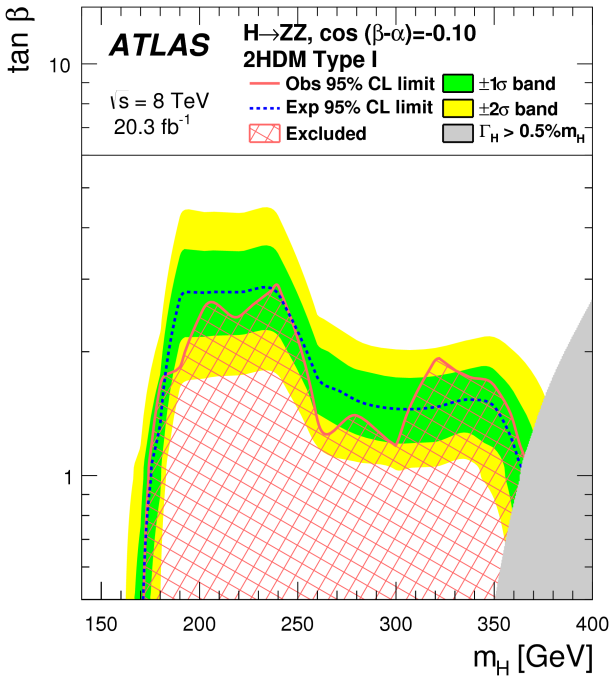

(a) ggF production mechanism

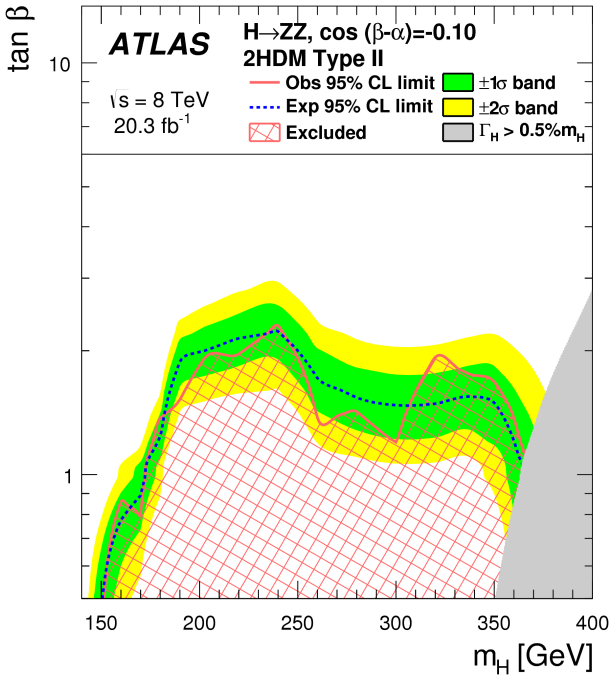

(b) VBF+VH production mechanism

Figure 7.15 95% CL exclusion contours in the 2HDM (a) Type I and (b) Type II models for $\cos(\beta - \alpha) = -0.1$, shown as a function of the heavy Higgs boson mass m_H and the parameter $\tan\beta$. The red hatched area shows the observed exclusion coverage. The dashed blue line represents the expected exclusion contour and the coloured bands are ± 1 and $\pm 2\sigma$ uncertainties on the expectation value. The grey area masks regions where the width of the boson is greater than 0.5% of m_H. For the choice of $\cos(\beta - \alpha) = -0.1$ the light Higgs couplings are not altered from their SM values by more than a factor of two.

Chapter 8

Kinematic Likelihood Fitter tool with the Z mass constraint

As mentioned in Section (5.3), it is of great importance to improve the mass resolution as much as possible because it will lead to improvements in the signal sensitivity. This will result in a more precise measurement of the Higgs boson mass or, maybe, more stringent upper limits on heavy Higgs boson searches. It is for this reason that we studied the feasibility of using the Kinematic Likelihood Fitter in the $H \to ZZ^{(*)} \to 4l$ channel to obtain an improved m_{4l} mass resolution.

In the following sections the Z mass constraint, used for the 2011 and 2012 measurements, will be explained followed by a description of the Kinematic Likelihood Fitter. Following this, the results of this study will be shown and a discussion of how to improve this will be presented.

8.1 The Z mass constraint

The Higgs mass resolution can be improved by constraining the 4-momenta of the leptons that come from the physical on-shell Z boson in such a way that the dilepton mass is consistent with the mass of the Z boson in that event within the resolution of the dilepton mass measurement. This is called the *Z mass constraint*.

The probability distribution of the mass of the Z boson, generated in a single event, m_Z^{true}, can be written as

$$\begin{aligned} p(m_Z^{true}|m_{2l}) &\propto p(m_{2l}|\sigma_{2l}, m_Z^{true}) \cdot p(m_Z^{true}|m_Z, \Gamma_Z), \\ &= G(m_{2l}|\sigma_{2l}, m_Z^{true}) \cdot BW(m_Z^{true}|m_Z, \Gamma_Z) \end{aligned} \tag{8.1}$$

where Bayes' Theorem is used. The first term on the right hand side represents a Gaussian distribution, G, which describes the smearing of the reconstructed dilepton mass, due to lepton momentum resolution, which yields an uncertainty σ_{2l} on m_{2l} around m_Z^{true}. The second term represents a Breit-Wigner distribution, BW, which describes the probability of producing a Z boson with mass m_Z^{true} given its pole m_Z and width Γ_Z.

The aim of the Z mass constraint fit is to first obtain in each event the maximum likelihood estimate of m_Z^{true} by maximising Equation (8.1), and to change the momenta (and covariance matrices) of the observed particles (two electrons or two muons) under the constraint

$$m_{2l} = m_Z^{true}. \tag{8.2}$$

In this way, the particle's momenta are constrained by the most likely true Z mass in that event.

Thus, the problem consists of a χ^2-fit of the particle momenta subject to a single non-linear constraint (Equation (8.2)). For this, it is defined:

$$\mathbf{p} = \begin{pmatrix} \vec{p_1} \\ \vec{p_2} \end{pmatrix}, \text{ and } V = \begin{pmatrix} V_1 & 0 \\ 0 & V_2 \end{pmatrix},$$

where $\mathbf{p}$ is a vector of dimension 1×6 which contains the two particles in the final state (3 momentum components for each of the two particles), and V a matrix of dimension 6×6 which contains the covariance matrices, V_1 and V_2, of the two particles.

The χ^2-fit is solved by the formalism of Lagrange multipliers [124]. The formalism is used to find local maxima and minima of a function subject to constraints by adding, counterintuitively, a new parameter, λ. In our case, we have:

$$\chi^2 = \chi'^2 - \lambda \cdot g(\mathbf{p}) \tag{8.3}$$

where χ'^2 is the χ^2 function without any constraint, λ is the set of Lagrange multipliers,

and $g(\mathbf{p})$ is the constraint which can be written as:

$$\begin{aligned} g(\mathbf{p}) &= \left[E_{tot}^2 - p_{tot}^2\right] - (m_Z^{true})^2, \\ &= g(\mathbf{p}_0) + \frac{\partial g(\mathbf{p})}{\partial \mathbf{p}}\Big|_{\mathbf{p}=\mathbf{p}_0} (\mathbf{p} - \mathbf{p}_0) + \mathcal{O}((\mathbf{p} - \mathbf{p}_0)^2), \\ &= \mathbf{d} + D\Delta\mathbf{p} + \mathcal{O}(\Delta\mathbf{p}^2) = 0, \end{aligned} \tag{8.4}$$

where $g(\mathbf{p})$ is expanded around the initial parameters $\mathbf{p}_0$. Here $\mathbf{d}$ is a one dimensional vector (the constraint evaluated at the initial parameters, $\mathbf{p}_0$), $\mathbf{\Delta p}$ is a vector of dimension 1×6 quantifying the deviations from the initial parameter estimates and $D = \frac{\partial g(\mathbf{p})}{\partial \mathbf{p}}\Big|_{\mathbf{p}=\mathbf{p}_0}$ a matrix with dimension 6×1.

Therefore, the final χ^2 to minimise is:

$$\chi^2 = \Delta\mathbf{p}^T V_{\mathbf{p}_0}^{-1} \Delta\mathbf{p} + \lambda^T (D\Delta\mathbf{p} + \mathbf{d}), \tag{8.5}$$

where the vector λ is of dimension 1(only one constraint) and $\mathbf{p}_0$ are the solutions of the unconstrained problem ($\lambda = 0$).

Now, we want to find the parameters, λ and $\mathbf{p}$. Therefore, the minimisation conditions

$$\frac{\partial \chi^2}{\partial \mathbf{p}} = 0 \qquad \text{and} \qquad \frac{\partial \chi^2}{\partial \lambda} = 0,$$

yield the equations

$$V_{\mathbf{p}_0}^{-1} \Delta\mathbf{p} + D^T \lambda = 0 \qquad \text{and} \qquad D\Delta\mathbf{p} + \mathbf{d} = 0.$$

The solution of the system is given by:

$$\begin{aligned} \lambda =& (D V_{\mathbf{p}_0} D^T)^{-1} \mathbf{d}, \\ \Delta\mathbf{p} =& \mathbf{p} - \mathbf{p}_0 = -V_{\mathbf{p}_0} D^T \lambda, \end{aligned} \tag{8.6}$$

The solution to the equations show that $\mathbf{p}$ is equal to $\mathbf{p}_0$ plus a term proportional to λ, i.e., the constraint pulls the parameters $\mathbf{p}$ away from their unconstrained values $\mathbf{p}_0$. This solution is exact in the case of linear constraints, while for non-linear constraints an iterative procedure is implemented where the estimates for the previous iteration become the initial parameter for the current iteration. The procedure continues until

the solution converges or reaches the maximum number of iterations.

Figure (8.1) shows the effect of applying the Z mass constraint on m_{12} and, in consequence, to m_{4l} for a Higgs boson with $m_H = 125$ GeV for the ggF production mechanism in the 4μ final state. In the $H \to ZZ^{(*)} \to 4l$ analysis, the Z mass constraint gives an approximately 15% improvement in the m_{4l} resolution [56].

It is proposed that further improvements on the mass resolution can be achieved by:

1. Taking into account all possible assignments of the leptons to the Z bosons. It can be possible that the Higgs candidate selection does not have the true combination of the dileptons.

2. Taking into account additional final state leptons in the event. The analysis selection discards any extra final state lepton in the event which it could have truly come from one of the Z bosons. The same can be applied to Final State Radiation (FSR) photons or to jets present in the final state.

These motivations can be addressed by the introduction of a Kinematic Likelihood Fitter.

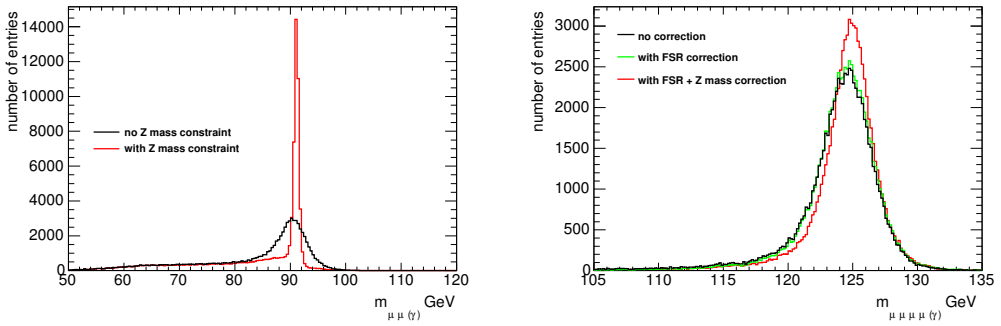

(a) **(b)**

Figure 8.1 Effect of the Z mass constraint on (a) m_{12} and (b) m_{4l} mass distributions in the 4μ final state for a simulated Higgs boson of 125 GeV from ggF production. On plot (b) the FSR recovery is also shown for comparison. The standard deviation obtained from a Gaussian fit to the peak of m_{4l} distribution is $1.79 \pm 0.01 (2.03 \pm 0.01)$ GeV with(without) Z mass constraint.

8.2 The Kinematic Likelihood Fitter

The Kinematic Likelihood Fitter (KLFitter) [125] is a package written in C++ for the estimation of precise physical parameters using the maximum likelihood method. The structure is based on ROOT [126], and the numerical maximisation of the

likelihood is performed by the Bayesian Analysis Toolkit (BAT) [127] which uses MINUIT [105]. Given a particular event topology, the KLFitter maximises the likelihood in consideration of the assumed kinematics and particle properties. The KLFitter has only been used in top quark related measurements at the ATLAS experiment. However, it has enough flexibility to be applied to any user-defined topology.

In general, the association of the measured particles to their parent particles is not unique. The KLFitter therefore is capable of calculating all possible meaningful associations (permutations) of the measured particles to the parent particles. All permutations are fitted individually and associated with a probability. Usually, the permutation with best probability is considered to be the true one.

In the context of this study, the KLFitter was changed to work for the $H \to ZZ^{(*)} \to 4l$ decay channel topology and it was implemented in the 2011-2012 event selection analysis package. The event selection described in Section (5.2) gives one combination of the assignment of the leading dilepton to the on-shell Z boson. The KLFitter was used to obtain the probabilities of all the possible assignments of the selected final state leptons to the leading Z boson using the Z mass constraint approach (see Section 8.1). Equation (8.1) is therefore interpreted as the probability of the input pair of leptons being the true leptons that came from the leading Z boson. This can be extended to add any additional leptons or jets in the final state but that was not implemented at this stage. FSR photons were included in the final state as discussed in Section (5.3.1), not as a fifth particle to permute but as a correction of the corresponding dilepton. Only the best permutation (the one with the highest probability) is considered in this study. In Section (8.5), a discussion of how it would be possible to use all of the allowed permutations is presented.

8.3 Permutations and first results

In principle, the allowed permutations of 4 leptons at the final state can be $4! = 24$. However, in a first step this is reduced to only 6 allowed permutations because we are interested in different mass combinations for the leading dilepton considered in the fit. For example, the permutation $l_1^+ l_2^- l_3^+ l_4^-$ is the same as $l_2^+ l_1^- l_3^+ l_4^-$ because they produce the same leading dilepton mass. In a second step, for the 4μ and $4e$ final states, four combinations survive due to the physical constraint of having opposite sign leptons in the pair. In the case of the $2\mu 2e$ or $2e2\mu$ final states, only two combinations survive

because the leptons in the pair must have the same flavour. For all of the allowed permutations, the probability is calculated as:

$$p_i = \frac{L_i}{\sum_i L_i}, \tag{8.7}$$

where L_i is the value of the likelihood for the best fitted parameters, in our case the leading dilepton mass, m_Z^{true}, and the sum is over the number of allowed permutations. The allowed permutations for all final states is presented in Table (8.1). It is important to mention that the combination $l_1^+ l_2^- l_3^+ l_4^-$ (the first one) is always the same one as the one given in the event selection described on Section (5.2).

Permutations	
$4\mu/4e$	$2\mu 2e/2e2\mu$
$l_1^+ l_2^- l_3^+ l_4^-$	$l_1^+ l_2^- l_3^+ l_4^-$
$l_1^+ l_4^- l_2^- l_3^+$	$l_3^+ l_4^- l_1^+ l_2^-$
$l_2^- l_3^+ l_1^+ l_4^-$	
$l_3^+ l_4^- l_1^+ l_2^-$	

Table 8.1 Allowed permutations using KLFitter in the $H \to ZZ^{(*)} \to 4l$ channel.

A first glance of how the KLFitter affects the final states by choosing the best permutation is presented in Table (8.2). It shows the percentage of events that have the best probability for a given permutation for hypothesised Higgs masses of 125, 300 and 480 GeV for all final states for the ggF production mechanism. For example, for a mass of 125 GeV 99.92% of the events have the first permutation as the best one in the 4μ final state. The results show a clear tendency to increase the percentage of events for the fourth permutation ($4\mu/4e$) and the second permutation ($2\mu 2e/2e2\mu$) of being occasionally the best one as the Higgs mass increases. This is due to the fact that when going to higher Higgs masses Z_2 becomes more on-shell making harder to choose which leptons corresponds to which Z boson. Also, the greatest improvements are achieved in the final states that contain electrons in the leading dilepton. This is due to the resolution of the electron energy and momentum, which is larger than for muons. Therefore, an improvement in the invariant mass m_{4l} resolution is expected and it will be larger as we go to higher Higgs boson masses.

As a first approach, Gaussian fits to the peak of the m_{4l} distribution were done for different hypothetical Higgs boson masses to compare the standard Z mass constraint with the KLFitter results. Figure (8.2) shows the results from the Gaussian fits for all four final states from the ggF production mechanism as a function of m_H. The red distribution shows the results for the standard Z mass constraint where no constraint

$m_H = 125$ GeV	4μ	$2\mu 2e$	$4e$	$2e2\mu$
$l_1^+ l_2^- l_3^+ l_4^-$	99.92%	99.97%	99.89%	99.99%
$l_1^+ l_4^- l_2^- l_3^+$	0.04%	0.03%	0.05%	0.01%
$l_2^- l_3^+ l_1^+ l_4^-$	0.04%	-	0.06%	-
$l_3^+ l_4^- l_1^+ l_2^-$	0.01%	-	0.01%	-
$m_H = 300$ GeV				
$l_1^+ l_2^- l_3^+ l_4^-$	95.52%	93.10%	91.38%	93.66%
$l_1^+ l_4^- l_2^- l_3^+$	0.13%	6.91%	0.24%	6.34%
$l_2^- l_3^+ l_1^+ l_4^-$	0.11%	-	0.32%	-
$l_3^+ l_4^- l_1^+ l_2^-$	4.24%	-	8.06%	-
$m_H = 480$ GeV				
$l_1^+ l_2^- l_3^+ l_4^-$	94.78%	92.91%	90.49%	90.84%
$l_1^+ l_4^- l_2^- l_3^+$	0.03%	7.09%	0.20%	9.16%
$l_2^- l_3^+ l_1^+ l_4^-$	0.03%	-	0.17%	-
$l_3^+ l_4^- l_1^+ l_2^-$	5.17%	-	9.14%	-

Table 8.2 Percentage of events with the best probability in a given permutation for $m_H = 125$, 300, and 480 GeV for the four final states for the ggF production mechanism.

is used for the subleading dilepton, given that in the analysis of Chapters 6 and 7 is not used. The blue distribution shows the results by taking the best permutation given by the KLFitter without applying the Z mass constraint to the subleading dilepton pair as well. A small, but significant, improvement in the resolution of m_{4l} can be seen from the KLFitter results as we go to higher Higgs boson masses. As it was already mentioned, this is due to Z_2 becoming more on-shell and the largest improvements come from the final states that contain electrons in the leading dilepton. This improvement will affect heavier Higgs boson searches producing stronger experimental limits or in the case of discovery a better mass measurement.

A validation of these results will be done more deeply in the following sections. Results for the m_{4l} range from 110 GeV to 140 GeV will be shown first, followed by results for the m_{4l} range from 140 GeV to 500 GeV by performing pseudo-experiments, as described in Section (6.7).

8.4 Results using the KLFitter through pseudo-experiments

Models are created in two separate m_{4l} ranges and are fitted simultaneously to pseudo-datasets created from MC samples to compare the standard Z mass constraint

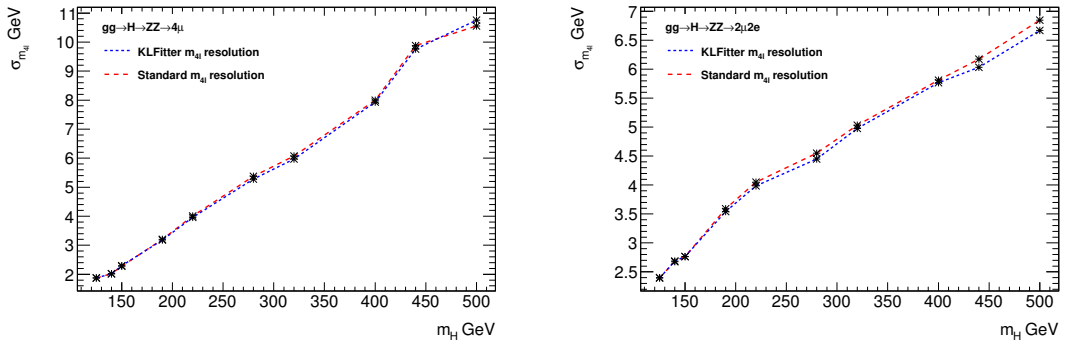

(a) $gg \to H \to ZZ^{(*)} \to 4\mu$ **(b)** $gg \to H \to ZZ^{(*)} \to 2\mu 2e$

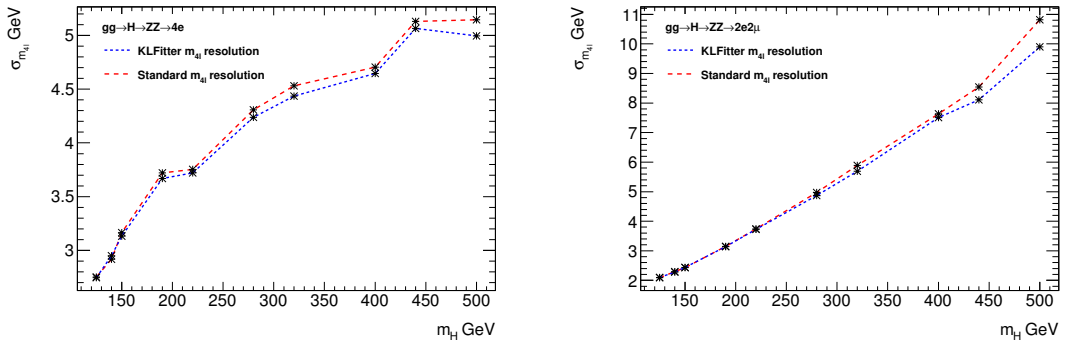

(c) $gg \to H \to ZZ^{(*)} \to 4e$ **(d)** $gg \to H \to ZZ^{(*)} \to 2e2\mu$

Figure 8.2 Distributions of $\sigma_{m_{4l}}$ as a function of m_H for all final states coming from the ggF production mechanism comparing the standard Z mass constraint (red dashed line) with the KLFitter results (blue dashed line) without constraining the subleading dilepton.

against the KLFitter approach. For convenience, we will refer to the standard Z mass constraint model as the Run I model and the model from the KLFitter approach will be referred as the KLFitter model. Both models used events from the 2012 MC samples but the only difference is that if the KLFitter finds a more probable combination of the leptons, within an event, it will use that combination to calculate m_{12}, m_{34}, and hence m_{4l}. No systematic uncertainties were considered in any of the models.

The analysis setup for both models in the mass range $110 < m_{4l} < 140$ GeV is the same as described in Chapter 6, expect that the profile likelihood is simpler and uses only the m_{4l} invariant mass as the observable. The 2012 MC signal and background samples are used exclusively for both models and are the same as described in Section (6.1.2). Only the ggF, VBF, VH and ttH production mechanisms are considered for the signal models and the histograms are smoothed and parameterised according to what is described in Section (6.2). Both models include $q\bar{q} \to ZZ^{(*)}$ and $gg \to ZZ^{(*)}$ events for the background and no smoothing was performed. The irreducible background is included as well, but for the KLFitter model no permutations of the final states were performed.

The analysis in the second mass range, $140 < m_{4l} < 500$ GeV, is similar to the one described in Chapter 6 as well. The main difference is that the 2012 signal and background MC samples used are the ones described in Section (7.1.1). For the signal models, the ggF and VBF production mechanisms are considered in the full mass range while the associated Higgs production ZH and WH mechanisms are considered only up to 280 GeV. The background models only include $q\bar{q} \rightarrow ZZ^{(*)}$ and $gg \rightarrow ZZ^{(*)}$ background contributions.

Pseudo-experiments are performed using the Run I and the KLFitter models by fitting the profile likelihood to MC pseudo-datasets as described in Section (6.7). This will return the expected error on the hypothesised Higgs mass to compare between both approaches and, in addition, check that the models used are correct. The following sections will show the results from the pseudo-experiments for both m_{4l} mass ranges.

8.4.1 Results for $110 < m_{4l} < 140$ GeV

Figure (8.3) shows the results from 2000 pseudo-experiments over the Run I and the KLFitter models for a Higgs boson mass of $m_H = 125$ GeV. The Run I expected mass is $m_H = 125.0 \pm 0.02$ GeV with a width of $\sigma_{m_H} = 0.74 \pm 0.01$ GeV. The KLFitter expected mass is of $m_H = 125.01 \pm 0.02$ GeV with and a width of $\sigma_{m_H} = 0.75 \pm 0.01$ GeV. No improvements in the mass resolution are seen for this mass range, as expected. This is due to almost all KLFitter events, with the highest probability, coming from the first permutation resulting in a m_{4l} distribution which is the same for both models, see Table (8.2). Let us remember that the first permutation from the KLFitter is the same one used in the Run I approach.

Pull distributions for m_H and the signal strength, μ, are also studied for both approaches. The m_H pull distribution shows no sign of deviations within uncertainties. The μ pull distribution has a small deviation from the mean also seen in the μ distribution. As mentioned in Section (6.7) this is a sign of low statistics. Therefore, both models are valid for this study.

8.4.2 Results for $140 < m_{4l} < 500$ GeV

Figure (8.4) shows the results from 2000 pseudo-experiments for $m_H = 300$ and 480 GeV for the Run I and the KLFitter models. For $m_H = 300$ GeV the Run I expected mass is $m_H = 299.99 \pm 0.02$ GeV with a width of of $\sigma_{m_H} = 0.85 \pm 0.01$ GeV. The KLFitter expected mass is of $m_H = 299.97 \pm 0.02$ GeV with a width of

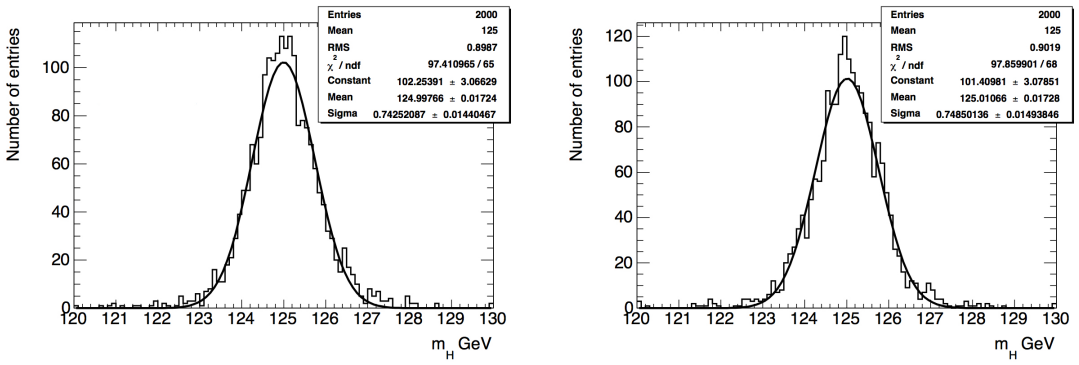

(a) **(b)**

Figure 8.3 The m_H distribution obtained from 2000 pseudo-experiments for the (a) Run I model and (b) KLFitter model for a Higgs mass of $m_H = 125$ GeV.

$\sigma_{m_H} = 0.83 \pm 0.02$. Comparing both results, only an approximate 1% improvement is seen over the Run I approach. For $m_H = 480$ GeV the Run I expected mass is $m_H = 479.96 \pm 0.05$ GeV with an error of $\sigma_{m_H} = 2.04 \pm 0.04$ GeV. The KLFitter expected mass is of $m_H = 279.92 \pm 0.04$ GeV with an error of $\sigma_{m_H} = 1.94 \pm 0.04$ GeV. A 5% improvement is seen on the expected error when comparing with the Run I approach.

Pull distributions for m_H and μ are also studied in this mass range. No significant deviations are seen, showing that both models are valid for this mass range.

Having in mind the results from Chapter 7, 95% CL expected upper limits on the signal strength σ/σ_{SM} are explored for both models in this mass range. Figure (8.5) shows the 95% CL expected upper limits on the signal strength σ/σ_{SM} as a function of m_H comparing the Run I and the KlFitter model. No noticeable improvements in the upper limits are seen for the KLFitter model compared with the Run I model. For both models, the expected upper limit is 0.14 pb for $m_H = 300$ GeV and 0.20 pb for $m_H = 480$ GeV.

8.5 Possible improvements of the results

Using the best permutation given by the KLFitter using the Z mass constraint only leads to small improvements on the m_{4l} mass resolution at higher hypothesised Higgs boson masses and no noticeable improvement in the upper limits of μ. However, the KLFitter is not being used to its full potential. There are several things that must be improved and this study has laid the pavement to achieve this.

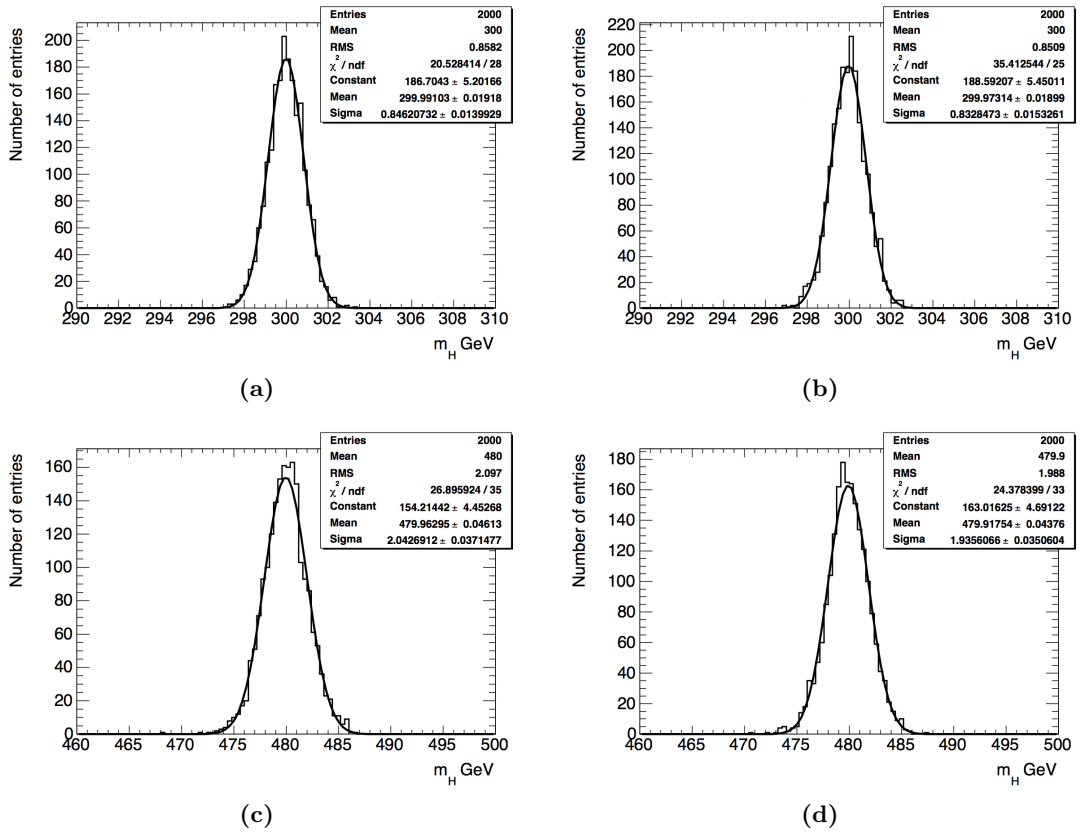

Figure 8.4 The m_H distribution obtained from 2000 pseudo-experiments for the (a) Run I model, (b) KLFfitter model for a Higgs mass of $m_H = 300$ GeV, (c) Run I model and (d) KLFitter model for a Higgs mass of $m_H = 480$ GeV.

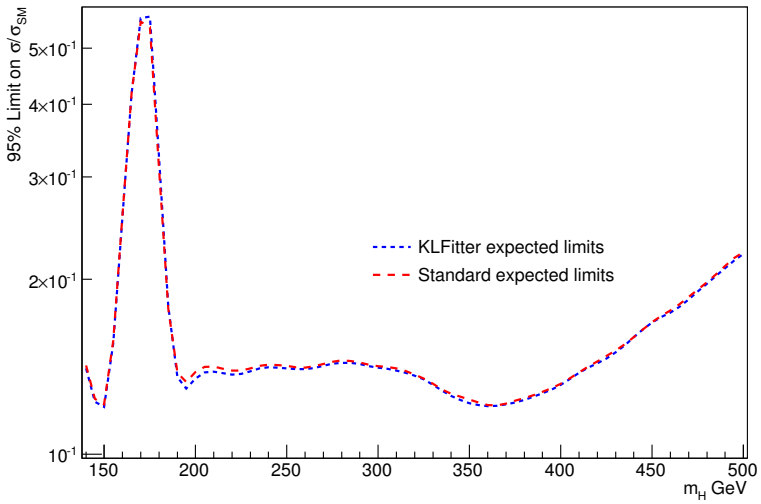

Figure 8.5 Logarithmic scale on the 95% CL expected upper limits on the signal strength σ/σ_{SM} as a function of m_H for the Run I model (red dashed line) and the KLFitter model (blue dashed line)

Including all the possible combinations of the four leptons in the final state, into the KLFitter model, is a study that must be explored. This means that, for every event, we will have four or two possible combinations, depending on the final state, with a defined m_{4l} value, and its corresponding probability which can be translated into a weight for that mass value. The likelihood function described in equation (8.1) only give us the most likely pair of leptons that come from the leading Z boson in the event; it does not give a global probability of a particular combination of the four leptons in the final state. Therefore, the Z mass constraint can not be used for this approach. In addition, the Z mass constraint can only be applied to the leading dilepton pair because, by construction, this Z boson is the one closest to the Z pole. Thus, a new likelihood must be defined that takes all of this into consideration.

The new likelihood proposed is:

$$\begin{aligned}\mathcal{L}(m_{Z_1}^{true}, m_{Z_2}^{true}|m_{12}, m_{34}, m_{4l}) =& G(m_{Z_1}^{true}|m_{12}, \sigma_{12}) \cdot G(m_{Z_2}^{true}|m_{34}, \sigma_{34}) \\ & \cdot P(m_{Z_1}^{true}, m_{Z_2}^{true}|m_{4l}),\end{aligned} \tag{8.8}$$

where, on the left hand side of the equation, $m_{Z_1}^{true}$ and $m_{Z_2}^{true}$ are the most likely masses given the reconstructed dilepton masses m_{ij} taking into account their uncertainties, σ_{ij}, and given the reconstructed mass, m_{4l}, of the event. On the right hand side, $G(m_{Z_i}^{true}|m_{ij}, \sigma_{ij})$ is a Gaussian distribution which describes the smearing of each of the reconstructed dilepton masses (as in equation (8.1)). The probability distribution function (pdf) $P(m_{Z_1}^{true}, m_{Z_2}^{true}|m_{4l})$ is a 2D function which depends on the parameters $m_{Z_1}^{true}$ and $m_{Z_2}^{true}$ which tells us the probability of those masses given the reconstructed m_{4l} of the event.

To establish the function $P(m_{Z_1}^{true}, m_{Z_2}^{true}|m_{4l})$, it is proposed to use templates to represent this distribution. For each MC sample we can obtain a 2D template using the truth information of m_{Z_1} and m_{Z_2} at generator level. As an example, Figure (8.6) shows the 2D templates for $m_H = 140$ and 480 GeV in the ggF production mechanism for the 4μ final state. The truth information used to obtain these templates uses the truth kinematics for the leptons and they are paired using the event selection from Section (5.2). Therefore, this distribution is telling us the most probable true dilepton masses for a given m_{4l} mass and, in addition, it allows us to forget the concern of whether the Z bosons are on shell or not, because this information is already included in these templates. Now, this approach only gives us templates for discrete values of m_H and the distributions are not smoothed. This problem is already addressed on Chapters 6 and 7 by means of the RooMomentMorph class in the ROOT framework

[118]. Using this class will allow us to interpolate in between the available Higgs masses to obtain templates for any mass in between a certain range. Also, to avoid statistical fluctuations from the raw histograms, the templates can be smoothed.

Therefore, using the proposed likelihood in equation (8.8) we will obtain the most probable m_{Z_1} and m_{Z_2} masses for a certain combination of the leptons in the final state and, in addition, the probability of each of the combinations to be the true one. As a result, these probabilities can be used as weights for each of the m_{4l} values obtained for each combination. The incorporation of the KLFitter weights can be done by multiplying the event weight by this weight. A new weighted distribution will be obtained where for each event four or two values of m_{4l} (depending on the final state) will be included with a weight $w = w_{event} \times w_{klfitter}$. Each of these new weighted m_{4l} values can be used to build the KLFitter model. This will improve the results shown in the previous sections by improving the mass resolution and the upper limits on the signal strength, μ. In addition, the incorporation of other leptons or jets in the final state must be explored as well.

Finally, as it was mentioned in Chapter 7, the $H \rightarrow ZZ^{(*)} \rightarrow 4l$ channel is most sensitive for Higgs boson masses below 500 GeV, compared with $ll\nu\nu$, $llqq$ and $\nu\nu qq$. As the previous results show a clear tendency to improve the mass resolution as higher Higgs masses are considered, this study could be performed in other $H \rightarrow ZZ$ channels which are more sensitive at higher masses, e.g. the $ll\nu\nu$, $llqq$ and $qq\nu\nu$ channels.

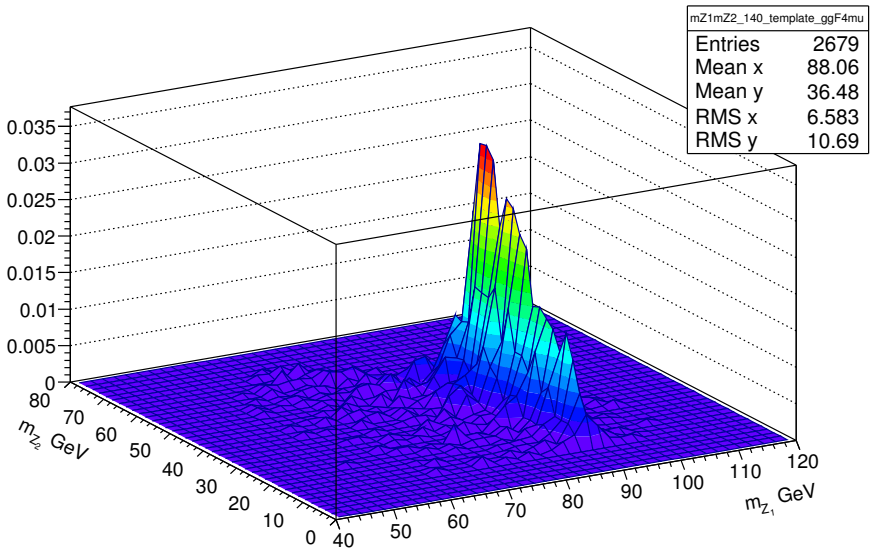

(a)

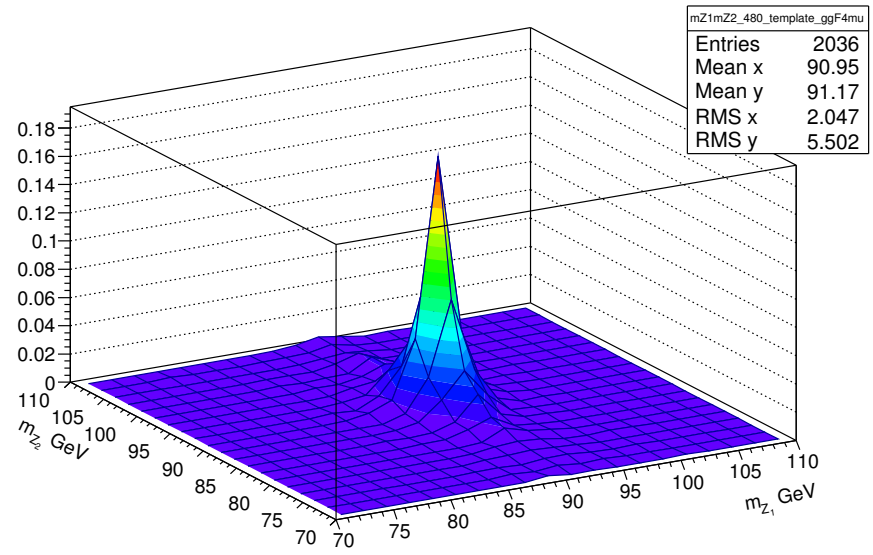

(b)

Figure 8.6 2D distribution of m_{Z_1} and m_{Z_2} for (a) $m_H = 140$ GeV and (b) 480 GeV in the ggF production mechanism for the 4μ final state, using the truth kinematic information.

Chapter 9

Conclusions

This thesis has presented the updated results obtained for the Standard Model (SM) Higgs boson mass measurement and the search for an additional heavy Higgs boson using $H \to ZZ^{(*)} \to 4l$ decay channel with the ATLAS detector at the Large Hadron Collider (LHC). In addition, a study to improve the invariant mass resolution through the Kinematic Likelihood Fitter (KLFitter) is presented.

An improved measurement of the mass of the SM Higgs boson has been derived from a two dimensional simultaneous fit to the invariant mass spectra, m_{4l}, and the BDT discriminant. The measurement was based on the $\sqrt{s} = 7$ TeV and $\sqrt{s} = 8$ TeV data samples collected by the LHC during 2011 and 2012 with a combined integrated luminosity of 25 fb^{-1}. The measured value of the SM Higgs boson mass is $m_H = 124.51 \pm 0.52(\text{stat}) \pm 0.06(\text{syst})$ GeV. This result is based on the improved calibrations for photons, electrons and muons, as well as the addition of a second observable, the BDT discriminant. Additionally, a validation of the two models used for this measurement, through pseudo-experiments, was performed. The 1D and 2D models without systematic uncertainties do not show any deviations from the input values demonstrating that the models are correct. When including systematic uncertainties, the models present some degree of biases. A study on the asymptotic limit was done to see if these biases are an effect of low statistics. The results show that the deviations were removed when away from the low statistic limit. In addition, the deviations are all within 2σ from the true value. Therefore, no corrections were applied, and the models are valid and behave as expected.

A search is presented for an additional heavy Higgs boson in the invariant mass range from 140 GeV up to 1 TeV. This search uses proton-proton collision data at a

centre-of-mass energy of 8 TeV corresponding to an integrated luminosity of 20.3 fb^{-1}. The results of the search are interpreted in the scenario of a heavy Higgs boson with a width that is small compared with the experimental resolution. No excess over the SM prediction was found, therefore upper limits on the cross-section times branching ratio were calculated. In order to set model independent limits, the analysis used separate categories to select gluon-gluon fusion (ggF) and vector boson fusion (VBF) combined with associated production (VH) like events (VBFVH) to set separated limits. In the ggF channel, for a heavy Higgs mass of $m_H = 200$ GeV($m_H = 1$ TeV) a 95% CL limit on $\sigma_{ggF} \times BR(H \to ZZ)$ of 0.33(0.04) pb is set with an expected limit of 0.32(0.04) pb. The corresponding limits on $\sigma_{VBFVH} \times BR(H \to ZZ)$ for a heavy Higgs mass of $m_H = 200$ GeV($m_H = 1$ TeV) are 0.28 pb (0.04 pb) with expected limits of 0.18(0.04) pb. The analysis of this channel is used in a combination with other ZZ channels ($llll$, $ll\nu\nu$, $llqq$ and $\nu\nu qq$). The observed 95% CL upper limits vary between 0.53 pb at $m_H = 195$ GeV and 0.008 pb at $m_H = 950$ GeV in the ggF channel and between 0.31 pb at $m_H = 195$ GeV and 0.009 pb at $m_H = 950$ GeV in the VBF channel.

The combined results are also interpreted in the context of the Type I and Type II Two Higgs Doublet Models (2HDM), with exclusion contours in the $\cos(\beta - \alpha)$ versus $\tan\beta$ plane for $m_H = 200$ GeV, and m_H versus $\tan\beta$ plane for $\cos(\beta - \alpha) = -0.1$. The 2HDM exclusion presented here is more precise than in previous analysis. The excluded regions for the Type I model are $\cos(\beta - \alpha) < 2$ and $1 < \tan\beta < 2$ and for the Type II is the same $\cos(\beta - \alpha)$ region but $\tan\beta$ is between 0.5 and 2. The model used is validated by means of a MC Asimov dataset. Biases are seen on the signal strength for the VBF+VH production mode, μ_{VBF+VH}. They are a symptom of low statistics, indicating that the model can not fully separate the ggF and the VBF+VH production modes. However, the inclusive signal strength, μ, does not present any bias so no corrections were applied and the model is considered correct.

Lastly, the feasibility of using the Kinematic Likelihood Fitter (KLFitter) with the Z mass constraint is studied in this channel. An improvement of 1% for $m_H = 300$ GeV and of 10% for $m_H = 480$ GeV is seen on the mass resolution when using the most probable permutation of the four leptons in the final state. No effect is seen on setting upper limits from this approach when comparing with the standard Z mass constraint approach. Even though the improvements are small, the full potential of the KLFitter is not yet at its maximum and a new approach is discussed to achieve this.

Bibliography

[1] The ATLAS Collaboration. Observation of a new particle in the search for the Standard Model Higgs boson with the ATLAS detector at the LHC. *Phys. Lett. B 716 (2012) 1-29*, 2012.

[2] The CMS Collaboration. Observation of a new boson at a mass of 125 GeV with the CMS detector at the LHC. *Phys. Lett. B 716 (2012) 30-61*, 2012.

[3] The ATLAS Collaboration. Measurement of the Higgs boson mass from the $H \to \gamma\gamma$ and $H \to ZZ^{(*)} \to 4l$ channels with the ATLAS detector using 25 $\text{fb}^{-1}$of pp collision data. *arXiv:1406.3827*, 2014.

[4] F. Englert and R. Brout. Broken Symmetries and the Masses of Gauge Vector Mesons. *Phys. Rev. Lett. 13 (1964) 312-323*, 1964.

[5] P. Higgs. Broken Symmetries and the Masses of Gauge Bosons. *Phys. Rev. Lett. 13 (1964) 508-509*, 1964.

[6] J. F. Gunion et al. The Higgs Hunter's Guide. *Front. Phys. 80 (2000) 1-448*, 2000.

[7] B. W. Lee et al. Weak interactions at very high energies: The role of the Higgs-boson mass. *Phys. Rev. D 16 (1977) 15191531*, 1977.

[8] A. Wingerter. Implications of the Stability and Triviality Bounds on the Standard Model with Three and Four Chiral Generations. *Phys.Rev. D84 (2011) 095012, arXiv:1109.5140 [hep-ph]*, 2011.

[9] LHC Cross Section Working Group. Handbok of LHC Higgs Cross Sections: 3. Higgs Properties. *CERN-2013-004*, 2013.

[10] LHC Cross Section Working Group. Handbok of LHC Higgs Cross Sections: 1. Inclusive Observables. *CERN-2011-002*, 2011.

[11] LHC Cross Section Working Group. Handbok of LHC Higgs Cross Sections: 2. Differential Distributions. *CERN-2012-002*, 2012.

[12] The ATLAS Collaboration. Measurements of the Higgs boson production and decay rates and coupling strengths using pp collision data at $\sqrt{s}$ =7 and 8 TeV in the ATLAS experiment. *arXiv:1507.04548 [hep-ex]*, 2015.

[13] The ATLAS Collaboration. Study of the spin and parity of the Higgs boson in diboson decays with the ATLAS detector. *arXiv:1506.05669 [hep-ex]*, 2015.

[14] H. E. Haber and G. L. Kane. The Search for Supersymmetry: Probing Physics Beyond the Standard Model. *Phys. Rep. 117 (1985) 75*, 1985.

[15] G. Branco et al. Theory and phenomenology of two-Higgs-doublet models. *Phys. Rept. 516 (2012) 1102, arXiv: 1106.0034 [hep-ph]*, 2012.

[16] M. Lamont. LHC, HL-LHC and beyond. `https://indico.cern.ch/event/218030/session/27/material/slides/1?contribId=857`, 2014.

[17] The ATLAS Collaboration. Luminosity public results. `http://www.myurl.com`.

[18] The ATLAS Collaboration. The ATLAS Experiment at the CERN Large Hadron Collider. *JINST 3 (2008) S08003*.

[19] The ATLAS Collaboration. ATLAS magnet system: Technical Design Report. *CERN-LHCC-97-018*.

[20] The ATLAS Collaboration. ATLAS inner detector: Technical Design Report. 1.

[21] The ATLAS Collaboration. ATLAS inner detector: Technical Design Report. 2.

[22] W. Blum et al. *Particle Detection with Drift Chambers*. Springer, Geneva, Switzerland, 2008.

[23] R. Gluckstern. Uncertainties in track momentum and direction, due to multiple scattering and measurement errors. *Nuclear Instruments and Methods 24 (1963) 196 no. 0, 381 389*.

[24] The ATLAS Collaboration. Expected Performance of the ATLAS Experiment. *CERN-OPEN-2008-020*.

[25] G. Aad et al. ATLAS pixel detector electronics and sensors. *JINST 3 P07007*.

[26] The ATLAS Collaboration. ATLAS Insertable B-Layer Technical Design Report. *CERN-LHCC-2010-013*.

[27] The ATLAS Collaboration. ATLAS calorimeter performance: Technical Design Report. *CERN-LHCC-96-040*.

[28] A. Krasznahorkay. The evolution of the Trigger and Data Acquisition System in the ATLAS experiment. *Tech. Rep. ATL-DAQ-PROC-2013-018*.

[29] O. Igonkina. ATLAS trigger menu and performance in Run 1 and prospects for Run 2. *Nuclear Science Symposium and Medical Imaging Conference (NSS/MIC), 2013 IEEE (2013) 14*.

[30] J. G. Panduro Vazquez. Atlas Data Acquisition: from Run I to Run II. *Tech. Rep. ATL-DAQ-SLIDE-2014-387*.

[31] The ATLAS Collaboration. Performance of the ATLAS Electron and Photon Trigger in pp Collisions at $\sqrt{s} = 7$ TeV in 2011,. *ATLAS-CONF-2012-048*.

[32] The ATLAS Collaboration. Performance of the ATLAS muon trigger in 2011. *ATLAS-CONF-2012-099*.

[33] I. Bird. Computing for the Large Hadron Collider. `http://www.annualreviews.org/doi/abs/10.1146/annurev-nucl-102010-130059`, 2011.

[34] G. Cowan et al. Asymptotic formulae for likelihood-based tests of new physics. *arXiv:1007.1727, Eur.Phys.J.C71:1554*, 2011.

[35] S.S Wilks. The large-sample distribution of the likelihood ratio for testing composite hypotheses. *Ann. Math. Statist. 9 (1938), no. 1.*

[36] A. Wald. Tests of Statistical Hypotheses Concerning Several Parameters When the Number of Observations is Large. *Transactions of the American Mathematical Society*, 54.

[37] G. Cowan. Statistics for Searches at the LHC. *Lectures presented at the 69th Scottish Universities Summer School in Physics, arXiv:1307.2487*, 2013.

[38] A. L. Read. Presentation of search results: the CL_s technique. *Nucl. Part. Phys. 28 (2002) 2693-2704*, 2002.

[39] The ATLAS Collaboration. Procedure for the LHC Higgs boson search combination in Summer 2011. *ATL-PHYS-PUB-2011-011*, 2011.

[40] The ATLAS Collaboration. Measurement of the Higgs boson mass from the $H \to \gamma\gamma$ and $H \to ZZ^{(*)} \to 4l$ channels with the ATLAS detector using 25 fb^{-1} of pp collision data. *arXiv:1406.3827, Phys. Rev. D 90, 052004 (2014)*, 2014.

[41] The ATLAS Collaboration. Search for an additional, heavy Higgs boson in the $H \to ZZ$ decay channel at $\sqrt{s} = 8$ TeV in pp collision data with the ATLAS detector. *arXiv:1507.05930, Eur. Phys. J. C76 (2016) 45*, 2016.

[42] The ATLAS Collaboration. Electron performance measurements with the ATLAS detector using the 2010 LHC proton-proton collision data. *arXiv:1110.3174*, 2012.

[43] The ATLAS Collaboration. Improved electron reconstruction in ATLAS using the Gaussian Sum Filter-based model for bremsstrahlung. *ATLAS-CONF-2012-047*, 2012.

[44] The ATLAS Collaboration. Measurements of the properties of the Higgs-like boson in the four lepton decay channel with the ATLAS detector using 25 $\text{fb}^{-1}$of proton-proton collision data. *ATLAS-CONF-2013-013*, 2013.

[45] The ATLAS Collaboration. Electron and photon energy calibration with the ATLAS detector using LHC Run 1 data. *arXiv:1407.5063*, 2014.

[46] The ATLAS Collaboration. Preliminary results on the muon reconstruction efficiency, momentum resolution, and momentum scale in ATLAS 2012 pp collision data. *ATLAS-CONF-2013-088*, 2013.

[47] M. Cacciari and G. P. Salam. Dispelling the N^3 myth for the k_t jet-finder. *arXiv:hep-ph/0512210 [hep-ph]*, 2006.

[48] W. Lampl et al. Calorimeter Clustering Algorithms: Description and Performance. *Tech. Rep. ATL-LARG-PUB-2008-002, ATL-COM-LARG-2008-003.*

[49] M. Cacciari, G. P. Salam and G. Soyez. The anti-k_t jet clustering algorithm. *arXiv:0802.1189 [hep-ph]*, 2008.

[50] The ATLAS Collaboration. Pile-up corrections for jets from proton-proton collisions at $\sqrt{s} = 7$ TeV in ATLAS in 2011. `https://atlas.web.cern.ch/Atlas/GROUPS/PHYSICS/CONFNOTES/ATLAS-CONF-2012-064/`, 2012.

[51] The ATLAS Collaboration. Pile-up subtraction and suppression for jets in ATLAS. `http://atlas.web.cern.ch/Atlas/GROUPS/PHYSICS/CONFNOTES/ATLAS-CONF-2013-083.`, 2013.

[52] The ATLAS Collaboration. Jet energy energy measurement and its systematic uncertainty in proton-proton collisions at $\sqrt{s} = 7$ TeV with the ATLAS detector. *arXiv:1406.0076 [hep-ex]*, 2015.

[53] A. Hoecker, P. Speckmayer, J. Stelzer, J. Therhaag, E. von Toerne, H. Voss. TMVA 4: Toolkit for Multivariate Data Analysis with ROOT. User Guide. *arXiv:physics/0703039*, 2009.

[54] J. Alwall, R. Frederix, S. Frixione, V. Hirschi, F. Maltoni, et al. The automated computation of tree-level and next-to-leading order differential cross sections, and their matching to parton shower simulations. *arXiv:1405.0301*, 2014.

[55] W. Lampl et al. Calorimeter clustering Algorithms: Description and Performance. *ATLAS-LARG-PUB-2008-002*, 2008.

[56] The ATLAS Collaboration. Measurements of the Higgs boson production and couplings in the four lepton decay channel with the ATLAS detector using 25 $\text{fb}^{-1}$of proton-proton collision data. *arXiv:1408.5191, Phys. Rev. D 91, 012006 (2015)*, 2015.

[57] The ATLAS Collaboration. Measurements of Higgs boson production and couplings in diboson final states with the ATLAS detector at the LHC. *arXiv:1307.1427, Phys. Lett. B 726 (2013) 88*, 2013.

[58] The ATLAS Collaboration. The ATLAS simulation Infrastructure. *arXiv:1005.4568, Eur. Phys. J. C 70 (2010) 823-874*, 2010.

[59] S. Agostinelli et al. GEANT4: A simulation toolkit. *Nucl. Instrum. Meth. A 506 (2003) 250-303*, 2003.

[60] S. Alioli et al. NLO Higgs boson production via gluon fusion matched with shower in POWHEG. *arXiv:0812.0578, JHEP 04 002*, 2009.

[61] P. Nason and C. Oleari. NLO Higgs boson production via vector-boson fusion matched with shower in POWHEG. *arXiv:0911.5299, JHEP 02 037*, 2010.

[62] D. de Florian, G. Ferrera, M. Grazzini and D. Tommasini. Transverse-momentum resumation: Higgs boson production at the Tevatron and the LHC. *arXiv:1109.2109, JHEP 11 (2011) 064*, 2011.

[63] T. Sjostrand, S. Mrenna and P. Z. Skands. A brief introduction to PYTHIA 8.1. *arXiv:0710.3820*, 2008.

[64] P. Golonka and Z. Was. PHOTOS Monte Carlo: A precision tool for QED corrections in Z and W decays. *arXiv: hep-ph/0201195 [hep-ph], Eur. Phys. J. C 45 97-107*, 2002.

[65] A. Djouadi, M.Spira and P.M. Zerwas. Production of Higgs bosons in proton colliders: QCD corrections. *Phys. Lett. B 264 (1991) 440-446*, 1991.

[66] S. Dawson. Radiative corrections to Higgs boson production. *Nucl. Phys. B 359 (1991) 283-300*, 1991.

[67] A. Djouadi, M.Spira, D. Graudenz and P.M. Zerwas. Higgs boson production at the LHC. *arXiv:hep-ph/9504378, Nucl. Phys. B 453 (1995) 17-82*, 2011.

[68] R. V. Harlander and W. B. Kilgore. Next-to-next-to-leading order Higgs production at hadron colliders. *arXiv:hep-ph/0201206, Phys. Rev. Lett. 88 (2002) 201801*, 2002.

[69] C. Anastasiou and K. Melnikov. Higgs production at hadron colliders in NNLO QCD. *arXiv:hep-ph/0207004, Phys. B 646 (2002) 220-256*, 2002.

[70] V. Ravindran, J. Smith and W. L. van Neerven. NNLO corrections to the total cross section for Higgs boson production in hadron collisions. *arXiv:hep-ph/0302135, Nucl. Phys. B 665 (2003) 325-366*, 2003.

[71] S. Catani, D. de Florian, M. Grazzini and P. Nason. Soft-gluon resummation for Higgs boson production at hadron colliders. *arXiv:hep-ph/0306211, JHEP 07 (2003) 028*, 2003.

[72] U. Aglietti, R. Bonciani, G. Degrassi and A. Vicini. Two-loop light fermion contribution to Higgs production and decays. *arXiv:hep-ph/0404071, Phys. Lett. B 595 (2004) 432-441*, 2004.

[73] S. Actis, G. Passarino, C. Sturm and S. Uccirati. NLO Electroweak Corrections to Higgs Boson Production at Hadron Colliders. *arXiv:0809.1301, Phys. Lett. B 670 (2008) 12-17*, 2008.

[74] M. Ciccolini, A. Denner and S. Dittmaier. Strong and electroweak corrections to the production of Higgs + 2 jets via weak interactions at the LHC. *arXiv:0707.0381, Phys. Rev. Lett. 99 (2007) 161803*, 2007.

[75] M. Ciccolini, A. Denner and S. Dittmaier. Electroweak and QCD corrections to Higgs production via vector-boson fusion at the LHC. *arXiv:0710.4749, Phys. Rev. D 77 (2008) 013002*, 2008.

[76] K. Arnold et al. VBFNLO: A parton level Monte Carlo for process with electroweak bosons. *arXiv:0811.4559, Comput. Phys. Commun. 180 (2009) 1661-1670*, 2009.

[77] P. Bolzoni, F. Maltoni, S. O. Moch and M. Zaro. Higgs production via vector-boson fusion at NNLO in QCD. *arXiv:1003.4451, Phys. Rev. Lett. 105 (2010) 011801*, 2010.

[78] T. Han and S. Willenbrock. QCD correction to the $pp \to WH$ and ZH total cross-sections. *Phys. Lett. B273 (1991) 167-172*, 1991.

[79] O. Brien, A. Djouadi and R. Harlander. NNLO QCD corrections to the Higgs-strahlung processes at hadron colliders. *arXiv:hep-ph/0307206, Phys. Lett. B 579 (2004) 149-156*, 2004.

[80] M. L. Ciccolini, S. Dittmaier and M. Kramer. Electroweak radiative corrections to associated WH and ZH production at hadron colliders. *arXiv:hep-ph/0306234, Phys. Rev. D 68 (2003) 073003*, 2003.

[81] Z. Kunszt. Associated production of heavy Higgs boson with top quarks. *Nucl. Phys. B247 (1984) 339*, 1984.

[82] W. Beenakker et al. Higgs Radiation of Top Quarks at the Tevatron and the LHC. *Phys. Rev. Lett. 87 (2001) 201805*, 2001.

[83] W. Beenakker et al. NLO QCD corrections to t anti-t H production in hadron colliders. *arXiv:hep-ph/0211352, Nucl. Phys. B 653 (2003) 151-203*, 2003.

[84] S. Dawson, L. H. Orr, L. Reina and D. Wackeroth. Next-to-leading order QCD corrections to $pp \to t\bar{t}H$ at the CERN Large Hadron Collider. *Phys. Rev. D67 (2003) 071503*, 2003.

[85] S. Dawson, C. Jackson, L. H. Orr, L. Reina and D. Wackeroth. Associated Higgs production with top quarks at the Large Hadron Collider: NLO QCD corrections. *arXiv:hep-ph/0305087, Phys. Rev. D 68 (2003) 034022*, 2003.

[86] A. Djouadi, J. Kalinowski and M. Spira. HDECAY: A program for Higgs boson decays in the standard model and its supersymmetric extension. *arXiv:hep-ph/9704448, Comput. Phys. Commun. 108 (1998) 56-74*, 1998.

[87] A. Bredenstein, A. Denner, S. Dittmaier and M. M. Weber. Precise predictions for the Higgs-boson decay $H \to WW/ZZ \to 4leptons$. *arXiv:hep-ph/0604011, Phys. Rev. D 74 (2006) 013004*, 2006.

[88] A. Bredenstein, A. Denner, S. Dittmaier and M. M. Weber. Radiative corrections to the semileptonic and hadronic Higgs boson decays $H \to WW/ZZ \to 4fermions$. *arXiv:hep-ph/0611234, JHEP 02 (2007) 080*, 2007.

[89] C. Anastasiou et al. Mixed QCD-electroweak corrections to Higgs boson production in gluon fusion. *arXiv:0811.3458 [hep-ph]*, 2009.

[90] D. de Florian and M. Grazzini. Higgs production through gluon fusion: Updated cross-sections at the Tevatron and the LHC. *Phys. Lett. B674, arXiv:0901.2427 [hep-ph]*, 2009.

[91] A. D. Martin et al. Parton distributions for the LHC. *arXiv:0901.0002 [hep-ph]*, 2009.

[92] R. D. Ball et al. Progress in CTEQ-TEA PDF analysis. *arXiv:1101.1300 [hep-ph]*, 2009.

[93] P. Nadolsky et al. Parton distributions for the LHC. *arXiv:1206.3321 [hep-ph], Year = 2009.*

[94] T. Melia, P.Nason, R. Rontsch and G. Zanderighi. W^+W^-, WZ and ZZ production in the the POWHEG BOX. *arXiv:1107.5051*, 2011.

[95] T. Binoth, N. Kauer and P. Mertsch. Gluon-induced QCD corrections to $pp \to ZZ \to l\bar{l}l'\bar{l}'$. *arXiv:0807.0024*, 2008.

[96] M. L. Mangano et al. ALPGEN, a generator for hard multiparton processes in hadronic collisions. *arXiv:hep-ph/0206293, JHEP 07 (2003) 001*, 2003.

[97] K. Melnikov and F. Petriello. Electroweak gauge boson production at hadron colliders through $O(\alpha_s^2)$. *arXiv:hep-ph/0609070, Phys. Rev. D 74 (2006) 114017*, 2006.

[98] C. Anastasiou, L. J. Dixon, K. Melnikov and F. Petriello. High precision QCD at hadron colliders: Electroweak gauge boson rapidity distributions at NNLO. *arXiv:hep-ph/0312266, Phys. Rev. D 69 (2004) 094008*, 2004.

[99] S. Jadach, Z. Was, R. Decker and J. H. Kuhn. The tau decay library TAUOLA: Version 2.4. *Comput. Phys. Commun. 76 (1993) 361-380*, 1993.

[100] P. Golonka at al. The tauola-photos-F environment for the TAUOLA and PHOTOS packages, release II. *Comput. Phys. Commun. 174 (2006) 818-835*, 2006.

[101] T. Gleisberg et al. Event generation with SHERPA 1.1. *arXiv:0811.4622, JHEP 02 (2009) 007*, 2009.

[102] K. S. Cranmer. Kernel estimation in high-energy physics. *arXiv:hep-ex/0011057, Comput.Phys.Commun. 136*, 2001.

[103] L. A. Piegl and W. Tiller. The NURBS book: Monographs in visual communication, ch. B-Spline Basis Function. *Springer, 2nd ed.*, 1997.

[104] L. Demortier and L. Lyons. Everything you always wanted to know about pulls. *http://physics.rockefeller.edu/luc/technical_reports/cdf5776_pulls.pdf*, 2002.

[105] F. James and M. Winkler. Minuit User's Guide. *http://seal.web.cern.ch/seal/documents/minuit/mnusersguide.pdf*, 2004.

[106] The ATLAS Collaboration. The simulation principle and performance of the ATLAS fast calorimeter simulation FastCaloSim. *ATL-PHYS-PUB-2010-013*, 2010.

[107] J. M. Campbell, R.K. Ellis and C. Williams. Gluon-gluon contributions to W^+W^- production and Higgs interference effects. *JHEP 1110 005, arXiv:1107.5569 [hep-ph]*, 2010.

[108] N. Kauer. Interference effects for $H \to WW/ZZ \to l\bar{\nu}_l\bar{l}\nu_l$ searches in gluon fusion at the LHC. *JHEP 1312 082, arXiv:1310.7011 [hep-ph]*, 2013.

[109] S. Goria, G. Passarino and D. Rosco. The Higgs Boson Lineshape. *Nucl. Phys. B864 530-579, arXiv:1112.5517 [hep-ph]*, 2012.

[110] SC. Uhlemann and N. Kauer. Narrow-width approximation accuracy. *Nucl. Phys. B814 195-211, arXiv:0807.4112 [hep-ph]*, 2009.

[111] J. Pumplin et al. New generation of parton distributions with uncertainties from global QCD analysis. *arXiv:hep-ph/050626, JHEP 0207 (2002) 012*, 2006.

[112] R. V. Harlander and S. Liebler and H. Mantler . SusHi: A program for the calculation of Higgs production in gluon fusion and bottom-quark annihilation in the Standard Model and the MSSM. *arXiv:1212.3249 [hep-ph], Comp. Phys. Comm. 184 (2013) 1605-1617*, 2013.

[113] D. Erikson, J. Rathsman and O. Stal. 2HDMC: Two-Higgs_Doublet Model Calculator Physics and Manual. *arXiv:0902.0851 [hep-ph], Comp. Phys. Comm. 181 (2010) 189-205*, 2010.

[114] F. Cascioli et al. ZZ production at hadron colliders in NNLO QCD. *arXiv:1405.2219, Phys. Lett B735*, 2014.

[115] J.M. Campbell, R. K. Ellis and C. Williams. Bounding the Higgs width at the LHC using full analytic results for $gg \to e^-e^+\mu^-\mu^+$. *arXiv:1311.3589, JHEP 1404 060*, 2014.

[116] G. Passarino. Higgs CAT. *arXiv:1312.2397 [hep-ph], Eur.Phys.J. C74 (2014) 2866*, 2014.

[117] The ATLAS Collaboration. Search for a standard model Higgs boson in the mass range 200 600 GeV in the $H \to ZZ \to l^+l^-q\bar{q}$ decay channel with the ATLAS detector. *1206.2443 [hep-ex], Phys. Lett. B 717 (2012) 70*, 2012.

[118] M. Baak et al. Interpolation between multi-dimensional histograms using a new non-linear moment morphing method. *arXiv:1410.7388 [physics.data-an]*, 2014.

[119] The ATLAS Collaboration. Search for the Standard Model Higgs boson in the decay channel $H \to ZZ^{(*)} \to 4l$ with 4.8 fb^{-1} of pp collision data at $\sqrt{s} = 7$ TeV with ATLAS. *arXiv:1202.1415 [hep-ex], Phys. Lett. B 710 (2012) 383*, 2012.

[120] The ATLAS Collaboration. Search for a standard model Higgs boson in the mass range 200600 GeV in the $H \to ZZ \to l^+l^-q\bar{q}$ decay channel with the ATLAS detector. *arXiv:1206.2443 [hep-ex], Phys. Lett. B 717 (2012) 70*, 2012.

[121] The ATLAS Collaboration. Search for a standard model Higgs boson in the $H \to ZZ \to l^+l^-\nu\bar{\nu}$ decay channel using 4.7 fb^{-1} of $\sqrt{s} = 7$ TeV data with the ATLAS detector. *arXiv:1205.6744 [hep-ex], Phys. Lett. B 717 (2012) 29*, 2012.

[122] The CMS Collaboration. Search for a Higgs boson in the mass range from 145 to 1000 GeV decaying to a pair of W or Z bosons,. *arXiv:1504.00936 [hep-ex], JHEP10(2015)144*, 2015.

[123] The ATLAS Collaboration. Constraints on new phenomena via Higgs boson couplings and invisible decays with the ATLAS detector,. *arXiv:1509.00672 [hep-ex], JHEP11(2015)206*, 2015.

[124] P. Avery. Applied Fitting Theory I: General Least Squares Theory. *CBX 01-72*, 1991.

[125] J. Erdmann, K. Kröninger, O. Nackenhorst and A. Quadt. Kinematic fitting of ttbar-events using a likelihood approach: The KLFitter package. 2009.

[126] R. Brun, F. Rademakers, P. Canal, I. Antcheva and D. Buskulic. ROOT - An Object-Orientated Data Analysis Framework. 2009.

[127] A. Caldwell, D. Kollar and K. Kröninger. BAT - The Bayesian Analysis Toolkit. 2008.

List of Figures

(2.1) Illustration of the Higgs potential $V(\Phi)$ for $\lambda > 0$ with $\mu^2 > 0$ (left) and $\mu^2 < 0$ (right). 10

(2.2) Illustration of the stability lower bound and the triviality upper bound on the Higgs mass (blue lines), from [8]. The horizontal lines indicate exclusions from LEP and LHC before the July 2012 observation[1, 2], and electroweak precision measurements of the other parameters of the SM theory. 14

(2.3) Lowest order feynman diagrams of the main production modes of the Higgs boson at the LHC. 15

(2.4) (a) Standard Model Higgs boson production cross-sections at $\sqrt{s} = 8$ TeV and (b) the total cross-sections for $\sqrt{s} = 7, 8$ and 14 TeV. 17

(2.5) (a) Standard Model Higgs boson decay branching ratios and (b) production cross-section times branching ratio at $\sqrt{s} = 8$ TeV for $m_H <$ 200 GeV [9–11]. 18

(2.6) (a) Standard Model Higgs boson decay branching ratios and (b) production cross-section times branching ratio at $\sqrt{s} = 8$ TeV for $m_H < 1$ TeV [9–11]. 19

(2.7) Invariant mass distributions of (a) the di-photon system in the $H \to \gamma\gamma$ search and (b) of the four-lepton system in the $H \to ZZ^*$ search. Both taken from [1]. 20

(2.8) (a) The total and (b) individual observed local significance p_0 as a function of the Higgs boson mass. The dashed curved indicates the expectation values for the SM Higgs boson signal hypothesis ($\mu = 1$) at the given mass and the horizontal lines show the corresponding significances in σ levels [1]. 21

(2.9) Value of $-2 \ln \Lambda$ for the mass fit as a function of m_H for the individual $H \to \gamma\gamma$ and $H \to ZZ^{(*)} \to 4l$ channels and their combination. The dashed lines show the results without systematic uncertainties. For the $H \to ZZ^{(*)} \to 4l$ channel this is indstinguishable from the solid line which includes the systematic uncertainties [3]. 22

(3.1) Schematic of the CERN accelerator complex. The LHC is represented in dark blue. 28

(3.2) Total integrated luminosity delivered by the LHC and the data recorded by ATLAS in 2011 and 2012 [17]. 30

(3.3) Schematic figure of the ATLAS detector at the LHC. 31

(3.4) View of the ATLAS detector with its coordinate system. 32

(3.5) Pseudorapidity values for different θ. 33

(3.6) Geometry of the ATLAS magnet system. 34

(3.7) Sensors and structural elements of the inner detector (in radial order): Beam Pipe, Pixel Detectors, Semi Conductor Tracker (SCT) and the Transition Radiation Tracker (TRT). 35

(3.8) Ilustration of the parameters measured in the ID. 36

(3.9) Ilustration of (a) a charged particle's path through a magnetic field and (b) a charged particle traversing detector layers (red dots) perpendicular to a uniform B field, where R is the radius of the curvature, s the sagitta of the arc with angle ϕ and L/2 the separation of the detector layers. . 37

(3.10) The ID material distribution in terms of radiation length X_0 (left) and interaction length λ (right) as a function of $|\eta|$ and averaged over ϕ [24]. 38

(3.11) Detailed scheme of the Inner Detector, with a zoom on the pixel layers [18]. 39

(3.12) Ilustration of a charged track through the different barrel layers of the ATLAS inner detector from the interaction point [18]. 40

(3.13) Ilustration of a charged track through the different end-cap layers of the ATLAS inner detector from the interaction point [18]. 41

(3.14) Ilustration of the ATLAS calorimeter system. 42

(3.15) An ilustration of the different layers of a barrel module of the ATLAS electromagnetic calorimeter. 44

(3.16) ATLAS Muon Spectrometer. 46

(3.17) Placement of the forward detectors along the beam line with respect to the ATLAS interaction point (IP) [18]. 48

(3.18) Schematic overview of the ATLAS Trigger and Data Acquisition system with design configuration [18]. The 2012 (Run-1) configurations are 20 MHz, 70 kHz, 6.5 kHz and 600 Hz [28–30]. 49

(3.19) Quarter section of the muon system in the rz plane: coincidence windows (red and blue) are shown for low and high p_{T} muons. 50

(3.20) Structure of calorimeter towers. In yellow it is shown the EM calorimeter tower, in purple the HAD calorimeter towers, and in green is shown the region of interest (ROI). 50

(3.21) Ilustration of the LHC Tier structure. At the centre it is shown the Tier-0, located at CERN, surrounded by the Tier-1 structure (yellow ovals) and the Tier-2 structure (green rectangles). 51

(4.1) The standard Gaussian distribution showing the relation between the significance Z and the p-value, where the p-value is the blue area under the curve [34]. 54

(4.2) Illustration of the relation between the p-value obtained from an observed value of the test statistic t_μ, where $f(t_\mu|\mu,\theta)$ is the probability distribution function (pdf) of t_μ under the assumption of μ [34]. 57

(4.3) Distributions of the probability distribution function, $f(Q)$, of the statistic Q under the assumption of s+b ($\mu = 1$) and background only hypothesis ($\mu = 0$) for the (a) low sensitivity case [37] and (b) high sensitivity case. 60

(4.4) Log-normal distributions with $\kappa = 1.10$, 1.20, 1.33 and 1.50 [39]. 62

(5.1) Lowest order Feynman diagram for the decay process $H \to ZZ^{(*)} \to 4l$. 64

(5.2) Lowest order Feynman diagrams for $q\bar{q} \to ZZ^{(*)}$and $gg \to ZZ^{(*)}$production. 65

(5.3) Lowest order Feynman diagram for the single resonant production mechanism. 65

(5.4) (a) Next to leading order (NLO) $pp \to ZZ \to 2e2\mu$ cross-section as a function of m_{4l}. The plot inside shows the ratio between $gg \to ZZ^{(*)}$ and $q\bar{q} \to ZZ^{(*)}$ cross-section as a function of m_{4l}. (b) Effect of the inclusion of the single resonant diagram at leading order (LO) $qq \to ZZ \to 2e2\mu$ (double resonant) cross-section as a function of m_{4l}, where a cut on the dilepton mass $m_{2l} > 12$ GeV was applied. Both plots were taken from Ref. [11]. 65

(5.5) Example of one of the lowest order feynman diagrams for the (a) $Z+jj$ and (b) $Z+bb$ irreducible backgrounds. 66

(5.6) Example of one of the lowest order feynman diagram for the $t\bar{t}$ background. 67

(5.7) Relative scale difference, ΔScale, between the measured electron energy scale and the nominal energy scale, as a function of E_{T} using $J/\Psi \to e^+e^-$ and $Z \to e^+e^-$ events (points with error bars), for four different η regions: (a) $|\eta| < 0.6$, (b) $0.6 < |\eta| < 1.37$, (c) $1.37 < |\eta| < 1.82$ and (d) $1.82 < |\eta| < 2.37$. The uncertainty on nominal energy scale for electrons is shown as the shaded area. The error bars include the systematic uncertainties specific to the $J/\Psi \to e^+e^-$ measurement [45]. 73

(5.8) Muon reconstruction efficiency as a function of η for muons with $p_{\mathrm{T}} > 20$ GeV, for different muon reconstruction types. Calo-tagged muons are used only in the region $|\eta| < 0.1$. Ratio between data and MC efficiencies is also shown. The deviation from 1 at $1.5 < \eta < 2.2$ is due to mismodelling of pixel subdetectors in the MC simulation [46]. . 75

(5.9) Muon reconstruction efficiency as a function of muon p_{T} for (a) Combined and segment-tagged muons ($0.1 < |\eta| < 2.5$) and (b) Calo-tagged muons ($|\eta| < 0.1$). Ratio between data and MC efficiencies as also shown [46]. 76

(5.10) Invariant mass distributions at generator level of (a) Z_1 at $m_H = 125$ GeV and (b) Z_2 at $m_H = 300$ GeV for gluon fusion production mechanism in the 4μ final state. 79

(5.11) (a) p_T, (b) η and (c) KD distributions for the signal (blue) and the ZZ background (red) after the event selection in the mass range $115 < m_{4l} < 130$ GeV used for the training of the BDT discriminant. 80

(5.12) (a) Distribution of the BDT response that allows the signal-background separation for the signal (blue) and the ZZ^* background (red) normalized to the same area. (b) Background rejection versus signal efficiency curves using only the KD discriminant (red) and the BDT (black). . . 81

(5.13) (a) Total decay width of the Standard Model Higgs boson Γ_H as a function of its mass [9–11] and (b) Mass resolution for the four lepton final states as a function of m_H. The mass resoultion is estimated from signal MC as the full width half maximum (FWHM) of the resolution $m_{4l} - \mathrm{m}_{4\mathrm{l}}^{\mathrm{true}}$, where $\mathrm{m}_{4\mathrm{l}}^{\mathrm{true}}$ is the true mass of the Higgs boson in the generated event. 82

(5.14) Effect of the FSR recovery on (a) m_{12} and (b) m_{4l} mass distributions in the 4μ final state for a simulated Higgs boson of 125 GeV from ggF production. 84

(6.1) Invariant mass distribution for a simulated 8 TeV signal sample from the ggF production mechanism at $m_H = 125$ GeV. The comparison between the histogram (black dots) and the resulting smoothed distribution (blue line) is shown. A +2 GeV shift (dotted blue line) in m_H is shown for illustration. 94

(6.2) B-spline basis functions for each control point (cubic interpolation). . . 94

(6.3) Continuous parametrisation in m_H for the four final states. The signal shapes shown are for the 8 TeV MC sampled in 1 GeV steps between 120 and 130 GeV and in steps of 0.5 GeV between 123 and 126 GeV. . 95

(6.4) Projection of the 2D $q\bar{q} \to ZZ^{(*)}$ background in m_{4l} overlaid with the generated MC sample for 8 TeV. 96

(6.5) Projection of the 2D $q\bar{q} \rightarrow ZZ^{(*)}$ background in the BDT variable overlaid with the generated MC sample for 8 TeV. 97

(6.6) (a) $ll + \mu\mu$ and (b) $ll + ee$ reducible background distribution for the Z+jets and $t\bar{t}$ contribution to m_{4l} for the smoothed pdf templates (red) and the input histograms (black). 98

(6.7) (a) Full m_{4l} pdf for a signal at $m_H = 125$ GeV for the 4μ final state and (b) m_{4l} signal pdf for $gg \rightarrow H \rightarrow ZZ^* \rightarrow 4l$ at $m_H = 125$ GeV (red) and for background $q\bar{q} \rightarrow ZZ \rightarrow 4\mu$ pdf (green) using the 8 TeV MC dataset. 101

(6.8) (a) Full BDT pdf for a signal at $m_H = 125$ GeV for the 4μ final state and (b) BDT signal pdf for $gg \rightarrow H \rightarrow ZZ^* \rightarrow 4l$ at $m_H = 125$ GeV (red) and for background $q\bar{q} \rightarrow ZZ \rightarrow 4\mu$ pdf (green) using the 8 TeV MC dataset. 101

(6.9) Number of events generated for each pseudo-dataset for the ggF production mechanism for the four final states. 103

(6.10) Example of a pseudo-dataset with 10000 times the number of expected events, from each pdf component, generated from the MC samples (blue) and from the pdfs (red) for the m_{4l} observable. 104

(6.11) Example of a pseudo-dataset with 10000 times the number of expected events, from each pdf component, generated from the MC samples (blue) and from the pdfs (red) for the BDT observable. 105

(6.12) (a) The m_H distribution and (b) the pull m_H distribution obtained from 2000 pseudo-experiments for the 7+ 8 TeV 2D model without systematic uncertainties. 106

(6.13) (a) The μ distribution and (b) the pull μ distribution obtained from 2000 pseudo-experiments for the 7+ 8 TeV 2D model without systematic uncertainties. 106

(6.14) (a) m_H distribution and (b) pull m_H distribution obtained from 2000 pseudo-experiments for the 7+8 TeV 2D model with systematic uncertainties. 108

(6.15) (a) μ distribution and (b) pull μ distribution obtained from 2000 pseudo-experiments for the 7+8 TeV 2D model with systematic uncertainties. . 108

(6.16) Distribution of the fitted values of (a) QCD scale theory uncertainty and (b) muon momentum scale uncertainty obtained from 2000 pseudo-experiments for the 7+8 TeV 2D model including systematic uncertainties. This uncertainties are the ones that have the largest impact on μ and m_H. 108

(6.17) (a) μ distribution and (b) pull μ distribution obtained from 2000 pseudo-experiments in the asymptotic limit for the 7 + 8 TeV 2D model including systematic uncertainties. 109

(6.18) (a) m_H and (b) μ distributions obtained from 2000 pseudo-experiments for the 7+8 TeV 2D model for the measured SM Higgs boson mass of 124.51 GeV and signal strength of 1.64. 110

(6.19) (a) Distribution of the four lepton invariant mass for the selected candidates for $80 < m_{4l} < 170$ GeV. Superimposed are the expected distributions of a SM Higgs boson signal for $m_H = 124.5$ GeV normalised to the measured signal strength, as well as the expected ZZ^* and reducible backgrounds. (b) Distribution of the BDT_{ZZ^*} output for the selected candidates for $110 < m_{4l} < 140$ GeV. The contribution of the reducible background is also separately displayed as well as the systematic uncertainties drawn as a hatched grey area. (c) Distribution of the BDT_{ZZ^*} output vs. m_{4l} for the selected candidates for $110 < m_{4l} < 140$ GeV. The expected distribution for a SM Higgs with $m_H = 124.5$ GeV is indicated by the size of the blue boxes, and the total background is indicated by the intensity of the red shading. All plot used the combined 7 and 8 TeV data samples. 111

(6.20) The profile likelihood as a function of m_H for the combination of all $H \to ZZ^* \to 4l$ final states and for the individual final states for the combined 7 and 8 TeV data samples. The combined result is shown both with and without systematics (solid and dashed line). The two are almost indistinguishable. 114

(7.1) The m_{4l} spectrum for the $gg \to ZZ$ process, comparing the expected spectrum with (black line) and without (red line) the light Higgs boson effect at $m_h = 125$ GeV, shown on (a) linear and (b) log scale. 117

(7.2) Schematic figure of the event categorisation. 120

(7.3) The distributions used in the likelihood fit of the four-lepton invariant mass m_{4l} for the $H \to ZZ^{(*)} \to 4l$ search in the (a) ggF, (b) VBF and (c) VH categories. The Z+jets and $t\bar{t}$ entry includes all backgrounds other that ZZ, as measured from data. No events are observed beyond the upper limit of the plots. The simulated $m_H = 200$ GeV signal is normalized to a cross-section corresponding to five times the observed limit. Both the VBF and the VH signal modes are shown in (b) as there is a significant contamination of VH events in the VBF category [41]. . 122

(7.4) Smoothed KEYS pdf for the $q\bar{q} \to ZZ^{(*)}$ background compared with the generated MC events. The light blue band indicates the MC statistical uncertainty. The red lines show the boundaries of the bins used in the adaptive binning procedure. 124

(7.5) Smoothed KEYS pdf for the $gg \to ZZ^{(*)}$ background compared with the generated MC events. The light blue band indicates the MC statistical uncertainty. The red lines show the boundaries of the bins used in the adaptive binning procedure. 125

(7.6) Smoothed KEYS pdfs for the ggF signal at $m_H = 300$ GeV (solid blue line) over the generated MC events (black dots). The light blue band indicates the MC statistical uncertainty. 127

(7.7) Signal shapes as a function of m_H for the ggF production mechanism for each of the categories. The pdf has unit normalisation. 128

(7.8) Expected yields, assuming the SM cross-sections and branching ratios, for the different production mechanisms and categories. The shaded band indicates the MC statistical uncertainties on the yield. 129

(7.9) Signal plus background model (blue) assuming the SM Higgs cross-section with $\mu = 1$ and $m_H = 600$ GeV, showing the full m_{4l} range. The black points show the generated MC pseudo-dataset. 132

(7.10) Negative logarithmic likelihood (NLL) function for (a) μ, (b) μ_{ggF} and (c) μ_{VBFVH} for $m_H = 600$ GeV and $\mu = 1$. 135

(7.11) Results for the heavy Higgs search in the NWA approximation in the $H \to ZZ^{(*)} \to 4l$ channel. The solid curve shows the observed 95 % CL limits on $\sigma \times BR(H \to ZZ)$. The dashed curve shows the expected limit and the coloured bands are the 1σ and 2σ ranges around the expected limit. 136

(7.12) The distribution of (a) the transverse mass m_T^{ZZ} for the $ll\nu\nu$ search from the ggF production mode, (b,c) the invariant mass of the dilepton+jet system m_{lljj} in the $llqq$ search for the tagged and untagged resolved ggF subchannels and (d,e) the distribution of the transverse mass m_T of the Z($\nu\nu$)Z(jj) system for the $\nu\nu qq$ search for the tagged and untagged subchannels of the ggF production mode at $m_H = 400$ GeV. For all plots the bottom pane shows the ratio of the observed data to the predicted background and the simulated signal is normalised to a cross-section corresponding to 5 times the observed limit [41]. 141

(7.13) 95% CL upper limits on $\sigma \times BR(H \to ZZ)$ as a function of m_H, resulting from the combination af all the searches in the (a) ggF and (b) VBF channels. The solid black line and points indicate the observed limit. The dashed black line indicate the expected limit and the bands the ± 1 and $\pm 2\sigma$ uncertainties on the expectation. The dashed coloured lines indicate the expected limits obtained from the individual searches. For the llqq and $\nu\nu$qq searches, only the combination of them is shown as they share control regions [41]. 142

(7.14) 95% CL exclusion contours in the 2HDM (a) Type I and (b) Type II models for $m_H = 200$ GeV, shown as a function of the parameters $\cos(\beta - \alpha)$ and $\tan\beta$. The red hatched area shows the observed exclusion coverage. The dashed blue line represents the expected exclusion contour and the coloured bands are ± 1 and $\pm 2\sigma$ uncertainties on the expectation value. The vertical axis range is set such that regions where the light Higgs couplings are enhanced by more than a factor of three from their SM values are avoided. 143

(7.15) 95% CL exclusion contours in the 2HDM (a) Type I and (b) Type II models for $\cos(\beta-\alpha) = -0.1$, shown as a function of the heavy Higgs boson mass m_H and the parameter $\tan\beta$. The red hatched area shows the observed exclusion coverage. The dashed blue line represents the expected exclusion contour and the coloured bands are ± 1 and $\pm 2\sigma$ uncertainties on the expectation value. The grey area masks regions where the width of the boson is greater than 0.5% of m_H. For the choice of $\cos(\beta-\alpha) = -0.1$ the light Higgs couplings are not altered from their SM values by more than a factor of two. 144

(8.1) Effect of the Z mass constraint on (a) m_{12} and (b) m_{4l} mass distributions in the 4μ final state for a simulated Higgs boson of 125 GeV from ggF production. On plot (b) the FSR recovery is also shown for comparison. The standard deviation obtained from a Gaussian fit to the peak of m_{4l} distribution is $1.79 \pm 0.01(2.03 \pm 0.01)$ GeV with(without) Z mass constraint. 148

(8.2) Distributions of $\sigma_{m_{4l}}$ as a function of m_H for all final states coming from the ggF production mechanism comparing the standard Z mass constraint (red dashed line) with the KLFitter results (blue dashed line) without constraining the subleading dilepton. 152

(8.3) The m_H distribution obtained from 2000 pseudo-experiments for the (a) Run I model and (b) KLFitter model for a Higgs mass of $m_H = 125$ GeV. 154

(8.4) The m_H distribution obtained from 2000 pseudo-experiments for the (a) Run I model, (b) KLFfitter model for a Higgs mass of $m_H = 300$ GeV, (c) Run I model and (d) KLFitter model for a Higgs mass of $m_H = 480$ GeV. 155

(8.5) Logarithmic scale on the 95% CL expected upper limits on the signal strength σ/σ_{SM} as a function of m_H for the Run I model (red dashed line) and the KLFitter model (blue dashed line) 155

(8.6) 2D distribution of m_{Z_1} and m_{Z_2} for (a) $m_H = 140$ GeV and (b) 480 GeV in the ggF production mechanism for the 4μ final state, using the truth kinematic information. 158

List of Tables

(2.1) The branching ratios of the decay modes of the Standard Model Higgs boson at $m_H = 125$ GeV. 18

(3.1) LHC beam parameters and performance overview for 2010, 2011 and 2012 data taking in comparison with design values [16]. 29

(3.2) ATLAS performance requirements for each detector component [18], where E is the energy, p_{T} is the transverse momentum, σ_E is the energy resolution, $\sigma_{p_{\mathrm{T}}}$ is the transverse momentum resolution and η the pseudorapidity. 32

(3.3) Detailed dimension and layout of the ID. 36

(3.4) ATLAS calorimeter range of pseudorapidity. 42

(3.5) Summary of the main parameters of the different ATLAS muon spectrometer subdetectors [18]. 47

(5.1) Summary of the triggers used during the 2011 data taking. The E_{T} threshold of the single electron trigger varied during the data taking, corresponding to different detector conditions (increasing interaction rate). When multiple triggers are indicated (rows), the logic OR ($\vee$) among them is requested. The index on the lepton p_{T} and E_{T} is to enumerate each lepton. 68

(5.2) Summary of the triggers used during the 2012 data taking. When multiple triggers are indicated (rows), the logic OR ($\vee$) among them is requested. The index on the lepton p_{T} and E_{T} is to enumerate each lepton. 68

(5.3) Summary of the estimated yields of the $ll + \mu\mu$ reducible backgrounds for the 7 and 8 TeV data in the full m_{4l} range. The systematic uncertainties are estimated from the transfer factor error. 86

(5.4) Summary of the estimated yields of the $ll + ee$ reducible backgrounds for the 7 and 8 TeV data in the full m_{4l} range. 87

(5.5) Summary of the estimated yields of the reducible backgrounds for the 7 and 8 TeV data in the m_{4l} range $110 < m_{4l} < 140$ GeV. 87

(6.1) Impact of the nuisance parameters on the m_H fit to data for individual final states and all final states combined for the $7 + 8$ TeV data samples. All values are given in MeV. 99

(6.2) Impact of the nuisance parameters on the μ fit to data for individual final states and all final states combined for the $7 + 8$ TeV data samples. All values are given as per mille. The relative weights of 4μ, $2\mu 2e$, $4e$ and $2e2\mu$ are 0.36, 0.09, 0.18 and 0.37, respectively. 100

(6.3) Summary table of the results of a Gaussian fit on m_H and μ and their pull distribution. The fitted m_H and μ values comes from a conditional 1D likelihood fit using pseudo-datasets generated from MC at $m_H = 125$ GeV and $\mu = 1$. 105

(6.4) Summary table of the results of a Gaussian fit on m_H and μ and their pull distribution. The fitted m_H and μ values comes from a conditional 2D likelihood fit using pseudo-datasets generated from MC at $m_H = 125$ GeV and $\mu = 1$. 106

(6.5) Summary table of the results of a Gaussian fit on m_H and μ and their pull distribution. The fitted m_H and μ values comes from a conditional 1D likelihood fit using toys generated from MC at $m_H = 125$ GeV and $\mu = 1$. 107

(6.6) Summary table of the results of a Gaussian fit on m_H and μ and their pull distribution. The fitted m_H and μ values comes from a conditional 2D likelihood fit using pseudo-datasets generated from MC at $m_H = 125$ GeV and $\mu = 1$. 107

(6.7) Summary table of the results of a Gaussian fit on m_H and μ and their pull distribution for pseudo-experiments in the asymptotic limit. The fitted m_H and μ values comes from a conditional 1D and 2D likelihood fits using pseudo-datasets generated from MC at $m_H = 125$ GeV and $\mu = 1$. 109

(6.8) The number of expected and observed events for a $m_H = 125$ GeV hypothesis for the four lepton final states. The second column shows the number of expected signal events for the full mass range. The other columns show the number of expected signal events, the number of ZZ^* and reducible background events, the signal to background ratio (s/b) and the number of observed events in the mass range of $120 < m_{4l} < 130$ GeV for the 7 and 8 TeV data as well as for the combined sample. . 112

(6.9) Measured Higgs boson masses and signal strengths in the different final states and after combination as obtained from the 2D conditional model using the 7 TeV and 8 TeV datasets. 113

(7.1) Summary of the reducible background estimates for $140 < m_{4l} < 1000$ GeV. The quoted uncertainties include the combined statistical and systematic components. 123

(7.2) Expected results from Asimov data generated from the pdfs for $m_H = 140, 300, 600$ and 900 GeV and $\mu = 1$, with and without light Higgs included in the background. No lower errors are assigned for some of the values because they escape the allowed range of the signal strength assuming that it has to be positive. 133

(7.3) Expected results from pseudo-data generated from MC samples for $m_H = 300, 600$ and 900 GeV and $\mu = 1$, with and without systematic uncertainties. The "no syst" columns include the statistical MC uncertainties. No lower errors are assigned for some of the values because they escape the allowed range of the signal strength assuming that it has to be positive. 134

(7.4) Expected results from pseudo-data generated from MC for $m_H = 300, 600$ and 900 GeV and $\mu = 10$, with and without systematic uncertainties. The "no syst" columns include the statistical MC uncertainties. 134

(7.5) Number of selected events compared to the fitted background predictions for the $H \to ZZ^{(*)} \to 4l$ search in the ggF, VBF and VH channels. Also, the signal predictions are shown for $m_H = 400$ GeV and $m_H = 900$ GeV normalised to $\sigma \times BR = 1$ pb. 137

(8.1) Allowed permutations using KLFitter in the $H \to ZZ^{(*)} \to 4l$ channel. . 150

(8.2) Percentage of events with the best probability in a given permutation for $m_H = 125$, 300, and 480 GeV for the four final states for the ggF production mechanism. 151